

Durham E-Theses

Solid-state NMR of tin, lithium and phosphorus compounds

Cherryman, Julian Christopher

How to cite:

Cherryman, Julian Christopher (1998) *Solid-state NMR of tin, lithium and phosphorus compounds*, Durham theses, Durham University. Available at Durham E-Theses Online:
<http://etheses.dur.ac.uk/4667/>

Use policy

The full-text may be used and/or reproduced, and given to third parties in any format or medium, without prior permission or charge, for personal research or study, educational, or not-for-profit purposes provided that:

- a full bibliographic reference is made to the original source
- a [link](#) is made to the metadata record in Durham E-Theses
- the full-text is not changed in any way

The full-text must not be sold in any format or medium without the formal permission of the copyright holders.

Please consult the [full Durham E-Theses policy](#) for further details.

Solid-State NMR of Tin, Lithium and Phosphorus Compounds

by

Julian Christopher Cherryman

M. A. Cantab.

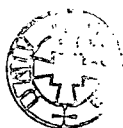
The copyright of this thesis rests
with the author. No quotation
from it should be published
without the written consent of the
author and information derived
from it should be acknowledged.

A thesis submitted in partial fulfilment of the requirements for
the degree of Doctor of Philosophy

Department of Chemistry

University of Durham

1998



24 FEB 1999

Solid-State NMR of Tin, Lithium and Phosphorus Compounds

Julian Christopher Cherryman, M. A. Cantab.

Submitted for the degree of Doctor of Philosophy, 1998.

Abstract

NMR spectroscopy is a powerful technique that allows the study of short-range electronic effects and local structure. The aim of the work has been to separate and manipulate the many different interactions so that they can be individually measured. For this we have used multinuclear techniques and probes. We have measured a range of spectra for different organotin, iminophosphorane and lithium compounds.

We have obtained a selection of spectra including ^{19}F (^1H) and doubly-decoupled ^{119}Sn (^1H , ^{19}F) for the organotin fluorides $^n\text{Bu}_3\text{SnF}$, Me_3SnF , SnF_2 , Me_2SnF_2 and $^n\text{Bu}_2\text{SnF}_2$. These have been used to calculate the effective shielding anisotropies, asymmetries, effective dipolar coupling (D'), and the anisotropy in the indirect coupling (ΔJ), using analyses of the spinning-sideband manifolds. Simulation programs have been written to simultaneously fit multiple sets of data, which reduce the fitting errors and give the relative orientations of the tensor interactions. The ^{19}F chemical shifts, indirect coupling $^1J(\text{SnF})$ and $^1\Delta J(\text{SnF})$ data have been summarised. For $^n\text{Bu}_2\text{SnF}_2$, a structure has been proposed based on comparisons with the NMR results from the other compounds.

For the iminophosphoranes, the dipolar tensor and its orientation can be measured from the ^{31}P static spectrum, whilst in the MAS spectrum residual dipolar coupling lineshapes are visible. These give information about the electric dipole nature of the P-N bond and the nature of its bonding. For the lithium nuclei, the quadrupolar interaction is small, but can be directly studied. With the two NMR-active isotopes both the shielding and quadrupolar interactions can be measured.

Ab initio calculations have been used to calculate certain NMR parameters such as the shielding, quadrupolar and indirect coupling tensors from the molecular structure. Experimental data have been compared against the calculations to verify the accuracy of the model. At present, there is good agreement between experimental and calculated results for $^6,7\text{Li}$, ^{13}C , $^{14,15}\text{N}$ and ^{31}P , though ^{119}Sn remains a challenge.

Table of Contents

MEMORANDUM AND ACKNOWLEDGEMENTS	iv
LIST OF ABBREVIATIONS	v
1 INTRODUCTION - RATIONALE AND AIMS	1
2 EXPERIMENTAL	6
2.1 <i>Chemagnetics CMX-200</i>	7
2.2 <i>Nuclear resonances: referencing and frequencies</i>	12
2.3 <i>Pulse sequences</i>	15
2.4 <i>Sample preparation</i>	20
3 NMR THEORY AND SIMULATIONS	23
3.1 <i>Relevant Hamiltonians</i>	24
3.2 <i>Rotations between frames</i>	24
3.3 <i>Powder averaging techniques</i>	28
3.4 <i>Modelling the data</i>	30
3.5 <i>Errors and reliability of parameters</i>	33
3.6 <i>Programs</i>	34
3.7 <i>Molecular modelling and computational chemistry</i>	39
3.8 <i>Molecular mechanics</i>	39
3.9 <i>Quantum mechanics</i>	40
3.10 <i>Evaluating the shielding tensor</i>	42
3.11 <i>Scalar couplings calculated by CLOPPA-AM1 theory</i>	49

4 REVIEW OF PREVIOUS WORK ON ORGANOTIN	
COMPOUNDS	54
4.1 <i>Molecular structure from ^{119}Sn NMR</i>	55
4.2 <i>Polymerisation of organotin compounds</i>	59
5 TRIORGANOTIN FLUORIDE COMPOUNDS	65
5.1 <i>Tri-n-butyltin fluoride</i>	66
5.2 <i>Trimesityltin fluoride</i>	81
5.3 <i>Summary of results for D' and ΔJ</i>	98
6 DIFLUOROTIN COMPOUNDS	101
6.1 <i>Tin (II) fluoride</i>	102
6.2 <i>Dimethyltin difluoride</i>	108
6.3 <i>Di-n-butyltin difluoride</i>	120
6.4 <i>Summary of ^{19}F NMR data for the organotin fluorides</i>	135
7 STRUCTURAL AND ELECTRONIC INFORMATION OF	
IMINOPHOSPHORANES	141
7.1 <i>Samples</i>	142
7.2 <i>Phosphorus-31 NMR</i>	148
7.3 <i>Carbon-13</i>	170
7.4 <i>Other NMR results</i>	174
7.5 <i>Conclusions from the NMR data</i>	176

8 LITHIUM NMR	179
8.1 <i>NMR properties</i>	180
8.2 <i>Experimental techniques</i>	181
8.3 <i>Second-order quadrupolar effects</i>	188
8.4 <i>Simulations and experimental results</i>	192
8.5 <i>Summary of results and ab initio calculations</i>	197
9 SUGGESTIONS FOR FUTURE WORK	206
APPENDICES	207
A <i>Tensor Rotations and Orientation</i>	207
B <i>Papers Presented and Conferences Attended</i>	210
C <i>Colloquia</i>	212

Memorandum

The research presented in this thesis has been carried out in the Department of Chemistry, University of Durham, between October 1995 and September 1998. It is the original work of the author unless otherwise stated. None of this work has been submitted for any other degree.

The copyright of this thesis rests with the author. No quotation from it may be published without his prior consent and information derived from it should be acknowledged.

Acknowledgements

I would like to thank the many people in Durham who have helped me during my Ph. D. These include my supervisor Prof. Robin Harris, the NMR group, particularly: John, Susan, Lindsey, Helen, Stefan, Eric Hughes, Alison, Gary, Gustavo, Minoru and Ulrich, not forgetting the many foreign visitors who have been in the group at various points in the last three years: Eric Brouwer, Phillipe, Regis, Shinji, Pierre, Jerome, Claudia, Naser, Raouf, Graham, Marco and Anna, and the stalwarts of the department, without whom, the spectrometers would not work: Barry, Alan, Ian, David and Nicola.

I would particularly like to thank my family and Janette for supporting me during my many studies and, hopefully, in my future endeavours. I would like to thank Dr. Melinda Duer for introducing me to the field of NMR and also Prof. Ed Constable and his group in Basel, who convinced me that doing a Ph. D. would be worthwhile and enjoyable!

List of Abbreviations

Bz	Benzyl
Chx	Cyclohexyl, C ₆ H ₁₁
CP	Cross Polarisation
CRAMPS	Combined Rotation and Multiple-Pulse Spectroscopy
CW	Continuous Wave
DC	Direct Current
DFT	Density Functional Theory
EFG	Electric Field Gradient
FID	Free Induction Decay
FT	Fourier Transform
fwhh	Full Width at Half Height
GAMMA	General Approach to Magnetic Resonance Mathematical Analysis
GIAO	Gauge Including Atomic Orbitals
HETCOR	Heteronuclear Correlation
HF	Hartree-Fock
HF	Proton-Fluorine probe
HFX	Proton-Fluorine-X triple-channel probe
HMPA	Hexamethylphosphoramide
HX	Proton-X channel probe
HXY	Proton-X-Y triple-channel probe
IGLO	Individualised Gauge for Local Orbitals
LORG	Localised Orbital Local Origin
LUMO	Lowest Unoccupied Molecular Orbital
MAS	Magic-Angle Spinning
MAT	Magic-Angle Turning
Me	Methyl
Mes	Mesityl, 2,4,6-trimethylphenyl
MQMAS	Multiple-Quantum Magic-Angle Spinning

MREV-8	Mansfield-Rhim-Elleman-Vaughan (pulse sequence)
ⁿ Bu	n-butyl, CH ₂ CH ₂ CH ₂ CH ₃
Neo	Neophyl, -CH ₂ C(CH ₃) ₂ C ₆ H ₅
NOE	Nuclear Overhauser Effect
NQS	Non-Quaternary Suppression
PAS	Principal Axis System
PDMSO	Polydimethylsiloxane
Ph	Phenyl
PMDETA	Pentamethyldiethylenetriamine
ppm	Parts Per Million
PVDF	Polyvinylidene fluoride
RDC	Residual Dipolar Coupling
REDOR	Rotational-Echo Double-Resonance
rf	Radio Frequency
RMS	Root Mean Squared
SA	Shielding Anisotropy
SCF	Self-Consistent Field
ssb	Spinning Sideband
thf	Tetrahydrofuran
TMEDA	Tetramethylethylenediamine
TOSS	Total Suppression of Sidebands
TPPM	Two-Pulse Phase Modulation
TTMSS	Tetrakis(trimethylsilyl)silane
VT	Variable Temperature
WISE	Wideline Separation
XRD	X-ray Diffraction

Note that all standard symbols used herein follow the IUPAC convention.¹

¹ R. K. Harris, J. Kowalewski, and S. C. de Menezes, *Pure & Appl. Chem.*, **12**, 2489 (1997)

1 Introduction - Rationale and Aims

NMR spectroscopy is a powerful technique that allows the study of short-range electronic effects and local structure. NMR spectra are rich with different interactions such as shielding, quadrupolar, dipolar coupling and scalar coupling. The aim of this work has been to separate and manipulate these interactions so that they can be measured and quantified. For this we have used multinuclear techniques and probes. By studying different nuclei within the same molecule, it is possible to obtain complementary information.

The shielding, quadrupolar, dipolar coupling and scalar coupling interactions are described by tensors. These are in turn related to the molecular frame so that three-dimensional information can be obtained by their measurement. The shielding and quadrupolar tensors are related to the electronic structure around the nucleus being measured. The isotropic scalar coupling can give information about the strength of bonding, whilst the multiplet pattern can show the number of atoms involved in the bonding. The dipolar coupling constant can be used to estimate the distance between atoms and is assumed to be orientated parallel to the relevant internuclear vector. The effective dipolar coupling constant is measured by NMR and needs correcting by a factor, the anisotropy in J , to give the dipolar coupling constant. This correction factor is often ignored, but for the organotin compounds it turns out to be significant.

The work in this Ph. D. has measured a range of spectra for different organotin, phosphorus and lithium compounds. The organotin compounds contain only spin- $\frac{1}{2}$ nuclei. The phosphorus spectra show details from the interaction of quadrupolar nuclei, whilst the last chapter looks directly at the quadrupolar nuclei $^{6,7}\text{Li}$.

The broad experimental details are given in Chapter 2. As general experimental techniques are now well-documented, only specific details have been given. Chapter 3 begins with an overview of the different interactions that can be observed in solid-state NMR spectroscopy. These interactions are now well-understood with ample theoretical grounding to link the NMR observations and the calculated values. Several simulation programs have been written and modified during the course of the Ph. D. These allow multiple sets of spinning sidebands to be calculated together. This multiple-fit technique reduces the fitting error when measuring the effective dipolar coupling constant. Non-colinear tensor interactions have also been considered for both static and spinning samples. When the dipolar tensor is one of the interactions, the shielding tensor can be orientated relative to the molecular frame.

The second part of Chapter 3 looks into *ab initio* calculations of NMR parameters. In recent years, commercial programs have become available that can find a minimum energy structure for a molecule. These have now been extended so that it is possible to calculate certain NMR parameters such as the shielding, quadrupolar and scalar coupling tensors from the molecular structure for small and medium-sized molecules. The theories behind these calculations are briefly presented, with more emphasis on the practical limitations and accuracy of these methods. The quadrupolar tensor is calculated from the electric field gradient tensor. This theory is described in Chapter 7, where it has been used to calculate the quadrupolar tensor for ^{14}N . Experimental data can be compared against the calculations to verify the accuracy of the model. At present, there is good agreement between experimental and calculated NMR results for $^{6,7}\text{Li}$, ^{13}C , $^{14,15}\text{N}$ and ^{31}P , though ^{119}Sn remains a challenge.

Currently, only bond lengths derived from dipolar coupling constants measured by the nuclear Overhauser effect (NOE) have been used as constraints for refining protein structures from NMR. However, measured ^{13}C NMR shielding tensors have recently been used as three-dimensional constraints to further refine the structure.^{1,2} The torsion angles within the molecule can be estimated by comparison with values from *ab initio* calculations. Once calculations have been verified against

experimental data, future calculations may be used to estimate the molecular structure by optimising the fit between experimental and calculated NMR parameters as the structure is changed.

Solid-state ^{119}Sn NMR spectra have been measured for over 20 years. Tin is present in many inorganic and organometallic compounds. An introduction to the previous work that has been done on organotin compounds is given in Chapter 4. This summary was felt necessary as Chapters 5 and 6 build from and extend this previous work.

The triorganotin fluorides, described in Chapter 5, can be considered to be model systems. The interactions present include shielding, heteronuclear dipolar and scalar coupling. These interactions have been measured and are given in the text. With the recent acquisition of a double-resonance HF probe, it has become possible to observe ^{19}F in addition to the previously measured ^{119}Sn . This can give complementary information. The triple-resonance HFX probe has been used to observe combinations of ^1H , ^{19}F and ^{119}Sn in one or two-dimensions. This has allowed double decoupling and double resonance experiments. A study of double-decoupling efficiency shows that when the two nuclei being decoupled are at the Hartmann-Hahn match with respect to each other then the decoupling is much more efficient than if only single decoupling is used.

Since the earlier papers, more single-crystal X-ray diffraction (XRD) structures of compounds have become available. The Sn-F bond lengths from these structures can be combined with current and previous NMR measurements of the effective dipolar coupling constant to give estimates for the anisotropy in J . The values of D' , D and ΔJ for the organotin fluorides are summarised at the end of Chapter 5.

Chapter 6 examines three difluorotin compounds, SnF_2 , Me_2SnF_2 and $^n\text{Bu}_2\text{SnF}_2$. The XRD structures have been solved for the first two compounds, but not the third. The ^{19}F NMR spectra of SnF_2 have been measured previously and reported in the literature. However, the results here disagree with the reported isotropic shift for fluorine in one of the recent papers. Me_2SnF_2 and $^n\text{Bu}_2\text{SnF}_2$ have not been studied

in depth by solid-state NMR before. As the structure for Me_2SnF_2 is known, the ^{13}C , ^{19}F and ^{119}Sn NMR spectra were measured to confirm this structure.

A range of solid-state NMR spectra have been measured for $^n\text{Bu}_2\text{SnF}_2$, with the interpretation based on results from the other compounds. From the NMR data, a structure has been proposed, whilst another previously suggested structure that was analogous to Me_2SnF_2 has been discounted. Semi-empirical calculations of the isotropic scalar coupling have been used to examine different possible structures. The Sn-F bond lengths have been estimated by comparison with these calculations and the experimentally measured values for $^1\text{J}(\text{SnF})$. These bond lengths have been used to estimate values for ΔJ , which are compared to those tabulated in the previous chapter. This chapter concludes with a summary and rationalisation of the ^{19}F chemical shifts and $^1\text{J}(\text{SnF})$ scalar coupling data for the series of organotin fluorides that have been studied.

Chapter 7 looks mainly at the ^{31}P NMR spectra from a range of iminophosphoranes. Iminophosphoranes contain a strong P-N bond. They have been suggested as strong ligands and as an alternative to ylides for Wittig reactions. In Wittig reactions, the strength of the P-C bond is important. This is analogous to the P-N bond in the iminophosphoranes. Nitrogen-14 is hard to observe directly as it is a spin-1 quadrupolar nucleus and has a very low resonance frequency. However, the effect of the quadrupole moment is seen indirectly at the ^{31}P nucleus, for which the resonance peak is split into an asymmetric doublet by residual dipolar coupling. Both the shielding tensor on the phosphorus atom and the quadrupole coupling constant on the ^{14}N atom have been calculated by ab initio methods. These values are in good agreement with experimentally measured values found from the ^{31}P MAS spectrum. The static ^{31}P spectrum allows the orientation of the shielding tensor relative to the P-N bond, and hence the dipolar tensor, to be measured by finding the best simulated fit to the experimental spectrum. This shows that in one of the iminophosphorane compounds, the tensors are non-colinear with the angle β in broad agreement with that found from the ab initio calculations.

The thesis concludes with Chapter 8, where the direct observation of the quadrupolar nuclei $^{6,7}\text{Li}$ is reported. The quadrupole moments of these nuclei are small compared to those of most other quadrupolar nuclei. This is fortunate in that the whole quadrupolar ssb manifold can be measured, but a hindrance in that many experiments that rely on the selectivity of weak pulses are not possible. The advantage of studying both isotopes of lithium is that the ratio of the quadrupole coupling constants are fixed between the nuclei. For ^6Li , the quadrupole moment is very small and the shielding anisotropy dominates, whilst for ^7Li the quadrupole coupling dominates. Programs have been written that allow for the simulation of combinations of shielding and quadrupolar tensors. It has been suggested that a significant part of the signal linewidth in ^6Li spectra arises from heteronuclear dipolar coupling to ^7Li . The contribution from this effect has been estimated experimentally, and discounted, by using a triple-channel probe that allowed the decoupling of ^7Li and protons whilst observing ^6Li .

¹ C. Glaubitz and A. Watts, *J. Magn. Reson.*, **130**, 305 (1998)

² A. E. Walling, R. E. Pargas, and A. C. de Dios, *J. Phys. Chem. A*, **101**, 7299 (1997); R. H. Havlin, H. B. Le, D. D. Laws, A. C. de Dios, and E. Oldfield, *J. Am. Chem. Soc.*, **119**, 1951 (1997)

2 Experimental

Most of the work in this thesis has been recorded on a Chemagnetics CMX-200, with a few spectra recorded using a Varian VXR-300. The Varian system has only been used where a different magnetic field or a fast spinning HX probe were needed. This setup will not be described in detail, as it does not differ significantly from that for the Chemagnetics system.

Background NMR theory is discussed in the next chapter along with some programs that have been used to simulate the data. Before any spectra can be simulated they must be acquired. It is important to maximise the signal to noise ratio and minimise any artefacts. This chapter describes how the data have been acquired and includes how things such as the magic angle, variable temperature and shift referencing have been set and calibrated. The standard pulse sequences are mentioned briefly so that their modifications can be described. A good introduction to experimental methods and techniques can be found in standard texts such as that by Derome.¹

Whilst all samples have been obtained from external sources, some of them are air sensitive and require sealing in glass inserts. Although this has been described before, the technique has been improved and modified for the samples studied here.

2.1 Chemagnetics CMX-200

This spectrometer has a 4.7 Tesla magnet, which gives the resonant frequency for protons of 200.13 MHz. The spectrometer is controlled by a Sun UNIX computer running Spinsight software. This is complemented by a range of probes, described below, with Magic Angle Spinning (MAS) and Variable Temperature (VT) capabilities.

2.1.1 Spinsight

The Spinsight software controls the acquisition and processing of data and related accessories. The current version is 3.5.2. For the acquisition, a pulse program and parameters are selected. Pulse programs control the sequence of pulses used. These are written in a block fashion rather than in pseudo program code. This has complicated the use of certain pulse sequences such as ramped and amplitude-modulated adiabatic-passage cross polarisation (CP),² where the pulse shape needs fine adjustment. Parameters can also be run in either single or multiple arrays that allow the acquisition of multiple-dimension data sets. The transmitter frequencies can have a variable offset of ± 1 MHz. For certain amplifiers, the power can be adjusted via the transmitter output voltages by using a software amplitude value from 255 (full) to 0 (off). The adjustment was not exactly linear and needed calibrating each time. For values down to about 150, the decay in power was reasonably linear. Below this point, the power levels are very low, ~ 5 kHz.

In addition to the usual features for data processing, extended interpretation was available through deconvolution and an xy panel. The latter allows arrayed relaxation and variable contact-time data to be extracted by integration or peak picking and fitted to a theoretical function. The order of the arrayed values can also be randomised for the acquisition and then sorted for processing, which reduces systematic errors. A macro programming language, similar to C, is available to automate acquisition and processing. Macros have been written to calculate the Ernst

angle (described later), provide 2D plots with projections along the axes, and to simulate infinite spinning speeds. This latter macro works by shifting the spinning sidebands by multiples of the spinning speed onto the centreband.

The room-temperature shim sets and MAS can be controlled as accessories from the computer. The values for the shim coils change between probes and are stored in files. The shimming is checked periodically and the files are updated. The MAS speed is controlled automatically for both the bearing and the drive. It is also possible to manually control the spinning speed. The speed can be locked to ± 1 Hz for the range 1 to about 12 kHz. It is possible to automatically change the speed between experiments, though this was rarely used.

2.1.2 Probes

Four probes have been used with the CMX-200. These are referred to as HX, HF, HFX and HXY, depending on the combinations of nuclei that are observable. For X and Y, the tuning ranges can be adjusted by changing capacitors in the probe. The range covers most nuclei from ^{15}N (20 MHz) to ^{31}P (81 MHz).

The HX probe is used for most measurements. The HFX probe is a triple-channel probe that allows simultaneous decoupling of both proton and fluorine whilst observing on the X channel. A single adjustable trap between the proton and fluorine channels gives reasonable isolation. This allows double-channel decoupling, but not observation of one channel whilst simultaneously decoupling the other. Both probes have the same stator that uses a 7.5 mm rotor with possible spinning speeds of up to 7 kHz. The probes will handle powers up to 62.5 kHz ($4\ \mu\text{s}$ 90° pulse durations), though 50 kHz ($5\ \mu\text{s}$) was used as standard.

Powers were calibrated by increasing the pulse duration and finding the 180° null point. For very low powers, the offset between the signal and the transmitter can be comparable to the power being calibrated. In this case, it may not be possible to find a null point. Also, the effective power must be considered. For decoupling channels, the crossed diodes were usually removed from the circuit and placed on the

observe channel. This led to an increase in the power reaching the probe and gave higher powers and shorter pulse durations, closer to 55.6 kHz (4.5 μ s).

The HXY probe has a 5 mm rotor, which can spin up to 12 kHz. The traps and capacitors are adjustable and allow most combinations of frequencies provided that the X and Y frequencies are not too close. High-power external filters are needed to further isolate the channels when simultaneously decoupling and observing on the X and Y channels. It is possible to use powers up to 83 kHz (3 μ s pulse duration) simultaneously on all three channels for 50 ms, but lower powers equivalent to 5 μ s pulse durations are normally used.

The HF probe, when combined with narrow pass filters, allows the observation of either proton or fluorine whilst decoupling the other. The resonant frequencies of ^1H and ^{19}F are only ca. 6 % apart, which complicates the observation of ^{19}F signals while simultaneously applying proton decoupling. The isolation between the two channels is greatly improved by having two adjustable traps and very narrow pass filters. These filters cannot be used with the HFX probe to achieve higher isolation as the powers required to generate the pulses are higher than the specification of the filters. The HF probe uses small (4 mm) rotors that are capable of spinning up to 18 kHz.

This probe can handle powers up to 200 kHz (1.2 μ s 90° pulse durations), though 83 kHz (3 μ s) was used as standard. These higher powers make it useful for Combined rotation and multiple pulse spectroscopy (CRAMPS) measurements, although the B_1 homogeneity is not ideal. The B_1 inhomogeneity can also affect fluorine linewidths when proton decoupling is used. This occurs as the Bloch-Siegert shift³ varies across the sample volume. Restricting the sample to the central 4 mm using extra spacers has been found to give the best results.⁴ Typical linewidths, given as full width at half height (fwhh), for polydimethylsiloxane (PDMSO) acquired with single-pulse excitation and no decoupling, were 29 Hz (HF), 16 Hz (HX), 21 Hz (HFX) and 17 Hz (HXY).

All the pencil rotors are made from zirconia. There are spacers above and below the sample, made of Teflon, boron nitride or Vespel, that confine its volume to the more homogeneous B_0 and B_1 in the centre of the coil. This choice is always a

compromise between sample volume and homogeneity. The inserts and the drive tips are made from a range of materials designed to reduce the background signal. The drive tips are made from KelF or Vespel and fluted for normal operation. For slow controlled spinning, a smooth drive tip in conjunction with a constrictor in the drive line is used. Double air bearings are used, which give very stable spinning.

2.1.2.1 Setting the magic angle

When the sample is spun at the magic angle the spectrum is narrowed and has peaks at integral multiples of the spinning speed. If the sample is spun about another angle a scaled powder pattern is observed for each peak. To achieve narrow linewidths, the magic angle must be checked. For the three probes with an X channel, this is most easily done by using KBr.⁵ Bromine-79 is a quadrupolar nucleus with a large quadrupole moment and resonance frequency close to carbon-13. When at the magic angle, the peak heights of the quadrupolar spinning sidebands will be maximised. This can be observed in the processed spectrum or by the number of rotor echoes visible in the free induction decay (FID).

Until recently, it has been difficult to set the magic angle on the HF probe as KBr cannot be observed. The magic angle can be set by observing the proton CRAMP spectrum of KHSO_4 , but this requires setting up the probe for CRAMPS operation. Trifluorotoluene contains only one fluorine environment with a large shielding anisotropy. The three fluorines are equivalent due to rapid internal motion. Trifluorotoluene can be used as a guest within a host calixarene ring to form a solid inclusion compound. This compound is then easier to handle and has a single signal in the fluorine spectrum. The scaled powder pattern on the spinning sideband peaks can be used to set the magic angle with an estimated accuracy of 0.1° .⁶

2.1.2.2 Variable temperature and its calibration

The sample temperature can be varied from -140 to +250°C on all probes except the HFX probe, where the minimum temperature is -30°C. The sample temperature is changed by passing nitrogen around the outside of the rotor. With the Chemagnetics system, the bearing and drive gases are fed from a separate room-temperature supply, which can lead to temperature gradients along the length of the sample. The VT gas is passed through a copper coil submerged in liquid nitrogen, which allows temperatures down to about -140°C to be reached. A heater in the VT stack controls the temperature of gas reaching the sample. This temperature is measured after the heater but before the sample, and is controlled automatically. Errors can arise as the temperature of the sample is not directly measured. The gas temperature is controlled automatically and is stable to $\pm 1^\circ\text{C}$ after a few minutes. However, the sample can take much longer to equilibrate. There is evidence that up to 20 minutes is required to get complete homogeneity of the sample temperature.

There are many ways to calibrate the actual sample temperature relative to the displayed temperature. In Durham, the proton shift differences in methanol adsorbed on tetrakis(trimethylsilyl)silane (TTMSS)⁷ have been measured from -140°C up to room temperature for the HX and HF probe. This shift difference is dependent on the temperature and needs no external reference. Using the ²⁰⁷Pb signal from lead nitrate, Pb(NO₃)₂,⁸ requires a known fixed point for absolute temperature calibration but it also allows the temperature gradients within a sample to be studied. As different parts of the sample are at different temperatures, the shifts are different and this is reflected in the peak shape and width. The temperature variation over the sample volume can be up to 4°C.

Frictional or pressure heating is significant when the sample is spinning and increases as the square of the spinning speed. Samples can be at significantly higher temperatures at high spinning speeds, e.g. 10°C higher with the sample spinning at 10 kHz, compared to a static sample. The calibration curves between the actual and set temperatures at a fixed spinning speed are linear, with an offset to account for the sample spinning speed. Values given herein are actual temperatures that have been corrected.

2.2 Nuclear resonances: referencing and frequencies

A wide variety of nuclei are NMR active. In this work, although I have concentrated on the spectra from ^{119}Sn , ^{31}P and ^{19}F , other nuclei have been both directly and indirectly observed. Indirect effects can be observed through scalar and dipolar coupling interactions. A summary of the resonant frequencies, natural abundances⁹ and reference compounds for spin- $1/2$ nuclei is given in Table 1. The approximate resonant frequencies can also be derived from the same reference. The values given here were used on the Durham Chemagnetics CMX-200 system.

Table 1: Summary of NMR data for spin- $1/2$ nuclei

Nucleus	Natural Abundance / %	Resonant Frequency / MHz	Reference compound	Shift ^a / ppm
^1H	99.985	200.130	PDMSO	0.0
^{13}C	1.108	50.329	Adamantane	38.4
^{15}N	0.37	20.288	$\text{NH}_4^{15}\text{NO}_3$	-5.1
^{19}F	100	188.288	C_6F_6	-166.4
^{31}P	100	81.015	Brushite	1.2
^{115}Sn	0.35	65.772	$(\text{C}_6\text{H}_{11})_4\text{Sn}$	-97.4
^{117}Sn	7.61	71.652		
^{119}Sn	8.58	74.630		

^a Shift given relative to the relevant primary reference compound.

Proton spectra are rarely observed in solid-state NMR as the high natural abundance leads to strong homonuclear dipolar coupling. This can broaden the spectrum to over 100 kHz, which removes any resolution. PDMSO is used to calibrate ^1H pulse durations, as most spectra are recorded with high-power proton decoupling.

By contrast, ^{19}F has a wide shift range which allows the separation of signals from many sites. Although there can be strong homonuclear dipolar coupling, there is sometimes only one fluorine atom per molecule, which makes the nucleus dilute

within the compound. The primary reference compound is the low-boiling liquid CFCl_3 , which is difficult to handle. C_6F_6 is a higher boiling liquid and has been made up in a glass insert for ease of use. The relative referencing has been measured in Durham. Values given in the literature vary slightly depending on the environment of the C_6F_6 .

When a fluorine spectrum is recorded with proton decoupling, the peaks are shifted due to the Bloch-Siegert effect.³ This shift is only significant for nuclei that are close in frequency and depends on the decoupling power and the frequency separation. With the decoupling powers used on the CMX-200, the shift is about -2.3 ppm. To account for this shift, the reference spectrum of C_6F_6 is measured with proton decoupling. This means that the shift values given can be compared between different spectrometers and for different decoupling powers.

The Hartmann-Hahn CP match was initially set using polyvinylidene fluoride (PVDF). However, it was found that setting equal pulse durations for the proton and fluorine channels gave as good a match and was easier. This latter method is now used as standard.

For ^{31}P , brushite (CaHPO_4) has been used in preference to H_3PO_4 (aq). It is a solid, stored in an insert and can also be used to set the CP match between ^1H and ^{31}P .

Tin has three NMR-active isotopes with spin $\frac{1}{2}$. Of these, ^{119}Sn has been used due to its appreciable natural abundance and slightly higher magnetic moment than ^{115}Sn or ^{117}Sn . Its good sensitivity and large chemical shift range (ca. 2500 to -2500 ppm with respect to the signal for SnMe_4) make it valuable for structure determination. Also, the shielding anisotropy (SA) is often large and its size can give an indication of the coordination at the ^{119}Sn centre. A recent review of SA for various ^{119}Sn compounds¹⁰ has shown that it is very sensitive to the coordination number.

Where the nucleus is not 100 % naturally abundant, the weighted contribution must be considered. When observing nuclei that are coupled to tin, the scalar coupling is observed as satellite peaks. In principle, the satellite peaks for ^{117}Sn and ^{119}Sn are separated due to the different magnetogyric ratios. These are visible as

separate peaks in solution-state spectra. However, in solid-state spectra the linewidths are too large to observe the separate peaks and the satellite peaks arise from $^{117,119}\text{Sn}$ with a combined natural abundance of 16.2 %. It is important to note that the magnetogyric ratio for the tin isotopes is negative. This leads to negative dipolar coupling constants for most heteronuclear interactions. The shift of the secondary reference, $(\text{C}_6\text{H}_{11})_4\text{Sn}$, with respect to SnMe_4 has been previously measured.¹¹ This compound has also been used to optimise the CP match.

Quadrupolar nuclei have been studied in less detail even though they represent 70 % of the nuclei in the periodic table. The nuclei studied herein are listed in Table 2 with the resonant frequencies given for the Chemagnetics CMX-200 system.

Table 2: Summary of NMR data for quadrupolar nuclei

Nucleus	Spin	Natural abundance /%	Resonant frequency /MHz	Quadrupole moment 10^{28} Q/m^2	Reference compound
^6Li	1	7.42	29.451	-0.0008	$\text{LiCl}_{(\text{aq})}$
^7Li	3/2	92.58	77.778	-0.04	
^{14}N	1	99.63	14.458	0.01	NH_4NO_3
^{79}Br	3/2	50.54	50.143	0.37	KBr

Both lithium isotopes have very small quadrupole moments, especially lithium-6. For this reason ^6Li is often treated as an honorary spin- $1/2$ nucleus. The ratio of isotopes in compounds is not always the same as the natural abundance, as the ^6Li isotope is used by the nuclear industry and hence depleted. Nitrogen-14 is not usually directly observed due to its large quadrupole moment, typically 4 MHz, and very low frequency. However, the dipolar coupling between ^{14}N and ^{31}P has been observed. Bromine-79 is mentioned in passing as it is used to check the magic angle and is close in frequency to ^{13}C .

2.3 Pulse sequences

2.3.1 Standard pulse programs

The probe must be tuned to the frequencies that will be used in the experiment. For this the tune pulse program sweeps through a 2 MHz width centred at the desired frequency. This is a low-power sequence: high powers would be used in the experiment. A check of the high-power tune and match of the probe can be carried out but the error is not usually significant. For broad spectral widths such as those required with quadrupolar nuclei, anomalous intensities will be observed if the probe is not well tuned. There may also be a reduction in the intensity of distant sidebands as the probe is further away from being ideally tuned.

The standard pulse sequences provided with the spectrometer give the option to generate transverse magnetisation by direct or cross polarisation, and to choose whether to decouple or not. If the proton magnetisation is decoupled after CP, it is spin locked through the whole pulse sequence and the remaining magnetisation can be flipped back to the +z axis after acquisition. This increases the effective rate of recovery of the magnetisation back to thermal equilibrium. There is software control over the power of the pulses so that an experiment can use cross polarisation and then decouple at a different power. Phase cycling is included in these pulse programs to remove the effects of direct magnetisation generated by the CP pulse, and of imperfect quadrature detection.

When a sample has a long recycle delay and a poor or zero signal from CP, then the best signal-to-noise ratio is achieved by using direct polarisation and tipping the magnetisation through the Ernst angle.¹² When the magnetisation is tipped through 90° the measured signal is at its maximum, but the time taken for the system to return to equilibrium is longer than for a smaller tip angle. With a shorter pulse delay more acquisitions may be made in a fixed amount of time. The total signal-to-noise ratio increases as the square root of the number of acquisitions. The optimum tip angle that will give the best signal-to-noise ratio in a fixed amount of time can be

shown to be β_{Ernst} , where $\cos \beta_{\text{Ernst}} = \exp(-t/T_1)$, where t is the recycle delay to be used and T_1 is the longitudinal relaxation time.

MAS spectra recorded using CP can show reduced intensities in the outer spinning sideband peaks when compared to a spectrum recorded with direct polarisation. This is noticeable when the shielding anisotropy is large. A multiple-contact CP pulse sequence combined with an empirical correction function has been suggested.¹³ For most of the spectra recorded herein, the loss of intensity is negligible. This has been checked by comparing the ^{119}Sn spectra for $^n\text{Bu}_3\text{SnF}$ measured with CP against direct polarisation with both a 90° pulse and one with a small tip angle. The exceptions to this situation are the ^{119}Sn spectra of the difluorotin compounds.

Although continuous-wave (CW) decoupling is normally used, some other decoupling schemes such as Lee-Goldburg off-resonance decoupling are also available. The Lee-Goldburg procedure is discussed in detail in Chapter 6. Two-Pulse Phase Modulation (TPPM)¹⁴ can reduce the linewidth in spinning solids where the decoupling power is insufficient. The efficiency over CW decoupling is sample dependent and has only occasionally improved the resolution for the samples studied here. This is probably because most heteronuclear interactions are weak and efficiently decoupled by CW irradiation. Multiple-pulse decoupling sequences for CRAMPS are available as standard and have been modified to include quadrature detection.¹⁵ Rotor-synchronised pulse sequences for high-speed CRAMPS have recently been suggested,¹⁶ which would remove both the homonuclear interactions and the shielding anisotropy. This last technique has not yet been implemented but would be an idea for the future.

2.3.2 Echoes, TOSS and REDOR

For static measurements and other broadened spectra, much of the useful information is lost during the probe ring-down and receiver dead time. By applying an echo, this signal can be refocused and then observed. A $90\text{-}\tau\text{-}180\text{-}\tau\text{-acq}$ sequence

will refocus the chemical shift components. The homonuclear scalar- and dipolar-coupling Hamiltonians are bilinear and unaffected by the echo. Using a quadrupolar (Hahn) echo will also refocus the dipolar and quadrupolar components. This pulse sequence is $90\text{-}\tau\text{-}90\text{-}\tau\text{-acq}$. Allowance needs to be made for pulse imperfections, so that often the post-echo delay is reduced to observe the FID before the top of the echo. The data can then be shifted to set $t = 0$ at the top of the echo. As a result, only zero-order phasing should be required. These echoes can be used for spinning samples, but consideration must be made of the pulse duration and sample spinning rate. It is assumed that the 180° or 90° pulse is a delta pulse taking negligible time. With a fast-spinning sample there will be some rotation whilst the pulse is applied, which can usually be ignored. More importantly, the pre- and post-echo delays must be multiples of the rotor period.

With carbon-13 NMR, by interrupting or changing the proton decoupling during part of the echo time, the non-quaternary carbons are rapidly dephased and suppressed (NQS). This can be used as a form of spectral editing.

For a sample with moderate SA, the spinning sidebands can be suppressed to leave only the isotropic peak. This technique, known as Total Suppression of Sidebands (TOSS),¹⁷ uses multiple π pulses to form echoes that dephase all but the isotropic peaks. Various schemes are possible with four to six π pulses and also compensated π pulses. For the organotin samples studied here, the ^{119}Sn SA is too large to give accurate dephasing and a clear spectrum.

Another commonly used echo technique is Rotational-Echo Double-Resonance (REDOR),¹⁸ which is used to measure weak heteronuclear dipolar couplings. Systems that are studied usually have an isolated spin pair and ignore motional averaging of the dipolar coupling constant. This technique can be used for dipolar coupling constants of less than 1000 Hz, whereas those between ^{119}Sn and ^{19}F in the organotin fluorides are around 4000 Hz. In this case, the signal dephases too rapidly to be measured.

2.3.3 Relaxation measurements

The characteristic longitudinal relaxation time, T_1 , required for the spin system to return to equilibrium needs to be measured so that time on the spectrometer can be optimised. Frequently used methods include inversion- and saturation-recovery. The former method totally inverts the magnetisation and then observes it after a time τ for an arrayed series of recovery times. A magnetisation recovery curve can be fitted but the equilibrium magnetisation needs to be fitted or known. This requires the use of long recovery times. A modified sequence by Torchia¹⁹ uses cross polarisation and a modified phase cycle so that for $\tau = \infty$ the averaged magnetisation is zero. The use of CP requires only a pulse delay long enough for the proton magnetisation to relax. This is the standard pulse sequence that has been used here. A further modified sequence with CP has been used to measure the ^{13}C T_1 value or the relevant nucleus. If the exact intensity of the signal is required, then a pulse delay of at least $5 T_1$ should be used. However, for the greatest signal in a fixed time with 90° pulses, using a pulse delay of $1.3 T_1$ and more acquisitions is optimum. By measuring the change in signal intensity with variable contact times, $T_{1\rho}$ for the nucleus that you are cross polarising from can be estimated. Pulse programs allow the direct measurement of $T_{1\rho}$ with, or without, cross polarisation.

2.3.4 2D pulse programs

With two-dimensional NMR sequences, the pulse sequence is generally divided into preparation, evolution and observation components. As the t_1 dimension is indirectly observed, it is not possible to record it with quadrature detection. Three methods have been devised to overcome this problem and have been reviewed by Keeler and Neuhaus.²⁰ For narrow spectral widths, the FID can be recorded off resonance and then symmetrised with half the information ignored. The other two hypercomplex methods involve changing the phase of one of the pulses in the sequence and recording two data sets. With careful writing of the pulse program, one

combined data set can be acquired that can be processed without the use of any macros. With this method, slices are acquired by alternating the phase of a pulse in the sequence.

The Heteronuclear Correlation (HETCOR) pulse sequence was used on the HFX probe to correlate ^{19}F and ^{119}Sn . As ^{119}Sn is not 100 % naturally abundant, a 1D ^{19}F spectrum would show J-coupled satellite peaks. For the HETCOR experiments, we only observe the signal arising from ^{19}F that can cross polarise to nearby ^{119}Sn . Thus with no ^{119}Sn decoupling in t_1 , only the scalar coupled peaks would be visible. Similarly, with ^{119}Sn decoupling in t_1 , only the uncoupled ^{19}F peak would be observed. The pulse sequence is shown in Figure 1, with the optional decoupling shown as a dashed pulse. The experiments utilised a phase cycle of length 8 and hypercomplex data acquisition.

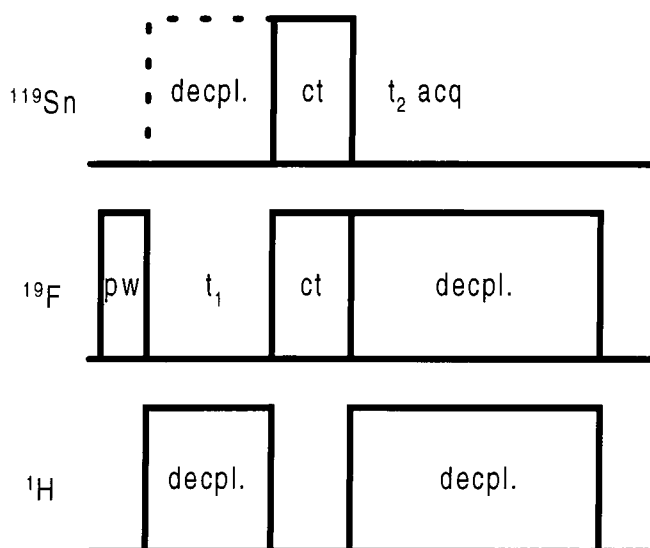


Figure 1: The HETCOR pulse sequence with the optional decoupling for ^{119}Sn during t_1 .

The other main group of 2D pulse sequences used separates the isotropic and anisotropic shielding interactions into two dimensions for a single nucleus. The sequence by Tycko²¹ directly observes the fast magic-angle spinning peaks, whereas the more recent Magic Angle Turning (MAT)²² sequences directly observe the slow spinning, pseudo-static spectrum. The Tycko sequence relies on multiple blocks of

four or six rotor-synchronised π pulses to stop the anisotropy being averaged by the spinning and to create pseudo-static magnetisation. At high spinning speeds, these pulses take a significant time relative to the rotor period so that the approximation of delta pulses breaks down. The indirect spectral width is scaled, with the scaling factor dependent on the sequence of π pulses and proportional to the spinning speed.

The MAT sequence gives much better static lineshapes as these are directly observed. The slow sample spinning with smooth rotor tips has been mentioned above. Although the spinning speed is stable over a short time period, it can drift by a few Hertz over a period of hours. This has been compensated for by using a macro that checks and changes the rotor period within the pulse program after each t_1 increment.

2.4 Sample preparation

Most solid samples are easy to manipulate and handle. However, some samples are used as standards, whilst others are air and moisture sensitive. Packing these samples into inserts reduces the amount of sample handling and (especially if a glove box is used) contact with the air. The disadvantage is that the sample volume is reduced, but this is not a problem for sensitive standards.

The inserts can be made from either machined plastic (Delrin or KelF) or glass. The plastic inserts can be reused and are reasonably airtight. KelF inserts are used when ^{13}C is observed with CP as it is proton-free. However, these inserts would give a fluorine background signal unless CP from proton to fluorine was used. The plastic inserts can be made to fit the rotor exactly and do not require any extra packing material around them. It is not possible to machine inserts for the HF probe due to its small rotor diameter.

Making glass inserts involves more work but they are then completely sealed, though this must be done very symmetrically. It is much harder to make the insert the correct size, so careful packing is needed in the rotor so that the sample can spin stably. Different packing materials such as KBr and sulphur have been used, but the

most efficient method used Teflon tape wrapped around the insert to give a tight fit inside the rotor. Using a range of shortened end-caps allowed the sample to be fixed lengthways as well. With these precautions, it is possible to get stable spinning speeds of up to 4 kHz on the HX probe.

Although the details of making the insert have been described before,²³ some modifications have been made to improve the technique. Only one constriction was made in the glass tube at the point where the final seal was to be made. The insert was filled in a glovebox to only 70% full before a small plug of silica wool was added on top. This has the effect of holding the sample in place, cleaning the constriction and acting as a heat sink. Silica wool was used because it does not melt below 500°C: glass wool melts at a much lower temperature. Once the sample was packed, the first rough seal was done by hand. With only one seal, packing the sample is easier and the constriction can be cleaned more efficiently.

Once the first rough seal has been made, the insert is held in a brass stock. This acts as a heat sink and shield around the sample. Previously, it has been cooled in liquid nitrogen before the final seal is made. This creates large temperature gradients and stresses within the glass and can cause it to shatter. With the plug of silica wool acting as a heat sink, it was found that the stock did not need extra cooling. This also allowed the tail of the insert to be sealed with a small piece of extra glass and then gently annealed.

-
- ¹ A. E. Derome, "Modern NMR Techniques for Chemistry Research," Pergamon Press, Oxford (1987)
- ² S. Hediger, P. Signer, M. Tomaselli, R. R. Ernst, and B. H. Meier, *J. Magn. Reson.*, **125**, 291 (1997)
- ³ S. A. Vierkötter, *J. Magn. Reson. A*, **118**, 84 (1996)
- ⁴ E. Hughes, personal communication
- ⁵ J. S. Frye and G. E. Maciel, *J. Magn. Reson.*, **48**, 125 (1982)
- ⁶ E. B. Brouwer and R. K. Harris, personal communication
- ⁷ A. E. Aliev, K. D. M. Harris, and D. C. Apperley, *J. Chem. Soc., Chem. Commun.*, 251 (1993);
A. E. Aliev and K. D. M. Harris, *Magn. Reson. Chem.*, **32**, 366 (1994)
- ⁸ A. Bielecki and D. P. Burum, *J. Magn. Reson. A*, **116**, 215 (1995); L. C. M. van Gorkom, J. M. Hook, M. B. Logan, J. V. Hanna, and R. E. Wasylshen, *Magn. Reson. Chem.*, **33**, 791 (1995)
- ⁹ R. K. Harris, "Nuclear Magnetic Resonance Spectroscopy," Longman, Essex (1987)
- ¹⁰ R. K. Harris, S. E. Lawrence, S. Oh, and V. G. Kumar Das, *J. Mol. Struct.*, **347**, 309 (1995)
- ¹¹ R. K. Harris and A. Sebald, *Magn. Reson. Chem.*, **25**, 1058 (1987)
- ¹² R. R. Ernst, G. Bodenhausen, and A. Wokaun, "Principles in NMR in One and Two Dimensions," Oxford University Press, Oxford (1987)
- ¹³ G. Jeschke and G. Grossmann, *J. Magn. Reson. A*, **103**, 323 (1993)
- ¹⁴ A. E. Bennett, C. M. Rienstra, M. Auger, K. V. Lakshmi, and R. G. Griffin, *J. Chem. Phys.*, **103**, 6951 (1995)
- ¹⁵ T. M. Barbara and L. Baltusis, *J. Magn. Reson. A*, **106**, 182 (1994); H. Cho, *J. Magn. Reson. A*, **121**, 8 (1996)
- ¹⁶ D. E. Demco, S. Hafner, and H. W. Spiess, *J. Magn. Reson. A*, **116**, 36 (1995); S. Hafner and H. W. Spiess, *J. Magn. Reson. A*, **121**, 160 (1996); S. Hafner and H. W. Spiess, *Solid State NMR*, **8**, 17 (1997)
- ¹⁷ W. T. Dixon, *J. Chem. Phys.*, **77**, 1800 (1982)
- ¹⁸ T. Gullion and J. Schaefer, *J. Magn. Reson.*, **81**, 196 (1989); T. Gullion and J. Schaefer, *Adv. Magn. Reson.*, **13**, 57 (1989)
- ¹⁹ D. A. Torchia, *J. Magn. Reson.*, **30**, 613 (1978)
- ²⁰ J. Keeler and D. Neuhaus, *J. Magn. Reson.*, **63**, 454 (1985)
- ²¹ R. Tycko, G. Dabbagh, and P. A. Mirau, *J. Magn. Reson.*, **85**, 265 (1989)
- ²² J. Z. Hu, W. Wang, F. Liu, M. S. Solum, D. W. Alderman, R. J. Pugmire, and D. M. Grant, *J. Magn. Reson. A*, **113**, 210 (1995)
- ²³ T. V. Thompson, Ph. D. Thesis, University of Durham (1995)

3 NMR Theory and Simulations

This chapter outlines the pertinent theory necessary to write the simulation programs and understand the later calculations. General introductions may be found in standard NMR texts by Schmidt-Rohr and Spiess,¹ and Haeberlen.²

With NMR spectroscopy, we directly measure the difference in energy levels within the system. This difference is dominated by the Zeeman interaction of the nuclear spin with the external magnetic field, B_0 . Other interactions include shielding from B_0 by the electron cloud, dipolar couplings between nuclear spins and the interaction of the nuclear electric quadrupole moment with the electric field gradient.

These interactions are not generally isotropic and have an orientation dependence. The samples studied in the solid state are usually powders, which means that the spectrum observed is from the sum of many individual crystallite spectra. In this case, the orientation of an interaction relative to the molecule is obscured, though the tensor information is still available. With multiple tensor interactions, it is possible to find the relative orientations of the tensors. When one of these is the dipolar interaction, which is fixed in the molecular frame, then the orientation of the second interaction can be established. These tensors can be obtained from simulating a model function and fitting it to the data. Several programs have been used, modified and written and are outlined later.

Commercial programs are now available to calculate the minimum energy structures of a molecule. From this or crystallographic data, *ab initio* calculations can be used to find the shielding and electric field gradient tensors. A summary of results for different nuclei shows that elements to the left of carbon and silicon are well described by moderate basis sets whilst those to the right require extended basis sets with multiple polarisation functions for accurate results. Collaboration with an Argentinian group has been aiming to calculate indirect (J) isotropic and anisotropic couplings from the molecular structure of simple group 14 compounds.

3.1 Relevant Hamiltonians

The internal Hamiltonians can be expressed in the general form for the interaction λ shown below. Here C^λ is a constant, \mathbf{I} is the observed nuclear spin vector and \mathbf{A}^λ may be either the same nuclear spin vector, a different nuclear spin vector, or the external magnetic field, \mathbf{B}_0 .

$$H_\lambda = C^\lambda \sum_{\alpha, \beta=1}^3 I_\alpha R_{\alpha\beta}^\lambda A_\beta^\lambda = C^\lambda \sum_{\alpha, \beta=1}^3 R_{\alpha\beta}^\lambda T_{\beta\alpha}^\lambda = C^\lambda \sum_1 \sum_{m=-1}^1 (-1)^m R_{1,-m}^\lambda T_{1m}^\lambda$$

\mathbf{T}^λ is the dyadic product of \mathbf{I} and \mathbf{A}^λ and is commonly given in the laboratory (LAB, B_0) frame of reference. \mathbf{R}^λ is a spatial tensor of rank two and may be decomposed into isotropic, symmetric and antisymmetric components. The symmetric component of the tensor can be rotated into its principal axis system (PAS), where it is diagonal, and can be expressed in terms of an anisotropy and asymmetry parameter. Not all Hamiltonians have an antisymmetric component. In all common situations, this component is not observable by NMR. The third version of the Hamiltonian in the above equation uses irreducible spherical tensors, which are easier to rotate. \mathbf{R} and \mathbf{T} can be derived and their values, tabulated in Haeberlen,² have been used.

The definition of the shielding anisotropy (SA) $\zeta = \sigma_{33} - \sigma_{\text{iso}}$ is used herein, with the components of the tensors labelled according to $|\sigma_{33} - \sigma_{\text{iso}}| \geq |\sigma_{11} - \sigma_{\text{iso}}| \geq |\sigma_{22} - \sigma_{\text{iso}}|$. We define the effective dipolar coupling constant D' as $D - \Delta J/3$, where D is the dipolar coupling constant in frequency units, $D = \left(\frac{\mu_0}{4\pi}\right) \gamma_{\text{Sn}} \gamma_{\text{F}} \left(\frac{\hbar}{2\pi}\right) r_{\text{SnF}}^{-3}$ and ΔJ is the anisotropy in \mathbf{J} , $\Delta J = J_{\parallel} - J_{\perp}$. The assumption of colinearity is made for \mathbf{D} and \mathbf{J} , which is reasonable especially considering that D is usually much larger than ΔJ .

3.2 Rotations between frames

The spatial tensor components are given in the tensor's principal axis system. This needs to be expressed in the same frame of reference as the spin tensor, which is

usually the laboratory frame. Using Wigner rotation matrices, $D_{m'm}^l$, the spatial tensor components become $R_{lm}^\lambda = \sum_m D_{m'm}^l(\alpha^\lambda, \beta^\lambda, \gamma^\lambda) \rho_{lm}^\lambda$, where the Euler angles α^λ , β^λ , γ^λ describe the relative orientation of the LAB and PAS frames. There are numerous conventions in the literature for these rotations depending whether the rotations are passive or active. We have used Haeberlen's convention² throughout this thesis. In rotating between frames, the shorthand $PAS_\lambda \rightarrow LAB$ indicates a rotation from the PAS to the LAB frame of reference. Two other common rotations that are used involve non-colinear tensor interactions and spinning samples.

3.2.1 Combining non-colinear tensors

In a given system, there will often be more than one interaction. These can be combined if the same crystallite is considered. When two interactions such as the dipolar and shielding tensors are colinear then they may be easily combined by considering just the anisotropy, asymmetry and the product of the dipolar coupling constant with the nuclear spin quantum number. For the spectra affected by both the relevant shielding tensor and by D' we designate the effective tensor components as σ_{ii}^{eff} and the related anisotropy and asymmetry by ζ^{eff} and η^{eff} respectively. There will be as many effective anisotropies as there are different values for m_s . When there is significant scalar coupling present each spinning-sideband manifold can be separately analysed. Analysis of the spectrum allows the determination of ζ and D' separately by the use of $\zeta^{\text{eff}} = \zeta - \frac{2D'}{\nu_0} m_s$, where ν_0 is the Larmor frequency and m_s is the appropriate spin component quantum number.

In the case where these tensors are non-colinear, one tensor must be rotated into the PAS of the other before addition e.g. $PAS_D \rightarrow PAS_{SA} \rightarrow LAB$. When expressed in the LAB frame the dipolar Hamiltonian becomes $H_D = C^D [1 - 3(\sin \beta \sin \theta \cos(\phi - \alpha) + \cos \beta \cos \theta)^2]$ which simplifies to $H_D = C^D (1 - 3 \cos^2 \theta)$ when the dipolar and shielding tensors are colinear. The

angles α and β are the polar coordinates relating the dipolar PAS to the shielding PAS as defined in Figure 2. θ and ϕ define the orientation of the shielding PAS to the external magnetic field. A third crystallite orientation around B_0 does not appear in the equations, as the interactions are invariant to rotation about the magnetic field vector.

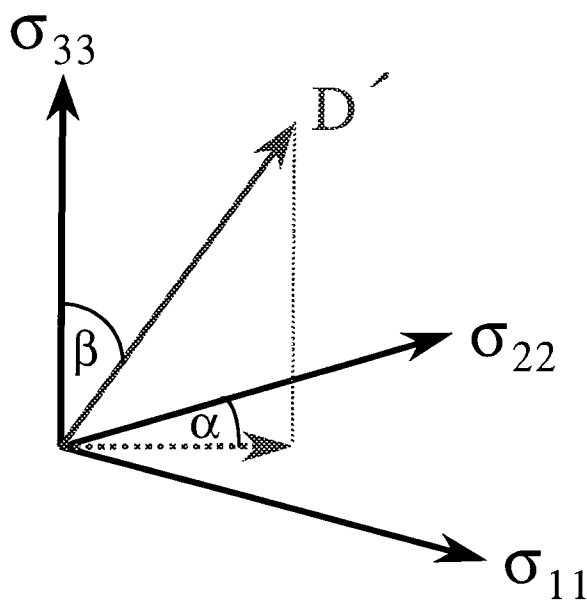


Figure 2: Definition of α and β between the effective dipolar and shielding tensors.

When the shielding tensor is calculated by ab initio methods, it is expressed relative to the internal coordinate system of the calculation. This coordinate system is used to optimise the speed of the calculation. The molecule's geometry is also given in the same coordinate system. From this, the interatomic vectors (\underline{r}_{ab}) can be calculated, which will be colinear with the dipolar tensor.

To rotate the tensor into its PAS, it must first be decomposed into its three components: isotropic, symmetric tensor and antisymmetric tensor. The symmetric component of the tensor, \mathbf{A} can then be diagonalised to $\mathbf{\Lambda}$ by a similarity transform $\mathbf{U}^\dagger \mathbf{A} \mathbf{U} = \mathbf{\Lambda}$, which is a rotation to a new coordinate system. The rotation matrix \mathbf{U} is constructed from the eigenvectors of the tensor \mathbf{A} . These eigenvectors give the orientation of the PAS in the internal coordinate system of the calculation. The diagonal matrix $\mathbf{\Lambda}$ contains the three components (eigenvalues) of the tensor in its

PAS. The theory of decomposing tensors, similarity transforms, eigenvalues and eigenvectors is explained in detail in Appendix A.

With the knowledge of the eigenvectors of the shielding tensor and the interatomic vector, given in the same coordinate system, the angles α and β between the principal axes of the dipolar and shielding tensors may be calculated. The equations are given below where $\underline{\sigma}_{xx}$ is the normalised eigenvector related to the tensor component. It can be seen from Figure 2 that when β is zero the tensors are colinear and α is undefined.

$$\beta = \cos^{-1}(\underline{\sigma}_{33} \cdot \underline{r}_{ab}) \quad \alpha = \sin^{-1}(\underline{\sigma}_{22} \cdot (\underline{\sigma}_{33} \wedge \underline{r}_{ab}))$$

3.2.2 Spinning samples

When the sample is spun, the orientation of the crystallite changes whilst the spectrum is being acquired. This may be accounted for by an extra rotation e.g. $\text{PAS}_{SA} \rightarrow \text{ROT} \rightarrow \text{LAB}$. The angles that relate the ROT (frame fixed within the spinning rotor) to the LAB frame are $(\Theta, \omega_r t, 0)$. The time dependence arises from the rotor spinning and Θ is the angle between the rotor axis and the B_0 field direction. When this angle is set to be 54.7° (the magic angle) the anisotropic shielding and heteronuclear dipolar interactions are averaged. The FID is periodic and spinning sidebands (ssb), separated by multiples of the spinning speed, are observed. At speeds greater than the magnitude of the interaction, only the isotropic peak remains and the sidebands are said to be spun out. At intermediate speeds, the intensity of the peaks contains information about the shielding tensor components. The theory was first published by Maricq and Waugh³ and the equations therein form the basis of most spinning-sideband simulation and fitting programs. The spinning-sideband equations have been extended for a combination of shielding and quadrupolar tensors (including non-colinear cases).⁴ The equations for the non-colinear shielding and heteronuclear dipolar case have been solved based on the case above.⁵

In principle, by calculating the moments of the spectrum up to third order, both the anisotropy and the asymmetry of the shielding tensor can be calculated. This relies on there being no loss of signal in the recorded spectrum as great emphasis is placed on signal intensity far from the isotropic shift. This method can be used to give an initial estimate of parameters for use in fitting but is unsuitable for accurate determinations.

Herzfeld and Berger⁶ re-expressed the equations for spinning sidebands to calculate the intensity of each ssb individually. This could then be evaluated for a wide range of anisotropy and asymmetry parameters. The results can be used to construct contour plots of the ratio of intensities of the centreband to the spinning sideband. These plots can then be used to find the best fit for a set of spinning sidebands without needing to recalculate all the peak intensities. It is also possible to fit using only a selection of the spinning sidebands. However, as the plots use the ratio of the centreband and spinning sideband intensities, the method is dependent on obtaining an accurate value for the centreband intensity.

The spinning-sideband intensities can be measured as integrals or peak heights. Using peak heights assumes that there are no overlapping peaks or second order effects such as residual dipolar coupling and off magic-angle spinning that will distort the individual lineshapes. These are specifically mentioned in Chapter 7.

3.3 Powder averaging techniques

Up to this point we have only considered one crystallite. With a single crystal, the NMR spectrum can be measured for various known orientations of the crystal. This would allow the tensor components and their various orientations relative to the crystallographic axes to be measured.

More commonly, only a powdered sample is available. In this case, there will be many different crystallite orientations, evenly distributed over all possible orientations. Although the crystallites are evenly distributed, a weighting proportional to the solid angle subtended in relation to the orientation of the

magnetic field vector is needed. Various powder-averaging schemes have been used, and more are regularly suggested. These vary in their simplicity of implementation and use of weighting factors. For static samples only two angles, θ and ϕ , need to be considered.

The easiest scheme to implement is a planar grid of points. Here, the two angles are stepped in small increments of less than 1° and each value is weighted by $\sin \theta$. The disadvantage of this is that the contribution of crystallites with θ near to zero or 180° is small but the calculation of the frequencies takes just as long as for other angles.

Better schemes, such as spherical grids, pick values for θ such that the solid angle is the same for each orientation. This requires some analytical function to describe the distribution of θ . Alderman et al.⁷ suggested subdividing the sphere into triangles by treating the sphere as an octahedron. This allows the possibility of interpolating extra points between the calculated ones to improve the averaging.

A recent technique called REPULSION⁸ treats the crystallite orientations like point charges over a sphere. It then minimises the repulsive 'coulombic forces' to get an even distribution of charges over the sphere. These are then used to find a set of evenly distributed crystallite orientations with similar solid angles. These values could then be saved in a subsidiary file for use on other runs but this procedure is not very flexible on changing the number of crystallites.

An alternative method is to use randomly selected crystallites, which on its own gives a poor distribution of crystallites. An improvement is to use quasi Monte Carlo techniques. These are pseudo-random number series, which give a good distribution. These numbers can be converted into crystallite orientations to give an even spread. One method is based on Conroy numbers and is a combination of the work done by Zaremba,⁹ Conroy¹⁰ and Wolfsberg¹¹ (ZCW). This method has the disadvantage that certain parameters need to be optimised for the function that is used, and the number of crystallites is limited to 6044. It has recently been used by Koons,¹² who showed that using a general function to find the parameters still gives good results. An improved Monte Carlo method is based on Hammersley numbers.¹³ These have been proved by Wozniakowski¹⁴ to give an optimum set of crystallites.

These schemes are very efficient as all variables are sampled simultaneously rather than in a grid search and the integration range is independent of the number of points used. The series is not limited by dimensions or number and has been implemented in C programming code by Hughes.¹⁵

The REPULSION paper⁸ also compared the convergence of the common techniques. It is hard to find a fully converged spectrum, but here a planar grid with 100,000 crystallites was used. The conclusion was that REPULSION was best for 50 – 250 crystallites, whereas beyond this the ZCW method is better. Use of Hammersley points was not studied but this would be expected to perform better than the ZCW method.

The comparisons have been made for low numbers of crystallites. With the greater computer power available, the frequencies of 100,000 orientations may be calculated in less than 1 second. This means that schemes have been chosen that are easier to implement rather than those which converge rapidly.

3.4 Modelling the data

The preceding discussion has shown how a model function can be constructed. We can now use this function to fit the experimental measurements provided that it is a good representation of the system. For this, we need to ensure that the data are free of artefacts and to define a goodness of fit parameter between the experimental and simulated data. As this function is non-linear and has no analytical derivatives, it is not possible to derive an analytical solution. Instead an iterative search algorithm must be used.

Artefacts can arise from spectrometer and probe limitations. Examples include: instability of the sample spinning or powers for decoupling and cross polarisation, poor shimming, off-magic angle spinning, inhomogeneous B_1 fields, uneven excitation across the spectral width, ring down, and the Q factor of the probe. The spectrometer is stable over the timescale of the experiment so that can be ignored. The main problems are visible when observing quadrupolar nuclei where

the spectral width is large. The Q response curve of the probe across a 1 MHz window has been measured for various pulse durations and can be corrected for with a sinc function. Rolling baselines have been removed experimentally using echo pulse sequences when necessary. Uneven CP excitation across the spectral width can be caused by Hartmann-Hahn mismatch and variations in CP dynamics.¹⁶ This was checked for the ^{119}Sn spectra of $^n\text{Bu}_3\text{SnF}$ samples by measuring a comparable spectrum with direct pulses at the Ernst angle. For most of the samples measured herein, with spectral widths of less than 50 kHz, it can be assumed that the sample is uniformly excited and the measurement errors lie within the random thermal noise of the spectrum. The exceptions to this are the R_2SnF_2 compounds where the shielding anisotropy is around 900 ppm and the static spectra visibly show the uneven excitation. This is discussed in more detail in the relevant chapters.

Molecular motion could affect the spectrum and would need to be included in the model functions. In the compounds studied herein, motion does not significantly affect the spectra so it has not been considered further.

The aim of modelling the data is to get the best-fit parameters. The best fit is found by minimising the goodness of fit parameter. The usual parameter is the sum of differences squared (R^2), though if the error in the measurement is known then this becomes chi squared (χ^2). The simplex¹⁷ and Levenberg-Marquardt¹⁸ search algorithms have been used in different programs and are briefly described below.

Close to the minimum, R^2 should be approximately quadratic in form. If we know the gradients at the fitting point then we should be able to jump straight to the minimum. The inverse of the second derivative, Hessian, matrix can be calculated to give the step direction and size to the minimum. Further away from the minimum, this approximation is poor and the best we can do is to step down the gradient, known as the steepest descent method. The Levenberg-Marquardt method combines both techniques, using steepest descent far from the minimum and gradually switching to the inverse Hessian with each successful step towards the minimum. The application of this method is described in 'Numerical Methods in C.'¹⁹ The disadvantage of this method is that it requires the first derivatives to be calculated. There are no known analytical derivatives available, so numerical derivatives have

been used to approximate the gradient. Small increments equal to 1% of the parameter's value, 0.05 for asymmetries, or 1° for angles, have been used.

The simplex method is very general, robust, straightforward to implement and does not require extra calculations to calculate the derivative. A simplex is a multi-dimensional geometrical figure. For N fitted parameters, a simplex with $N+1$ points is required. So for two fitted parameters the simplex has three points and is a triangle. These points are created from the initial guess and extra points found by changing each parameter in turn. From here, the point with the worst R^2 value is rejected and a new point is found by reflecting through the opposite face. If this new point is better then the simplex step is increased to try to obtain a better point. If it is worse then the step size is reduced. If no better point can be found then the whole simplex is contracted around the best point to get another set of points.

Both methods continue searching until some convergence criteria are met. These criteria are usually that the change on all the parameters for a successful step is smaller than a defined value or that R^2 reaches a small limiting value. In all the calculations there will be a limiting size placed by the accuracy with which the computer stores the data. This is usually much smaller than the convergence criteria when double precision numbers are used.

3.4.1 Boundary conditions

The minimisation algorithms above have no concept of the limits for certain parameters e.g. the asymmetry could go negative. In these cases, the individual tensor components have been labelled improperly. General transformations have been suggested that will relate the parameters back within their usual bounds.¹² For multiple-tensor interactions, these transformations can become quite complex. An alternative method, which has been used, is to return a large value of R^2 so that the guess is rejected. This will reduce the rate of convergence of parameters near to a boundary, but not stop it. Other boundary conditions include: line broadening not going negative, asymmetry not going over 1.0, and the angles α and β not extending

beyond $\pm 360^\circ$. Although β should not go over 180° , allowing it to range over a slightly larger area gives faster convergence.

3.5 Errors and reliability of parameters

The best-fit parameters found above need to be given with estimates of the fitting error if they are to be useful. From the Levenberg-Marquardt method, gradients are used to find the next fitting point. The steeper the gradient at the minimum, the better defined the parameter will be and the smaller its error. This is formalised in the equation below, which gives the lower bounds to the errors and assumes that the parameters are uncorrelated. α^{-1} is the inverse Hessian matrix, n is the number of data points and k is the number of fitted parameters. When chi squared is used, this error will be the standard deviation.

$$\text{Error}_i = \sqrt{\frac{R^2}{(n-k)} (\alpha^{-1})_{ii}}$$

As the gradient is calculated numerically, the step size should ideally be smaller than the error. The calculation of errors for the fitting of the shielding tensor components with spinning-sideband data has been recently described by Olivieri.²⁰

The accuracy and reliability of the determination of tensor parameters has recently been studied as the sample spinning speed is varied.²¹ It was found that the asymmetry of the shielding tensor is best determined from the static spectrum, whilst the anisotropy is most reliably found from the spinning-sideband spectrum. The best ratio of the spinning speed to the anisotropy depends on the size of the asymmetry but is 0.39 when the asymmetry is 0.5. This will give around five spinning sidebands. It has been previously noted that when the asymmetry is small ($\eta < 0.2$), it is poorly defined.^{22,23} For such low values of η , a ratio of spinning speed to anisotropy of 0.05 was found to be best. For the dipolar and quadrupolar parameters, static spectra proved²¹ the most reliable. This analysis has not allowed for practicalities such as

other peaks in the spectrum overlapping and the fact that the parameters are usually unknown before the experiment. It would be interesting to see how the reliability of a parameter fit for multiple tensor interactions varies with spinning speed.

3.6 Programs

3.6.1 GAMMA

GAMMA²⁴ (General Approach to Magnetic resonance Mathematical Analysis) is a set of objects that extend the C++ programming language. Hamiltonians, tensor rotations, imaginary numbers and many other functions are directly available by using the GAMMA library. This simplifies the writing of simulation programs and is not limited to simple ‘single pulse and acquire’ experiments. Other capabilities that were not used for these simulation programs include the simulation of real pulses, phase cycling, multiple-pulse sequences, and relaxation, to name but a few. Two things missing from GAMMA are powder averaging schemes and optimisation routines. The weakness of GAMMA is its generality. It has not been optimised to perform a single function but to do all things reasonably. For this reason, it was only used to develop the concepts for JCsim.

3.6.2 JCsim

JCsim has been written in the C programming language. It only uses standard libraries and so is portable between different operating systems. The program has been written in a modular style so that each function is clear and changes can be easily made. This program will simulate both static and spinning-sideband lineshapes for combinations of shielding, dipolar and quadrupolar interactions. It will also fit an experimental data set using the Levenberg-Marquardt search algorithm. This fit includes an error analysis as described above.

The static part of the program performs the calculations in the frequency domain. The spectral width is subdivided, then the resonance frequency of each crystallite is calculated and added to the corresponding bin. This gives a histogram that, with sufficient crystallite orientations and small divisions of the spectral width, gives the simulated spectrum. This can then be broadened by convolution with a Gaussian function. Any negative input value for the MAS speed will make the program use the static routines.

The static routines can simulate dipolar interactions from any nucleus including quadrupolar nuclei. The dipolar tensor can be combined with the quadrupolar or shielding tensors and may be non-colinear with them. This has been used to fit a static ^{31}P spectrum bonded to ^{14}N , as shown in Chapter 7.

The spinning part of the program was designed to produce simulations of spinning-sidebands for comparison to experimental data. It will simulate ssb patterns from shielding, dipolar coupling to spin- $1/2$ nuclei, and quadrupolar interactions. The fitting has been performed separately using the ssb97.o series of programs, which are described later. This simulation is performed in the time domain with incremental steps in the rotor angle. The step size is set to be an exact fraction of the dwell time and less than 5° . An FID is calculated for each crystallite. To increase the number of points in the FID, the FID for one sample rotation may be propagated. This total FID is then multiplied by a decaying exponential function to give a realistic linewidth to each peak.

3.6.2.1 Input file format

JCsim uses an input file called 'params.in' in the current directory to decide what to simulate. A description of the input format and an example of params.in is given below. For static spectra, a spectrum in XY format is also read in. The filename of this static spectrum is given within the input file.

```

/*****
*
* CSA          C isotropic anisotropy asymmetry units *
* J           J Jiso units *
* DIPOLE      D D' units *
* QUADRUPOLE  Q anisotropy asymmetry units *
* ANGLES      S theta, phi (in degrees) *
*             NB equivalent to beta and alpha normally *
*
* NUCLEUS 1   spin(I) Larmor_frequency(MHz) *
* NUCLEUS 2   spin(S) *
*
* SPECTRUM    G iterations speed (in Hz <0 for static) *
*             gw (line broadening in Hz) ruler units *
*
* STATIC case: filename, units *
* SPINNING case: ssb_min, ssb_max *
*               ssb intensities *
*
* Units either ppm, hz, kHz, or MHz (p,h,k,m) *
*
* First number is a switch i.e. *
*   3 for fit only first parameter, not asymmetry. *
*   2 for fit both parameters *
*   1 for include in calculation *
*   0 for not used *
*
* When fitting, the isotropic shift is always fitted *
*
*****/

```

Sample file - **params.in**

```

2 35.042538 -49.675838 0.736524 p
0 0.000000 h
1 859.993408 h
0 26.600000 0.000000 h
2 25.472010 14.471144

0.500000 80.000000
1.000000
2 100000 -0.300000 659.321472 p

Ph3PNH2Br_static p

```

The program also outputs certain files depending on what calculation it has performed. These are `ssb.fid`, `ssb.spec`, `static.spec`, `filename.norm` (the normalised static spectrum), and `params.out` (in the case of fitting).

3.6.3 Spinning sideband fitting

The `ssb97.o`²⁵ program is based on `ssb95.o`,²⁶ which is a FORTRAN program that uses NAG²⁷ routines for the simplex fitting and fast Fourier transform. It has been modified so that it now gives an error on the fitting parameters based on the paper by Olivieri.²⁰ A non-iterating version, `ssb97n.o`, has also been written.

When the scalar coupling is large enough to separate out the different spinning-sideband manifolds, it is possible to calculate a value for D' . Each spinning-sideband manifold may be analysed separately or in combination. This latter option has been implemented in a series of programs that aim to minimise the total R^2 value. Weighting the central set of data has been tried but does not affect the result significantly. The first program, `ssb97m.o`, assumes that the tensors are colinear and fits for the anisotropy, asymmetry and dipolar coupling constant with three sets of data. `ssb97m2.o` allows for the fitting of a doublet. The third program, `ssb97m5.o`, fits the anisotropy, asymmetry, and dipolar coupling constant, and allows non-colinearity with the two angles α and β . The minimum R^2 value is found by changing α and β in steps of 10° . The effective shielding tensor is found by combining the shielding and dipolar tensors using a static simulation and finding the new effective shielding tensor. This is then used in the spinning-sideband calculation.

3.6.3.1 Input file formats

The input for this program is read from `stdin` and written to `stdout`. These can be redirected to files using `<` and `>`. The format of the input file for `ssb97.o` is:

```
Text string
Spinning speed (Hz), Larmor frequency (MHz)
Number of spinning sidebands to simulate, minimum (high
frequency), maximum (low frequency)
Minimum, maximum values to use from data for  $R^2$  and fitting
Number of angular orientations in powder average
Spinning sideband intensities (separated by commas)
Shielding anisotropy, asymmetry, isotropic shielding
```

The triple fit program uses the modified input file:

Text string

Spinning speed (Hz), Larmor frequency (MHz)

Number of angular orientations in powder average

Three sets of:

Number of spinning sidebands to simulate, minimum (high frequency), maximum (low frequency)

Minimum, maximum values to use from data for R^2 and fitting

Spinning sideband intensities (separated by commas)

Shielding anisotropy, asymmetry, isotropic shielding

Only in ssb97m5.o

Factor to scale D' (1 for satellite and 2 for triplet peaks)

3.7 Molecular modelling and computational chemistry

With the increased computing power now available molecular modelling and computational chemistry are becoming readily available in the laboratory environment. These can be used to find low-energy structures of molecules, the molecular orbital coefficients and energies, and molecular properties such as the shielding tensor and electric field gradient. The quadrupolar tensor is directly proportional to the electric field gradient.

Whilst calculations will nearly always give a numerical answer, it is important to realise the assumptions that have been made and their limitations. Most calculations are performed at zero density in the gas phase where there are no intermolecular forces or solvent effects. Moreover, very few calculations account for relativistic effects, which are important for heavier nuclei. What follows is a synopsis of the techniques, followed by a discussion of the practicalities and reliabilities of calculations using Gaussian 94.²⁸ Useful books about molecular modelling and computational chemistry are given in reference 29.

3.8 Molecular mechanics

Molecular mechanics uses a force-field model to describe a molecule in terms of balls and springs. The total energy of the molecule is the sum of contributions from bond stretches, bond and dihedral angles, non-bonded van der Waals and electrostatic terms. This model neglects the contributions from electrons and can only give the ground state conformation of the molecule. The MM2 parameters for the energy terms have been derived from known molecules that are in stable conformations. This restricts the generality of the parameterisation to similar molecules, stable structures and thermodynamic data. Third generation parameterisations include cross terms and data for intermediate structures from ab initio calculations, which are necessary for accurate molecular dynamics simulations. Despite these restrictions, the big advantage is that the method is not computationally

demanding and can be used to study large molecular systems such as proteins and polymers.

3.9 Quantum mechanics

The quantum mechanical approach is based on solving the Schrödinger equation for the molecule. By rearranging it, it can be shown that a non-trivial solution exists only when the determinant $|H_{ik} - \epsilon S_{ik}| = 0$. In this $H_{ik} = \langle \chi_i | H | \chi_k \rangle$ where H is the one-electron Hamiltonian, ϵ is the orbital energy, $S_{ik} = \langle \chi_i | \chi_k \rangle$ is the overlap integral, and χ_i are the atomic orbitals. The eigenvalues and eigenvectors of the secular determinant give the molecular orbital energies and coefficients for the atomic orbital contributions. From these, molecular properties can be calculated.

This method is often called an *ab initio* method, as there are no parameters used. An initial guess is made for the wavefunction with a lower level of theory e.g. Extended Hückel. This wavefunction is put into the determinant above, and used to generate a better guess. The process is repeated until a self-consistent set of molecular orbitals is found.

The Hamiltonian can be approximated to different levels. The usual method is that of Hartree-Fock (HF). This takes no account of electron correlation or relativistic effects. Electron correlation is important when the system has multiple bonds or lone pairs of electrons. In these cases there are low-lying unoccupied molecular orbitals and small energy gaps for $n - \pi^*$ transitions. Relativistic effects become important for heavier elements such as tin, bromine and iodine. More numerically intensive methods such as Møller-Plesset (MPn) perturbation theory and Configuration Interaction take account of electron correlation but are only practical for very small systems. Very recently Density Functional Theory (DFT) has been used. This is less computationally demanding than HF and allows for electron correlation. The current implementation of Gaussian 94 only allows the calculation of energies, gradients and frequencies by this method as it does not have the magnetic field dependent terms necessary for shielding calculations. A hybrid

method is available that uses the Hartree-Fock approximations but adds in the exchange and correlation functionals from DFT.

The atomic orbitals need to be described in a form that allows computation. Slater formulated these as the product of an exponential function of the radial distance and a spherical harmonic. Whilst these are very accurate, exponential functions are hard to integrate whereas Gaussians converge rapidly. In the computations, the exponentials are replaced by a linear combination of Gaussians.

The atomic orbital descriptions are given in basis sets. These basis sets are described by the number and type of basis functions e.g. s, p, d. Each basis function is then described by the number of Gaussians used to approximate it. Basis sets can be enlarged by using a linear combination of two basis functions in place of one. This is then referred to as a double zeta, split-valence basis set. Examples include 3-21g and 6-31g. Triple zeta basis sets such as 6-311g extend this idea further. This allows the orbitals to change size but not shape, which is achieved by adding extra polarised functions e.g. d orbitals for carbon. The nomenclature varies: 6-31g* and 6-31g(d) are equivalent and add a d function to heavy elements, 6-311g** and 6-311(d, p) add a d function to heavy elements and p function to protons. Diffuse functions may be added to account for electron density relatively far from the nucleus e.g. 6-31+g.

The choice of basis set depends on the accuracy required, the size of the molecule and the resources available. The variational principle states that the better an atomic orbital is defined, i.e. the larger the basis set, the lower is the energy. Complete basis set methods do exist but are too computationally demanding for anything but the smallest of molecules.

Semi-empirical methods, such as AM1 and PM3, reduce the calculational demands by using empirical parameters for the core electrons and ab initio calculations for only the valence electrons. As with the molecular mechanics, these methods are dependent on how they are parameterised. However, they can take account of some relativistic and electron correlation effects via the effective core potential.

3.10 Evaluating the shielding tensor

Nuclei are surrounded by electrons that are constantly in motion. When these are placed in an applied magnetic field the energies are perturbed and a current flows that creates an opposing magnetic field at the centre of the extra motion. These effects change the magnetic field observed at the nucleus and hence its characteristic nuclear magnetic resonance frequency. This change is expressed by the shielding tensor and is a sensitive probe of the electronic structure around the nucleus. It can be divided into two components:³⁰ diamagnetic (from the opposing current) and paramagnetic (from a partial blocking of the electronic motion by the atomic nuclei). These two components are large and opposite in sign. The relative values of both terms are dependent on the position of the gauge origin. However, the total shielding is independent of this.

$$\sigma_{\alpha\beta} = \sigma_{\alpha\beta}^d + \sigma_{\alpha\beta}^p$$

The tensor can be determined using second-order perturbation theory, which gives the partial derivative shown below.³¹ Expanding the total Hamiltonian in powers of μ_N and B_0 gives the partial Hamiltonians where $H^{(1,0)}$ is the component associated with μ_N etc.. The two expanded terms below can be associated with the diamagnetic and paramagnetic components of the shielding tensor respectively.

$$\sigma_{\alpha\beta} = \frac{\partial^2 \langle H \rangle}{\partial \mu_{N,\alpha} \partial B_{0,\beta}} = \langle 0 | H_{\alpha\beta}^{(1,1)} | 0 \rangle + \sum_{m \neq 0} \frac{\langle 0 | H_{\alpha}^{(1,0)} | m \rangle \langle m | H_{\beta}^{(0,1)} | 0 \rangle + \langle 0 | H_{\beta}^{(0,1)} | m \rangle \langle m | H_{\alpha}^{(1,0)} | 0 \rangle}{E_0 - E_m}$$

Both terms have an r^{-3} dependence, so the electron density closest to the nucleus has the most effect. From the equation above, it can be seen that the diamagnetic term is dependent only on the ground state of the molecule and can be accurately calculated. The paramagnetic term is a sum over all the excited states and much harder to calculate. If there are errors in the calculation of this part then the invariance of the total shielding tensor to changing the gauge origin is no longer valid.

Empirical and *ab initio* methods for calculating the shielding tensor have been suggested which can give insight into the electronic structure of the molecule. The local symmetry at the nucleus can be used to predict the number of non-vanishing contributions to the shielding tensor.³² Distortions will lower the local symmetry and introduce additional contributions to those predicted. The diamagnetic terms are symmetric whilst the antisymmetric contributions can only come from the paramagnetic part. The latter are generally not observable with NMR as they only affect the shift to second order.

An empirical method based on the charge density and bond order matrix for the valence orbitals has been suggested.³³ This gives a qualitative insight into the changes of the paramagnetic shielding anisotropy and asymmetry with coordination and different ligands. It has been applied in the discussion of ^{199}Hg where the 5d electrons are in a closed shell and contribute little to the bonding.³⁴

3.10.1 *Ab initio* methods

Ab initio methods work by calculating the diamagnetic and paramagnetic components separately. The diamagnetic part may be calculated very accurately whilst the paramagnetic part is subject to much larger errors. The paramagnetic component is smallest when the gauge origin is at the centre of electronic charge. The error decreases as the basis set size increases and the wavefunction in the proximity of the studied nucleus is better described. The methods used aim to relax the basis set requirements and give good results with minimal basis sets. There have been various such methods including GIAO,^{35,36} IGLO³⁷ and LORG.³⁸ Other methods are only applicable to small molecules (less than six non-hydrogen atoms) and are not relevant to the systems of interest here. DFT methods are now becoming available and have the advantage of including electron correlation with calculations that are faster than Hartree-Fock.

Gauge-Including Atomic Orbitals (GIAO) adds a field-dependent term to each atomic orbital, equivalent to a first-order perturbation of the wavefunction by

the external magnetic field. This means that there is a local gauge origin at each atomic orbital. This method works well for small (double zeta) basis sets but has the disadvantage that all the electron integrals from the SCF determinant must be recalculated. With increased computing power and improvements by Pulay,³⁶ this is now realistically possible. This method has been used, as implemented in Gaussian 94, for the results herein.

The Individualised Gauge for Localised Orbitals (IGLO) method modifies the molecular orbitals to include the effects of the magnetic field. This requires a few recalculations for resonance and exchange terms but avoids the expensive recalculation of all integrals. As the shielding is localised, it can be interpreted in terms of bonds, electron lone pairs etc.. The Localised Orbital Local Origin (LORG) method is similar to IGLO in that it also allows the local effects of shielding to be studied.

3.10.2 Accuracy and reliability of calculations

Unless at absolute zero, molecules are not static. An NMR spectrum is the time average of many different molecular conformations. These are dependent on the Boltzmann distribution of molecules and their internal motions. An *ab initio* calculation of the shielding uses either the crystal or a minimised structure as the basis for the calculation. Both of these are only one of many conformations that are sampled during the acquisition time of an NMR spectrum. The calculation is also performed on an isolated molecule without regard for intermolecular contributions. At present, the errors associated with these assumptions are smaller than the accuracy of the calculations so they can be ignored. In the future, *ab initio* NMR shielding data may be extended to calculate across an ensemble of molecular conformations to study molecular dynamics and for use in structure refinement.

The calculated nuclear shielding is referenced to a bare nucleus. To compare this with experimental results, either the calculated shielding of a known reference compound must be used, or the absolute shielding of a molecule must be measured.

Using relative shielding can take account of some systematic errors but it will introduce other ones. The paramagnetic part of the shielding can be calculated from molecular beam studies in the gas phase that measure the spin-rotation constant.³⁹ This can be extrapolated to a zero density limit to remove the effect of intermolecular contributions. The diamagnetic part of the shielding can be accurately calculated by ab initio methods. These can then be combined to give the absolute shielding value. Care must be taken, as the ab initio calculations take no account of intermolecular interactions, often use the equilibrium geometry, and involve only a ground vibrational state. At present, the calculation errors are greater than these correction factors so they may be ignored. In the future careful analysis may need to include these effects. Experimental data for the absolute shielding of standard compounds measured in the gas phase are given in Table 3.

Table 3: Summary of the experimentally determined absolute shielding values for selected nuclei

Nucleus	Compound	Absolute shielding (ppm)	Relative shift (ppm)	Reference
¹³ C	TMS	188.1	0.0	40
¹⁵ N	NH ₃	264.5	0.0	41
¹⁷ O	H ₂ O	344.0	0.0	42
¹⁹ F	HF	410 ± 6	-214.4	39
¹⁹ F	CFCl ₃	195.6	0.0	39
³¹ P	PH ₃	594.45 ± 0.63	-266.10	43
³¹ P	H ₃ PO ₄	328.35	0.0	44
¹¹⁹ Sn	Sn(CH ₃) ₄	2180 ± 200	0.0	45

The accuracy of the calculations depends on the size of the basis sets used and the level of the theory. There is a trade off between the resources available and accuracy required. One way to improve calculations for minimal cost is to use locally dense basis sets.⁴⁶ The shielding values contain a term proportional to r^{-3} . Thus a good description of the wavefunction close to the nucleus studied is more important

than a good description for distant nuclei e.g. protons and phenyl rings. It is important to retain any symmetry present within the molecule when choosing which basis sets to assign to different atoms. The Oldfield group have used this concept to study heavy metal organometallic compounds, e.g. haeme-proteins, using a Wachters triple zeta basis set on the iron-57, triple zeta basis set on atoms directly bonded to the iron, and a double zeta basis set for the remainder.⁴⁷

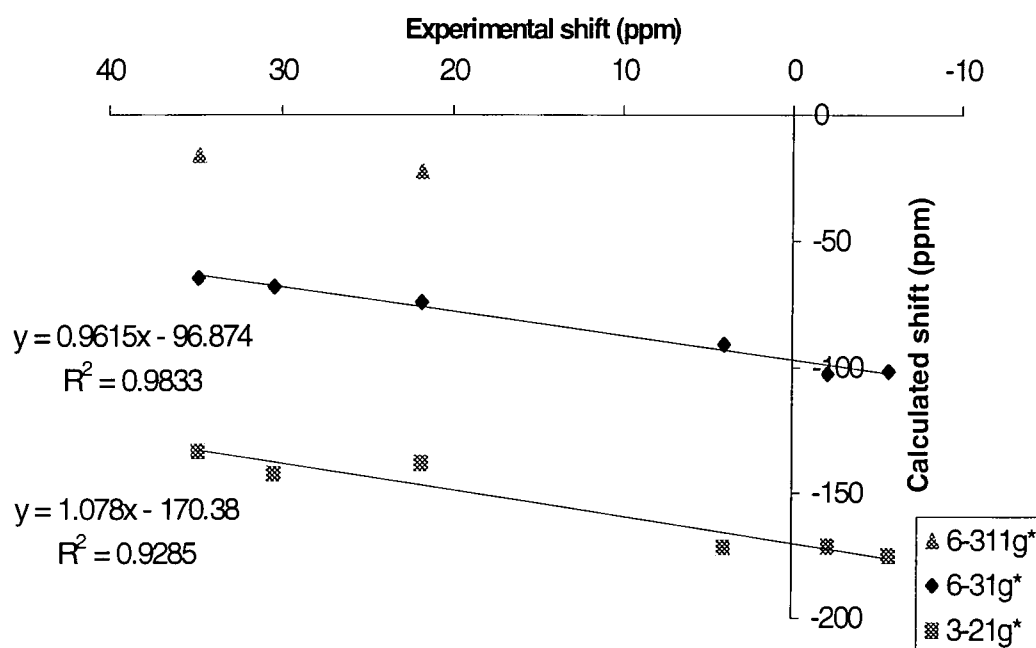


Figure 3: Experimental and calculated isotropic shifts for iminophosphoranes.

Figure 3 compares experimental ^{31}P data for iminophosphoranes with ab initio HF calculations using up to triple zeta basis sets, the measured crystal structures and the absolute shielding scale given above. It can be seen that there is a reasonable fit between experimental results and theoretical predictions, even for large molecules. The gradient is close to one, as expected. The difference in the intercept is mainly due to the use of truncated basis sets. Electron correlation will also be important, as there are multiple bonds and lone pairs in these molecules. Its inclusion would improve the fit further, as has been seen for the smaller molecules. Shielding anisotropies effectively have an internal reference and agree within 15% with the experimental values. The largest basis sets have only been used on the smaller

molecules, as otherwise the calculation times are too demanding. The compounds are discussed further in Chapter 7.

Carbon-13 is one of the most widely measured nuclei. A recent review⁴⁸ has looked at the accuracy of ab initio calculations with a variety of basis sets. The conclusions were that the GIAO method converges rapidly for reasonably sized (double zeta) basis sets. MP2 level calculations using a quadruple zeta basis set can give RMS errors as low as 2.3 ppm for a range of molecules. For practical purposes, optimising the molecule with B3LYP hybrid functional and the 6-31g* basis set gives a reasonable geometry. If possible, then use of the B3LYP/6-311+g(2d,p) method, which is a triple zeta basis set, gives an RMS error of 4.2 ppm. It includes the effect of electron correlation and is less computationally expensive than MP2. For larger molecules, e.g. taxol, using HF/6-31g* gives reasonable results,⁴⁸ with an RMS error across all the carbon atoms of 11.1 ppm. This is usually sufficient for qualitative assignment of a molecule. Using larger basis sets for the HF method gives no better results, as the basis set limit has been reached. The hybrid functionals give no better results for small basis sets than the Hartree-Fock method. DFT gives better results than HF for large basis sets, includes the effect of electron correlation and takes a shorter amount of time.

Nitrogen-15 and oxygen-17 shielding tensors were also studied in the same paper.⁴⁸ Both of these nuclei are more sensitive to the effects of electron correlation than carbon-13. The errors are larger than those for ¹³C, but are still reasonable: for a small range of compounds containing ¹⁵N using the 6-31g* basis set, HF gave a RMS error of 14.5 ppm, whilst B3LYP was 18.2 ppm. The small error for the HF theory is small due to a fortuitous cancelling of errors. With the larger 6-311g+(2d,p) basis set the RMS error for HF is 36.5 ppm. This shows the advantage of including electron correlation. Oxygen-17 errors are roughly 20 to 35 ppm when using a quadruple zeta basis set. Too few compounds were studied to give a statistical result. The effect of including electron correlation gives a minor improvement compared to the overall size of the error.

Hydrogen Fluoride was one of the first molecules where absolute shielding data were derived from the molecular beam results.³⁹ The derivation included

vibrational corrections so that the data could be compared to experimental data at 300 K. For a range of molecules, good agreement between experimental data⁴⁹ and ab initio IGLO calculations⁵⁰ was found for triple zeta basis sets with extra polarisation functions. The total range of errors at this size of basis set was 16 ppm. The results indicated that the basis set limit had not been reached, so that further improvements may be possible. They also showed that correlation effects were of little importance.

Shielding constants for a series of phosphorus-31 compounds at the zero-pressure limit have been compared by IGLO⁵¹ and GIAO⁵² calculations, which give comparable results to within 20 ppm. It was concluded for singly bonded molecules that multiple d atomic orbitals on phosphorus were needed to accurately describe the wavefunction. Larger, multiply bonded molecules were not studied but would be expected to require similar if not larger basis sets. The effects of including electron correlation have been recently studied and shown to give results that are different from Hartree-Fock calculations and in better agreement with experiment.⁵³

Recent studies have looked at the challenge of calculating ¹¹⁹Sn shielding.⁵⁴⁻⁵⁶ An absolute shielding scale has been found using molecular beam relaxation measurements and molecular dynamics simulations with solution-state relaxation data.⁴⁵ The derivation has not included relativistic effects. The values for SnH₄, SnCl₄ and Sn(CH₃)₄ have been compared to ab initio calculated values. Tin requires very large basis sets to saturate the calculation and suffers from electron correlation and relativistic effects. All the calculations predicted more shielded values than those measured. The average error with a large basis set was +606 ppm using HF and +243 ppm using DFT.⁵⁴ These are still outside experimental errors but are better than previously reported values. An ab initio study of relativistic effects in SnH₄ and the tetrahalide tin compounds concluded that the effect was negligible on the tin atom whilst it became significant, reaching 1000's of ppm, for bromine and iodine.⁵⁷

3.11 Scalar couplings calculated by CLOPPA-AM1 theory

Scalar, J , couplings are often measured and can give insight to the molecular electronic structure. More recently, values for the anisotropy in J , ΔJ , have been reported. This can be measured from D' as described earlier but is often subject to large experimental uncertainties. Use of theoretical methods can give further understanding as to how the coupling arises and what its contributions are. The CLOPPA⁵⁸ (Contributions from Localised Orbitals within the Polarisation Propagator Approach) method has been used to find isotropic coupling constants and has recently been extended to include the anisotropic terms.⁵⁹ For small molecules, it is possible to use ab initio calculations to describe the wavefunction. However, for larger molecules with heavier atoms this becomes impractical and relativistic effects also become important. Semi-empirical methods, such as AM1, include relativistic effects in the effective core potential as they have been parameterised from experimental data. Relativistic corrections are included for perturbations between the electrons and nuclei, but the valence electrons are treated non-relativistically as they are far from the tin centre. This level of theory is sufficient to give qualitative descriptions of the coupling and relate it to its physicochemical origin. The MNDO method has been used to successfully describe isotropic coupling for group 14 elements⁶⁰, but a mixed RPA-AM1 / MNDO method has been found to give better results for Sn-X couplings.

The scalar coupling interaction is composed of four main terms: Diamagnetic Spin-orbital (DSO), Paramagnetic Spin-orbital (PSO), Spin-Dipolar (SD), and the Fermi-Contact (FC). The DSO term is small and only a first order perturbation so it will be ignored. The FC term is isotropic and is the main component, though it will have no effect on the anisotropy. The dominant term for the anisotropy is the FC/SD cross term, which is symmetric and has a trace of zero. The PSO and SD terms are non-symmetric.

The reliability of the RPA-AM1 method has been checked for the reduced isotropic couplings for XH_4 and XMe_4 where X is a group 14 element. There is good qualitative agreement despite the calculations being based on minimised geometries, which may differ from the experimental ones. The couplings are seen to be sensitive

to the geometry, as will be discussed in Chapter 6. For the reduced coupling anisotropy, all terms are positive and the FC/SD term dominates. The general trend on going down group 14 is for the reduced coupling anisotropy to increase. With this method, the components can be localised in terms of bonding, antibonding and lone pair contributions. These have been used to explain the trends observed.

-
- ¹ K. Schmidt-Rohr and H. W. Spiess, "Multidimensional Solid-state NMR and Polymers," Academic Press, London (1994)
- ² U. Haebleren, "High resolution NMR in Solids," Academic Press, New York (1976)
- ³ M. M. Maricq and J. S. Waugh, *J. Chem. Phys.*, **70**, 3300 (1979)
- ⁴ J. Skibsted, N. C. Nielsen, H. Bildsøe, and H. J. Jakobsen, *Chem. Phys. Lett.*, **188**, 405 (1992)
- ⁵ J. C. Cherryman, Unpublished work
- ⁶ J. Herzfeld and A. E. Berger, *J. Chem. Phys.*, **73**, 6021 (1980)
- ⁷ D. W. Alderman, M. S. Solum, and D. M. Grant, *J. Chem. Phys.*, **84**, 3717 (1986)
- ⁸ M. Bak and N. C. Nielsen, *J. Magn. Reson.*, **125**, 132 (1997)
- ⁹ S. K. Zaremba, *Ann. Mat. Pura Appl.*, **73**, 293 (1966)
- ¹⁰ H. Conroy, *J. Chem. Phys.*, **47**, 5307 (1967)
- ¹¹ V. B. Cheng, H. H. Suzukawa, and M. Wolfsberg, *J. Chem. Phys.*, **59**, 3992 (1973)
- ¹² J. M. Koons, E. Hughes, H. M. Cho, and P. D. Ellis, *J. Magn. Reson. A*, **114**, 12 (1995)
- ¹³ J. M. Hammersley and D. C. Handscomb, in "Monte Carlo Methods," Meuthen's Monographs on Applied Probability and Statistics (M. S. Bartlett, Ed.), John Wiley, New York (1964)
- ¹⁴ H. Wozniakowski, *Bull. Am. Math. Soc.*, **24**, 185 (1991)
- ¹⁵ E. Hughes, Ph. D. Thesis, University of South Carolina (1995)
- ¹⁶ G. Jeschke and G. Grossmann, *J. Magn. Reson. A*, **103**, 323 (1993)
- ¹⁷ J. A. Nelder and R. Mead, *Comput. J.*, **7**, 308 (1965)
- ¹⁸ D. W. Marquardt, *J. Soc. Ind. Appl. Math.*, **11**, 431 (1963)
- ¹⁹ W. H. Press, S. A. Teukolsky, W. T. Vetterling, and B. P. Flannery, "Numerical Recipes in C: The Art of Scientific Computing," 2nd ed., Cambridge University Press, Cambridge (1992)
- ²⁰ A. C. Olivieri, *J. Magn. Reson. A*, **123**, 207 (1996)
- ²¹ P. Hodgkinson and L. Emsley, *J. Chem. Phys.*, **107**, 4808 (1997)
- ²² N. J. Clayden, C. M. Dobson, L. Lian, and D. J. Smith, *J. Magn. Reson.*, **69**, 476 (1986)
- ²³ R. K. Harris, P. Jackson, L. H. Merwin, B. J. Say, and G. Hägele, *J. Chem. Soc., Faraday 1*, **84**, 3649 (1988)
- ²⁴ S. A. Smith, T. O. Levante, B. H. Meier, and R. R. Ernst, *J. Magn. Reson. A*, **106**, 75 (1994); see also <http://gamma.magnet.fsu.edu/>
- ²⁵ J. R. Ascenso, L. H. Merwin, H. Bai, J. C. Cherryman, and R. K. Harris, unpublished work
- ²⁶ J. R. Ascenso, L. H. Merwin, and H. Bai, "In-house Sideband Fitting Program," University of Durham.
- ²⁷ Numerical Algorithms Group, Mark 17
- ²⁸ Gaussian 94, Revision E.2, M. J. Frisch, G. W. Trucks, H. B. Schlegel, P. M. W. Gill, B. G. Johnson, M. A. Robb, J. R. Cheeseman, T. Keith, G. A. Petersson, J. A. Montgomery, K.

-
- Raghavachari, M. A. Al-Laham, V. G. Zakrzewski, J. V. Ortiz, J. B. Foresman, J. Cioslowski, B. B. Stefanov, A. Nanayakkara, M. Challacombe, C. Y. Peng, P. Y. Ayala, W. Chen, M. W. Wong, J. L. Andres, E. S. Replogle, R. Gomperts, R. L. Martin, D. J. Fox, J. S. Binkley, D. J. Defrees, J. Baker, J. P. Stewart, M. Head-Gordon, C. Gonzalez, and J. A. Pople, Gaussian, Inc., Pittsburgh PA (1995)
- ²⁹ G. H. Grant and W. G. Richards, "Computational Chemistry," Oxford University Press, Oxford (1995); A. R. Leach, "Molecular Modelling Principles and Applications," Longman, Harlow (1996); J. B. Foresman and A. Frisch, "Exploring Chemistry with Electronic Structure Methods," 2nd Ed., Gaussian Inc., Pittsburgh, (1996)
- ³⁰ N. F. Ramsey, *Phys. Rev.*, **78**, 699 (1950)
- ³¹ A. C. de Dios, *Prog. NMR Spectr.*, **29**, 229 (1996); H. Fukui, *Prog. NMR Spectr.*, **31**, 317 (1997)
- ³² A. D. Buckingham and S. M. Malm, *Mol. Phys.*, **22**, 1127 (1971)
- ³³ G. A. Webb, "Factors contributing to the observed chemical shifts in heavy nuclei," in *NMR of Newly Accessible Nuclei*, vol. 1 (P. Laszlo, Ed.), Academic Press, New York (1983)
- ³⁴ G. A. Bowmaker, R. K. Harris, and S. Oh, *Coord. Chem. Rev.*, **167**, 49 (1997)
- ³⁵ R. Ditchfield, *Mol. Phys.*, **27**, 789 (1974)
- ³⁶ K. Wolinski, J. F. Hinton, and P. Pulay, *J. Am. Chem. Soc.*, **112**, 8251 (1990)
- ³⁷ W. Kutzelnigg, *Isr. J. Chem.*, **19**, 193 (1980)
- ³⁸ A. E. Hansen and T. D. Bouman, *J. Chem. Phys.*, **82**, 5035 (1985)
- ³⁹ D. K. Hindermann and C. D. Cornwell, *J. Chem. Phys.*, **48**, 4148 (1968)
- ⁴⁰ A. K. Jameson and C. J. Jameson, *Chem. Phys. Lett.*, **134**, 461 (1987)
- ⁴¹ S. G. Kukolich, *J. Am. Chem. Soc.*, **97**, 5704, (1975); C. J. Jameson, A. K. Jameson, D. Oppusunggu, S. Wille, P. M. Burrell, and J. Mason, *J. Chem. Phys.*, **74**, 81 (1981)
- ⁴² R. E. Wasylishen, S. Mooibroek, and J. B. Macdonald, *J. Chem. Phys.*, **81**, 1057 (1984)
- ⁴³ P. B. Davies, R. M. Neumann, S. C. Wofsy, and W. Klemperer, *J. Chem. Phys.*, **55**, 3564 (1971)
- ⁴⁴ C. J. Jameson, A. De Dios, and A. K. Jameson, *Chem. Phys. Lett.*, **167**, 575 (1990)
- ⁴⁵ A. Laaksonen and R. E. Wasylishen, *J. Am. Chem. Soc.*, **117**, 392 (1995)
- ⁴⁶ D. B. Chesnut and K. D. Moore, *J. Comput. Chem.*, **10**, 648 (1989)
- ⁴⁷ R. H. Havlin, N. Godbout, R. Salzmann, M. Wojdelski, W. Arnold, C. E. Schulz, and E. Oldfield, *J. Am. Chem. Soc.*, **120**, 3144 (1998)
- ⁴⁸ J. R. Cheeseman, G. W. Trucks, T. A. Kieth, and M. J. Frisch, *J. Chem. Phys.*, **104**, 5497 (1996)
- ⁴⁹ C. J. Jameson, A. K. Jameson, and P. M. Burrell, *J. Chem. Phys.*, **73**, 6013 (1980); C. J. Jameson, A. K. Jameson, and J. Honarbaksh, *J. Chem. Phys.*, **81**, 5266 (1984)
- ⁵⁰ U. Fleischer and M. Schindler, *Chem. Phys.*, **120**, 103 (1988)
- ⁵¹ U. Fleischer, M. Schindler, and W. Kutzelnigg, *J. Chem. Phys.*, **86**, 6337 (1987)
- ⁵² D. B. Chesnut and B. E. Rusiloski, *Chem. Phys.*, **157**, 105 (1991)

-
- ⁵³ D. B. Chesnut and E. F. C. Byrd, *Heteroatom Chem.*, **7**, 307 (1996)
- ⁵⁴ A. C. de Dios, *Magn. Reson. Chem.*, **34**, 773 (1996)
- ⁵⁵ N. Nakatsuji, T. Inoue, and T. Nakao, *Chem. Phys. Lett.*, **167**, 111 (1990)
- ⁵⁶ N. Nakatsuji, T. Inoue, and T. Nakao, *J. Phys. Chem.*, **96**, 7953 (1992)
- ⁵⁷ H. Kaneko, M. Hada, T. Nakajima, and N. Nakatsuji, *Chem. Phys. Lett.*, **261**, 1 (1996)
- ⁵⁸ A. C. Diz, C. G. Giribet, M. C. Ruiz de Azúa, and R. H. Contreras, *Int. J. Quantum. Chem.*, **37**, 663 (1990)
- ⁵⁹ J. A. González, G. A. Aucar, M. C. Ruiz de Azúa, and R. H. Contreras, *Int. J. Quantum. Chem.*, **61**, 823 (1997)
- ⁶⁰ G. A. Aucar, E. Botek, S. Gómez, E. Sproviero, and R. H. Contreras, *J. Organomet. Chem.*, **524**, 1 (1996)

4 Review of Previous Work on Organotin Compounds

This chapter aims to provide a background to the NMR of organotin compounds. These have previously been studied by solution- and solid-state ^1H , ^{13}C , and ^{119}Sn NMR, with some extensive interpretation. However, the fluorine-19 and multinuclear spectra of these compounds have not been studied. By using a multinuclear approach, it is possible to gain a greater understanding of the compounds.

Tin is present in a wide range of inorganic and organometallic compounds. In addition to the organotin halides, other tin systems include polymers,¹ chalcogenides,² and other cyclic and noncyclic organotin compounds.³ By studying one group of compounds in detail, we can attempt to understand the bonding and molecular structure for this group and then extend this understanding to other groups. Tin-119 is easily studied by NMR, being more sensitive than carbon-13. The ^{119}Sn spectra contain a wealth of detail including the chemical shift, shielding anisotropies and scalar coupling to other nuclei. With the use of fast-spinning multinuclear probes, these NMR features can be isolated, either by selectively removing components or by spreading the information out over two dimensions. With organotin fluorides, fluorine-19 is also a useful probe nucleus, with the scalar couplings to ^{119}Sn being used to understand the bonding structure at the tin centre.

The organotin fluorides tend to form polymers in the solid state with bridging fluorine groups. NMR data can give some insight into whether the compound is polymeric or not and the strength of the bonding. For longer-range structure and bond angles, XRD data are clearer. There have been a few previous ^{119}Sn NMR studies of the organotin halides. The compounds studied and the general conclusions are highlighted in the final section. Specific results are discussed, where relevant, in the following chapters.

There have been several general ^{119}Sn NMR review articles, the early ones (1978 to 1985) used data from solution-state measurements. The most recent review

by Sebald⁴ in 1994 includes the small amount of solid-state data that has been reported and summarises the earlier results.

4.1 Molecular structure from ^{119}Sn NMR

As the amount of ^{119}Sn NMR data available has increased, it has become possible to consider how the NMR parameters, particularly the isotropic shift and shielding anisotropy, vary with molecular structure and coordination number. Scalar coupling can give information about the type and number of atoms bonded to tin and about the strength of the bonding. It is not always possible to study the compound in the solution state, as many of the compounds are insoluble. For examples where it has been possible, the structure can be very different to that in the solid, e.g. the compound may no longer be a polymer. The first ^{119}Sn CPMAS spectra were reported in 1978⁵ and many more applications have followed.

The isotropic shift covers a wide range from ca. 2500 to -2500 ppm with respect to the signal for Me_4Sn . This makes it very sensitive to changes in molecular structure. The isotropic shift is often 150 to 200 ppm less shielded when comparing the solid- and solution-state ^{119}Sn measurements as the solvent interacts with the compound. The isotropic shift tends to decrease as the coordination number increases. It is not a reliable parameter for predicting coordination number as it can also be strongly influenced by the substituents on tin. This can be seen by the shift of four-coordinate Mes_3SnF (Mes = mesityl), which is higher than that for five-coordinate $^n\text{Bu}_3\text{SnF}$. By comparing the shifts of Mes_3SnF and Ph_3SnF , where both compounds have aryl groups and are four- and five-coordinate respectively, the shift of Mes_3SnF is indeed higher than that for Ph_3SnF . There is a slight temperature dependence of the shift, though this is not generally significant for the small range of temperatures measured here.

Recently, more shielding anisotropy (SA) data has become available. This is mainly from spinning-sideband (ssb) analysis of solid-state NMR spectra but also from solution-state relaxation measurements. The SA parameter is a better descriptor

for coordination number. It has been found that as the coordination number of tin increases from five to seven, the shielding anisotropy changes from being negative to increasingly positive.⁶ Six coordinate tin compounds have a range of positive SA's lying between these extremes. For large values of the SA, it is not possible to spin fast enough to fully average out the SA. In the extreme, there can be so many spinning sidebands that the signal-to-noise ratio is poor, signal is lost in the outer ssb peaks and there is uncertainty in the assignment of the centreband. It is also possible that four- and six-coordinate compounds have high symmetry when they have identical ligands. In this case, the SA would be expected to be zero. Often distortions reduce the symmetry to give a small SA. Table 4 summarises data from a small range of organotin compounds as given in reference 6, augmented by data from reference 7 and measurements herein for Mes_3SnF and ${}^n\text{Bu}_3\text{SnF}$.

Table 4: Summary of the shift and shielding anisotropy ranges observed for ${}^{119}\text{Sn}$ NMR for organotin compounds.

Coordination number	δ_{iso} / ppm	SA / ppm
4	200 to -200 ⁷	~10 (Mes_3SnF)
5	0 to -100	-160 to -210
6	-156 to -278	287 to 696
7	-488	1015

Scalar coupling to other nuclei is often visible in ${}^{119}\text{Sn}$ spectra. Single-bond coupling constants are large compared to the solid-state NMR linewidths. It is also possible to measure the coupling constants by observing the other nucleus. Coupling to ${}^{119}\text{Sn}$ will give satellite peaks in the spectrum. The ${}^{117}\text{Sn}$ satellite peaks cannot be separated from the ${}^{119}\text{Sn}$ peaks, as the separation is usually smaller than the peak linewidth.

In compounds where there are two directly-bonded tin atoms, the magnitude of the homonuclear scalar coupling ${}^1J({}^{119}\text{Sn}{}^{119}\text{Sn})$ can be measured. Where the tin atoms are in the same environment, it is possible to measure the heteronuclear scalar coupling, ${}^1J({}^{119}\text{Sn}{}^{117}\text{Sn})$. To find the homonuclear ${}^1J({}^{119}\text{Sn}{}^{119}\text{Sn})$, the previous

measurement needs to be scaled by 1.0465. This can be used for structure assignment and to consider bonding properties. One-bond coupling constants can be large when compared to scalar coupling constants to other nuclei. The $^1J(^{119}\text{Sn}^{119}\text{Sn})$ can range from -5 kHz to +15 kHz in size, e.g. $^1J(^{119}\text{Sn}^{119}\text{Sn}) = +4460$ Hz for $\text{Me}_3\text{SnSnMe}_3$.⁸

In the organotin fluorides, the tin atoms are separated by two bonds when fluorine-bridged. In the solid state, the $^2J(^{119}\text{Sn}^{119}\text{Sn})$ coupling constant is often too small compared to the linewidth to be easily measured, though using lower external magnetic field strengths would help. In solution-state, the linewidths are much narrower and two-bond coupling constants are regularly measured. $|^2J(^{119}\text{Sn}^{117}\text{Sn})|$ can be up to 35 kHz, in a compound where the intervening atom is platinum, though values of less than 1000 Hz are more common. The size depends on the nature of the intervening atom, the bond angle, and other directly-bonded atoms. Two-bond coupling constants have been reported for a wide range of organotin chalcogenides, e.g. $(\text{R}_3\text{Sn})_2\text{E}$. These results have been fitted by an equation to give a correlation between the Sn-E-Sn bond angle and the magnitude of $^2J(^{119}\text{Sn}^{119}\text{Sn})$.⁹ For the organotin fluorides, no appreciable two-bond coupling has been reported or observed.

One-bond coupling to carbon is smaller than the coupling constants given above and is comparable to the ^{119}Sn peak linewidths. It has only been clearly observed in the ^{119}Sn spectra of Me_3SnF . The ^{13}C linewidths are much narrower and the $^{117,119}\text{Sn}$ satellite peaks can usually be seen. For the organotin compounds, $^1J(\text{SnC})$ lies in the range +200 to -600 Hz. The sign of the coupling constant is negative except for tin(II) compounds and triorganotin anions. For the latter, there is a lone pair of electrons on the tin, which changes the sign of the coupling constant. A comparison has been made of the ^{13}C shifts and $^1J(\text{SnC})$ couplings from spectra of organotin compounds.¹⁰ The size of the $^1J(\text{SnC})$ coupling was found, empirically, to be related to the angle of the C-Sn-C bond. The angle is related to the bonding and hybridisation at the tin centre. For the comparison, only mono- to tri- methyl tin compounds were considered, which gave $^1J(\text{SnC})$ in the range 470 to 1160 Hz. The equation is given as $|^1J(\text{SnC})|/\text{Hz} = 11.4 \theta - 875$, with θ measured in degrees.

The coupling of tin to fluorine has been seen for the solid organotin fluorides. The multiplet pattern has been used to interpret the type of polymerisation. In most of the compounds, the tin peaks are split into a triplet, showing F-Sn-F bridges along one dimension. $^1J(\text{SnF})$ is moderate in size and ranges from about 1000 to 2500 Hz. The sign of the splitting is known to be positive.¹¹ This splitting is sufficient to separate the different spinning-sideband manifolds and to allow the calculation of the effective shielding anisotropy and thence the effective dipolar coupling constant, D' . If the bond length is known, then the anisotropy in $^1J(\text{SnF})$ ($^1\Delta J$) can be calculated. Few values of $^1\Delta J$ have been measured. The accuracy of $^1\Delta J$ is poor owing to the large errors that arise when calculating D' . In the organotin fluoride compounds, the magnitude of $^1\Delta J$ has been found to be 4500 Hz or less. For the current and reported results on the triorganyltin fluorides, the sign has been negative. The results for $^1\Delta J$ are collected and discussed at the end of Chapter 5.

It is possible to use ab initio calculations to calculate NMR properties from the molecular structure. For ^{13}C these calculations have reached the stage where they can be used to help interpret the chemical shift patterns in spectra of large molecules. At present, the accuracy of calculations for tin compounds is poor. The most recent ab initio calculations for the ^{119}Sn shift have errors of over 200 ppm between the calculation and experiment. Empirical methods based on trends have been suggested and work reasonably well, but only in a qualitative manner. Ab initio calculations of the coupling constant, $^1J(\text{SnF})$ and its anisotropy are in broad agreement with the experimental results. By increasing the amount of ^{119}Sn data that is available, it is hoped that the theoretician will be able to understand the tin systems better, leading to improved calculations.

4.1.1 Summary of reported ^{119}Sn NMR results

The ^{119}Sn CPMAS spectrum of $^n\text{Bu}_3\text{SnF}$ was reported in 1985.¹² The ^{119}Sn spectrum shows three equally spaced isotropic peaks, with the splitting arising from scalar coupling to two bridging fluorines. There are extensive spinning-sideband

patterns visible from the large SA. The paper included a ssb analysis with an interpretation of the shielding tensor. The ^{119}Sn shielding anisotropy and coupling pattern are indicative of penta-coordinate tin. A combined solid-state and solution-state study¹³ of $^n\text{Bu}_3\text{SnF}$ showed that this compound also exists as a polymer in solution. Solution-state relaxation data were used to calculate the SA and to probe molecular dynamics.

The results on a wider range of triorganyltin fluorides have been reported.²² This includes data for the polymeric structures Me_3SnF , $^i\text{Bu}_3\text{SnF}$, Ph_3SnF and the monomer Mes_3SnF . The polymeric compounds have similar ^{119}Sn spectra to the one discussed above for $^n\text{Bu}_3\text{SnF}$. The spectrum of Mes_3SnF has four peaks and only a few spinning sidebands. These four peaks arise from two slightly different molecules in the asymmetric unit giving two isotropic peaks that are then split into doublets by scalar coupling to one fluorine atom. Spectra obtained at two different magnetic fields confirm the existence of two isotropic chemical shifts and the size of the scalar coupling. Detailed analyses¹¹ of the ssb patterns for the four compounds listed above have given calculated values for the effective dipolar coupling constant, D' . For Me_3SnF , where the XRD structure is available, ΔJ was also calculated. Further analysis and other results for $^n\text{Bu}_3\text{SnF}$ and Mes_3SnF are discussed in the next two chapters. A paper¹⁴ has already been published based on some of this work.

Other similar organotin compounds that have also been measured include the chlorides,¹⁵ bromides and hydroxide,¹⁶ though they have not been studied further herein.

4.2 Polymerisation of organotin compounds

It has been found that organotin compounds with the general formula R_3SnX , where R is an organyl group and X is an oxygen- or fluorine-bearing ligand, tend to polymerise in the solid state. This polymerisation increases the coordination around the tin centre. For the organotin fluorides, polymerisation depends on the steric requirements of the organyl ligand. With the bulky mesityl group, the compound is

monomeric, though the monomers still align with near-linear F-Sn-F chains. For other known organyl groups, the compound is always polymeric. With the bulkier halides, Cl, Br and I, as the bridging atoms, the presence and type of polymerisation depends on the other groups attached to the tin centre.

The polymerisation can be inferred from the ^{119}Sn shift and shielding anisotropy. These parameters can be used to estimate the coordination number around the tin centre. For polymeric organotin fluorides, the shielding anisotropy tends to be large, with near axial asymmetry. Polymerisation can be clearly seen in the ^{119}Sn spectra from the scalar coupling to ^{19}F . In Me_3SnF , where there is no polymerisation, only a doublet is observed. For $^n\text{Bu}_3\text{SnF}$, a triplet is observed arising from the two equivalent bridging fluorine atoms in the polymer structure. With the diorganotin difluorides, a multiplet pattern is observed. This multiplet pattern is hard to observe clearly as each ssb peak has the multiplet pattern with the intensities dependent on both the effective SA and the splitting pattern. Fast sample spinning is needed (> 7 kHz) so that the ssb peaks are separated. The shielding anisotropy is too large to be fully averaged.

In the ^{19}F spectra, the $^1\text{J}(\text{SnF})$ coupling is observed as satellite peaks. The splitting is clearer than that in the ^{119}Sn spectra as there are fewer ssb peaks and only the doublet splitting is visible. For the diorganotin difluorides, the ^{19}F spectra allow the direct measurement of the scalar coupling constants without the complications of the multiplet pattern. It is not possible to directly use the ^{19}F spectra to confirm polymerisation as the splitting will only be observed from the coupling of each ^{19}F atom to one ^{119}Sn atom. In principle, the intensity of the satellite peaks can give an indication of the type of polymerisation. Also, the size of the coupling can give an indication of the strength of the Sn-F bond and hence an indication of whether there is polymerisation or not. Unsymmetrical bridging of the fluorine atom would result in two sets of satellite peaks that may be resolved in the spectrum. Fluorine-19 shift and shielding data have not been previously measured for these compounds and the new results are summarised at the end of Chapter 6.

Carbon-13 spectra for triorganyltin compounds can show whether all three organyl groups are equivalent. For Me_3SnOH , the methyl peaks are visible in a 2:1

ratio.¹⁷ This indicates that the polymeric chain is a zigzag rather than linear. For the organotin fluorides, the peaks are much broader and it is not possible to see separate peaks. Thus, the type of polymeric chain cannot be determined easily by NMR.

4.2.1 XRD results

The clearest way to determine the type and extent of polymerisation is by solving the structure from single-crystal XRD measurements. The XRD structure can show whether the bridging Sn-F bonds are equal or uneven and whether the polymeric chain is linear or kinked. Several XRD structures have been solved, though the quality of the refinement is often low and there is uncertainty about the placement of the fluorine and carbon atoms in some early structures. The Sn-F bond lengths range from 1.957 (4) Å in the monomer Me_3SnF to 2.1458 (3) Å in the polymerised Ph_3SnF with longer bonds in compounds where there is an uneven fluorine bridge, e.g. chx_3SnF (chx = cyclohexyl).

The simplest structure is that of Me_3SnF ,¹⁸ in which the tin atom is four coordinate and monomeric. The bulky mesityl groups inhibit polymerisation, though the monomers do still align along the SnFSn axis. The SnFSn angles are 174.6 (3)° and 179.5 (3)°. A figure of this structure is in the following chapter.

Ph_3SnF ¹⁹ is perfectly polymerised and has equal bridging Sn-F bond lengths (2.15 Å). The polymer backbone is linear. By comparison, chx_3SnF ²⁰ retains the linear backbone, but the cyclohexyl groups cause the bridging Sn-F bond lengths to be uneven (2.051 (10) and 2.303 (10) Å). The structure of Bz_3SnF ²¹ (Bz = benzyl) is linear, with bond lengths of 2.12 and 2.21 Å. These were claimed to be equal to within experimental error! The errors for these bond lengths are not readily available, though from a consideration of the errors in other compounds, the difference is significant. The ¹¹⁹Sn spectra of Ph_3SnF and ¹¹⁹Bu₃SnF show a triplet splitting from scalar coupling to two equivalent fluorines.²² For this reason, this evenly bridged structure has been assumed for ¹¹⁹Bu₃SnF. There have been no known NMR measurements of chx_3SnF or Bz_3SnF .

The XRD diffraction structure of Me_3SnF was measured in 1964²³ with the data reinterpreted by a second group.²⁴ This latter structure has a trigonal pyramidal tin atom with two uneven Sn-F bridging bond lengths (2.15 and 2.45 Å). The SnFSn bond is kinked with an angle of 141° , whilst the FSnF bond is linear. It was not possible to fully determine the position of the fluorine, as there were two equally probable positions. No errors were quoted in the references, though they would be expected to be large. A schematic diagram of the structure of Me_3SnF is shown in Figure 4. The same type of structure is observed for Me_3SnOH ,¹⁷ the staggered conformation of the methyl groups confirms the ^{13}C NMR observations on Me_3SnOH as mentioned above. The structure of Ph_3SnOH ²⁵ has a kink angle of $137.8 (3)^\circ$, similar to that for Me_3SnF found above. The bridging SnO bonds are uneven (2.197 (5) and 2.255 (5) Å), though they are not as different as the bond lengths in chx_3SnF .

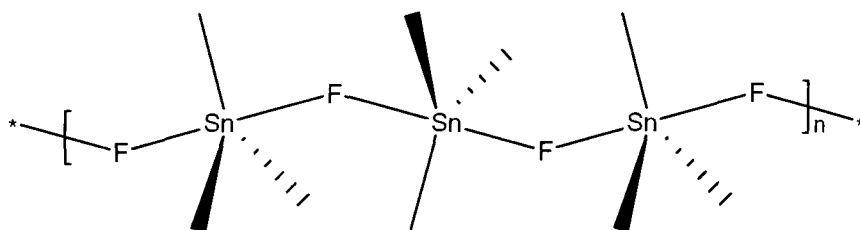


Figure 4: Schematic diagram of the zigzag structure of Me_3SnF

With the diorganyltin difluorides, there is the possibility of multiple bridging. The structure of Me_2SnF_2 ²⁶ has an extensive planar lattice of hexa-coordinate tin atoms connected to four bridging fluorine atoms in the plane with two methyl groups above and below the plane. The structure is shown in Chapter 6. It is worth noting that Me_2SnCl_2 ,²⁷ shown in the same figure as Me_2SnF_2 , has a completely different structure.

The compounds are often insoluble which makes growing single crystals complicated. For Ph_3SnF , powder XRD data have also been measured. This gave the unit cell and space group, but no powder XRD data have yet been able to solve the full structure. Solving the full structure is complicated as the tin diffracts much more

strongly than either carbon or fluorine so only the peaks for the tin atoms are clearly visible.

A focus of the work herein has been to interpret the structure of ${}^n\text{Bu}_2\text{SnF}_2$ from the NMR data, as there is no XRD structure available.

-
- ¹ D. C. Apperley, N. A. Davies, R. K. Harris, S. Eller, P. Schwarz, and R. D. Fischer, *J. Chem. Soc., Chem. Commun.*, **10**, 740 (1992)
- ² R. K. Harris and A. Sebald, *Magn. Reson. Chem.*, **27**, 81 (1989)
- ³ T. B. Grindley, R. E. Wasylishen, R. Thangarasa, W. P. Power, and R. D. Curtis, *Can. J. Chem.*, **70**, 205 (1992)
- ⁴ A. Sebald, *NMR Basic Principles and Progress*, **31**, 91 (1994)
- ⁵ E. T. Lippmaa, M. A. Alla, T. J. Pekh, and G. Engelhardt, *J. Am. Chem. Soc.*, **100**, 1929 (1978)
- ⁶ R. K. Harris, S. E. Lawrence, S. Oh, and V. G. Kumar Das, *J. Mol. Struct.*, **347**, 309 (1995)
- ⁷ B. Wrackmeyer, *Annu. Rep. NMR Spectrosc.*, **16**, 73 (1985)
- ⁸ R. K. Harris and B. E. Mann, "NMR and the Periodic Table," Academic Press, London (1978)
- ⁹ T. P. Lockhart, H. Puff, W. Schuh, H. Reuter, and T. N. Mitchell, *J. Organomet. Chem.*, **366**, 61 (1989)
- ¹⁰ T. P. Lockhart and W. F. Manders, *J. Am. Chem. Soc.*, **107**, 5863 (1985)
- ¹¹ H. P. Bai and R. K. Harris, *J. Magn. Reson.*, **96**, 24 (1992)
- ¹² R. K. Harris, K. J. Packer, and P. Reams, *Chem. Phys. Lett.*, **115**, 16 (1985)
- ¹³ Y. W. Kim, A. Labouriau, C. M. Taylor, W. L. Earl, and L. G. Werbelow, *J. Phys. Chem.*, **98**, 4919 (1994)
- ¹⁴ J. C. Cherryman and R. K. Harris, *J. Magn. Reson.*, **128**, 21 (1997)
- ¹⁵ R. K. Harris, A. Sebald, D. Furlani, and G. Tagliavini, *Organometallics*, **7**, 388 (1988)
- ¹⁶ R. K. Harris, K. J. Packer, and P. Reams, *J. Magn. Reson.*, **61**, 564 (1985); R. K. Harris, K. J. Packer, P. Reams, and A. Sebald, *J. Magn. Reson.*, **72**, 385 (1987)
- ¹⁷ A. G. Davies, personal communication
- ¹⁸ H. Reuter and H. Puff, *J. Organomet. Chem.*, **379**, 223 (1989)
- ¹⁹ D. Tudela, E. Gutiérrez-Puebla, and A. Monge, *J. Chem. Soc., Dalton. Trans.*, 1069 (1992)
- ²⁰ D. Tudela, R. Fernández, V. K. Belsky, and V. E. Zavodnik, *J. Chem. Soc., Dalton. Trans.*, 2123 (1996)
- ²¹ H. Reuter, Ph. D. Thesis, University of Bonn (1987)
- ²² H. P. Bai, Ph. D. Thesis, University of Durham (1991); H. P. Bai, R. K. Harris, and H. Reuter, *J. Organomet. Chem.*, **408**, 167 (1991)
- ²³ H. C. Clark, R. J. O'Brien, and J. Trotter, *J. Chem. Soc.*, 2332 (1964)
- ²⁴ K. Yasuda, Y. Kawasaki, N. Kasai, and T. Tanaka, *Bull. Chem. Soc. Jpn.*, **38**, 1216 (1965)
- ²⁵ C. Glidewell and D. C. Liles, *Acta Cryst. B*, **34**, 129 (1978)
- ²⁶ E. O. Schlemper and W. C. Hamilton, *Inorg. Chem.*, **5**, 995 (1966)
- ²⁷ A. G. Davies, H. J. Milledge, D. C. Puxley, and P. J. Smith, *J. Chem. Soc. (A)*, 2862 (1970)

5 Triorganotin Fluoride Compounds

This chapter examines two triorganotin fluorides ${}^n\text{Bu}_3\text{SnF}$ and Mes_3SnF (Mes = mesityl). Both have been studied before by ${}^{119}\text{Sn}$ NMR. Here, we have used new triple- and double-channel probes to measure novel and different NMR spectra. The doubly-decoupled ${}^{119}\text{Sn}$ spectra show the usefulness of the new HFX probe to simplify the spectra by removing the scalar coupling to fluorine. The ${}^{19}\text{F}$ spectra have not been measured before and are presented here. The information from these spectra is complementary to that from the ${}^{119}\text{Sn}$ spectra. With both the ${}^{19}\text{F}$ and ${}^{119}\text{Sn}$ spectra, it is possible to perform a more detailed analysis of the compounds. The spinning-sideband simulation and fitting programs have been extended to allow for a triple fit of the spinning-sideband manifolds. This triple fitting allows a more accurate interpretation of the shielding and dipolar tensors including their mutual orientation.

Although both compounds have the same general type of formula, their structures are very different. In the solid state, ${}^n\text{Bu}_3\text{SnF}$ is found as a linear polymer. The evidence for this comes from NMR studies as there is no XRD structure available. The structure of Mes_3SnF has been solved by XRD. It does not form a polymeric structure due to the bulk of the mesityl ligands. This compound has been studied with double decoupling for the first time. Use of this and the non-colinear, triple-fitting technique, gives a more accurate value for the shielding anisotropy and the effective dipolar coupling constant than has been given previously. It also shows that one of the ${}^{119}\text{Sn}$ shielding tensors is non-colinear with the dipolar tensor. This compound is close to a model isolated two-spin ${}^{119}\text{Sn}$ - ${}^{19}\text{F}$ system. The protons are distant and mobile, so that cross polarisation is still effective but proton decoupling does not narrow the linewidths significantly. This has allowed the study of the effects of double and off-resonance decoupling.

The chapter concludes with a summary of values for D' and ΔJ for these and other compounds. These have not been collected together before. With the enhanced spinning-sideband analysis and some new XRD structures, they are more accurate than previously reported values.

5.1 Tri-n-butyltin fluoride

Tri-n-butyltin fluoride, ${}^n\text{Bu}_3\text{SnF}$, is thought to be a linear polymer with Sn-F bridges based on NMR data (discussed later). The features of the ${}^{119}\text{Sn}$ NMR spectra of ${}^n\text{Bu}_3\text{SnF}$ are similar to Ph_3SnF , for which the XRD structure is known. The structure of Ph_3SnF is shown schematically in Figure 5 below.¹ The Sn-F bond lengths in Ph_3SnF are all 2.15 Å, the bridging fluorines being centrally placed. As a first approximation, the bond length in ${}^n\text{Bu}_3\text{SnF}$ would be expected to be similar to this. The structure is a linear polymer with the angles Sn-F-Sn and F-Sn-F both equal to 180°. Equatorial substituents on successive tin atoms are staggered.

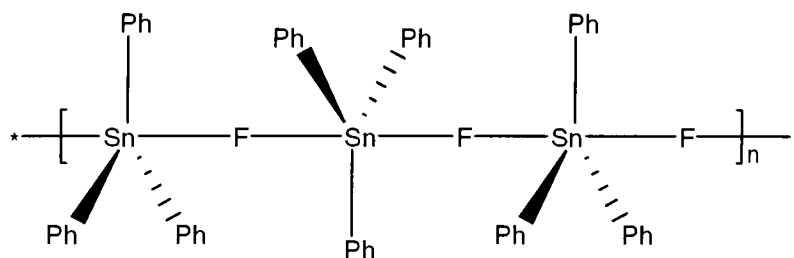


Figure 5: The schematic structure of Ph_3SnF believed to be analogous to ${}^n\text{Bu}_3\text{SnF}$.

5.1.1 NMR data

5.1.1.1 Carbon-13

The solid-state ${}^{13}\text{C}$ NMR spectra have been recorded at resonance frequencies of 50.329 and 75.430 MHz. The spectra measured at 50.329 MHz are shown in Figure 6. Figure 6(a) was recorded at room temperature, whilst Figure 6(b) was recorded at -17°C . The room temperature spectra, measured at two different field strengths, are identical, with both spectra giving a sharp peak at 14.2 ppm, a broad peak around 27.6 ppm and a small impurity peak at 38.0 ppm. Taking into account the usual precautions to obtain accurate intensity values, the integral ratio of the sharp peak to the broad peak is 1:2. These signals are explained as arising from the

methyl group and two CH₂ groups respectively. The CH₂ group that is directly bonded to tin is not observed in the room temperature spectra. None of the peaks in the room temperature spectrum are suppressed with a NQS sequence for a range of dephasing times up to 80 μ s. This implies that there is rapid motion of the CH₂ groups. This rapid motion can also be seen by comparison of relaxation data between ¹¹⁹Bu₃SnF and Mes₃SnF, as discussed later.

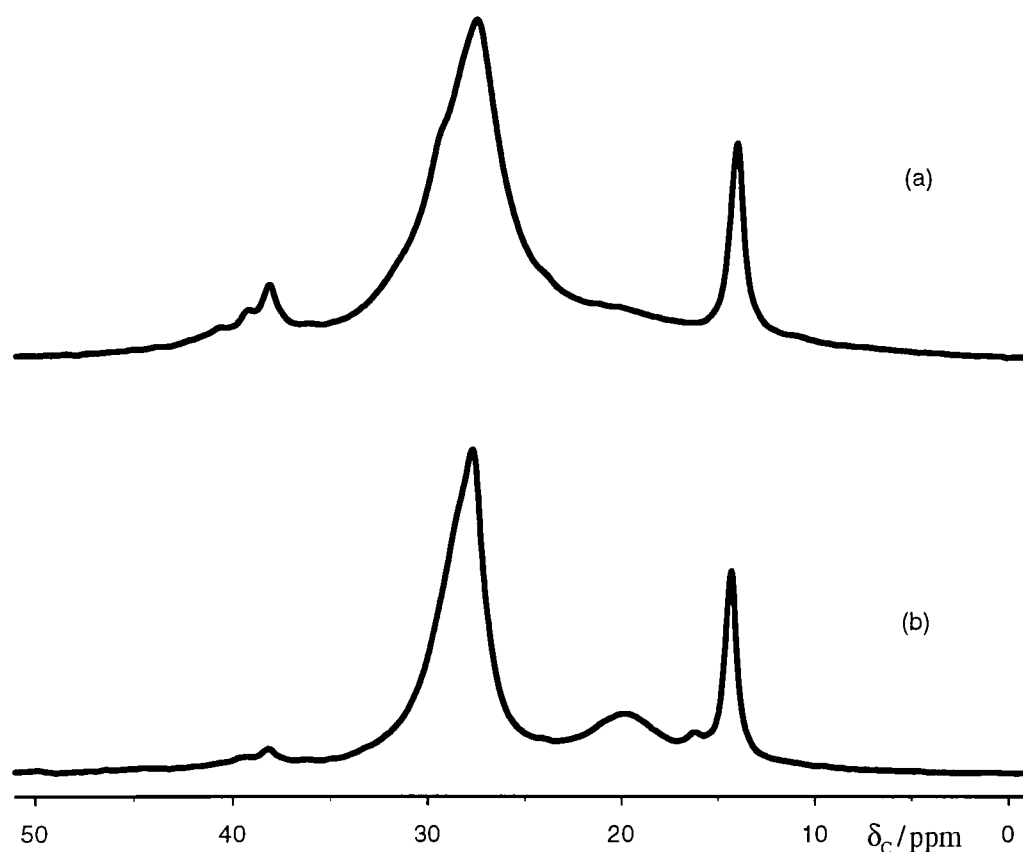


Figure 6: Carbon-13 spectra of ¹¹⁹Bu₃SnF at (a) room temperature and (b) -17°C. Acquisition parameters were: (a) pulse duration 4 μ s, contact time 1 ms, recycle delay 5 s, and number of acquisitions 5000; (b) pulse duration 5 μ s, contact time 1 ms, recycle delay 5 s, and number of acquisitions 200. In both cases, the spinning speed was 3 kHz.

On reducing the nominal probe temperature below -25°C, a new broad peak can be seen at 19 ppm when compared with the room temperature spectrum. The spectrum measured with the set temperature at -30°C (actual temperature is -17°C) is shown in Figure 6(b). This broad peak is presumed to arise from the CH₂ group

bonded to tin. At room temperature, the peak is too broad to be visible. On cooling, the motional regime changes and the peak narrows. It is possible that the peak narrows due to an interplay with either the MAS rate or the decoupling power. This was considered unlikely here. The other peaks become slightly broader, with no change in their shift, implying that there is no major change in the structure. Differential Scanning Calorimetry (DSC) measurements show a phase transition at -7.5°C . Variable temperature measurements of proton $T_{1\rho}$ show a minimum in its value at room temperature and no obvious step change at the phase transition temperature.

Solution-state ^{13}C NMR spectra, with $^n\text{Bu}_3\text{SnF}$ in deuterated chloroform, show two sharp peaks at 27.5 and 27.7 ppm where the main broad peak was before in the low temperature solid-state NMR spectrum. There is also a sharp peak at 13.6 ppm presumably from the methyl group. A broader peak is visible at 18.5 ppm and is thought to arise from the CH_2 group directly bonded to the tin atom. This peak would be broad as the CH_2 group is effectively tethered to the tin and has restricted motion. No different ^{13}C peaks were observed for this CH_2 group, as might be expected if the Sn-F chain was kinked. However, the peak is broad and small differences in the shift could not be ruled out. It was not possible to measure the ^{119}Sn spectrum of the compound in solution, due to the poor solubility of $^n\text{Bu}_3\text{SnF}$. However, previous solution-state ^{119}Sn measurements made in a mixture of pentane / diethyl ether show that the compound remains polymerised whilst in solution.²

5.1.1.2 Fluorine-19

The solid-state ^{19}F spectrum recorded with CPMAS and proton decoupling is shown in Figure 7. The central and satellite peaks are clearly visible. With the sample spinning above 10 kHz, only the centreband is observed. From this $\delta = -157.0$ ppm with $^1J(\text{SnF}) = 1310$ Hz (known to be positive). The intensity ratio of the satellite peaks to the centreband agrees quantitatively with calculations when considering the combined natural abundance of ^{117}Sn and ^{119}Sn .

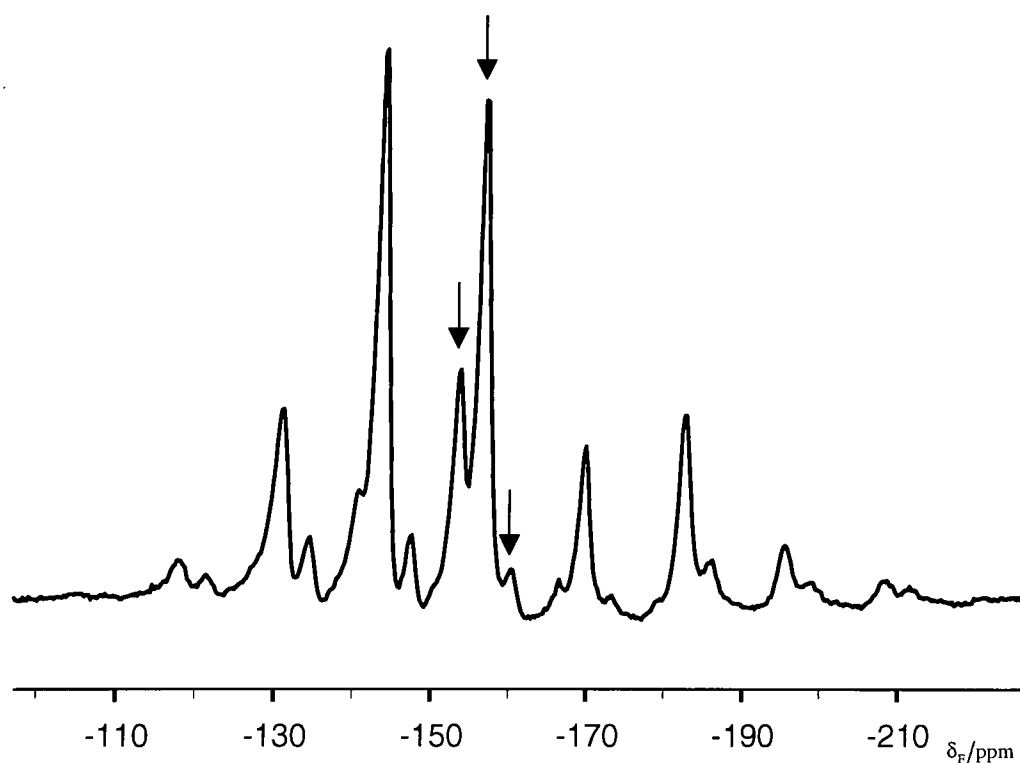


Figure 7: Fluorine-19 CPMAS NMR spectrum, obtained with spinning at 2400 Hz and proton decoupling. The centrebands are indicated by vertical arrows. The Bloch-Siegert correction of +2.3 ppm has been applied to the frequency scale. Acquisition parameters were: pulse duration 3 μ s, contact time 2 ms, recycle delay 3 s, and number of acquisitions 512.

For spinning-sideband (ssb) analysis, spectra were recorded at relatively slow spinning speeds. The triple-fit analysis used the spectra shown in Figure 7, where the sample is spinning at 2400 Hz. This was the slowest spinning speed that could be obtained with the sample spinning stably. The spin speed could not be locked but did not change over the time of the experiment. Slower spinning speeds would give overlapping peaks.

The triple-fit simulation shows that the shielding and effective dipolar tensors are coaxial. The triple-fit results are summarised in Table 5. From these data, $D' = -4340$ Hz. This value and that derived from the ^{119}Sn NMR data will be discussed later. For the centreband, $\eta = 0.3$ when fitted individually (Table 6), but the triple fit gave $\eta = 0.0$. As the triple-fit value is believed to be the more accurate it has been used here. The difference in the two single-fit simulations for the centreband (taking

$\eta = 0.3$ and 0.0) gave the same value for the anisotropy within error and R^2 values of 44 and 50 respectively.

Table 5: Summary of the ^{19}F spinning-sideband triple-fit analysis for Figure 7.

δ_{iso} (ppm)	ζ^{eff} (ppm)	η^{eff}	$\sigma_{11}^{\text{eff}} - \sigma_{\text{ref}}$ (ppm)	$\sigma_{22}^{\text{eff}} - \sigma_{\text{ref}}$ (ppm)	$\sigma_{33}^{\text{eff}} - \sigma_{\text{ref}}$ (ppm)
-153.7 ^a	18	0.0	145	145	172
-157.0	41	0.0	136	136	198
-160.7 ^a	64	0.0	129	129	225

^a Values are for the Sn satellite spinning-sideband manifolds

Table 6: Summary of the ^{19}F spinning-sideband single-fit analysis for Figure 7.

δ_{iso} (ppm)	ζ^{eff} (ppm)	η^{eff}	$\sigma_{11}^{\text{eff}} - \sigma_{\text{ref}}$ (ppm)	$\sigma_{22}^{\text{eff}} - \sigma_{\text{ref}}$ (ppm)	$\sigma_{33}^{\text{eff}} - \sigma_{\text{ref}}$ (ppm)
-153.7 ^a	18.4 (0.7)	0.00 (0.23)	144.5	144.5	172.1
-157.0	40.7 (1.3)	0.30 (0.04)	130.5	142.9	197.7
-160.7 ^a	64.8 (1.0)	0.00 (0.09)	128.3	128.3	225.5

^a Values are for the Sn satellite spinning-sideband manifolds

The fitting error from the single-fit analysis is given in brackets for the anisotropy and asymmetry. This fitting error has been derived from the paper by Olivieri³ and was discussed earlier. The triple-fit program does not calculate errors for the parameters. However, the errors would not be expected to be very different to the fitting error in the single-fit data. The error in the asymmetry is large as the tensor is nearly axial. The fitting errors for the individual components are not given so as to simplify the tables. They have been calculated in the fitting program by the propagation of errors.

The static spectrum, recorded with an echo, is extensively broadened. It is still possible to observe that the lineshape is near axial, but it is not possible to measure any accurate values for this spectrum. An alternative method to measure the

static lineshape is to use a 2D experiment such as the one suggested by Tycko.⁴ In this experiment, the sample is spinning rapidly to give a MAS spectrum in one dimension and the pseudo-static spectrum in the other. Such a spectrum, recorded with the sample spinning at 8 kHz, is shown in Figure 8. Although the satellite peaks have much less intensity than the centreband, it is possible to extract the static lineshape for all three peaks. The turning points in these lineshapes agree well with the calculations from the ssb spectra given above. The static lineshapes shown are a single slice in the indirect dimension, taken from the top of each peak in the direct (MAS) dimension. Overall, the ssb measurements are more accurate.

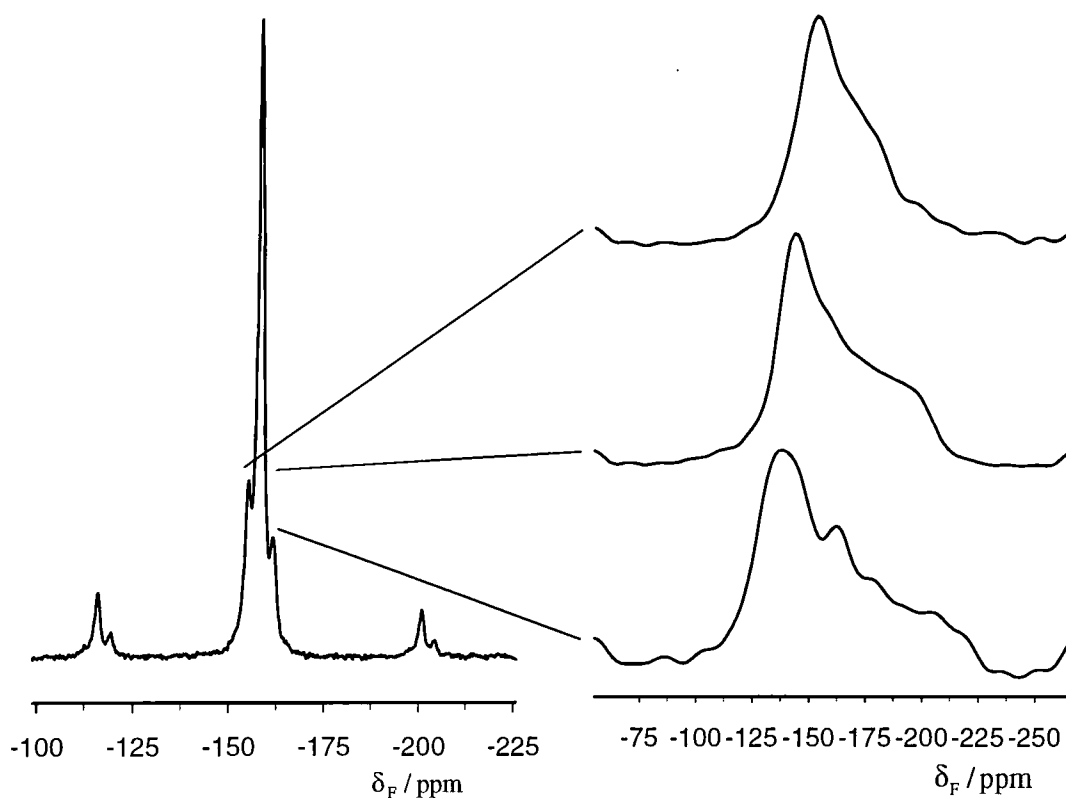


Figure 8: NMR spectra from a Tycko 2D experiment. The spectrum on the left is the first slice of the 2D dataset. The spectra on the right are single slices extracted from the indirect dimension of the 2D spectrum (not to scale). The lines indicate the positions of the peaks where the slices were extracted from. Acquisition parameters were: pulse duration 2.5 μ s, contact time 2 ms, recycle delay 10 s, number of acquisitions per slice 32, number of slices 16 and spinning speed 8 kHz.

5.1.1.3 Tin-119

The proton-decoupled ^{119}Sn spectrum has been measured before.⁵ The spectra shown in Figure 9 were recorded with single (proton) and double (proton and fluorine) decoupling. Using the HFX probe and double decoupling allowed the spectrum to be measured with a slower spinning speed (2.5 kHz) than previously. Comparing this to Figure 9(a) confirmed the centreband value as $\delta = -9.0$ ppm. The slower spinning speed also gave a spectrum with more spinning sidebands for fitting.

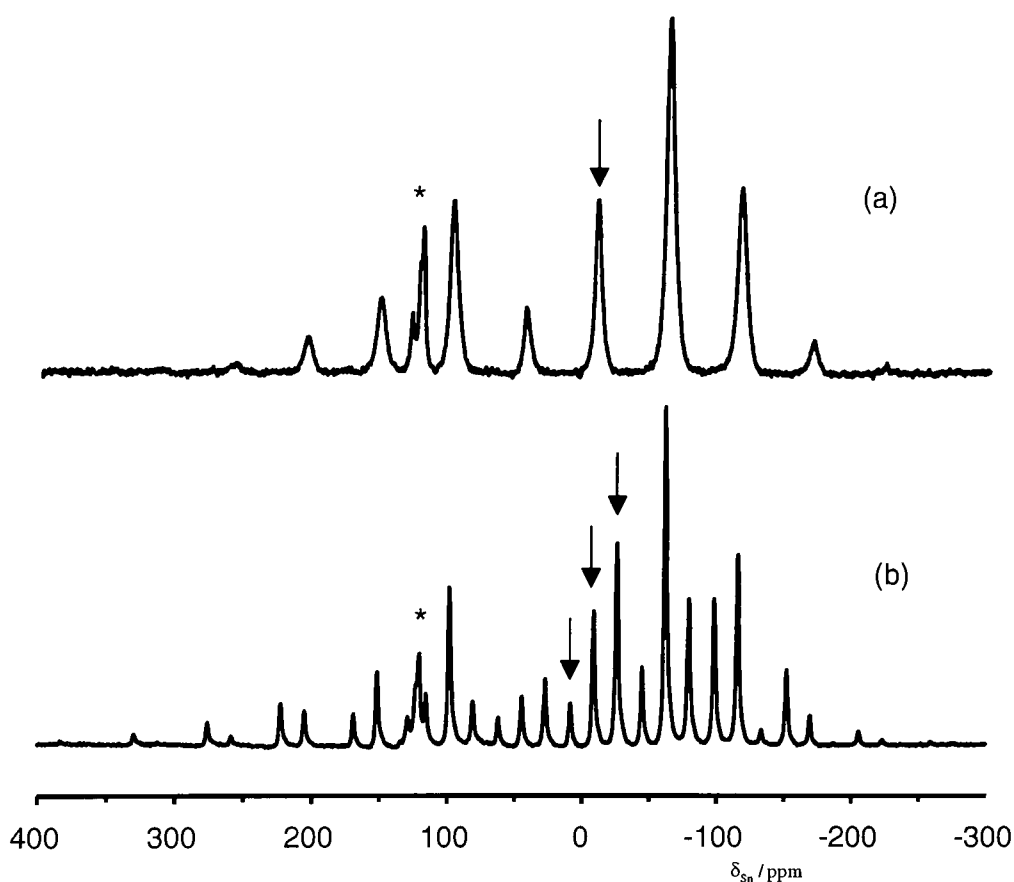


Figure 9: Tin-119 CPMAS NMR spectra, obtained with spinning at 4 kHz together with (a) double decoupling, and (b) only ^1H decoupling. The centrebands are indicated by vertical arrows. The peak marked by an asterisk at $\delta = 121$ ppm is an impurity. Acquisition parameters were: (a) pulse duration $5\ \mu\text{s}$, contact time 1 ms, recycle delay 2 s, and number of acquisitions 21000; (b) pulse duration $5\ \mu\text{s}$, contact time 1 ms, recycle delay 2 s, and number of acquisitions 27000.

However, the proton (only)-decoupled spectrum measured at this slow speed would be too complicated to allow for fitting. The triplet splitting arises from scalar coupling to two equivalent fluorine nuclei with $^1J(\text{SnF}) = 1310$ Hz, which is the same, within experimental error, as that found from the fluorine spectrum. The peak at $\delta = 121$ ppm arises from an impurity which overlaps with two of the ssb peaks. Thus, deconvolution of the lineshape in this region has been used to get integral values of the peaks.

For the spinning-sideband simulation, all three sets of ssb from Figure 9(b) were fitted together and the total sum of the differences squared was minimised. The triple-fit results are shown in Table 7. Individual ssb manifold fittings, shown in Table 8, gave results in agreement, within the fitting error, to the triple fit. The triple fit shows that the effective dipolar and chemical shift tensors are coaxial, and gives a value for $D' = -3770$ Hz. This value of D' differs from that found from the ^{19}F spectrum ($D' = -4340$ Hz). For further calculations, an average value of $D' = -4000$ Hz has been used. Although the anisotropy here is much larger than that for the ^{19}F measurements, the fitting error is not proportionately so. This discrepancy may be due to the fact that in the ^{119}Sn spectrum there is no overlap of the peaks and there are more ssb's available for fitting. As for the ^{19}F case, the ^{119}Sn shielding is found to be axial.

Table 7: Summary of the ^{119}Sn spinning-sideband triple-fit analysis for Figure 9(b).

δ_{iso} (ppm)	ζ^{eff} (ppm)	η^{eff}	$\sigma_{11}^{\text{eff}} - \sigma_{\text{ref}}$ (ppm)	$\sigma_{22}^{\text{eff}} - \sigma_{\text{ref}}$ (ppm)	$\sigma_{33}^{\text{eff}} - \sigma_{\text{ref}}$ (ppm)
8.6 ^a	-332	0.0	157	157	-341
-9.0	-231	0.0	125	125	-222
-26.7 ^a	-130	0.0	92	92	-103

^a Values are for the scalar coupled lines of the Sn-F coupled triplet

Table 8: Summary of the ^{119}Sn spinning-sideband single-fit analysis for Figure 9(b).

δ_{iso} (ppm)	ζ^{eff} (ppm)	η^{eff}	$\sigma_{11}^{\text{eff}} - \sigma_{\text{ref}}$ (ppm)	$\sigma_{22}^{\text{eff}} - \sigma_{\text{ref}}$ (ppm)	$\sigma_{33}^{\text{eff}} - \sigma_{\text{ref}}$ (ppm)
8.6 ^a	-334.8 (4.8)	0.00 (0.07)	158.8	158.8	-343.4
-9.0	-229.5 (1.4)	0.00 (0.08)	123.7	123.7	-220.5
-26.7 ^a	-130.2 (0.4)	0.05 (0.05)	95.3	88.3	-103.5

^a Values are for the scalar coupled lines of the Sn-F coupled triplet

As the anisotropy is large, losses in the signal intensity of the outer ssb peaks, due to either the probe tuning profile or CP were checked. A direct polarisation experiment using a small pulse duration appropriate for the Ernst tip angle was carried out. The ^{119}Sn longitudinal relaxation time has been measured to be 13 s. Thus, with a pulse duration of 2 μs (equivalent to a tip angle of 36° for the calibrated 5 μs 90° pulse), the optimum recycle delay is 2.7 s. This showed little difference for values of the anisotropy and D' between the spectrum shown in Figure 9(b) and that measured as described above, indicating no significant loss of intensity due to CP.

The tin shielding anisotropy for $^n\text{Bu}_3\text{SnF}$ is consistent with the previous result of $\zeta = -207$ ppm.⁵ The asymmetry was quoted as $\eta = 0.42$, whereas the current results make the shielding tensor axial. We believe that the data here are more accurate, and that the system is indeed axial. Results for other penta-coordinate, trigonal bipyramidal, fluorine-bridged compounds have values for the anisotropy lying between -200 and -255 ppm. Anisotropy values for trigonal bipyramidal compounds of tin with C_3O_2 and C_3N_2 nearest neighbours are similar in magnitude and are also negative.⁶

The static spectrum, recorded overnight, is shown in Figure 10(a). The spectrum is dipolar broadened, and the intensity is spread over a large range, making the turning points hard to discern accurately. However, it shows axial character and $\sigma_{\perp}^{\text{eff}} - \sigma_{\text{ref}}$ values of 150, 120, and 90 ppm may be derived, in good agreement with the spinning-sideband fitted data.

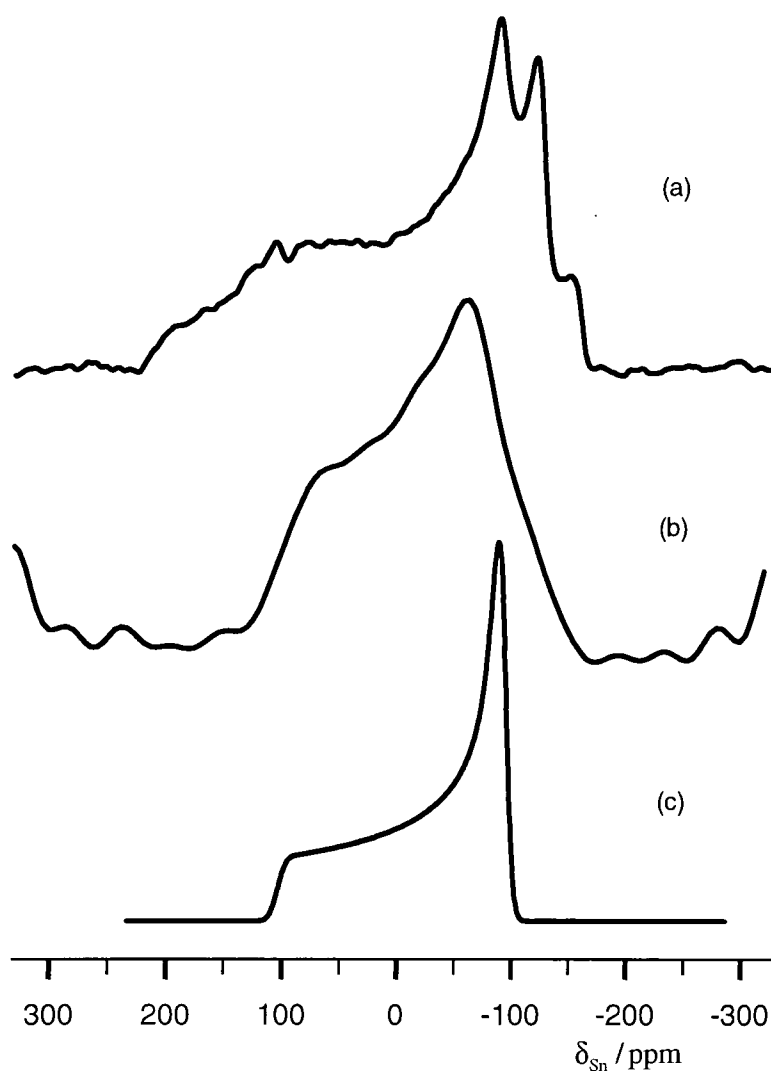


Figure 10: Static ^{119}Sn NMR spectra of ${}^t\text{Bu}_3\text{SnF}$ (a) recorded with a chemical shift echo, (b) sum of the pseudo-static spectra from -20 to -30 ppm extracted from a Tycko 2D experiment, and (c) simulation of the sub-spectrum for $\delta = -26.7$ ppm. Acquisition parameters were: (a) pulse duration $5\ \mu\text{s}$, contact time $1\ \text{ms}$, echo time $\tau\ 20\ \mu\text{s}$, recycle delay $10\ \text{s}$, and number of acquisitions 4096 ; (b) pulse duration $4\ \mu\text{s}$, contact time $2\ \text{ms}$, recycle delay $5\ \text{s}$, number of acquisitions per slice 440 , number of slices 16 , and spinning speed $5\ \text{kHz}$; (c) simulation with $\delta = -26.7$ ppm, $\zeta = -130$ ppm, $\eta = 0.0$ and 1000 Hz of exponential line broadening.

Both the Tycko and more recent MAT experiments were run in an attempt to separate the isotropic and anisotropic data. For the Tycko experiment, the large spectral width required in the anisotropic dimension required fast sample spinning and the six π -pulse version of the pulse sequence. These factors introduced large errors in the anisotropic dimension to give barely discernible static lineshapes. The

extracted pseudo-static spectrum is shown in Figure 10(b) for the peak at $\delta = -26.7$ ppm, which has the smallest value for the anisotropy. The intensity at the edges of the spectrum arises from pulse errors and the breakdown in the assumption of short π -pulses. The simulated spectrum, Figure 10(c), is included for comparison. No fit was attempted using the static lines extracted from the 2D experiments.

The MAT experiment was unable to clearly separate the isotropic peaks. The static lineshape in the first slice was clear, but in the two-dimensional spectrum, the isotropic peaks were indistinct. Both experiments had a glitch at the transmitter position, near to 0 ppm, that might have been improved with fine tuning. Overall, these two pulse sequences have difficulty for systems with large SA, not least because the signal is spread out giving poor overall signal-to-noise ratio.

Variable temperature measurements of the proton-decoupled ^{119}Sn spectrum show a slight temperature dependence on cooling the sample. The isotropic shift of the central peak in the triplet has been plotted against the corrected sample temperature. It can be seen that there is a step change in the shift at the phase transition and that the gradient is different on the two sides of the transition. A triple-fit simulation of the data recorded at -80°C gives the effective anisotropies as -357 , -243 , and -128 ppm, zero asymmetry and $D' = -4283$ Hz. The anisotropy has not changed significantly compared to the results given in Table 7. The apparent change in D' suggests that the Sn-F bond length has shortened. The difference compared to the value above may be significant and is slightly larger than the estimated error in this measurement. All measurements were recorded with a delay of 10 minutes after the temperature had been changed to allow the sample to reach equilibrium. A measurement that was recorded immediately after a step change from room temperature to a set temperature of -50°C (-33.3°C actual) showed the presence of the sample at both temperatures. Presumably, the core of the sample was still at the higher temperature, whilst the outer part had already been cooled. Spectra measured at the set temperature of 20°C at the start and end of the experiment were the same, suggesting that the phase transition is reversible.

Table 9: ^{119}Sn NMR isotropic shift of $^n\text{Bu}_3\text{SnF}$ on changing the sample temperature.

Displayed Temperature / °C	Sample Temperature / °C	Shift / ppm
20	22.8	-9.1
-20	-9.3	-10.0
-40	-25.3	-16.8
-50	-33.3	-18.0
-80	-57.4	-20.6
-100	-73.4	-22.7

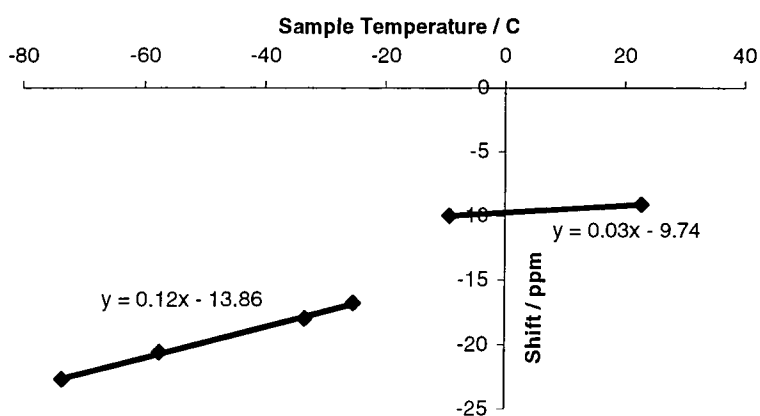


Figure 11: Plot of the data given in Table 9. The lines are the best fit as found by linear regression with the equation given beside each line. Although the high temperature region only has two data points, the error in the shift measurements is small so the change in the offset and gradient of the fitted line is thought to be significant.

5.1.1.4 Cross-polarisation dynamics and relaxation data

Cross-polarisation dynamics and relaxation data have been measured for this compound with the results summarised in Table 10. Experimental methods have been described earlier in Chapter 2. A comparison with data from Mes_3SnF is given later. The longitudinal relaxation times, T_1 , of ^{19}F and ^{119}Sn for $^n\text{Bu}_3\text{SnF}$ are

relatively short compared to data for these nuclei in other compounds. However, the value of $T_1(^1\text{H})$ is shorter still so that using CP would be expected to give a better signal-to-noise ratio in a fixed time than direct polarisation. The short relaxation times suggest that there is rapid internal motion. Spin-locked, $T_{1\rho}$, relaxation has been measured directly for ^1H , ^{19}F and ^{119}Sn .

Table 10: Summary of the relaxation data obtained for $^n\text{Bu}_3\text{SnF}$.

$T_1(^1\text{H}) / \text{s}$	1.5	$T_{1\rho}(^{19}\text{F}) / \text{ms}$	3.4
$T_1(^{19}\text{F}) / \text{s}$	3.4	$T_{1\rho}(^{119}\text{Sn}) / \text{ms}$	12
$T_1(^{119}\text{Sn}) / \text{s}$	13	$T_{\text{HF}} / \text{ms}$	0.4
$T_{1\rho}(^1\text{H}) / \text{ms}$	1.9	$T_{\text{HSn}} / \text{ms}$	0.6

Variable contact-time experiments, with proton decoupling, were used to measure the cross-relaxation time, T_{IS} , and spin-locked relaxation time, $T_{1\rho}$, for CP from proton to either ^{19}F or ^{119}Sn . The standard cross-polarisation equation is given below as Equation 1 where M_t^{S} and M_0^{I} are the size of the magnetisation for the S-spins at time $t > 0$ and for the I-spins at time zero respectively. In this context, the I-spins are protons and the S-spins are either ^{19}F or ^{119}Sn . For both ^{19}F and ^{119}Sn , the signal was enhanced relative to the signal from direct polarisation. For ^{19}F , the standard cross-polarisation equation was found to fit the variable contact-time data well. Although it was not measured, the CP dynamics from ^{19}F to another nucleus would be expected to be complex, as there is only one fluorine atom per molecule and this could not be assumed to be an infinite spin bath. However, for $^1\text{H} \rightarrow ^{119}\text{Sn}$, although the standard cross-polarisation equation fitted the variable contact-time data well, the value found for $T_{1\rho}(^1\text{H})$ found from the variable contact time experiment (6.6 ms) did not agree with that found directly (1.9 ms).

$$M_t^{\text{S}} = M_0^{\text{I}} \left[\exp\left(-\frac{t}{T_{1\rho}^{\text{I}}}\right) - \exp\left(-\frac{t}{T_{\text{IS}}}\right) \right]$$

Equation 1: The standard cross-polarisation equation.

It has been found, from direct measurements, that $T_{1\rho}(^1\text{H})$ is small and similar in size to T_{HSn} , so the extended cross-polarisation equation, given by Mehring⁷ and summarised in Equation 2, is necessary to describe the variable contact-time data. This equation takes account of the spin-locked relaxation time for both nuclei, the relative populations of spins, ϵ , and the Hartmann-Hahn mismatch parameter, α . In this case, $\epsilon = 0.003$, as there are many more protons present than ^{119}Sn atoms. The Hartmann-Hahn mismatch parameter is assumed to be equal to 1, i.e. no mismatch. This assumption is reasonable as the terms $\epsilon\alpha^2$ are small.

$$M_t^S = \frac{M_0^I}{(a_+ - a_-)} \left[\exp\left(-\frac{a_- t}{T_{\text{IS}}}\right) - \exp\left(-\frac{a_+ t}{T_{\text{IS}}}\right) \right]$$

Equation 2: The extended cross-polarisation equation⁷ simplified by assuming zero S-spin magnetisation at time $t = 0$. The symbols are described in the text, Equation 3 and Equation 4.

$$a_{\pm} = a_0 \left[1 \pm \left(1 - \frac{b}{a_0^2} \right)^{\frac{1}{2}} \right] \quad a_0 = \frac{1}{2} \left(1 + \epsilon\alpha^2 + \frac{T_{\text{IS}}}{T_{1\rho}^I} + \frac{T_{\text{IS}}}{T_{1\rho}^S} \right) \quad b = \frac{T_{\text{IS}}}{T_{1\rho}^I} \left(1 + \frac{T_{\text{IS}}}{T_{1\rho}^S} \right) + \epsilon\alpha^2 \frac{T_{\text{IS}}}{T_{1\rho}^S}$$

Equation 3: Factors used in the extended cross-polarisation equation. The values are $a_+ = 1.31$, $a_- = 0.10$, $a_0 = 0.70$ and $b = 0.37$

$$\epsilon = \left(\frac{N_S S(S+1)}{N_I I(I+1)} \right) \quad \alpha = \frac{\omega_S}{\omega_I}$$

Equation 4: Equations for the relative populations of spins, ϵ , and the Hartmann-Hahn mismatch parameter, α .

To fit the experimental variable contact-time data shown in Figure 12, M_0^I , T_{IS} and $T_{1\rho}(^1\text{H})$ were varied. The value of $T_{1\rho}(^{119}\text{Sn})$ was used as directly measured, as the fit was fairly insensitive to this parameter. The best fit, found by eye, gives a good fit to the experimental data and agrees with the direct $T_{1\rho}(^1\text{H})$ measurement. The cross-relaxation time, T_{HSn} , measured with either equation, turns out to be the same.

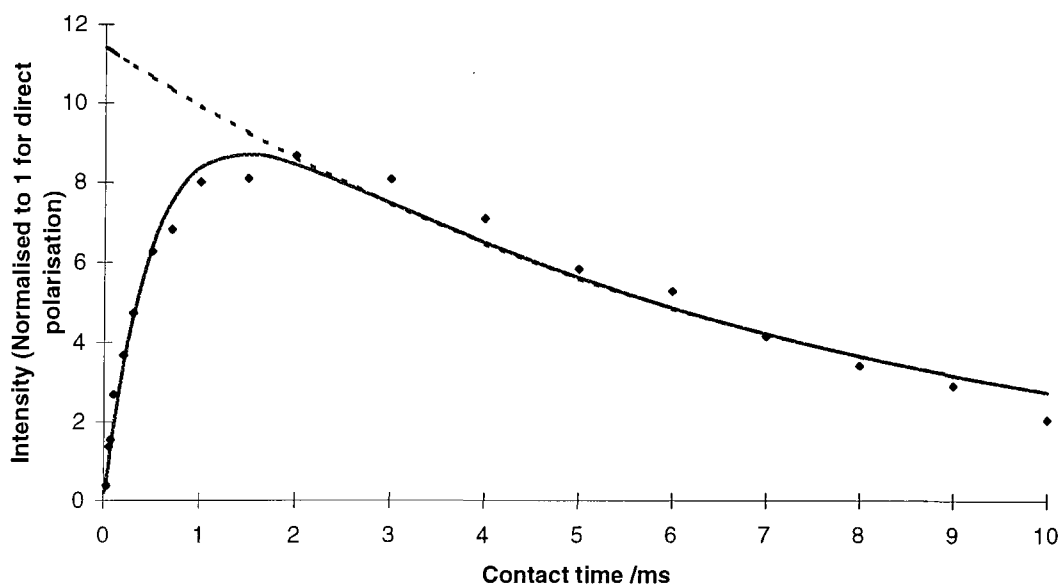


Figure 12: Cross polarisation profile for ^{119}Sn the line shows the best fit curve described by the extended CP equation.

It was found that the signal enhancement from CP was not as large as predicted theoretically. The relative intensity of ^{119}Sn signals given by cross polarisation (from ^1H) using the optimum contact time of 1 ms and those from direct polarisation spectra for ^{119}Sn show an 8-fold improvement for the former at constant time. The figure has been normalised so that the intensity from the direct polarisation spectrum was unity. The theoretical signal enhancement is

$$\left[\frac{T_1(^{119}\text{Sn})}{T_1(^1\text{H})} \frac{\nu_L(^1\text{H})}{\nu_L(^{119}\text{Sn})} \right] = 23.2.$$

Projecting the measured signal back to a contact time of 0 ms (dashed line), so as to account for the initial cross-relaxation term, gives a signal enhancement of 11.4. This loss of signal may be due to $T_{1\rho}(^{119}\text{Sn})$ being small or CP imperfections e.g. offset, mismatch and anisotropy.

5.2 Trimesityltin fluoride

The structure of trimesityltin fluoride, Mes_3SnF , is atypical compared to those of the other triorganotin fluorides. With a bulky group such as mesityl (Mes), steric hindrance prevents the close approach of two molecules, and diffraction data have shown that there are two tetra-coordinate molecules in the asymmetric unit. Having two molecules complicates the NMR spectra, as will be discussed later. The structure is shown schematically in Figure 13 below.

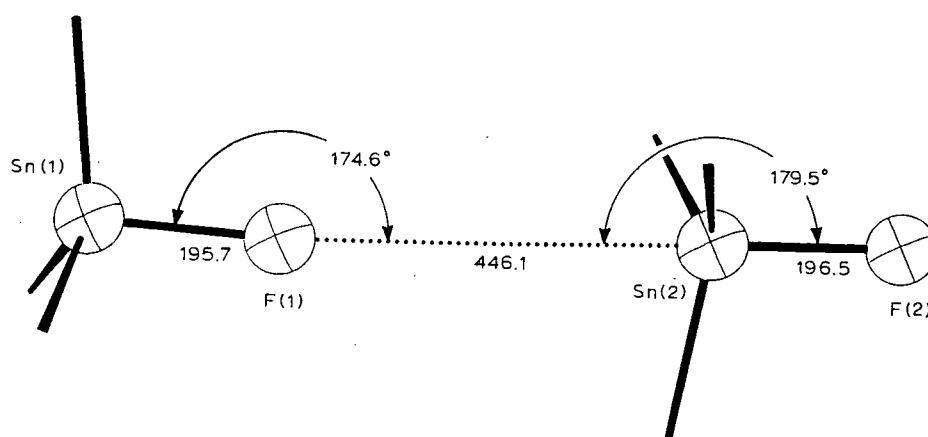


Figure 13: Schematic structure of Mes_3SnF from the XRD structure (Ref. 8). Bond lengths are given in pm. Figure reproduced from ref. 15.

5.2.1 NMR data

The MAS proton NMR spectrum of Mes_3SnF , Figure 14, shows dipolar broadened spinning sidebands. Superimposed on this are some sharp peaks: four lie in the region 0 to 5 ppm and one has a shift of 16.6 ppm. This high frequency peak is further split, possibly into a triplet. The inset spectrum in Figure 14 was recorded with a rotor-synchronised chemical shift echo to remove the broad peak and its spinning sidebands. The sharp peaks are still visible in CRAMP spectra of the compound though the peak at 16.6 ppm is very broad. The origin of the sharp peaks is unknown; they could arise from methyl protons on the mesityl groups, or from an

impurity. A spectrum measured with ^{19}F decoupling, not shown, gave a broad peak where the triplet had been observed. The line was too broad to be able to state whether the triplet remained or had been decoupled to become a single broadened peak. A wideline separation (WISE) experiment that used normal CP from proton to fluorine showed only the dipolar broadened peaks. These broadened peaks, observed with CP, might be expected to be assigned to the protons attached directly to the mesityl ring, which have fairly restricted motion.

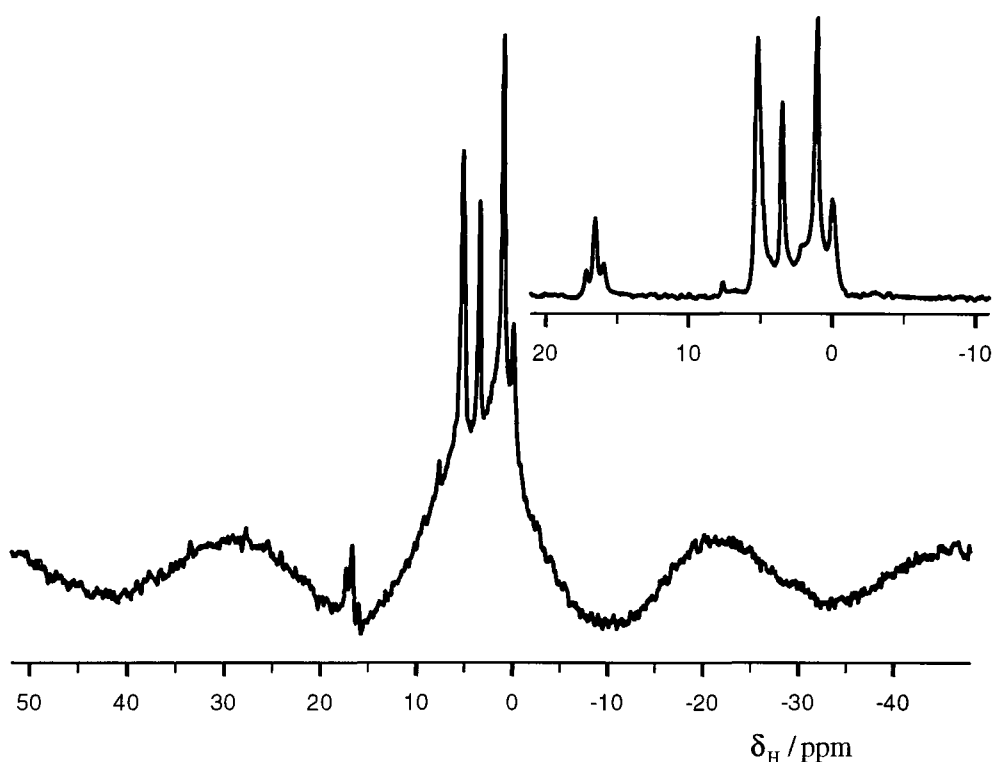


Figure 14: Proton NMR spectra of Mes_3SnF recorded with no decoupling and spinning at 4 kHz. Acquisition parameters were: spectral width 20 kHz, pulse duration 4 μs , recycle delay 5 s, and number of acquisitions 4. For the inset spectrum, a rotor-synchronised echo was used. Other acquisition parameters were: spectral width 50 kHz, pulse duration 4 μs , recycle delay 5 s, and number of acquisitions 16.

The carbon-13 NMR spectrum measured here is the same as that reported previously by Bai.⁹ The peaks could not be assigned precisely in either work as each of the 27 carbons in the molecule are expected to be different. Peaks were observed with $\delta = 20 - 27$ ppm (methyl), 128.7 and 129.6 ppm (meta carbons), and 137 -

147 ppm (remaining carbons on phenyl ring). Using TPPM decoupling narrowed the peaks when compared to normal CW decoupling. The measured linewidths were: methyl carbons 41 to 37 Hz and phenyl carbons 38 to 31 Hz for CW and TPPM decoupling respectively. Despite the narrower lines, the spectrum was still too complicated to assign individual peaks. It might be possible to separate the peaks according to which molecule they are in by using a form of heteronuclear correlation (HETCOR) experiment with CP from ^{19}F to ^{13}C , but there would still be too many peaks to give a clear assignment.

5.2.1.1 Fluorine-19

The ^{19}F NMR spectrum of Me_3SnF is shown in Figure 15. The spectrum is complicated by the existence of the two molecules in the asymmetric unit. When the sample is spun at 8 kHz, only the centreband is visible along with the usual $^{117,119}\text{Sn}$ satellite peaks. To spin at 1505 Hz, for the spectrum shown below, a smooth rotor tip was used. The spinning speed could not be locked automatically, but the speed did not drift detectably during the measurement. The centreband peaks are indicated by vertical arrows and the low-frequency satellite peaks by daggers. The high-frequency satellite peaks are too weak to be visible. For spinning-sideband analysis of the ^{19}F spectrum, the satellite peaks have very little intensity and lie on the shoulders of the main peaks. This feature makes their intensity hard to measure, even by deconvolution. All measurements were made without restricting the sample to the central part of the rotor.

Spinning-sideband analysis of just the centreband peaks gave $\zeta = -19$ and -27 ppm, with near-axial tensors, for the peaks at $\delta = -190.9$ and -194.2 ppm. The value of D' was initially measured from the ^{119}Sn spectrum (see later). From the ^{119}Sn results for D' and the ^{19}F anisotropy, the values for the effective anisotropy of the satellite peaks could be estimated. This estimate showed that the low-frequency peaks had a very small effective anisotropy and hence had most of the signal intensity in the isotropic peak. The high-frequency peaks had much larger anisotropy

so that the signal intensity was spread between many ssb peaks. This estimate is in agreement with the observed spectrum, Figure 15.

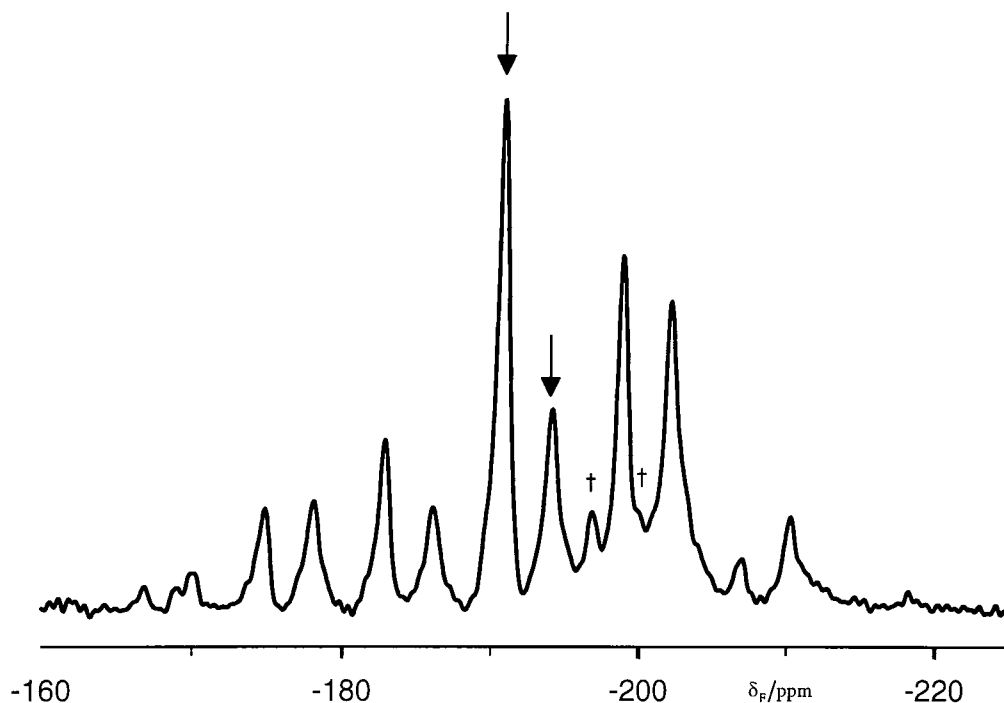


Figure 15: Fluorine-19 CPMAS NMR spectrum of Me_3SnF , obtained with spinning at 1505 Hz together with proton decoupling. The centrebands are indicated by vertical arrows, and the low frequency satellites are marked by a dagger. The Bloch-Siegert correction of +2.3 ppm has been applied to the frequency scale. Acquisition parameters were: pulse duration 3 μs , contact time 5 ms, recycle delay 3 s, and number of acquisitions 64.

An alternative method to measure the intensity in the satellite peak ssb manifolds would be to separate the intensity into two dimensions. Two-dimensional HETCOR spectra measured with the sample spinning at 4 kHz, with direct observation of the ^{119}Sn and indirect observation of the ^{19}F , are shown in Figure 16. The contact time is very short (0.3 ms), allowing only transfer of ^{19}F magnetisation to nearby ^{119}Sn nuclei. Figure 16(b) shows the ^{19}F spectrum in ω_1 (vertical dimension) for fluorines directly bonded to ^{119}Sn . This is equivalent to the tin satellite peaks in the normal ^{19}F spectrum (Figure 15). The first low-frequency ssb peaks, marked with an asterisk, are also visible. The high-frequency ssb peaks are predicted to have low intensity, which is confirmed by their absence in the spectrum.

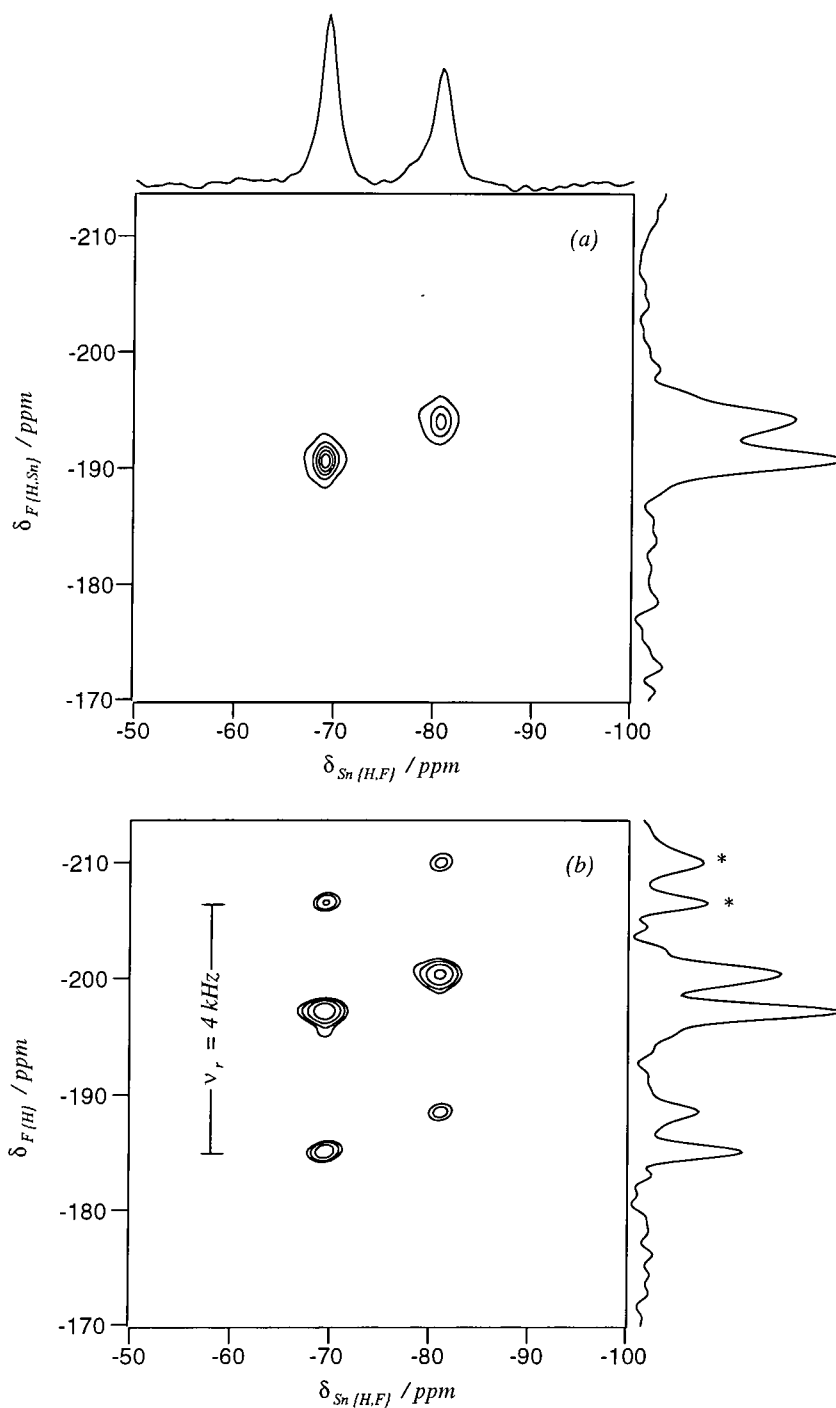


Figure 16: Two-dimensional heteronuclear correlation spectra obtained by observing $^{119}\text{Sn}\{^1\text{H}, ^{19}\text{F}\}$ in t_2 and (a) $^{19}\text{F}\{^1\text{H}, ^{119}\text{Sn}\}$, (b) $^{19}\text{F}\{^1\text{H}\}$ in t_1 . Acquisition parameters were: (a) ^{19}F transmitter frequency 188.275 MHz, pulse duration 5 μs , dwell (t_1) 100 μs , points in t_1 32, zero-filled to 256, contact time 0.3 ms, recycle delay 10 s, and number of acquisitions per slice 16; (b) ^{19}F transmitter frequency 188.275 MHz, pulse duration 5 μs , dwell (t_1) 100 μs , points in t_1 64, zero-filled to 256, contact time 0.3 ms, recycle delay 10 s, and number of acquisitions per slice 64.

For comparison, Figure 16(a) has ^{119}Sn decoupling on during t_1 so that the ω_1 spectrum is equivalent to the ^{19}F spectrum without the satellite peaks present, i.e. just the centreband.

These spectra clearly show the two molecules in the asymmetric unit with their ^{19}F and ^{119}Sn chemical shifts correlated. No cross peaks are observed for the other permutation of peaks. The correlation of the ^{19}F and ^{119}Sn shifts had previously been hypothesised, but most of the NMR properties of the two sites were too similar to separate them. These molecules are labelled as site 1 and 2 in the following tables.

A 2D HETCOR experiment, similar to Figure 16(b) but with the sample spinning at 1500 Hz (not shown) separates the two sites and gives more spinning sidebands in the ^{19}F dimension. These ssb's only arise from the ^{119}Sn satellite peaks and are not complicated by the ssb's arising from the more intense centreband peaks. For this experiment, 80 points were collected in the second dimension. This was zero-filled to 128 points before Fourier transformation. The measured ssb intensities have a large error as the signal-to-noise ratio is low and the peak is not defined by many points. Another possibility for processing would have been to use a maximum entropy method. The two satellite peaks to low frequency have effective anisotropies near zero, giving single peaks at $\delta = -196.8$ and -200.1 ppm. The high-frequency satellites have larger effective anisotropies, so their intensities are spread over a number of spinning sidebands, giving many low-intensity peaks.

A triple fit of the spinning-sideband manifolds for the centreband, from the 1D spectrum, and for the satellite peaks, from the 2D spectrum, has been performed. In both spectra, the sample was spinning at approximately 1500 Hz. This triple fit allows approximate values for ζ^{eff} to be calculated, as shown in Table 11. The single-fit data is given in Table 12 for comparison. It can be seen that the values for the anisotropy are similar for both fitting techniques. However, the anisotropy for $\delta = -200.1$ ppm has the opposite sign to that predicted by the triple fit. This shows that using the triple fit gives more consistent results than for the single fit, where the error in the anisotropy is larger.

The errors are given for the single-fit data, shown in brackets. This is only the statistical error associated with the fitting, as can be seen from the fact that the errors

for peaks with small anisotropies are small. In these cases, there is only one ssb peak on each side of the centreband so the fit to simulation is ‘good’ and hence the fitting error is small. In reality, the value for the anisotropy is poorly constrained and the error would be expected to be much larger. For comparison, the high-frequency satellite peaks have significantly larger errors, as would be expected due to the many peaks and poor signal-to-noise ratio in the 2D spectrum. The asymmetry is poorly defined by the experimental data, partly due to the small size of the anisotropy.

Table 11: Summary of the ^{19}F spinning-sideband triple-fit analysis for Figure 15 and the HETCOR spectrum (not shown).

	δ_{iso} (ppm)	ζ^{eff} (ppm)	η^{eff}	$\sigma_{11}^{\text{eff}} - \sigma_{\text{ref}}$ (ppm)	$\sigma_{22}^{\text{eff}} - \sigma_{\text{ref}}$ (ppm)	$\sigma_{33}^{\text{eff}} - \sigma_{\text{ref}}$ (ppm)
	-185.0 ^a	-36	0.3	209	198	149
Site 1	-190.9	-18	0.6	205	195	173
	-196.8 ^a	6	0.5	192	195	203
	-188.3 ^a	-49	0.2	218	207	139
Site 2	-194.2	-26	0.4	213	202	168
	-200.1 ^a	7	0.0	196	196	208

^a Values are for the Sn satellite spinning-sideband manifolds

Table 12: Summary of the ^{19}F spinning-sideband single-fit analysis for Figure 15 and the HETCOR spectrum (not shown).

	δ_{iso} (ppm)	ζ^{eff} (ppm)	η^{eff}	$\sigma_{11}^{\text{eff}} - \sigma_{\text{ref}}$ (ppm)	$\sigma_{22}^{\text{eff}} - \sigma_{\text{ref}}$ (ppm)	$\sigma_{33}^{\text{eff}} - \sigma_{\text{ref}}$ (ppm)
	-185.0 ^a	-43.4 (5.3)	0.75 (0.02)	223.0	190.5	141.6
Site 1	-190.9	-19.1 (0.1)	0.32 (0.01)	203.5	197.4	171.8
	-196.8 ^a	5.8 (0.2)	0.00 (0.36)	193.9	193.9	202.6
	-188.3 ^a	-53.3 (4.8)	0.64 (0.02)	232.0	197.9	135.0
Site 2	-194.2	-27.0 (0.2)	0.00 (0.06)	207.7	207.7	167.2
	-200.1 ^a	-7.5 (0.1)	0.00 (0.22)	203.9	203.9	192.6

^a Values are for the Sn satellite spinning-sideband manifolds

Using the values for the effective anisotropies gives the effective dipolar coupling constant as $D' = -3420$ Hz (site 1) and -4290 Hz (site 2). The triple-fit simulation shows that the two tensors are probably coaxial, as might be expected for a terminal fluorine atom, though the data used here are not well defined. The errors in D' are large, though the differences between the two sites are possibly significant. The values of D' are smaller than that found from the ^{119}Sn spectrum (see later), but there is reasonable agreement considering the large errors in both the ^{19}F and ^{119}Sn measurements.

The Tycko 2D experiment measured with the sample spinning at 8 and 9 kHz confirms the size of the shielding anisotropy. With only 40 points collected in the second dimension, the static lineshape is poorly defined and it is not possible to accurately measure the asymmetry. It is possible to confirm the small anisotropy of the peaks, which is not possible with the simple 1D static ^{19}F NMR spectrum.

5.2.1.2 Tin-119

The ^{119}Sn spectra of Mes_3SnF in Figure 17 show splittings arising from scalar isotropic coupling to both fluorine and carbon with average $^1J(\text{SnF}) = 2275$ Hz and $^1J(\text{SnC})$ of about -550 Hz, the latter obtained from the small satellite peaks indicated by a dagger in Figure 17(b). The doubly-decoupled spectrum unambiguously confirms the assignment of the splitting caused by coupling to ^{19}F (reinforcing earlier variable-field experiments). Mes_3SnF is the only organotin compound that has been studied where coupling to ^{13}C is visible in the ^{119}Sn spectrum. Presumably the line broadening caused by dipolar broadening two bridging fluorines in the other compounds is greater than the magnitude of the scalar coupling to ^{13}C in other compounds.

By contrast to $^n\text{Bu}_3\text{SnF}$, Mes_3SnF has small ^{119}Sn effective anisotropies, so the spectra show few spinning sidebands with significant intensity. This is especially true for the doubly-decoupled spectra, showing that D' is substantially larger in magnitude than the true shielding anisotropy. As there are also two molecules in the asymmetric unit, the spectrum cannot be easily interpreted when recorded at a slow

spinning speed as it becomes too cluttered. This results in the occurrence of few spinning sidebands, which leads to poorly defined anisotropies.

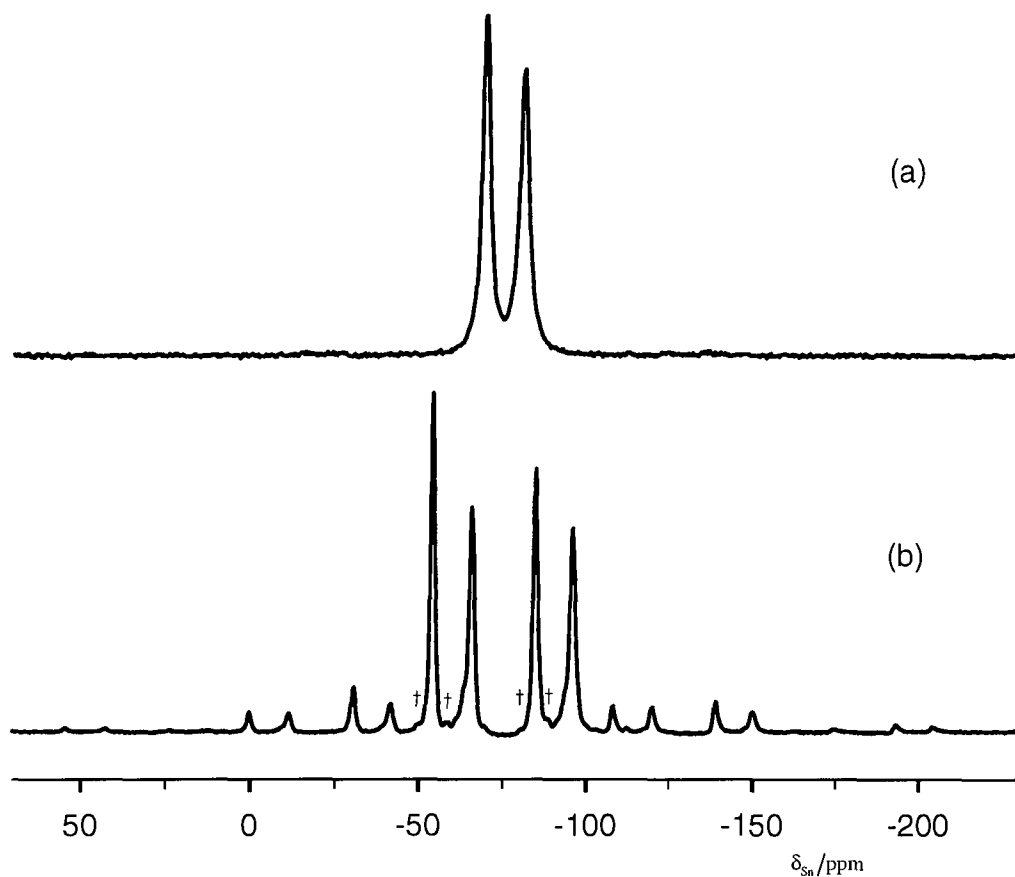


Figure 17: Tin-119 CPMAS NMR spectra of Mes_3SnF , obtained with spinning at 4 kHz together with (a) double decoupling, and (b) only ^1H decoupling. The weak ^{13}C satellites are marked by a dagger. Acquisition parameters were: (a) pulse duration 4 μs , contact time 4 ms, recycle delay 3 s, and number of acquisitions 1256; (b) pulse duration 5 μs , contact time 5 ms, recycle delay 5 s, and number of acquisitions 9045.

However, a proton (only)-decoupled spectrum has been recorded with the sample spinning at 2 kHz. At this speed the peaks are interleaved, so that useful information can be obtained by careful deconvolution. There are still only two spinning sidebands, but their intensities are significant, giving a better signal-to-noise ratio than for Figure 17(b) and thus a smaller error. A combined fit of the three sets of data, two from the singly-decoupled spectrum, and one from the doubly-decoupled spectrum (recorded at the same spin rate), has been performed, with the results summarised in Table 13.

Table 13: Summary of the ^{119}Sn spinning-sideband triple-fit analysis for the spectra recorded with the sample spinning at 2 kHz (not shown).

	δ_{iso} (ppm)	ζ^{eff} (ppm)	η^{eff}	$\sigma_{11}^{\text{eff}} - \sigma_{\text{ref}}$ (ppm)	$\sigma_{22}^{\text{eff}} - \sigma_{\text{ref}}$ (ppm)	$\sigma_{33}^{\text{eff}} - \sigma_{\text{ref}}$ (ppm)
	-54.0 ^a	-51	0.2	85	74	3
Site 1	-69.2	12	0.9	58	69	81
	-84.8 ^a	75	0.1	42	53	160
	-65.9 ^a	-62	0.3	107	87	3
Site 2 ^b	-80.6	19	0.1	70	72	100
	-96.0 ^a	63	0.3	55	74	159

^a Values are for the scalar coupled lines of the Sn-F coupled multiplets.

^b In this case non-axiality between the dipolar and shielding tensors was found.

Table 14: Summary of the ^{119}Sn spinning-sideband single-fit analysis for the spectra recorded with the sample spinning at 2 kHz (not shown).

	δ_{iso} (ppm)	ζ^{eff} (ppm)	η^{eff}	$\sigma_{11}^{\text{eff}} - \sigma_{\text{ref}}$ (ppm)	$\sigma_{22}^{\text{eff}} - \sigma_{\text{ref}}$ (ppm)	$\sigma_{33}^{\text{eff}} - \sigma_{\text{ref}}$ (ppm)
	-54.0 ^a	-49.5 (0.9)	0.48 (0.02)	90.5	67.0	4.5
Site 1	-69.2	12.6 (0.3)	0.00 (0.21)	62.9	62.9	81.8
	-84.8 ^a	75.4 (1.0)	0.22 (0.04)	38.8	55.4	160.2
	-65.9 ^a	-62.1 (0.4)	0.25 (0.02)	104.8	89.1	3.7
Site 2	-80.6	19.0 (0.3)	0.00 (0.18)	71.1	71.1	99.7
	-96.0 ^a	62.4 (0.9)	0.53 (0.01)	48.3	81.3	158.4

^a Values are for the scalar coupled lines of the Sn-F coupled multiplets.

The double decoupling is particularly significant for the measurement of the shielding anisotropies, free from the effects of D' . Previous work⁹ considered the symmetry of the molecule to estimate the orientation of the shielding tensor. From this and the proton-decoupled ^{119}Sn spectrum, a value for $D' = -1.27$ and -1.97 kHz was calculated for the $\delta = -80.6$ and -69.2 ppm sites respectively, with an average

value of $\zeta^0 = 57$ ppm. The shielding anisotropy has now been directly measured from the doubly-decoupled ^{119}Sn spectra (Figure 17(a) and one with the sample spinning at 2 kHz) and found to be much smaller than this. The value for D' is much larger than that given above and is also corroborated by analysis of the ^{19}F spectrum. The previous assumptions about molecular symmetry and the orientation of the shielding tensor are incorrect, presumably due to further distortions within the molecule.

For the case when the system is treated as coaxial, the anisotropies are found to be 12 and 1 ppm for the two sites. When this condition is relaxed, they are obtained as 12 and 19 ppm, in better agreement with the single-fit data. This indicates that the tensors are not coaxial. The triple-fit data shows that site 1 appears to be almost colinear, with $D' = -4690$ Hz. However, for site 2 the shielding tensor is tilted by approximately 50° from the dipolar tensor. For this site, the effective dipolar tensor is $D' = -4500$ Hz, compared with -4720 Hz if colinearity is assumed.

For the small values of the anisotropy, e.g. the centreband peak for site 1 ($\delta = -69.2$ ppm), the asymmetry parameter is not a useful descriptor. A slight change in any of the individual tensor components will have a large effect on the asymmetry as seen by the large fitting error of 0.21 for the asymmetry of this peak. With so few ssb peaks and high asymmetry for site 1, changing the sign of the anisotropy makes little difference to the fit, this sign is better constrained in the triple fit.

The static ^{119}Sn spectra are uninformative as the small anisotropy is dwarfed by the much larger line broadening. The doubly-decoupled spectrum confirms that the anisotropy is small, but is too featureless to give information about the asymmetry. Using the MAT pulse sequence allows the static spectra to be separated for each isotropic peak. The doubly-decoupled MAT experiment, Figure 18, shows that the anisotropy is larger for site 2 than site 1. A DC offset spike can be seen in the direct dimension where the transmitter was centred at -75 ppm. The effects of truncation can be seen in the indirect dimension by the sinc function of the baseline. For the proton-decoupled MAT spectrum, the axial nature of the lineshape can be seen. These sub-spectra agree with the values given above that are derived from the ssb triple-fit simulation.

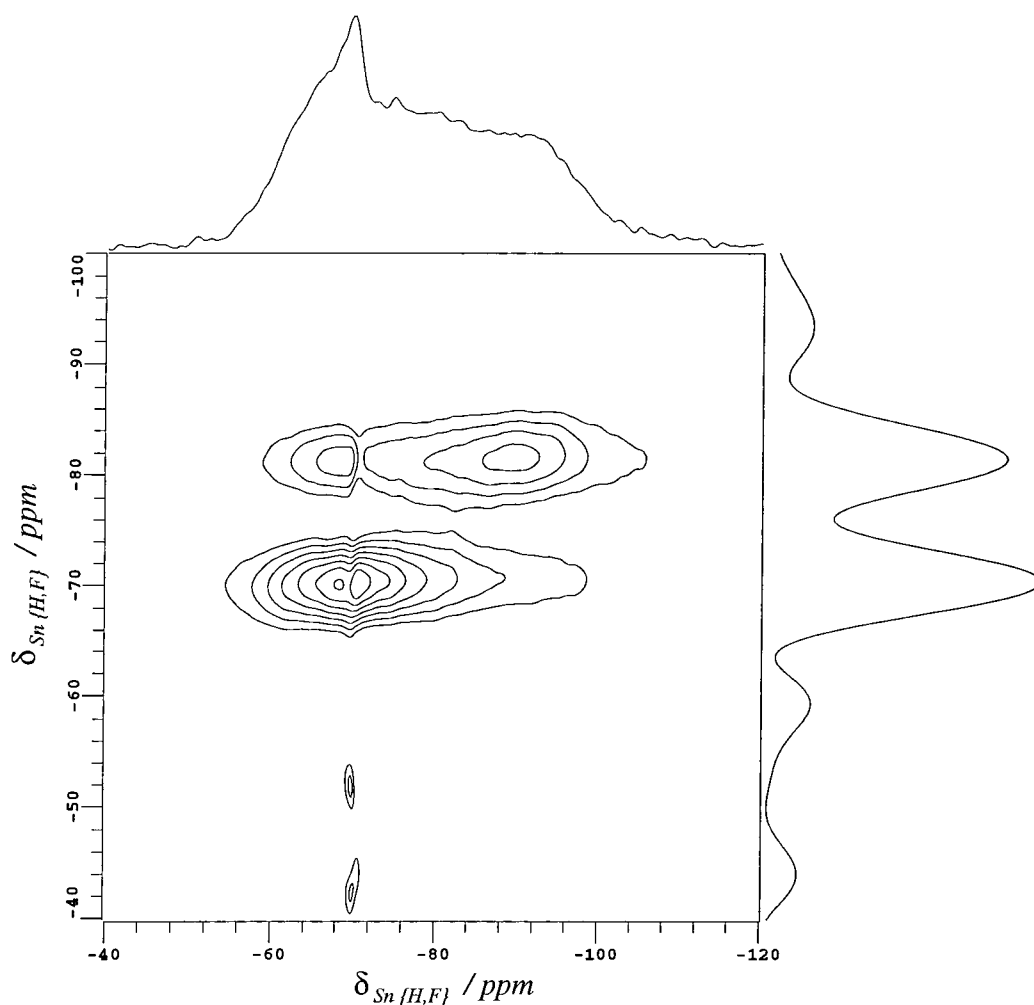


Figure 18: ^{119}Sn MAT spectrum of Mes_3SnF recorded with double decoupling. Acquisition parameters were: pulse duration $4.5 \mu\text{s}$, contact time 2 ms , recycle delay 2 s , number of acquisitions per slice 640 , number of slices 256 , spinning speed 30 Hz .

The REDOR experiment¹⁰ was used in an attempt to measure D' . This experiment had previously been implemented and checked using doubly labelled $20\% [^{13}\text{C}, ^{15}\text{N}]$ -glycine. Fitting the dipolar dephasing curve by simulation programs found, in this case, that the dipolar coupling was 950 Hz . For Mes_3SnF the signals dephased too rapidly to estimate the size of D' . This would be expected if D' is around -4 kHz , though if it is nearer to -1.5 kHz , as had been thought, then some signal should have been observed.

5.2.1.3 Relaxation data

The relaxation data for Mes_3SnF are summarised in Table 15. The longitudinal relaxation times, T_1 , of ^{19}F and ^{119}Sn for Mes_3SnF are longer than those for $^n\text{Bu}_3\text{SnF}$, implying reduced motion in the Mes_3SnF system. The value of $T_1(^1\text{H})$ for Mes_3SnF is short, which is favourable for CP. Spin-locked, $T_{1\rho}$, relaxation for Mes_3SnF is long for all nuclei studied and could not be determined for ^{19}F . For such long $T_{1\rho}$ values, only the initial gradient could be measured. Thus, the best contact times for CP from proton to other nuclei were also long: 5 ms for ^{19}F and 3 ms for ^{119}Sn . It would be possible to use a multiple-contact cross polarisation sequence due to the long value for the proton $T_{1\rho}$. However, the short value for $T_1(^1\text{H})$ and the hardware complications that arise with long spin-lock times meant that normal single contact CP was used. Oscillations in the initial rise of the variable contact time profile from proton to fluorine were observed for times up to 0.5 ms. This effect has been seen for other compounds where the spin-pair is relatively isolated.¹¹ In ideal cases, the variable contact time curve can be simulated to obtain the usual parameters and also the effective dipolar coupling constant, D' . For this compound, the oscillations were not studied further as they were rapidly damped and the ^{19}F spectrum is complex.

Table 15: Summary of the relaxation data obtained for Mes_3SnF .

$T_1(^1\text{H}) / \text{s}$	1.1	$T_{1\rho}(^{19}\text{F}) / \text{ms}$	Long
$T_1(^{19}\text{F}) / \text{s}$	7.5	$T_{1\rho}(^{119}\text{Sn}) / \text{ms}$	700 / 1000 ^a
$T_1(^{119}\text{Sn}) / \text{s}$	29 / 51 ^a	$T_{\text{HF}} / \text{ms}$	0.4
$T_{1\rho}(^1\text{H}) / \text{ms}$	58	$T_{\text{HSn}} / \text{ms}$	0.5

^a For the two sites at $\delta = -69.2$ and -80.6 ppm respectively.

In many respects, Mes_3SnF is an ideal reference compound for the ^{119}Sn chemical shift and setting the Hartmann-Hahn match for CP from either ^1H or ^{19}F to ^{119}Sn . Its small ^{119}Sn anisotropy gives sharp peaks that have a good signal-to-noise ratio with few free induction decays. Measuring only four transients gives a reasonable ^{119}Sn NMR spectrum when the sample is spinning at 4 kHz. The proton

T_1 is short, which is ideal for CP. This compound has been used herein to set the Hartmann-Hahn match for CP from ^{19}F to ^{119}Sn . Na_2SnF_6 has been previously suggested as a $^{19}\text{F} \rightarrow ^{119}\text{Sn}$ matching standard,¹² but it requires a long recycle delay of 20 s and has a large linewidth. The main advantage of Na_2SnF_6 over Me_3SnF is its wide availability from commercial sources.

5.2.1.4 Double decoupling with the HFX probe

As the ^{119}Sn spectrum of Me_3SnF can be rapidly measured, the effect of double and off-resonance decoupling has been studied on the HFX probe. The spectra shown in Figure 17 were recorded with proton and double decoupling. Surprisingly, when measuring the spectrum with no decoupling the four peaks are still visible, though each peak is slightly more broadened compared to the proton-decoupled spectrum. Using only high-power fluorine decoupling gives a broad featureless lineshape.

Varying the ^{19}F decoupler power, but with high-power proton decoupling, leads to a change in the spectrum, Figure 19, which can be explained as arising from off-resonance effects. As the decoupling power is increased, the effective splitting reduces. The effective coupling between ^{119}Sn and ^{19}F is dependent on both the power and the offset of the ^{19}F decoupling field,¹³ as given in Equation 5, where B_2 is the decoupler field strength, $\delta\nu$ is the offset of irradiation from ^{19}F resonance, and J_r is the observed reduced splitting.

$$\left(\frac{\gamma}{2\pi}\right)B_2 = \delta\nu \frac{\sqrt{J^2 - J_r^2}}{|J_r|}$$

Equation 5: Off-Resonance Decoupling

Figure 20 shows the effect on the reduced splitting as the decoupling frequency is offset from 188.29 MHz, its usual position in our operations. The most efficient decoupling, when on resonance, can be seen to occur with an offset of

10.5 kHz from the standard frequency. Using this value for $\delta\nu$, the decoupling powers can then be calculated from the spectra in Figure 19 (which used the standard frequency) by measuring the value of J_r for each slice. This is consistent with those powers found from 90° pulse duration experiments and produces a quick and accurate method to calibrate the decoupler powers. Similarly, the offset can be calculated if the powers are known. Another advantage of reduced splittings is to simplify the spectrum without fully removing the coupling, which can give valuable information, e.g. on multiplicities in crowded spectra.

When the proton decoupling power was varied with full ^{19}F decoupling, the two peaks seen with high-power proton decoupling changed to four closely spaced peaks and then a broad peak on reducing the power. The splitting at intermediate powers was around 350 Hz. It was not thought that this was due to the effect of off-resonance decoupling, though no alternative suggestions have been given.

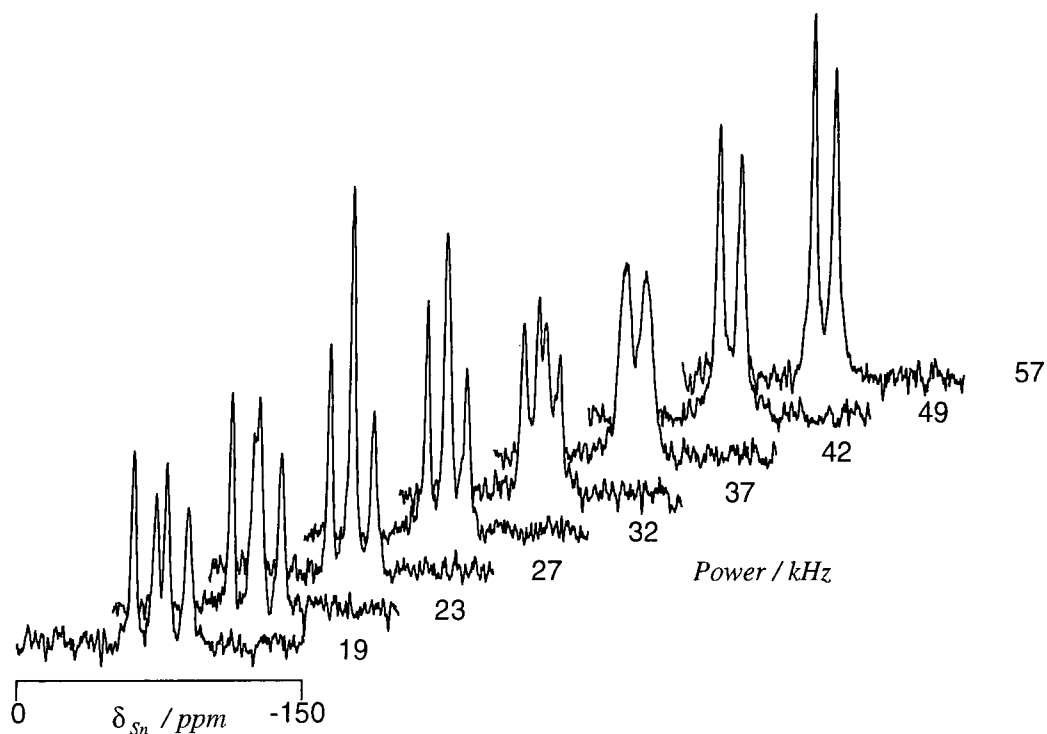


Figure 19: Tin-119 CPMAS NMR spectra of Me_3SnF , obtained with spinning at 4 kHz together with proton decoupling and variable-power ^{19}F decoupling. These powers were calibrated by measuring 90° pulse durations on C_6F_6 and are given in kHz beside each spectrum. The ^{19}F decoupler was offset by 10.5 kHz from the centreband resonance as measured from Figure 20. Acquisition parameters were: pulse duration 4 μs , contact time 5 ms, recycle delay 5 s, and number of acquisitions 8. The ^{19}F power was adjusted manually.

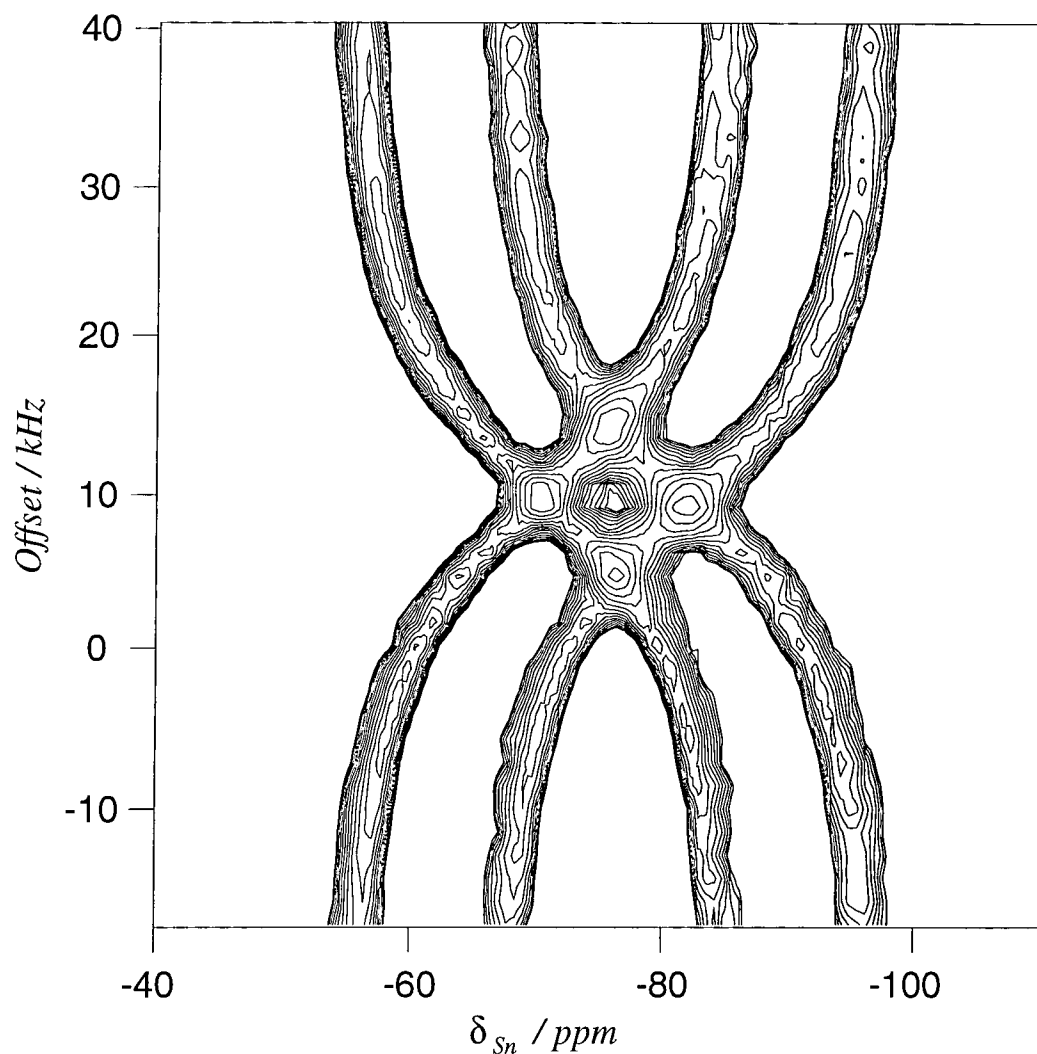


Figure 20: Contour plot of tin-119 CPMAS NMR spectra of Me_3SnF , obtained with spinning at 4 kHz together with proton decoupling and variable-offset ^{19}F decoupling. Acquisition parameters were: pulse duration 4.5 μs , contact time 4 ms, recycle delay 3 s, and number of acquisitions 32.

A final experiment was run where both the proton and fluorine decoupling powers were varied in a grid pattern with powers from 50 to 20 kHz. This showed that there was efficient decoupling, i.e. only two peaks for Me_3SnF , when the two decoupling powers were matched. This efficient decoupling was still observed with low powers down to 20 kHz for decoupling of both nuclei. The spectrum recorded with matched decoupling powers of 25 kHz is shown in Figure 21(a). If the decoupling power for either nucleus was increased from this matched situation, while

the other was kept constant, the observed spectrum had four peaks and was inefficiently decoupled compared to at the lower powers as seen in Figure 21(b).

This effect of efficient double decoupling when the powers were matched appears to be independent of sample spinning speed. The same effect was observed when the offset was changed such that the effective decoupling power, taking into account the effect of the offset, of a channel matched the on-resonance decoupling power of the other channel. These measurements contradict previous experiments on fluorinated adamantane where it was found that double decoupling was more efficient when the two decoupler channels were not matched.¹⁴ With Me_3SnF , it is easier to observe the efficiency of double decoupling than it would be for the more dipolar-broadened fluorinated adamantane. As yet, the only possible explanation is that when the decoupling powers are matched, there is efficient CP between ^1H and ^{19}F . This would increase the rate of flip-flops between the nuclei and hence the effective relaxation rates of both nuclei, which should improve the decoupling efficiency.

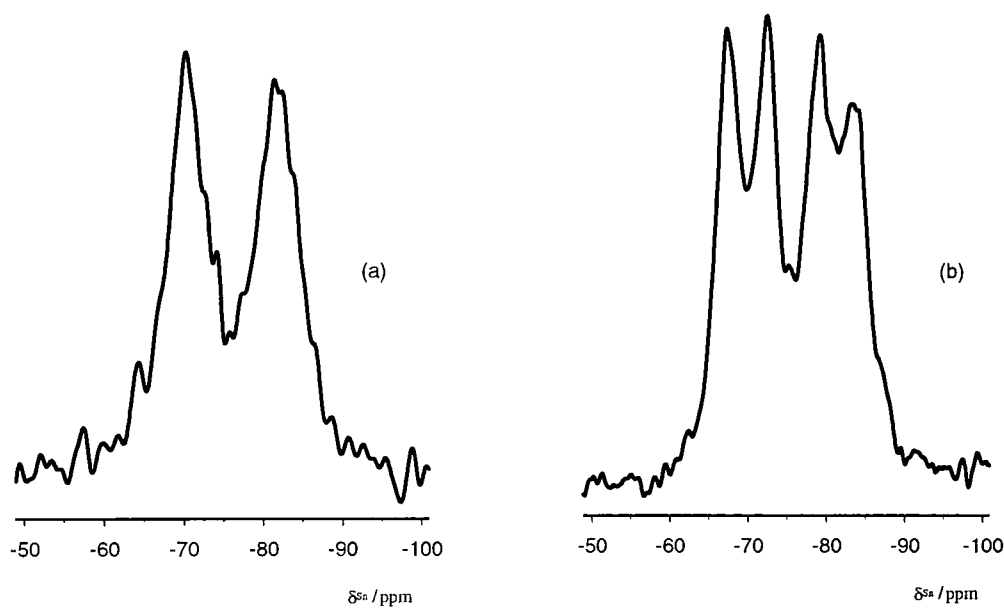


Figure 21: Comparison of double decoupling at different powers: (a) 25 kHz on both channels, (b) 25 kHz on proton and full (50 kHz) power on fluorine. Acquisition parameters were: pulse duration 4.5 μs , contact time 4 ms, recycle delay 3 s, and number of acquisitions 32.

5.3 Summary of results for D' and ΔJ

In this chapter we have obtained values for D' from measuring and fitting both the ^{19}F and ^{119}Sn spectra for $^n\text{Bu}_3\text{SnF}$ and Me_3SnF . Other papers have reported values for D' from other triorganotin fluorides. At that time, the XRD structures were unavailable so ΔJ was not calculated. Instead, a graph was plotted showing the variation of ΔJ for each compound as the bond length, and hence D , was changed. This summary is given here in preparation for the results from the difluorotin compounds in the following chapter.

Table 16 summarises the data from this chapter ($^n\text{Bu}_3\text{SnF}$ and Me_3SnF) and a recent paper.¹⁵ The value of D' given for $^n\text{Bu}_3\text{SnF}$ is an average of the ^{119}Sn and ^{19}F measured values. For Me_3SnF , the fluorine data have large errors so the value for D' is an average from the values measured in the ^{119}Sn spectrum for the two molecules in the asymmetric unit. Other values have been derived from ^{119}Sn data. The value of ΔJ given for Me_3SnF has been widely quoted as ca. -4 kHz, though this value was not given in the original reference! The original work gives $\Delta J = +4$ kHz.¹⁶ This calculation is based on early, less accurate ^{119}Sn NMR measurements and the average Sn-F bond length of 2.30 Å from the XRD structure of Me_3SnF .

Table 16: Summary of the calculated values of D' and ΔJ from current and previous¹⁵ results.

Compound	δ_{Sn} / ppm	$^1J(\text{SnF})$ / Hz	D' / Hz	r_{SnF} / Å	D / Hz	ΔJ / Hz
Me_3SnF	24.3	1300	-4020	(2.15)	(-4260)	-720
$^n\text{Bu}_3\text{SnF}$	-9.0	1310	-4000	(2.15)	(-4260)	-780
$^1\text{Bu}_3\text{SnF}$	-13.1	1260	-3740	(2.15)	(-4260)	-1560
Me_3SnF	-69.2, -80.6	2300	-4600	1.96	-5620	-3060
Ph_3SnF	-211.9	1530	-3260	2.15	-4260	-3000

The error in calculating D' is ± 400 Hz, which propagates to an error of over 1 kHz for ΔJ , recalling that $D' = D - \Delta J/3$. In addition, only the bond lengths of Mes_3SnF and Ph_3SnF ¹ are accurately known from XRD structures. There is a structure for Me_3SnF , that has bond lengths of 2.15 and 2.45 Å, but the refinement of the fluorine and carbon atom positions was poor, so it has not been used here. Instead the bond length from Ph_3SnF has been used and is given in brackets in the table. A change of 0.1 Å in the bond length would result in a change of D by ca. 60 Hz and ΔJ by ca. 200 Hz.

In conclusion, it may be stated that there is little difference between most of the values calculated for ΔJ that are outside the experimental error. Three of the compounds have values in the range -700 to -1600 Hz, whilst the other two have values around -3000 Hz. These latter two, Mes_3SnF and Ph_3SnF , both contain phenyl rings, but have different coordination numbers around the tin centre. It had been thought that ΔJ may be roughly proportional to the isotropic value of the scalar coupling, though the value for Ph_3SnF does not support this. There are also insufficient data to check if there is any correlation between the coordination number and ΔJ . *Ab initio* calculations for Me_3SnF ¹⁷ give the value of $\Delta J = -1770$ Hz, which is the same as the measured value, within the large experimental error. More complex systems involving other coordination numbers for the tin atom and phenyl ring substituents have not been theoretically studied, and may be beyond the currently available computational resources. Further experimental and *ab initio* data are necessary to understand these results better.

-
- ¹ D. Tudela, E. Gutiérrez-Puebla, and A. Monge, *J. Chem. Soc., Dalton. Trans.*, 1069 (1992)
- ² Y. W. Kim, A. Labouriau, C. M. Taylor, W. L. Earl, and L. G. Werbelow, *J. Phys. Chem.*, **98**, 4919 (1994)
- ³ A. C. Olivieri, *J. Magn. Reson. A*, **123**, 207 (1996)
- ⁴ R. Tycko, G. Dabbagh, and P. A. Mirau, *J. Magn. Reson.*, **85**, 265 (1989)
- ⁵ R. K. Harris, K. J. Packer, and P. Reams, *Chem. Phys. Lett.*, **115**, 16 (1985)
- ⁶ D. C. Apperley, N. A. Davies, R. K. Harris, A. K. Brimah, S. Eller, and R. D. Fischer, *Organometallics*, **9**, 2672 (1990); J. Kummerlen, A. Sebald, and H. Reuter, *J. Organomet. Chem.*, **427**, 309 (1992); J. Kummerlen and A. Sebald, *J. Am. Chem. Soc.*, **115**, 1134 (1993)
- ⁷ M. Mehring, "Principles of High Resolution NMR in Solids" in *NMR - Basic Principles and Progress*, ed. J.S. Waugh, **12**, 282, Springer-Verlag, Berlin (1983)
- ⁸ H. Reuter and H. Puff, *J. Organomet. Chem.*, **379**, 223 (1989)
- ⁹ H. P. Bai, Ph. D. Thesis, University of Durham (1991)
- ¹⁰ T. Gullion and J. Schaefer, *J. Magn. Reson.*, **81**, 196 (1989); T. Gullion and J. Schaefer, *Adv. Magn. Reson.*, **13**, 57 (1989)
- ¹¹ G. E. Hawkes, M. D. Mantle, K. D. Sales, S. Aime, R. Gobetto, and C. J. Groombridge, *J. Magn. Reson. A*, **116**, 251 (1995)
- ¹² A. Sebald, L. H. Merwin, T. Schaller, and W. Knöllner, *J. Magn. Reson.*, **96**, 159 (1992)
- ¹³ A. E. Derome, "Modern NMR Techniques for Chemistry Research," p158, Pergamon Press, Oxford, (1987)
- ¹⁴ U. Scheler, personal communication
- ¹⁵ H. P. Bai and R. K. Harris, *J. Magn. Reson.*, **96**, 24 (1992)
- ¹⁶ P. W. Reams, Ph. D. Thesis, University of Durham p.253 (1986)
- ¹⁷ J. A. González, G. A. Aucar, M. C. Ruiz de Azúa, and R. H. Contreras, *Int. J. Quantum. Chem.*, **61**, 823 (1997)

6 Difluorotin Compounds

The dialkyltin fluorides Me_2SnF_2 and ${}^n\text{Bu}_2\text{SnF}_2$ along with SnF_2 have been studied during the 1960s by spectroscopic and X-ray diffraction methods which led to tentative structural assignments, revisited both here and recently in the literature. Although the present solid-state NMR data support some of the earlier structural assignments for Me_2SnF_2 , the original structure proposed for ${}^n\text{Bu}_2\text{SnF}_2$ is in disagreement with the new NMR data presented in this chapter.

The organotin compounds studied in the previous chapter are well characterised by both NMR and other methods. By comparison, the difluorotin compounds are poorly characterised by NMR. This situation arises from the poor solubility of the dibutyl and dimethyltin difluoride compounds in common organic solvents. In addition, the structures in solution can be different to those in the solid state. The presence of two fluorine atoms gives the possibility of single- and double-bridging fluorine compounds, with the latter forming a chain or a planar polymeric structure.

Compared with the previous organotin compounds, these compounds are more difficult to study by solid-state NMR as the ${}^{119}\text{Sn}$ shielding anisotropy is large, and there is the potential for extensive ${}^{19}\text{F}$ - ${}^{19}\text{F}$ homonuclear dipolar broadening of the fluorine spectrum. These factors give spectra with a poorer signal-to-noise ratio and increased uncertainty in assignments and calculations.

The solid-state NMR data for SnF_2 and Me_2SnF_2 are discussed first, as the structures have been previously determined by XRD. This is followed by the evaluation of solid-state NMR data for ${}^n\text{Bu}_2\text{SnF}_2$, postulated to have the same structure as Me_2SnF_2 . Comparison of the solid-state NMR data for SnF_2 , Me_2SnF_2 and other compounds suggests that ${}^n\text{Bu}_2\text{SnF}_2$ has a structure with one bridging and one terminal fluorine. The chapter concludes with a summary and rationalisation of the ${}^{19}\text{F}$ NMR data for all the organotin compounds.



6.1 Tin (II) fluoride

Tin (II) fluoride, SnF_2 , is used in dentistry as a source of fluoride to reduce the acid solubility of dental enamel. SnF_2 is often present as a small component in toothpaste. The products of the reaction of SnF_2 with calcium hydroxyapatite, an approximation to dental enamel, have been studied by solid-state ^{19}F NMR.¹ Samples of SnF_2 have been found to vary in appearance, solubility and physical properties depending on their source. A standard method, with optimised reaction conditions, for making tin (II) fluoride from the reaction of tin (II) oxide with HF is well established.²

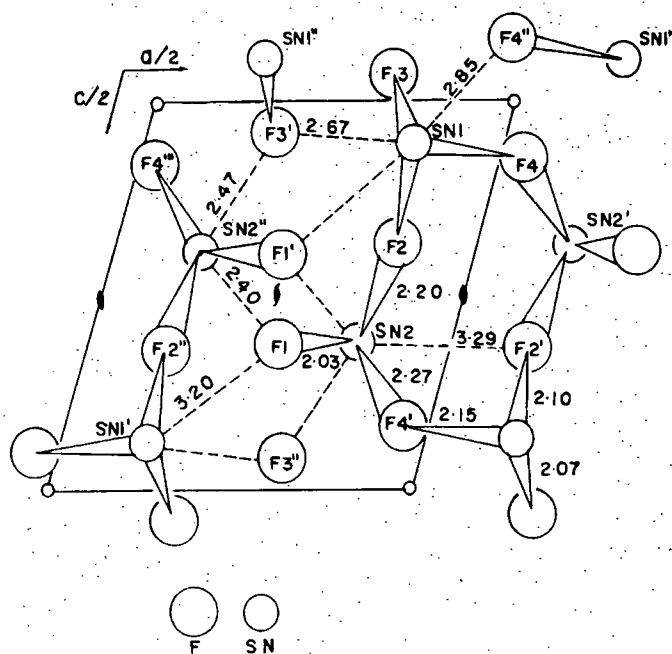


Figure 22: SnF_2 asymmetric unit, projected along the b axis (from Ref. 3)

Three crystal phases have been discovered for SnF_2 , with crystal structures determined for all three. The α form^{3,4} is stable up to 453 K and has been studied herein. The crystal structure is shown in Figure 22. SnF_2 forms Sn_4F_8 rings with both bridging and terminal fluorines. The tin atom is three coordinate and at the apex of a trigonal pyramid. It is presumed that the region above the apex is occupied by the non-bonding pair of 5s electrons.³ There are two types of tin and four types of fluorine atoms that are characterised by their bond lengths. SN1 has three strong and

three weak bonds to fluorine, whilst SN2 has one strong, four intermediate and one weak bond to fluorine. Weak bonds, taken to be longer than the sum of the ionic radii (2.27 Å), are labelled by dashed lines. Intermediate bonds are not distinguished from strong or weak bonds in the figure, but lie in the range 2.20 to 2.47 Å. From the fluorine-fluorine bond lengths, homonuclear dipolar interactions of up to 5.5 kHz are expected.

The β and γ forms have recently been identified and their structures determined by XRD.⁵ The γ form appears above 453 K and is stable until the melting point of 483 K. The β form is metastable and is formed by cooling the γ form below 339 K. In these phases, the structures have higher symmetry and fluorine atoms are more tightly bound to tin atoms.

With the absence of protons in the molecular structure, proton decoupling is not required for NMR experiments. A solid-state NMR proton spectrum was recorded to check for any impurities but showed nothing. Cross Polarisation (CP) from protons to fluorine had no effect as observed in the ^{19}F spectrum, as expected.

The ^{19}F MAS NMR spectrum shows a broad peak that breaks into dipolar-broadened spinning sidebands (ssb) at 17 kHz, and a sharp impurity peak. The presence of the broad peak is consistent with the crystal structure. With fast MAS ($\nu_r = 17$ kHz), the linewidth is narrowed from 22.5 kHz when static to 5 kHz. The broad peak is centred at $\delta = -45 \pm 3$ ppm. The error arises as the peak is broad and some time-domain signal has been lost at the start of the FID due to the receiver delay. The sharp impurity peak is more visible when the broad peak is removed. This has been achieved both by using a Hahn echo pulse sequence and by using the 'memory effect',⁶ which shifts the data to remove the first few points. Both methods rely on the rapid dephasing of the broad peak. The sharp peak has a shift $\delta = -112.5$ ppm and scalar coupling $^1J(\text{SnF}) = 1530$ or 1950 Hz for the two methods respectively. The extra data processing may affect the apparent splitting found by the latter method.

In a recent paper,⁷ the peak at $\delta = -112.5$ ppm has been identified as arising from solid SnF_2 , with a coupling constant $^1J(\text{SnF}) = 1660$ Hz. Two other broad peaks

near -50 ppm have neither been identified nor discussed. The paper does not mention whether an echo pulse sequence has been used, which would give the result as shown. For comparison, the ^{19}F MAS NMR spectrum of SnF_4 , from the same paper,⁷ shows broad peaks as would be expected from a homonuclear dipolar-broadened compound.

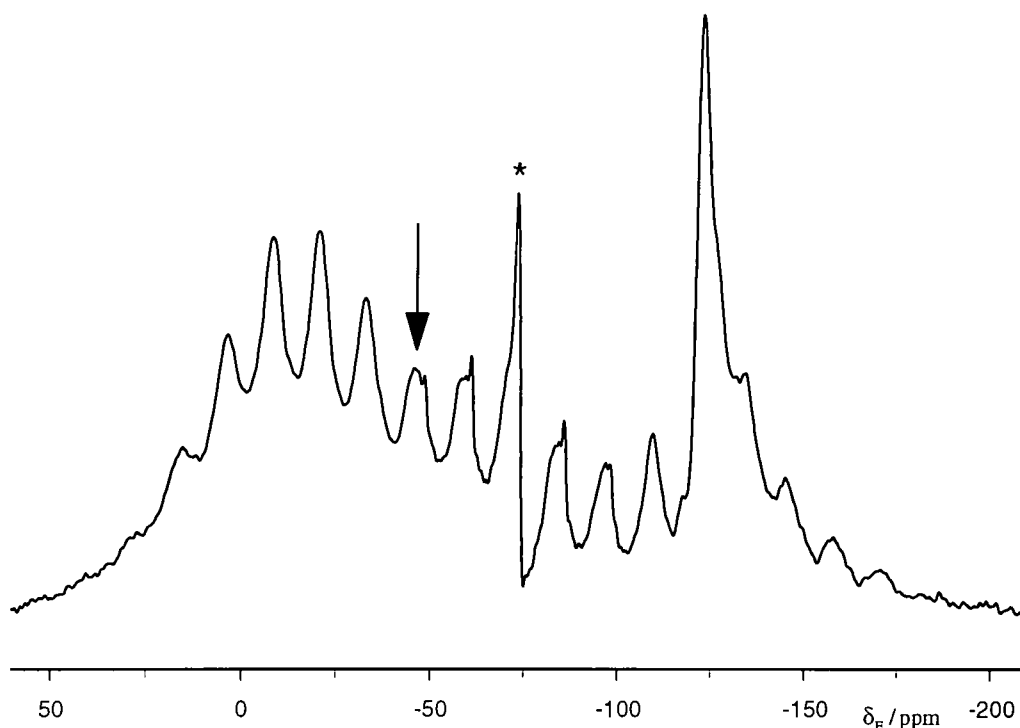


Figure 23: Quadrature detected ^{19}F MREV-8 CRAMP spectrum of SnF_2 with the sample spinning at 1107 Hz. Acquisition parameters were: pulse duration 1.56 μs , tau 3 μs , recycle delay 10 s, and number of acquisitions 16. The centrebanded is marked by an arrow and the quadrature glitch by an asterisk.

CRAMPS was used to remove the homonuclear dipolar broadening to first order. The quadrature-detected MREV-8 pulse sequence,⁸ allows a larger fluorine spectral width to be used compared to that without quadrature detection. The spectrum is shown in Figure 23, with the sample spinning slowly at 1107 Hz. This shows a set of spinning sidebands, the impurity including its satellite peaks, and the quadrature glitch (marked by an asterisk). The centrebanded is marked by an arrow. Spectra collected with spinning faster than 5 kHz reveal two possible peaks under the spinning-sideband manifold at $\delta = -45$ and -56 ppm. The spectrum was referenced

post acquisition, which may explain the difference in isotropic shift values between the CRAMP and the fast MAS data.

The ^{19}F shielding tensors of $\alpha\text{-SnF}_2$ have been determined previously from a high-resolution single crystal study.⁹ The spectra were acquired with multiple-pulse decoupling to remove the fluorine homonuclear dipolar coupling. This decoupling did not remove the heteronuclear Sn-F dipolar coupling, which broadens the lineshape. The tensors were assigned by the size of their anisotropy and their orientation relative to the local symmetry axis. Referencing was relative to C_6F_6 . The shifts have been corrected by -166.4 ppm to be relative to CFCl_3 . The bridging fluorines have a lower frequency isotropic shift ($\delta = -43.7$ and -44.9 ppm) and larger anisotropy ($\zeta = 140.2$ and 110.0 ppm respectively). The terminal fluorines have smaller anisotropies ($\zeta = 64.9$ and 70.7 ppm) as they are only bonded to one tin atom, and higher frequency isotropic shifts ($\delta = -30.6$ and -36.0 ppm). The asymmetry, $0.20 < \eta < 0.35$, is small as would be expected for nearly axial systems. The difference of about 15 ppm between the isotropic shifts of the two types of fluorine agrees well with the above CRAMPS measurements although the referencing differs slightly. In the above measurements, it was not possible to resolve all four fluorine signals. Only signals from the two different environments were observed.

As the ^{119}Sn signals were very weak, the $T_{1\rho}$ of fluorine was directly measured so that the optimum contact time for cross polarisation from fluorine to tin could be estimated. The signal decay under spin-locked conditions gives a short component of 3.2 ms for the broad peak and 175 ms for the sharp impurity peak. Assuming an average Sn-F cross relaxation parameter of 1 ms gives the best contact time of 2 ms.

The doubly-decoupled ^{119}Sn NMR spectrum, Figure 24, shows broad peaks covering the range from -500 ppm to -1600 ppm. As the spectral width used was large (500 kHz), the first 15 μs of the FID have been lost due to acquisition delay during probe ring-down time. The missing 7 points have been inserted into the FID and their intensity predicted by back linear prediction. From the crystal structure, two different ^{119}Sn NMR environments are expected. However, earlier data from

Mössbauer spectroscopy¹⁰ failed to resolve them. The spectrum was measured with the sample spinning at 5.5 kHz, CP from fluorine and fluorine decoupling. It shows two spinning-sideband manifolds (92 and 7 %) with large shielding anisotropies and a sharp impurity peak (1 %). The main spinning-sideband manifold has been analysed to give $\delta = -950$ ppm, $\zeta = 582$ (12) ppm and $\eta = 0.34$ (0.01). The values in brackets are the estimated errors from fitting whilst the errors in the measurement are expected to be larger than this. As some intensity has been lost from the outside ssb peaks, there is slight uncertainty in the assignment of the isotropic peak. Spinning the sample at slower speeds does not give the resolution necessary to separate the peaks and confirm the identity of the centreband. It is not possible to measure any scalar coupling constant in the proton decoupled spectrum, as the peaks are expected to be too broad and complex.

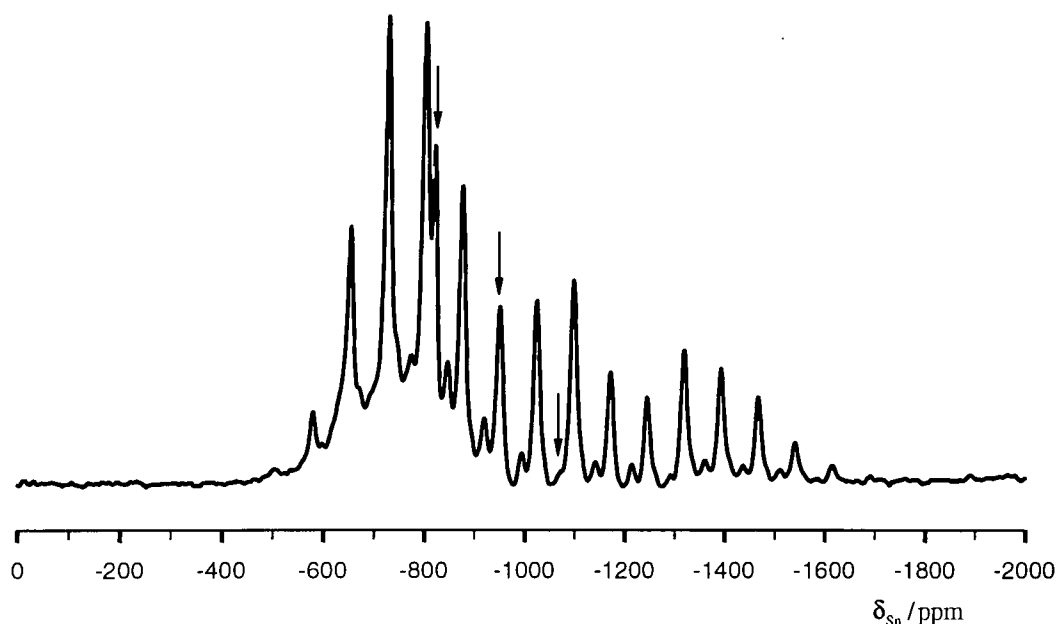


Figure 24: Tin-119 CPMAS spectrum of SnF_2 , obtained with spinning at 5.5 kHz and double (proton and fluorine) decoupling. Acquisition parameters were: ¹¹⁹Sn transmitter frequency 74.57 MHz (-1000 ppm), pulse duration 4.0 μs , contact time 2 ms, recycle delay 3 s, and number of acquisitions 7200. The three centreband peaks are marked by arrows.

The static ¹¹⁹Sn NMR spectrum shows a greater loss of signal intensity away from the transmitter position than the MAS spectrum. In both cases CP was used, the

efficiency of which decreases as the offset increases. Under MAS, the offset is a time average over the whole rotor cycle. This reduces the effective offset and reduces the loss of signal intensity away from the transmitter compared to the static case. With the static lineshape numerically corrected for this loss of intensity, the anisotropy was fitted to give $\zeta = 344$ (2) ppm and $\eta = 0.4$ (0.01). The static anisotropy is smaller than that found from the ssb fitting, implying that the lost intensity cannot be fully corrected by a numerical function.

The remaining two peaks are presumed to be impurities. The minor ssb manifold, has been analysed to give $\delta = -1070$ ppm, $\zeta = 555$ (5) ppm and $\eta = 0.00$ (0.06). The sharp peak at $\delta = -820$ ppm increases in relative intensity with a long contact time (10 ms). This long contact time would suggest that the sharp peaks seen in the ^{119}Sn and ^{19}F spectra may arise from the same impurity. The anisotropy is estimated to be less than 50 ppm from the lack of ssb peaks. A possibility for the second impurity is SnF_6^{2-} with a suitable counter ion e.g. K^+ . Potassium hexafluorostannate has a solid-state ^{119}Sn NMR shift of -810 ppm¹¹ and would be expected to have near cubic symmetry. Ammonium hexafluorostannate in water gives values of $\delta_{\text{F}} = -152.6$ ppm and $^1\text{J}(\text{SnF}) = 1625$ Hz.¹² These values are reasonably close to those observed for the impurity.

The original ^{119}Sn NMR spectrum was recorded with direct polarisation and without ^{19}F decoupling with the sample spinning at 4 kHz. It shows an apparent doublet splitting with peaks at $\delta = -825$ and -847 ppm. This arises from an unfortunate alignment of spinning sidebands from the sharp impurity and main ssb manifold. These peaks are still visible when the spectrum is decoupled, and the peak at $\delta = -847$ ppm shifts once the spinning speed is changed. The relaxation time for ^{119}Sn is $T_1 = 53 \pm 10$ s.

Solution-state ^{119}Sn NMR measurements give shifts at $\delta = -609$, -623 , -716 and -796 ppm for SnF_2 in the solvents HMPA, DMSO, methanol and H_2O respectively.^{11,13} The values from the latter two non-coordinating solvents have not been extrapolated to zero solvent concentration. They are closer to the solid-state shift compared to the values from the coordinating solvents, though they still differ by about 200 ppm.

6.2 Dimethyltin difluoride

Dimethyltin difluoride, Me_2SnF_2 , has a higher than expected melting point of 360°C , at which point it decomposes. This result indicates that there is strong intermolecular bonding and suggests that its structure is atypical compared to other diorganotin dihalides. For example, the dichloride, Me_2SnCl_2 , melts at 90°C .¹⁴ The Me_2SnF_2 structure has been characterised by XRD, IR and now solid-state NMR data.

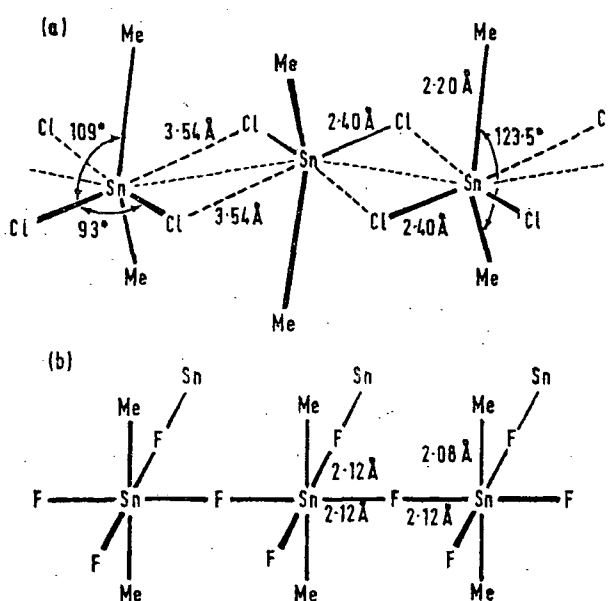
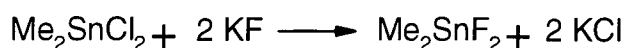


Figure 25: XRD structures of (a) Me_2SnCl_2 ¹⁶ and (b) Me_2SnF_2 ¹⁴ (the figure is taken from Ref. 16)

The single crystal XRD structure of Me_2SnF_2 ¹⁴ is shown in Figure 25. The structure shows an infinite, planar SnF_2 lattice with octahedral tin atoms connected by four bridging fluorine atoms. Each tin atom has two terminal methyl groups that lie above and below the plane of the bridging fluorine atoms. The structure is analogous to the structure of SnF_4 where the methyl groups are replaced by terminal fluorine atoms.¹⁵ From this type of structure, we expect to observe strong fluorine homonuclear dipolar interactions and little effect from the mobile methyl protons in the NMR spectra. The highly ionic nature of Me_2SnF_2 is seen with the Sn-C bonds,

which, at 2.08 Å, are shorter than the sum of covalent radii (2.17 Å). From consideration of the shorter bridging Sn-F bonds in SnF₄, cf. Me₂SnF₂, the formula may be written as Me₂Sn²⁺(F⁻)₂ compared to Sn⁴⁺(F⁻)₄. The dichloride forms a linear structure¹⁶ which results in much weaker overall bonding.

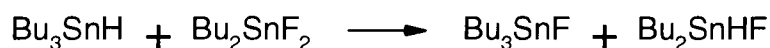
Organotin halides readily disproportionate in solution, a property which allows the synthesis of the difluoro compound from its dichloro counterpart as shown in Scheme 1.¹⁶



Scheme 1

The reaction was performed with addition of an ethanolic solution of Me₂SnCl₂ to aqueous KF. A white precipitate immediately formed. This was allowed to settle overnight before being separated on a filter and washed with ethanol. The solid was dried and used without further purification. A commercially available sample (Organometallics Inc., USA) has also been used. Both samples have been used for the solid-state NMR measurements. The differences in the NMR spectra between the samples come from the impurities present. The commercial sample contains the SnF₆²⁻ ion as an impurity.

The disproportionation of the n-butyl tin halide and hydride in equal molar quantities gives the mixed product shown in Scheme 2.¹⁷ With excess hydride, the reaction goes to completion.



Scheme 2

6.2.1 NMR data

In Me_2SnF_2 , the only protons belong to the methyl groups. These protons have a long T_1 relaxation time of 15 s at 200 MHz. The rapid methyl group rotation isolates the protons. The rotational motion of the methyl groups has been previously studied.¹⁸ In this work, data from solid-state proton NMR, heat capacity and neutron scattering results were compared. The NMR data showed that the correlation time is short and in the extreme narrowing condition. The correlation time follows the simple Arrhenius law and variable temperature measurements indicate a low activation energy barrier to rotation. Due to rapid rotation, the homonuclear dipolar coupling between protons is averaged and effectively reduced. The proton NMR lineshape can be seen to break into dipolar spinning sidebands at speeds above 5 kHz. This gives poor CP efficiency above this speed and means that proton decoupling, whilst observing another nucleus, will not narrow the lines significantly.

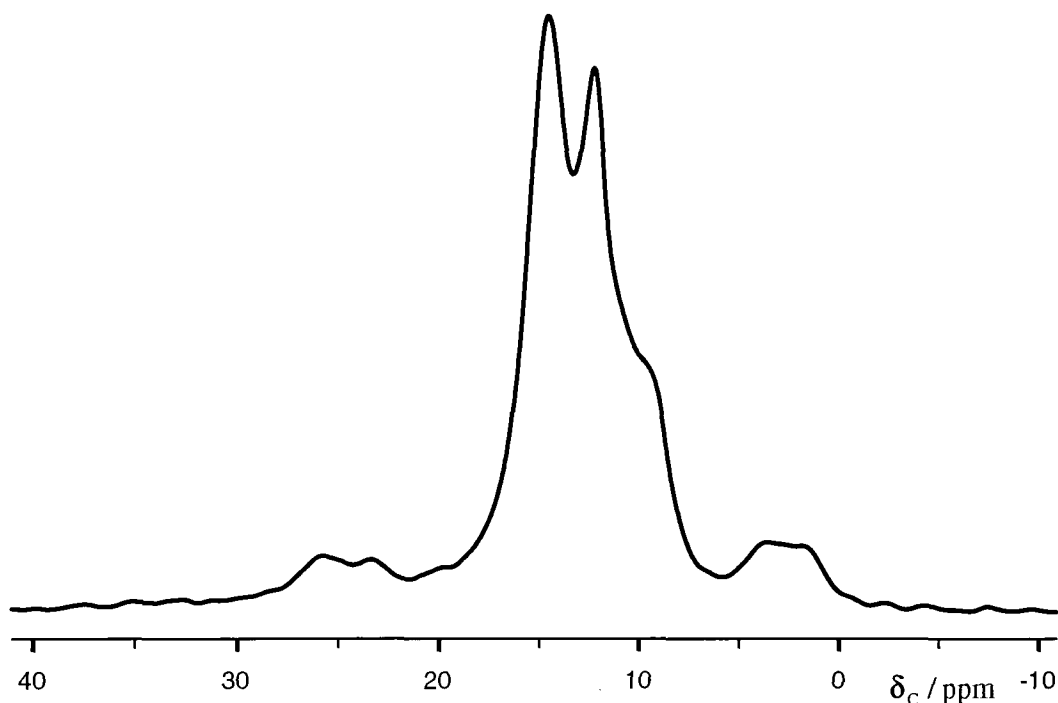


Figure 26: Carbon-13 CPMAS spectra of the Durham sample of Me_2SnF_2 , obtained with spinning at 3 kHz with proton and fluorine decoupling. Acquisition parameters were: pulse duration 5.0 μs , contact time 1 ms, recycle delay 30 s, and number of acquisitions 1912

The proton-decoupled carbon-13 spectrum of solid Me_2SnF_2 has a broad peak centred at $\delta = 13.0$ ppm. The linewidth at half-height is 400 Hz, which hinders the accurate determination of the scalar-coupled ^{119}Sn satellite peaks. By using high-power proton and fluorine decoupling, as seen in Figure 26, the linewidth narrows to 83 Hz. Major and minor peaks are visible at $\delta = 14.7$ and 12.4 ppm respectively. The shoulder to low frequency may be another peak of unknown origin. None of the peaks are close to the value of the starting material, Me_2SnCl_2 ($\delta = 27.0$ ppm).¹⁹ The ^{119}Sn satellite peaks are clearly visible from both peaks and give $^1\text{J}(\text{SnC}) = 1100 \pm 20$ Hz. It has not been possible to confirm whether one of the peaks is an impurity, or if the two methyl groups in Me_2SnF_2 are in slightly different environments. The spectra from both the Durham and commercial samples are the same.

A comparison has been made of the ^{13}C shifts and couplings from spectra of similar organotin compounds.¹⁹ The size of the $^1\text{J}(\text{SnC})$ coupling was found empirically to be related to the angle of the C-Sn-C bond, which in turn is related to the bonding and hybridisation at the tin centre. For the comparison, only mono-, di- and tri-methyl tin compounds were considered. In Me_2SnF_2 , the two methyl groups give a C-Sn-C angle of 180° and the $^1\text{J}(\text{SnC})$ coupling is expected to be around 1180 Hz, which is close to what is observed.

The fluorine MAS NMR spectrum of the commercial sample of Me_2SnF_2 is shown in Figure 27. Proton decoupling had no effect on the spectrum except to reduce the signal-to-noise ratio. The ^{19}F NMR spectrum measured with no proton decoupling shows four main peaks at $\delta = -132.4, -135.3, -150.1$ and -159.9 ppm. The first and second of these peaks have long and short relaxation times of 68 and 0.6 s respectively. The middle peak has only a small signal intensity, less than 10% of the total signal. This suggests that these peaks may result from unknown impurities except for the peak at $\delta = -150.1$ ppm. This signal may be from the SnF_6^{2-} ion which is observed as an impurity in the ^{119}Sn spectrum. For this peak, $T_1(^{19}\text{F}) = 5.7$ s.

This leaves the peak at -159.9 ppm with $T_1(^{19}\text{F}) = 16.5$ s as the probable signal from Me_2SnF_2 . This peak has some scalar-coupled satellite peaks with a

splitting of ${}^1J(\text{SnF}) = 1450 \pm 100$ Hz. A further low-frequency peak separated from the centreband by 1090 Hz could be a second set of satellite peaks with ${}^1J(\text{SnF}) = 2180$ Hz. If this were the case then the other satellite peak would be lost beneath the broad impurity signal. A second set of impurity peaks would not be expected from the crystal structure and the ${}^{119}\text{Sn}$ results given below. The SA is small ($\zeta < 40$ ppm) and gives no spinning sidebands with the sample spinning at 5 kHz (not shown). As direct polarisation was used, the broad ${}^{19}\text{F}$ probe background signal, centred at -75 ppm, also complicated the spectrum.

The features in this spectrum are unclear. Ideally, a wider range of one- and two-dimensional NMR experiments could be used to further understand this compound. However, such experiments would be complicated by the long recycle delays that are required and the large anisotropy observed in the ${}^{119}\text{Sn}$ NMR spectra (see below). For the ${}^{19}\text{F}$ spectrum measured in Figure 27, direct polarisation has been used as CP is ineffective. This requires long recycle delays to allow the ${}^{19}\text{F}$ nuclei to relax.

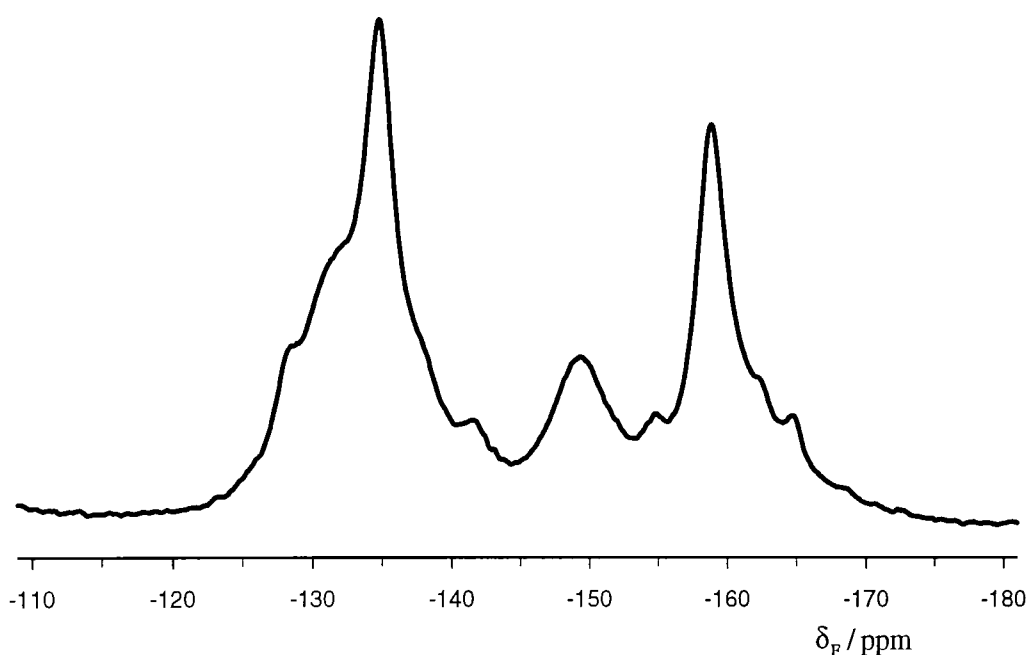


Figure 27: Fluorine-19 MAS spectra of the commercial sample of Me_2SnF_2 , obtained with direct polarisation, no proton decoupling and spinning at 10 kHz. Acquisition parameters were: pulse duration 3.0 μs , recycle delay 30 s, and number of acquisitions 128

The tin-119 CPMAS NMR spectrum of the Durham sample was measured on the HX probe (Figure 28(a)). The spinning sidebands are only just separated at 5 kHz due to the broad peaks arising from multiple coupling to fluorine. Cross polarisation from protons was more efficient than direct polarisation. For speeds above 5 kHz, the CP efficiency decreases rapidly, necessitating direct polarisation. Using the HFX probe to decouple both proton and fluorine gave much narrower lines and a better signal-to-noise ratio, as seen in Figure 28(b). The contact time and proton recycle delay were optimised to give the best contact time as 5 ms for a proton T_1 of 15 s. The ^{119}Sn relaxation time was measured as $T_1 = 34$ s. This was used to calculate pulses for the Ernst angle for fast MAS experiments recorded on the 300 MHz spectrometer.

From measuring the spectra for the commercial sample at different spinning speeds, on the 300 MHz spectrometer, the peak at $\delta = -164$ ppm was identified as the centreband. The fast spinning speeds, 11.00 and 9.46 kHz, meant that there were fewer spinning sidebands compared to the spectra shown in Figure 28. In these spectra, the transmitter was centred at -500 ppm and the spinning-sideband peaks were observed from 200 to -900 ppm. The scalar coupling to ^{19}F was not visible as it was comparable in size to the linewidth. The spectra were measured using direct excitation with pulses at the Ernst angle. A multiplet impurity peak is visible at ca. $\delta = -810$ ppm with $^1J(\text{SnF}) = 1600$ Hz, identified as the SnF_6^{2-} ion. As the spectra were not quantitative, it is only possible to estimate that the impurity is less than 10 % of the overall signal. This impurity was not observed in the spectra shown in Figure 28, either because it was not present in the Durham sample, or because CP from protons was used and the impurity may be proton free. Despite a long acquisition time, the signal-to-noise ratio was poor and some low-frequency peaks were expected to be lost in the noise. The best fit of the spinning-sideband data, without correction, gave $\zeta = 635$ (7) ppm and $\eta = 0.30$ (0.01).

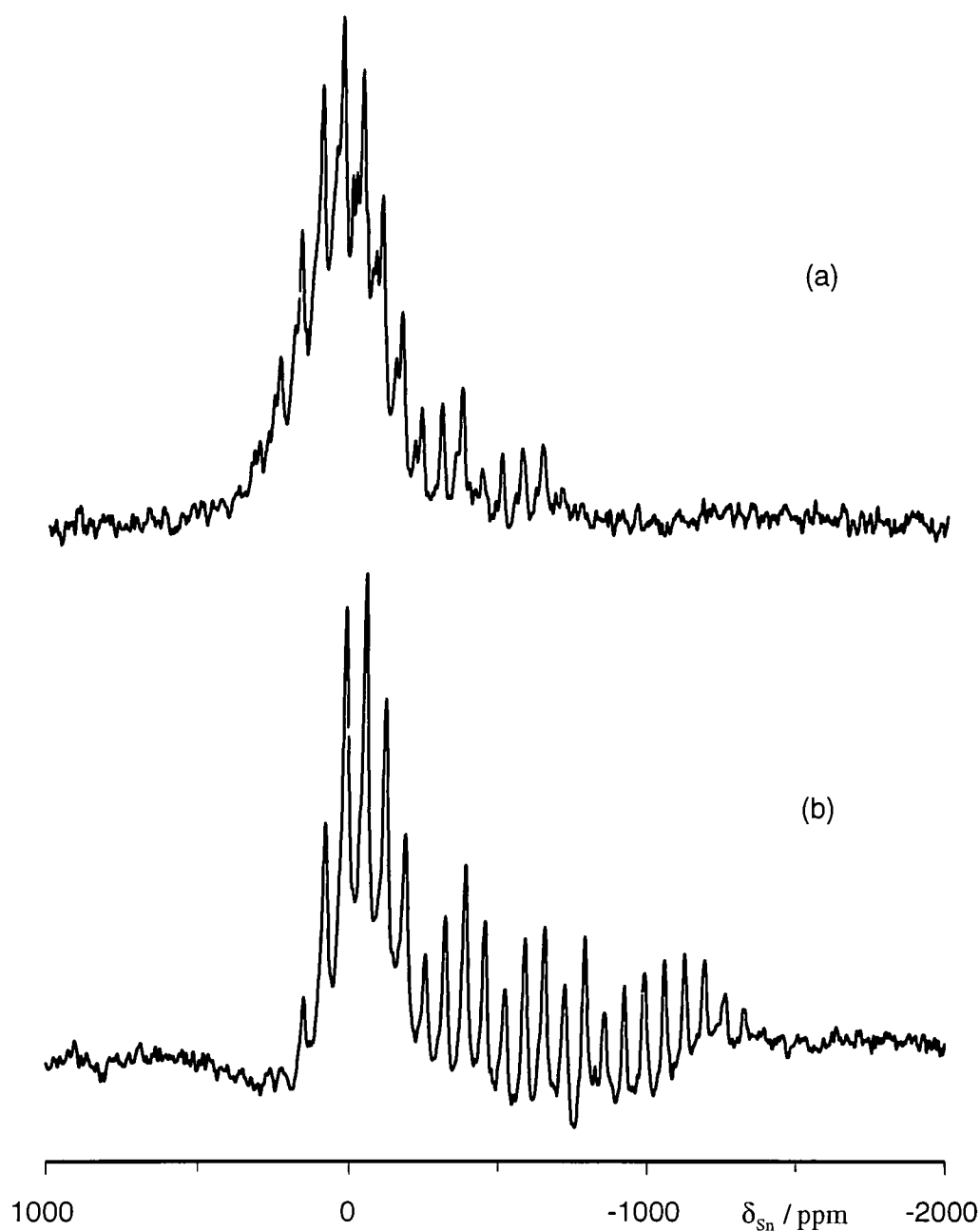


Figure 28: Tin-119 CPMAS spectra of Me_2SnF_2 , obtained with spinning at 5 kHz together with (a) proton decoupling and (b) proton and fluorine decoupling. Acquisition parameters were: (a) transmitter at 74.63 MHz (0 ppm), pulse duration 4.3 μs , contact time 5 ms, recycle delay 20 s, and number of acquisitions 500; (b) transmitter at 74.56 MHz (-1000 ppm), pulse duration 4.5 μs , contact time (arrayed) 1, 2, 5 and 10 ms, recycle delay 15 s, and number of acquisitions per slice 1320. The spectrum shown is obtained from a sum of the four arrayed FIDs.

The spectrum measured on the HFX probe, Figure 28(b), covers a range from 300 to -1300 ppm, with much of the intensity near to 0 ppm. The large spectral width accentuates any loss of data at the start of the FID due to probe ring-down time and gives the spectrum a rolling baseline. This rolling baseline has been corrected by using back linear prediction to estimate the lost initial points of the FID. This processing can introduce slight errors in measuring the shifts. Due to the already poor signal-to-noise ratio of the spectra, an echo pulse sequence was not used.

With the wide spectral width, signal intensity can be lost at the edges of the spectrum. This would reduce the intensity from the outer spinning sidebands and give a smaller fitted value for the SA than expected. The effect was particularly noticeable for Figure 28(a) where the transmitter is centred at 0 ppm and much of the signal intensity beyond 600 ppm has been lost. A spectrum of the commercial sample measured on the HX probe using direct polarisation at the Ernst angle is the same as that shown in Figure 28(a), showing that the loss of intensity is due to the probe and not CP. This also confirms that both the commercial and Durham samples give similar spectra, excepting the impurities. The tuning range for the X channel of the HX probe is small. A wider overall tuning range is achieved by changing capacitors in the probe. This small tuning range contributes to the high Q value of the HX probe which is three times larger than that for the HFX probe and explains the significant losses in signal intensity observed with offset on the HX probe. The practical spectral width on this probe is estimated as 1200 ppm (180 kHz). The spectrum recorded on the HFX probe, with the transmitter centred at -1000 ppm, appears less affected by probe losses. However, a moment analysis using the centreband as found above shows that intensity has been lost at the high frequency end of the spectrum. Before the centreband was assigned by variable spinning speed measurements, it had been estimated to be ca. $\delta = -390$ ppm!

The best fit of the doubly decoupled spinning-sideband data, without correction, gives $\zeta = 898$ (28) ppm and $\eta = 0.64$ (0.01). With the centreband erroneously at $\delta = -390$ ppm, the same calculation gives $\zeta = 883$ (16) ppm and $\eta = 0.20$ (0.01). It is worth noting that for these two results, the anisotropy is the same within the fitting error, but the asymmetry is different. Assuming a high

symmetry structure, the asymmetry would be expected to be zero. The difference can be explained by a combination of distortions in the molecule that reduce the symmetry, errors in fitting spinning sidebands with small values of the asymmetry and signal losses.

The static proton decoupled ^{119}Sn spectrum, recorded with an echo and proton decoupling, shows signal intensity from ca. 200 to -900 ppm. The transmitter was centred at -400 ppm, which may explain why the signal is reduced at low frequency. However, no signal was observed beyond 200 ppm, contrary to the SA tensor predicted from the HFX measurement. This predicted the shift tensor components to be 572, -2 and -1062 ppm. In this case, either the anisotropy or asymmetry are smaller than predicted from the ssb data. For the spectrum recorded on the 300 MHz system, the shift tensor components are 247, 60 and -800 ppm. Again, this last value is too small when compared with the static spectrum. In conclusion, it is hard to measure the SA for this compound due to its large size and the long recycle delay required. The shielding tensor would be expected to lie with $\zeta = 635$ to 898 ppm and $\eta = 0.30$ to 0.64. These are the limiting values, with the actual values expected to lie nearer to the average of these values i.e. $\zeta = 770$ ppm and $\eta = 0.47$.

Although the fluorine decoupling simplifies the spectrum, information about the SnF scalar coupling is lost. A binomial pentet is expected from four equivalent fluorines with the intensity ratio 1:4:6:4:1. This feature would be observed in the solid state at infinite spinning speed. However, the spinning speeds that are obtainable are only a small fraction of the magnitude of the anisotropy. This situation will give spinning sidebands that will have the pentet coupling structure but whose intensities will be dependent on both the binomial distribution and the effective anisotropy for each combination of fluorine spins. The outer peaks of the pentet is expected to be obscured by the background noise leaving the inner three peaks visible.

It was not possible to measure the $^1\text{J}(\text{SnF})$ coupling from the initial proton decoupled ^{119}Sn NMR spectra. For this reason, consideration of the ssb linewidths

with various decoupling schemes has been used to estimate the size of the $^1J(\text{SnF})$ coupling. Of these decoupling schemes, Lee-Goldburg decoupling removes the homonuclear dipolar and scalar couplings but retains the heteronuclear couplings albeit scaled by a factor of $\sqrt{3}$. The theory and background to this technique is given in section 6.2.1.1. An advantage of this technique is that it scales the heteronuclear scalar coupling so that the overall linewidth of each ssb is reduced. The linewidths for different decoupling schemes are given in Table 17.

Table 17: ^{119}Sn NMR linewidth observed for $^n\text{Bu}_2\text{SnF}_2$ with different decoupling schemes.

Decoupling	$\nu_{1/2}$ / Hz	Leaves
$^1\text{H}, ^{19}\text{F}$	1500	-
^{19}F	2550	^1H
^{19}F (Lee-Goldburg)	4000	^1H , scaled ^{19}F
^1H	5300	^{19}F
None (extrapolated)	6500	$^1\text{H}, ^{19}\text{F}$

It can be seen that proton decoupling only narrows the lines slightly. For the Lee-Goldburg fluorine decoupling, no proton decoupling has been used. The difference between the fully and partially ^{19}F decoupled linewidths should come only from the scaled J coupling. If it is assumed that only the three central peaks of the pentet make up this linewidth then this leads to an estimated coupling $^1J(\text{SnF}) = 1250$ Hz, though with a sizeable error.

The spectrum in Figure 28(a) was recorded after the above analysis had been completed. In this, the three main peaks of the multiplet are visible, though the low frequency peak is less intense than the high frequency one. The effective anisotropy for the low-frequency peak is larger, as would be expected for a negative value for D' and a positive anisotropy. This situation gives more spinning sidebands whose intensity far from the transmitter frequency has been lost. The same trend is observed when summing up all the spinning sidebands to give a spectrum with an effectively infinite spinning speed. It is possible to measure the scalar coupling as

$^1J(\text{SnF}) = 1410 \pm 30$ Hz. This analysis shows that the $^1J(\text{SnF})$ value determined above from linewidth considerations is reasonable considering the approximations that were made. The extra peak near 0 ppm arises from a small DC offset of the FID.

6.2.1.1 Lee-Goldburg decoupling

When the transmitter is placed off resonance, the spins precess about an axis which is inclined to the transmitter axis. When the offset, ΔLG , is chosen such that $\Delta LG = \omega_I / \sqrt{2}$, then the rotating frame precesses at the magic angle to the static field B_0 . This cancels out the first two terms in the homonuclear dipolar expansion, which dominate the line broadening. For precession about the magic angle, the chemical shift, heteronuclear dipolar and heteronuclear scalar couplings are scaled by $\sqrt{3}$.

Lee and Goldburg²⁰ suggested using this as a decoupling technique with MAS for heteronuclear spectroscopy. It has subsequently been shown that switching the frequency and phase of the transmitter once the magnetisation has precessed by 2π significantly improves the efficiency of decoupling.²¹ This technique has been abbreviated to FS-LG and has been used to give the heteronuclear-correlated spectrum for L-tyrosine with homonuclear proton decoupling.²² Upon moving to two dimensions and using homonuclear decoupling, the peaks are spread out further allowing the correlations to be clearly seen.

FS-LG decoupling has been tested using adamantane as a model compound. The aim was to find how sensitive the offset and 2π pulse width (or frequency-switching time) were to mis-setting. The simple LG sequence for off-resonance proton decoupling does narrow the ^{13}C lines, but the splittings are not clearly resolved. However, the decoupling sequence is still as effective, as assessed from the ^{13}C linewidth, when the offset is moved by ± 5 kHz from its optimum position. Using FS-LG decoupling gives much better proton homonuclear decoupling as observed in the ^{13}C spectrum. When fully optimised, the ^{13}C , ^1H multiplets are almost resolved down to the baseline. There are now two parameters to optimise and

the sensitivity to mis-setting is greater. Reasonable results are still obtained from mis-setting either the offset ± 3 kHz or the 2π pulse duration ± 0.5 μ s.

Constraining the adamantane sample in the HX probe rotor had a minimal effect. With a sample thickness of only 3 mm (cf. 11 mm normally), the peaks were shifted by -0.3 ppm. This was presumed to arise from the bulk magnetic susceptibility of the surrounding packing material. Spinning the sample faster than 2 kHz, whilst losing the CP efficiency, does narrow the lines further.

Although proton shifts cover a narrow range, fluorine shifts can cover a much wider range. Early NMR experiments used a single crystal of CaF_2 , as a model compound,²⁰ which is believed to have a ^{19}F NMR lineshape broadened almost exclusively by homonuclear dipolar broadening. The ^{19}F shielding is small and the natural abundance of ^{43}Ca is negligible (0.145 %). For Me_2SnF_2 the shielding anisotropy is also small. However, the static B_0 field is larger here than for the original experiments, so that in this case the offset dependence will be more important.

6.3 Di-n-butyltin difluoride

Based on IR and proton NMR studies it has been suggested over 35 years ago that di-n-butyltin difluoride, ${}^n\text{Bu}_2\text{SnF}_2$, exists with the same structure as Me_2SnF_2 .²³ With the advantage of multinuclear magnetic resonance, the structure assignment has been revisited. The next few sections aim to show that this compound does not form an extended 2D lattice and to suggest some alternative structures. The preparation of ${}^n\text{Bu}_2\text{SnF}_2$ has been described in reference 24.

6.3.1 NMR data

6.3.1.1 Carbon-13

The carbon spectrum recorded at 50.329 MHz with proton and fluorine decoupling and spinning at 3 kHz, Figure 29, shows five peaks at $\delta = 33.0, 28.8, 16.5, 15.9$ and 14.4 ppm. The peak at $\delta = 16.5$ ppm appears as a shoulder in this spectrum, but is observed as a separate peak in spectra recorded with the resonant frequency for ${}^{13}\text{C}$ equal to 75.49 and 150.99 MHz. The integrals found from the figure by deconvolution are approximately 1.1 : 2.0 : 0.25 : 0.86 : 0.43. Direct polarisation and a long recycle delay were used to try to minimise errors. However, there is still some overlap between peaks and they are not perfect gaussian lineshapes, as assumed in the deconvolution. The two high-frequency peaks are noticeably broadened, suggesting some restricted motion. In the proton decoupled spectrum, the peak at $\delta = 33.0$ ppm appears as a shoulder on the larger peak, which suggests that there may be some broadening from nearby fluorine atoms. A non-quaternary suppression pulse sequence was used to remove the two, broad, high-frequency peaks leaving the other three peaks.

It is hard to estimate the effect of the tin atom on the shift of the adjacent carbon atom. With Me_2SnF_2 , the observed ${}^{13}\text{C}$ NMR peak is not significantly different from that predicted for Me_2CF_2 . For a solid tri-n-butyltin compound containing no fluorine atoms, the carbon atom adjacent to the tin atom has a shift of

$\delta = 20$ ppm, with the ^{119}Sn satellite peaks clearly visible. However, the peaks in the ^{13}C NMR spectrum of $^n\text{Bu}_2\text{SnF}_2$ did not narrow sufficiently to observe ^{119}Sn satellite peaks when using ^{19}F decoupling, neither was there any peak visible around 20 ppm. Thus the peak at $\delta = 33.0$ ppm is tentatively assigned to the carbon adjacent to the tin atom. The methyl carbon signal will be one of the sharper peaks. The largest integral is for the peak at $\delta = 15.9$ ppm. The other sharp peaks are presumed to arise from unknown impurities. From these results, the shifts are tentatively assigned as:

Sn-	CH_2 -	CH_2 -	CH_2 -	CH_3
	33.0	28.8	28.8	15.9

The integrals agree reasonably well with this assignment considering the errors involved in their measurement.

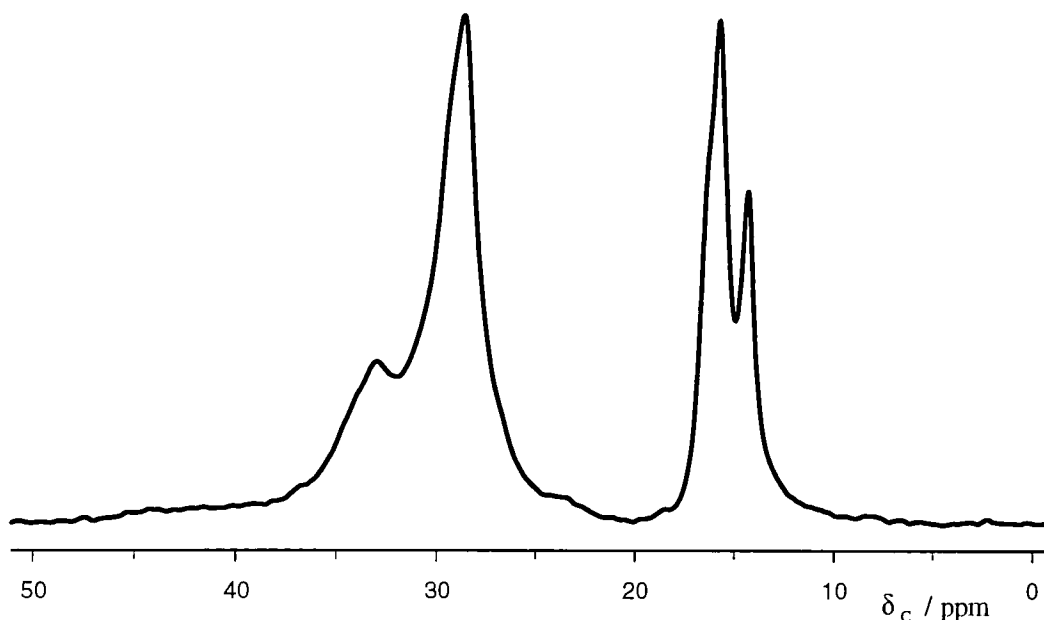


Figure 29: Carbon-13 MAS spectra of $^n\text{Bu}_2\text{SnF}_2$, obtained with spinning at 3 kHz with proton and fluorine decoupling. Acquisition parameters were: resonant frequency 50.329 MHz, pulse duration 5.0 μs , recycle delay 15 s, and number of acquisitions 2000

6.3.1.2 Fluorine-19

The ^{19}F CPMAS NMR spectrum is shown in Figure 30. The linewidth is similar to those for other organotin fluorides and much narrower than for SnF_2 . Experimental linewidths are shown in Table 18, the linewidth given for $^n\text{Bu}_2\text{SnF}_2$ is the final result after optimisation.

Table 18: Summary of ^{19}F NMR shifts and linewidths for the difluorotin compounds.

Compound	δ_{iso} /ppm	$\nu_{1/2}$ / kHz
SnF_2	-45, -56	4.8
$^n\text{Bu}_2\text{SnF}_2$	-107.8, -124.5	0.4
$^n\text{Bu}_3\text{SnF}$	-157.0	0.4
Me_2SnF_2	-159.9	0.5

The baseline resolution improved markedly upon restricting the sample in the rotor to the central 4 mm. Line broadening with a fully packed sample (11 mm) is caused by B_1 inhomogeneity across the sample volume resulting in variations in the Bloch-Siegert shift from different decoupling field strengths. Restricting the sample to the central 4 mm using extra spacers was found to be optimum.²⁵ Checking the setting of the magic angle and using TPPM decoupling narrowed the linewidths further, in this case by 80 Hz.

The ^{19}F shift values given above exclude the peak at $\delta = -138.5$ ppm, believed to be an impurity (indicated by an asterisk in Figure 30). This peak is broader than the other two and has a shorter $T_{1\rho}$. The measured fluorine $T_{1\rho}$ values for the peaks were 15.5, 10.9, and 0.9 ms for the peaks at $\delta = -107.8$, -124.5 , and -138.5 ppm respectively. The sample was thought to be air sensitive so a new sample was purchased and a rotor was packed under N_2 in a glove box. The spectrum observed was the same as for the old sample, which implies that this compound is not particularly air sensitive. No further explanation can be given for what the impurity is.

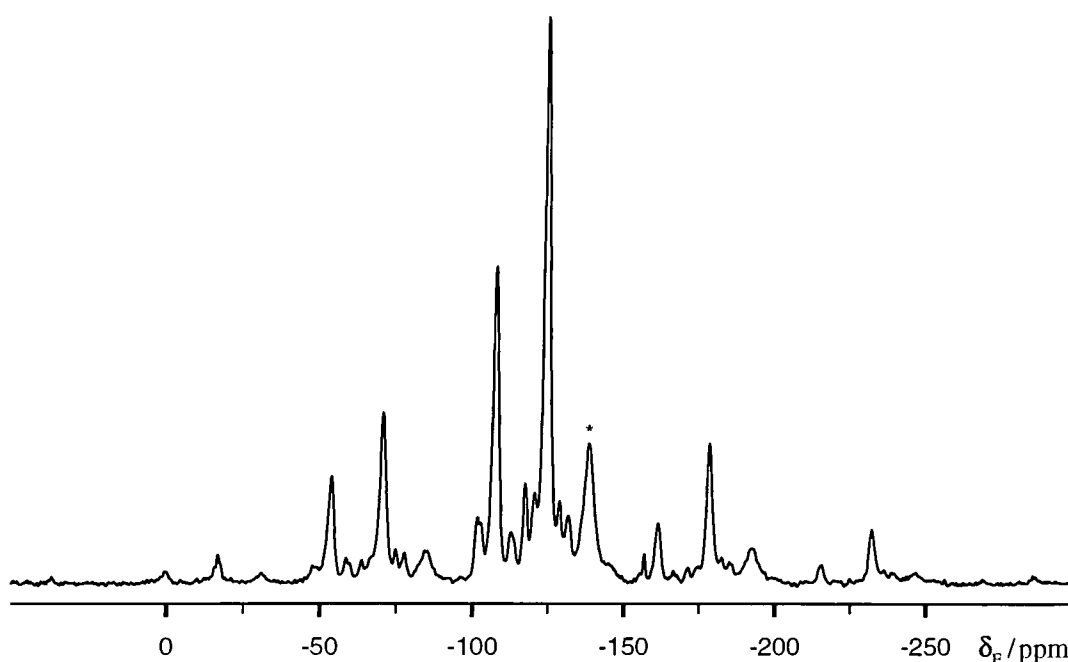


Figure 30: Fluorine CPMAS NMR spectrum of ${}^n\text{Bu}_2\text{SnF}_2$ with the sample spinning at 10 kHz and TPPM proton decoupling. Acquisition parameters were: pulse duration 2.25 μs , contact time 1 ms, recycle delay 10 s, number of acquisitions 1000. The asterisk marks the impurity peak.

With the improved resolution, multiple tin satellite peaks are visible. For $\delta = -107.8$ ppm, ${}^1J(\text{SnF}) = 2055$ Hz with the satellite peaks further split into two peaks separated by 200 Hz (origin unknown). The peak at $\delta = -124.5$ ppm, thought to arise from bridging fluorines, has two sets of satellite peaks visible with ${}^1J(\text{SnF}) = 2644$ and 1470 Hz. All the couplings have an estimated error of ± 20 Hz. As the coupling is seen as satellite peaks, it is possible that an equivalent bridging fluorine will couple differently to the two tin atoms with only one of the splittings visible. The two coupling values suggest that the bridging is uneven with strong and weak Sn-F bonds. Thus, the high-frequency peak arises from a terminal fluorine. It is interesting to note that one of the bridging scalar coupling constants is larger than the value for the terminal scalar coupling constant. A theoretical discussion of the coupling constants is found below.

For MAS speeds of 5 kHz, the different ssb manifolds overlap and prevent analysis, whereas at 10 kHz, the ssb manifolds are separated. For the terminal fluorine, $\zeta = 96.4$ (1.2) ppm and $\eta = 0.22$ (0.07). A relatively symmetrical tensor

would be expected for a terminal fluorine. The bridging fluorine has a more asymmetrical SA tensor with $\zeta = 93.6$ (1.4) ppm and $\eta = 0.69$ (0.01). The impurity peak has the opposite sign for the anisotropy with $\zeta = -85.6$ (1.4) ppm and $\eta = 0.64$ (0.01). The pseudo-static lineshapes from a Tycko 2D experiment²⁶ are in agreement with the values given above. A MAT experiment was not attempted, as the resolution was not expected to be sufficient to resolve the tin satellites at the slow spinning speeds. Were this possible, it would have been possible to measure the effective shielding anisotropies of the satellite peaks.

The resolution of the ^{119}Sn satellite peaks allows an approximate ssb analysis of these to be made. Individual fits of these satellite ssb manifolds have large errors as the measured intensities are weak and there are few spinning sidebands to measure. A triple fit assuming colinearity between the shielding and dipolar tensors gives a poor fit so a non-colinear triple fit has been used. This gives a value of $D' = -5072$ Hz for the terminal fluorine, -6800 and -4727 Hz for the outer and inner satellite peaks of the bridging fluorines respectively. The error in these measurements is large, perhaps 1000 Hz. Calculation of ΔJ will be discussed in section 6.3.1.4 once estimates for the bond length have been presented.

The intensity ratio of the peaks is 1 : 2 : 0.5, the latter being the broad impurity. The usual precautions relating to relaxation have been taken to make the integrals as accurate as possible. There is no explanation as to why the bridging fluorine integral should be twice the size of the terminal fluorine. At temperatures below -140 °C, the bridging fluorine signal splits into two peaks. This may be due to two crystallographically inequivalent sites. Differential Scanning Calorimetry (DSC) shows no sign of a phase transition down to -100 °C. The resolution of the VT spectra was insufficient to tell whether the two sets of ^{119}Sn satellite peaks seen at room temperature are associated with a particular peak at low temperature. It is noted that the sample was not confined to the centre of the rotor and so may suffer from low resolution.

An ideal method to confirm which ^{19}F NMR peaks correspond to those in the ^{119}Sn spectrum would be to measure a 2D HETCOR spectrum. Cross polarisation from ^{19}F to ^{119}Sn gives a good signal for short contact times. A disadvantage of using

the HFX probe is that it cannot spin samples at speeds above 6 kHz. At 6kHz, the peaks in the indirect fluorine dimension overlap. The 2D spectrum recorded showed cross peaks at multiples of the spinning speed, but there was insufficient resolution within each cross peak to observe the individual peaks. An indirect method of checking the correlations is to measure the $^{19}\text{F} \rightarrow ^{119}\text{Sn}$ CP build-up curve. This build-up curve was measured using double decoupling and measuring the total signal intensity. The best fit gives $T_{\text{FH}} = 0.2$ ms and $T_{1\rho}(^{19}\text{F}) = 5$ ms. As there is no component with a very rapid decay, i.e. short $T_{1\rho}$, the impurity peak does not contribute to the ^{119}Sn spectrum and cannot be an organotin fluoride.

6.3.1.3 Tin-119

The ^{119}Sn NMR spectra were interpreted before the well-resolved fluorine spectra were measured. The proton decoupled ^{119}Sn CPMAS NMR spectrum shown in Figure 31 was recorded at 111.83 MHz with the sample spinning at 9.64 kHz. In this spectrum, each ssb appears as a multiplet arising from scalar coupling to the three fluorine atoms. There are two bridging fluorines with different Sn-F bond lengths. At this fast spinning speed, the spinning sidebands are just separated. The spinning sidebands extend over a wide range, similar to Me_2SnF_2 . The coupling was initially interpreted as being a triplet of doublets with $^1J(\text{SnF}) = 2539$ (t) and 1514 (d) Hz, taking the two bridging fluorines to have identical J couplings to ^{119}Sn . The signal-to-noise ratio of the spectrum was poor owing to the signal being spread over a large number of spinning sidebands.

Double decoupling of both proton and fluorine gives a clear spectrum but loses the coupling information. The centreband was found by measuring spectra with varying spinning speeds to give $\delta = -400$ ppm. The anisotropy was measured by fitting as $\zeta = 891$ (12) ppm and $\eta = 0.19$ (0.01). This SA is larger than that for Me_2SnF_2 . This result is surprising as the tin atom in Me_2SnF_2 is six coordinate whereas that in $^n\text{Bu}_2\text{SnF}_2$ appears to be five coordinate from the ^{19}F NMR evidence. However, Me_2SnF_2 has a fourth bridging fluorine atom and the structure may have

high symmetry. The isotropic shift values are also in the reverse order to that which would be expected from consideration of the coordination number alone.

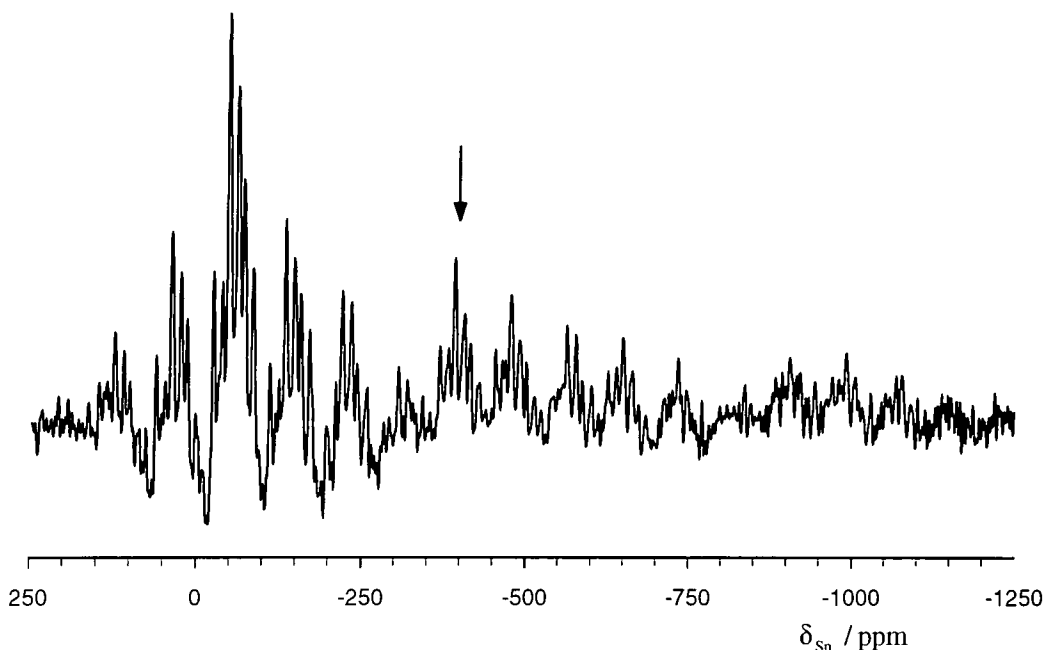


Figure 31: Proton decoupled ^{119}Sn spectrum of ${}^n\text{Bu}_2\text{SnF}_2$ recorded using CP with the sample spinning at 9.64 kHz. The frequency of ^{119}Sn was 111.83 MHz. Other parameters were: pulse duration 5 μs , contact time 5 ms, recycle delay 2 s, number of acquisitions 39,000.

The proton and fluorine doubly-decoupled static ^{119}Sn NMR spectrum, measured at 74.63 MHz, is shown in Figure 32 along with a simulated lineshape from the fitted ssb data. The figure clearly shows the loss of signal intensity from CP and probe tuning losses. The arrow marks the position of the transmitter. An experiment using a range of transmitter positions showed that much of the signal loss is due to the offset from the transmitter and not the probe tuning profile, which was left unchanged.

From the proposed structure for ${}^n\text{Bu}_2\text{SnF}_2$, it is expected to have approximate C_{2v} local symmetry at the tin centre. From an approximate Gaussian 94 calculation, or point charge considerations, the σ_{33} component of the ^{119}Sn shielding tensor would be expected to lie perpendicular to the plane containing both bridging and terminal fluorine atoms. This would make the D' and the SA tensors non-colinear for

both fluorine atoms. Though the values for the effective SA can be predicted, the difference in the size of ζ^{eff} and ζ is too small to be accurately measured.

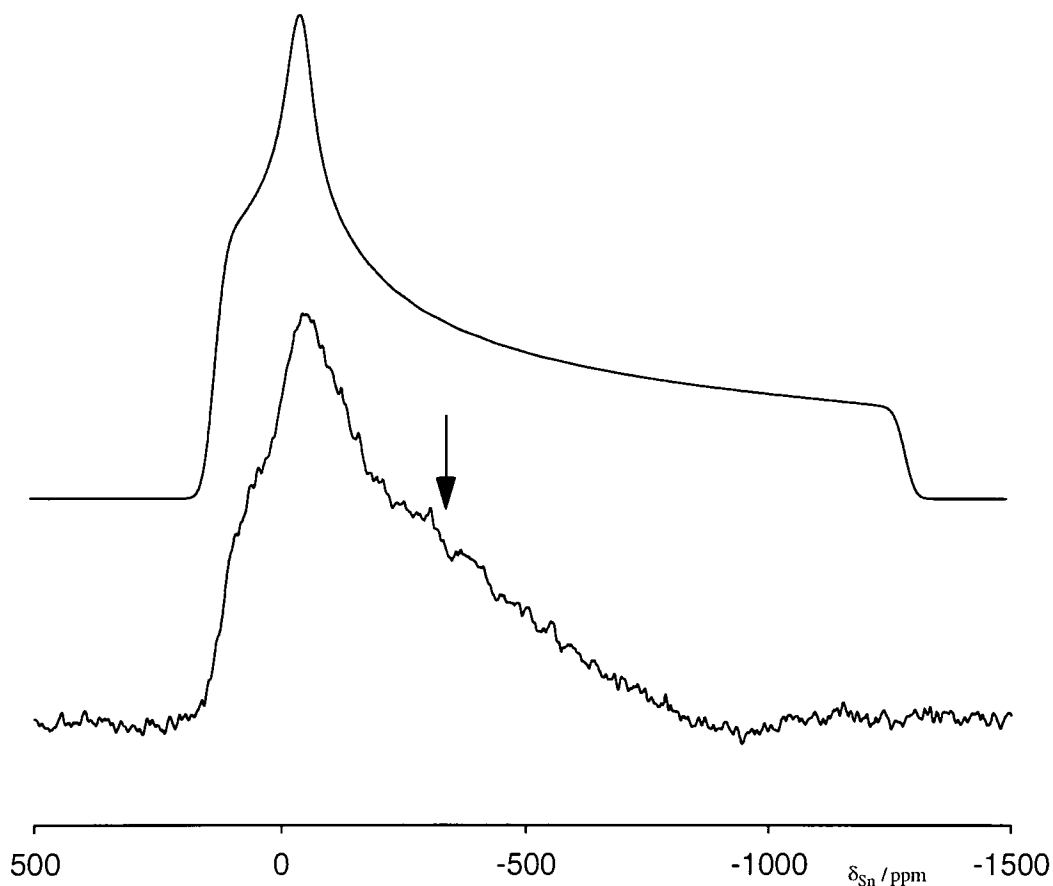


Figure 32: Doubly-decoupled static ^{119}Sn spectrum of ${}^n\text{Bu}_2\text{SnF}_2$ recorded using CP and a quad echo with a simulation using the parameters given in the text. The arrow marks the position of the transmitter (-300 ppm). Other parameters were: pulse duration 4.5 μs , contact time 2 ms, echo time τ 10 μs , recycle delay 3 s, number of acquisitions 18,000, exponential line broadening 500 Hz.

It is hard to reconcile the different coupling information that is available from the ^{119}Sn and ^{19}F NMR spectra. The ^{19}F MAS NMR spectrum is much clearer and free of noise compared to the ^{119}Sn spectrum. In addition, the ^{119}Sn MAS NMR spectrum has many spinning sidebands. It is only possible to discuss relative intensities within the coupling multiplet if all the intensity in these spinning sidebands were correctly measured and these were then summed together to give a spectrum at effectively infinite spinning speed. The central peaks within the multiplet

appear to have greater intensity than the outer ones, which could support the idea of a triplet splitting. From the $^1J(\text{SnF})$ coupling constants found from the ^{19}F NMR spectrum, the multiplet pattern in the ^{119}Sn spectrum can be calculated. This gives differences between the experimental and calculated peaks of between 160 and 350 Hz. The overall ssb peak width is in broad agreement. The linewidth in the double-decoupled ^{119}Sn NMR spectrum is 1100 Hz, so the accuracy of measuring the splittings in the ^{119}Sn spectra is much lower and hence the ^{19}F values are more accurate.

6.3.1.4 Theoretical calculations of the scalar coupling

Calculating NMR properties for polymeric organotin fluorides is prone to large errors due to the approximations made within the calculation. Previously, scalar coupling in Me_3SnF has been examined on a molecular basis relevant to the solid.²⁷ Semi-empirical AM1 parameters were used and the experimental and theoretical results agreed well. The theoretically-calculated values were $^1J(\text{SnF}) = 1182$ Hz (1300 Hz) and $\Delta^1J(\text{SnF}) = -1770$ Hz (-720 Hz), with experimental values given in brackets. The theoretical calculations were based on the optimised gas-phase geometry, which may differ from the experimental geometry. Furthermore, the calculated value for the scalar coupling is very sensitive to the geometry used. The errors in measuring Δ^1J are large, so this agreement between experiment and theory is reasonable.

The calculations were performed by Aucar and González in Argentina based on the experimental NMR measurements recorded in Durham. A wide range of different structures have been studied, with the results summarised in Figure 34. The compound has been approximated by the trimer, $\text{H}_2\text{SnF}_2\text{-Me}_2\text{SnF}_2\text{-H}_2\text{SnF}_2$, shown in Figure 33 and as a linear polymer. For the linear polymer, a single Me_2SnF_2 unit is placed in a one-dimensional cell with given periodic boundary conditions that replicate on each side. The difference between experimental $^1J(\text{SnF})$ scalar coupling constants for $^n\text{Bu}_3\text{SnF}$ (1310 Hz) and Me_3SnF (1300 Hz) is small. In these compounds, the structure is expected to be very similar so there is little difference in

the values caused by changing the alkyl groups. Hence, the approximation of methyl groups in place of n-butyl groups is reasonable.

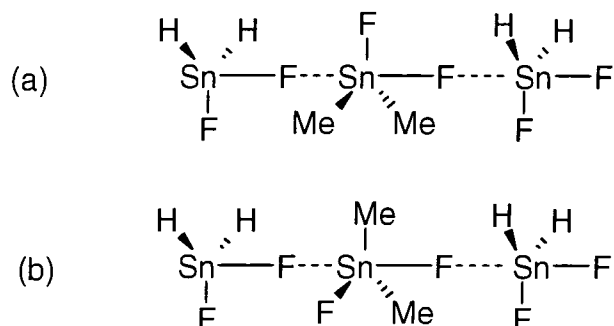


Figure 33: (a) Trans and (b) Gauche conformers of $\text{H}_2\text{SnF}_2\text{-Me}_2\text{SnF}_2\text{-H}_2\text{SnF}_2$ used in the calculations.

The model has assumed complete polymerisation. No simulations have included the effect of weak polymerisation and different bridging bond lengths. Some organotin compounds are known to have bent Sn-X-Sn bridges. This has also been ignored in these simulations. With the model structure for ${}^n\text{Bu}_2\text{SnF}_2$, one fluorine in each monomer unit will be in a terminal position. The energy difference between the gauche and trans conformers is small (20.8 kJ mol^{-1}) and favours the gauche conformation. The different conformers have each been optimised to give bridging bond lengths of 1.97 and 2.00 Å for the gauche and trans conformers respectively. The terminal Sn-F bond length is 1.90 Å in both cases. Intermolecular forces and crystal packing are expected to affect the geometry but have not been included in the modelling.

The effects of changing the bridging and terminal bond lengths, and varying angles have been studied. Results are described below:

- The results from treating the molecule as a linear polymer or a trimer are similar. As the trimer is easier to model, it has been used. This shows that local effects are more pronounced than long range effects.
- Calculations for the isolated Me_2SnF_2 molecule have quite different values for the scalar couplings from those found above and experimentally.

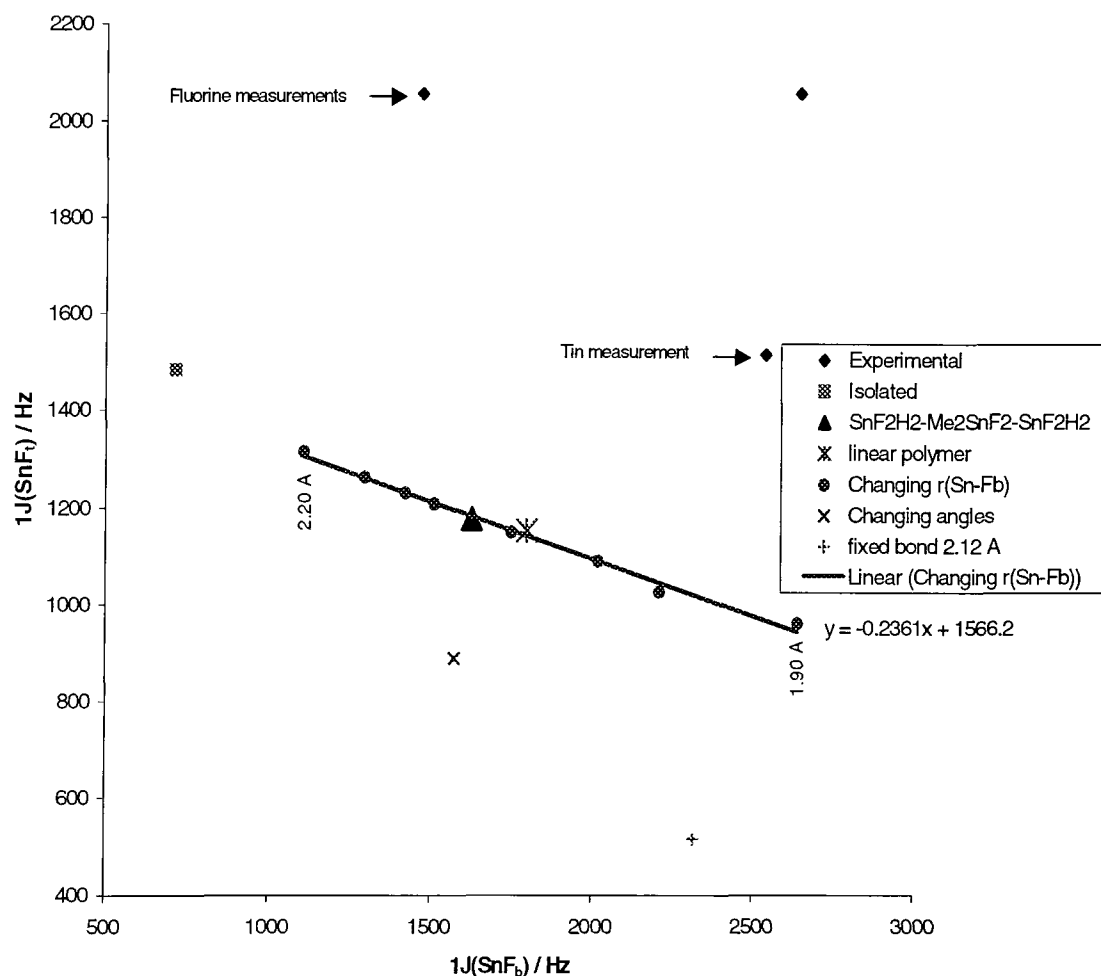


Figure 34: Graphical summary of the experimental data and calculations for the scalar coupling constants in ${}^n\text{Bu}_2\text{SnF}_2$ with various geometries as discussed in the text. Bridging Sn-F bond lengths are given for the ends of the linear fit.

- The calculated results show that the coupling constant for the bridging fluorines is larger than that for the terminal fluorine. This agrees with the experimental observations but seems to be counterintuitive. Analysis of the calculated values would be expected to give some explanation of the cause.
- The value for the scalar coupling is sensitive to changes in the bridging bond length, and insensitive to changes in the terminal bond length (not shown). A linear relation exists between the two values for the scalar coupling on changing the bond length. A similar linear relation exists

between the bridging bond length and the calculated scalar coupling to give:

$${}^1J(\text{SnF}_b) / \text{Hz} = -4973 * r_{\text{SnF}} / \text{\AA} + 11981$$

- Fixing the bond length and angles to be similar to the XRD structure of Me_2SnF_2 gives a strained structure and coupling values that lie far from the line. This point is labelled 'fixed bond'.

Although the model has not included the effect of weak polymerisation, the calculated values for ${}^1J(\text{SnF}_b)$ cover the range of experimentally observed values. Ignoring the value for the terminal coupling constant, it can be seen from the graph that the observed bridging coupling constants would correspond to bridging bond lengths of 1.90 and 2.10 \AA approximately. An example of a weak polymer is tricyclohexyltin fluoride, where bond lengths of 2.05 and 2.30 \AA were found from an XRD study.²⁸ It is unclear how different bridging bond lengths would affect the terminal fluorine bond length and scalar coupling constant.

As the XRD structure is unknown, the bond lengths can only be estimated. This estimate is made from comparison with XRD data from other organotin compounds, the optimised structures and the discussion from the theoretically calculated values for the scalar coupling.

The overall bond lengths predicted from the coupling data appear to be shorter than those found by XRD data or optimisation of the molecule. The theoretical scalar coupling data show that the difference in bridging Sn-F bond lengths, which is less prone to error than the absolute bond lengths, is 0.2 \AA . This gives the bridging Sn-F bond lengths as 2.00 and 2.20 \AA . The larger, bridging coupling constant is associated with the shorter bond length. The optimised terminal bond length is found to be around 1.90 \AA and has been used here. Table 19 summarises these data and the result of calculating ΔJ .

Table 19: Summary of the NMR data for ${}^{\text{m}}\text{Bu}_2\text{SnF}_2$ and predicted bond lengths used to calculate ΔJ .

	${}^1J(\text{SnF}) / \text{Hz}$	D' / Hz	$r_{\text{SnF}} / \text{\AA}$	D / Hz	$\Delta J / \text{Hz}$
F_t	2055	-5072	1.90	-6173	-3303
F_b	2644	-6800	2.00	-5293	4521
	1470	-4727	2.20	-3977	2250

The error in calculating ΔJ is large as there are large errors in the values of both D' and D . Here, the magnitude of ΔJ is roughly proportional to the size of ${}^1J(\text{SnF}_b)$. In the previous chapter no clear trend was observed. The trend for D' does not mirror the size of the Sn-F bond length as the values of ΔJ for the bridging fluorines are both positive. Previous values for other organotin fluorides have been negative.

6.3.2 Other techniques

6.3.2.1 Powder XRD

Powder X-ray diffraction has the potential to confirm the structure predictions given above. It has been used previously to find the space group and size of the unit cell for Ph_3SnF .²⁹ For ${}^{\text{m}}\text{Bu}_2\text{SnF}_2$ strong reflections, presumably from the tin atoms, are visible up to 50° . The reflections correspond to d-spacings and could in theory be used to find the unit cell. No structure refinement has been made at present as similar structures that could be used as starting points are not known.

6.3.2.2 Infrared (IR)

The IR spectrum for ${}^{\text{m}}\text{Bu}_2\text{SnF}_2$ was measured. Measurements from similar compounds³⁰ allow the prediction and assignment of the observed spectrum. The Sn- F_t stretch is derived from MeSnF_3 , which is believed to have one terminal and two bridging fluorines. This supports the assignment of the bonding conformation for

${}^n\text{Bu}_2\text{SnF}_2$ as a linear polymer with one bridging and one terminal fluorine. The rocking motion has a higher frequency, than predicted from similar compounds, indicating a stronger bond to the CH_2 group. The Sn-F_b stretch has not been measured here, though it would be expected to lie in the range 330 to 425 cm^{-1} and be broad. The peak splitting observed is thought to arise from vibrational coupling within the polymer. The peaks observed and their assignments are given in Table 20.

Table 20: Summary of IR measurements and assignments for ${}^n\text{Bu}_2\text{SnF}_2$.

Wavenumber / cm^{-1}		Type
Predicted	Observed	
550 s	-	SnC_3 symmetric Planar stretch
640 s	687, 643	Sn-F_t stretch
800 s	873, 885	Rocking motion
1216 w	1085, 1165	Symmetric deformation
1412 w	1465	Asymmetric deformation

6.3.3 Conclusions on the structure of ${}^n\text{Bu}_2\text{SnF}_2$

It has been shown by comparison of ${}^{19}\text{F}$ NMR spectra that ${}^n\text{Bu}_2\text{SnF}_2$ does not appear to have the extended 2D structure similar to Me_2SnF_2 . A bridging structure has been suggested as shown in Figure 35. The structure is similar to ${}^n\text{Bu}_3\text{SnF}$ but with one n-butyl group replaced by a fluorine atom and with bridging fluorines unsymmetrically placed between the tin atoms. This gives two different fluorine environments, bridging and terminal. These are observed, though with little shift difference between the two peaks. There are two possible polymer conformations, with the terminal fluorines either trans or gauche along the chain, which cannot be easily distinguished by NMR. The energy difference between the two conformations is smaller than the errors that arise from assumptions made in the calculation.

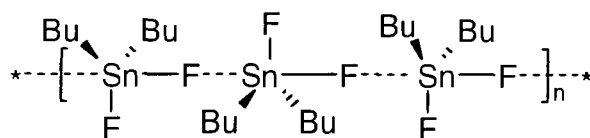


Figure 35: Proposed structure of ${}^n\text{Bu}_2\text{SnF}_2$, shown in the trans conformation.

Problems remain, which lead to some uncertainty. The scalar couplings in the ${}^{119}\text{Sn}$ NMR spectrum are still unclear. The ${}^{19}\text{F}$ NMR spectra have an unexplained impurity peak and a discrepancy of the integrals for the other two peaks. Calculations of the scalar couplings have given some insight into the system but they remain only qualitative. Ab initio calculations give too large an error for physical properties because the basis sets for tin become rapidly unmanageable and no account of relativistic effects is usually included.

Despite these reservations, assuming that the structure assignment is correct, approximate bond lengths have been derived from the NMR data. These can then be tested by other methods to improve on the results herein.

6.4 Summary of ^{19}F NMR data for the organotin fluorides

Much of the new work in this thesis has involved the measurement of ^{19}F NMR spectra. In the last two chapters measurements of the ^{19}F shifts of $^n\text{Bu}_3\text{SnF}$, Me_3SnF , $^n\text{Bu}_2\text{SnF}_2$ and Me_2SnF_2 have been given. In addition, the ^{19}F shifts of Me_3SnF , $^i\text{Bu}_3\text{SnF}$, Ph_3SnF and neo_3SnF (neo = neophyl, see Figure 36) have been recently reported.³¹ These shifts and other ^{19}F NMR data are collected in Table 21, along with the coordination number of the tin atom. The data for SnF_2 , SnF_4 , $(\text{NH}_4)_2\text{SnF}_6$ and $(\text{PhF}_2\text{PNMe})_2$ ³² are included for comparison.

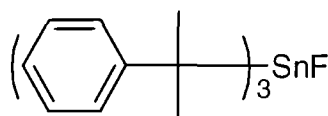


Figure 36: The structure of neo_3SnF

SnF_2 and $^n\text{Bu}_2\text{SnF}_2$ are the only compounds in Table 21 with two different fluorine environments. It can be seen that in both cases the terminal fluorine atom is ca. 15 ppm more deshielded than the bridging fluorine atom. For SnF_2 , where both fluorine atoms are extremely deshielded, the assignment was based on the size of the shielding anisotropy. For $^n\text{Bu}_2\text{SnF}_2$, the scalar coupling from unevenly bridged fluorine atoms to ^{119}Sn was used to assign the fluorine atoms. The anisotropies do not follow the same pattern for $^n\text{Bu}_2\text{SnF}_2$ as observed for SnF_2 . Instead, the two values for $^n\text{Bu}_2\text{SnF}_2$ are the same, within experimental error. This could show that the bonds in $^n\text{Bu}_2\text{SnF}_2$ are intermediate between bridging and terminal, and confirm the uneven nature of the bridging bond lengths. Presumably, the bridging fluorine atoms are more shielded as they are shared between two tin atoms.

Table 21: Summary of the shifts and other ^{19}F NMR data, along with the coordination number of the tin atom.

Compound	Sn CN	δ_{F} / ppm	$1J(\text{SnF})$ / Hz	ζ / ppm
$\text{F}_t \text{SnF}_2$	3	-45	-	68
$\text{F}_b \text{SnF}_2$	3	-56	-	125
$\text{F}_t \text{}^n\text{Bu}_2\text{SnF}_2$	5	-108	2055	96
$\text{F}_b \text{}^n\text{Bu}_2\text{SnF}_2$	5	-125	1470, 2644	94
Me_3SnF	5	-129	1300	53 ^a
$^i\text{Bu}_3\text{SnF}$	5	-145	1285	37
Ph_3SnF	5	-149	1594	48 ^a
SnF_4	6	-150	-	-
$(\text{NH}_4)_2\text{SnF}_6$	6	-153	1625	-
$^n\text{Bu}_3\text{SnF}$	5	-157	1310	41
Me_2SnF_2	6	-160	1450	< 30
NeO_3SnF	4	-192	2200	10 ^{a,b}
Me_3SnF , site 1	4	-191	2275	-18
Me_3SnF , site 2	4	-194	2275	-26
$\text{F}_{\text{axial}} (\text{PhF}_2\text{PNMe})_2$	5 (^{31}P)	-43	645	97
$\text{F}_{\text{equatorial}} (\text{PhF}_2\text{PNMe})_2$	5 (^{31}P)	-78	900	105

^aSubject to large error as fitted from spectra with only ± 1 spinning sidebands.

^bThe sign of the anisotropy could be reversed within experimental error, thus showing the same trend as for Me_3SnF .

It could also be argued that the fluorine atoms are either axial or equatorial in $^n\text{Bu}_2\text{SnF}_2$. However, it is necessary to separate the two effects of axial vs. equatorial and bridging vs. terminal, as the fluorine atoms that would be classed as axial are also those that are bridging. For $(\text{PhF}_2\text{PNMe})_2$, the phosphorus centre is penta-coordinate, with the atoms in a trigonal bipyramidal configuration. The fluorine atoms are bonded to a phosphorus atom in axial and equatorial positions and are both terminal. In this case it can be seen that the equatorial fluorine atoms are 35 ppm more shielded than the axial fluorine atoms. This is explained as the equatorial

fluorine atoms have greater s character in the bonding to the phosphorus. This makes them more shielded and the stronger bond can be seen via the larger scalar coupling constants. For ${}^n\text{Bu}_2\text{SnF}_2$, the difference between axial and equatorial fluorine atoms is not observed, since the bridging atom (axial) is more shielded than the terminal fluorine (equatorial). So the bridging nature of the bonding must dominate over the effect of the fluorine atom being axial to the tin atom.

It appears that the coordination number of the tin atom is also important to the ${}^{19}\text{F}$ NMR shift. For a coordination number of 4 compared to 5, the tin atom is more deshielded which in turn makes the fluorine atom more shielded. However, this trend with the ${}^{19}\text{F}$ NMR shift is not observed for compounds with a coordination number of 6. These have ${}^{19}\text{F}$ NMR shifts that all lie in the small range from -150 to -160 ppm. Perhaps the octahedral geometry around the tin atom changes the orbital hybridisation and hence the nature of the bonding to fluorine.

It is harder to evaluate the electronic effect of the carbon substituent on the tin atom. The steric effect is important in determining the overall coordination number at the tin atom and whether the fluorine atoms can be close enough to form bridging bonds. In the ${}^{119}\text{Sn}$ NMR spectra, changing from an alkyl to an aryl group, e.g. n-butyl to phenyl, shields the tin atom. In the ${}^{19}\text{F}$ NMR spectra, these peaks are only 8 ppm different, with ${}^n\text{Bu}_3\text{SnF}$ slightly more shielded than Ph_3SnF . The ${}^i\text{Bu}_3\text{SnF}$ shift is 4 ppm less shielded than that for Ph_3SnF . It seems that the electronic effect of the carbon substituent is small and can be ignored.

The ${}^{119}\text{Sn}$ NMR spectrum of neo_3SnF could not be interpreted as there were too many impurity signals present. Its ${}^{19}\text{F}$ NMR shift is similar to that for Mes_3SnF . From the preceding discussion, the different carbon substituents are only likely to change the shift by a few ppm and thus neo_3SnF would be predicted have a four coordinate tin atom, similar to Mes_3SnF . This might be expected with the bulky neophyl group. The size of the scalar coupling is also indicative of a terminal Sn-F bond.

There is insufficient data to tell if the uneven bridging of the fluorine atoms has an effect on the fluorine shift. ${}^n\text{Bu}_2\text{SnF}_2$, known to have uneven bridging fluorine atoms, is ca. 25 ppm more deshielded than Ph_3SnF , known to have even bridging

fluorine bonds. It is unknown how much effect having two fluorine atoms bonded to the tin atom, compared with only one, would have on the ^{19}F NMR shift. The ^{19}F NMR shift for Me_3SnF is noticeably more deshielded than for the other penta-coordinate compounds. This might be due to uneven fluorine bridging, though there is little ^{19}F NMR information to support this.

The shielding anisotropy is large for SnF_2 and $^n\text{Bu}_2\text{SnF}_2$, but for the other compounds it is small, less than 40 ppm, and hard to measure. For the four coordinate compound, Me_3SnF , the sign of the anisotropy is negative.

-
- ¹ D. J. White, E. R. Cox, N. Westrick, Y. Pan, A. Gwynn, and J. Arends, *J. Dent. Res.*, **75**, 1881 (1996)
 - ² W. H. Nebergall, J. C. Muhler, and H. G. Day, *J. Am. Chem. Soc.*, **74**, 1604 (1952)
 - ³ R. C. McDonald, H. H. Hau, and K. Eriks, *Inorg. Chem.*, **15**, 762 (1976)
 - ⁴ G. Dénès, J. Pannetier, J. Lucas, and J. Y. Le Marouille, *J. Solid State Chem.*, **30**, 335 (1979)
 - ⁵ G. Dénès, J. Pannetier, and J. Lucas, *J. Solid State Chem.*, **33**, 1 (1980)
 - ⁶ S. Ding and C. A. McDowell, *J. Magn. Reson. A*, **117**, 171 (1995)
 - ⁷ A.T. Kreinbrink, C. D. Sazavsky, J. W. Pyrz, D. G. A. Nelson, and R. S. Honkonen, *J. Magn. Reson.*, **88**, 267 (1990)
 - ⁸ T. M. Barbara and L. Baltusis, *J. Magn. Reson. A*, **106**, 182 (1994); H. Cho, *J. Magn. Reson. A*, **121**, 8 (1996)
 - ⁹ M. Le Floch-Durand, U. Haeberlen, and C. Müller, *J. Physique*, **43**, 107 (1982)
 - ¹⁰ T. Birchall, G. Dénès, K. Ruebenbauer, and J. Pannetier, *J. Chem. Soc., Dalton. Trans.*, 1831 (1981)
 - ¹¹ A. Marshall, Ph. D. Thesis, University of Durham, (1982)
 - ¹² P. A. W. Dean and D. F. Evans, *J. Chem. Soc. (A)*, 1154 (1968); D. Dakternieks and H. Zhu, *Organometallics*, **11**, 3820 (1992)
 - ¹³ H. M. Yeh and R. A. Geanangel, *Inorg. Chim. Acta*, **52**, 113 (1981)
 - ¹⁴ E. O. Schlemper and W. C. Hamilton, *Inorg. Chem.*, **5** 995 (1966)
 - ¹⁵ R. Hoppe and W. Dähne, *Naturwissenschaften*, **49**, 254 (1962)
 - ¹⁶ A. G. Davies, H. J. Milledge, D. C. Puxley, and P. J. Smith, *J. Chem. Soc. (A)*, 2862 (1970)
 - ¹⁷ A. K. Sawyer and J. E. Brown, *J. Organomet. Chem.*, **5**, 438 (1966)
 - ¹⁸ H. den Adel, H. B. Brom, D. J. Ligthelm, and R. A. Wind, *Physica B&C*, **111**, 171 (1981)
 - ¹⁹ T. P. Lockhart and W. F. Manders, *J. Am. Chem. Soc.*, **107**, 5863 (1985)
 - ²⁰ M. Lee and W. I. Goldberg, *Phys. Rev. A*, **140**, 1261 (1965)
 - ²¹ A. Bielecki, A. C. Kolbert, and M. H. Levitt, *Chem. Phys. Lett.*, **155**, 341 (1989)
 - ²² B. J. van Rossum, H. Förster, and H. J. M. de Groot, *J. Magn. Reson.*, **124**, 516 (1997)
 - ²³ I. R. Beattie and T. Gilson, *J. Chem. Soc.*, 2585 (1961)
 - ²⁴ D. L. Alleston and A. G. Davies, *J. Chem. Soc.*, 2050 (1962)
 - ²⁵ E. Hughes, personal communication
 - ²⁶ R. Tycko, G. Dabbagh, and P. A. Mirau, *J. Magn. Reson.*, **85**, 265 (1989)
 - ²⁷ J. A. González, G. A. Aucar, M. C. Ruiz de Azúa, and R. H. Contreras, *Int. J. Quantum. Chem.*, **61**, 823 (1997)
 - ²⁸ D. Tudela, R. Fernández, V. K. Belsky, and V. E. Zavodnik, *J. Chem. Soc., Dalton. Trans.*, 2123 (1996)

-
- ²⁹ D. Tudela, E. Gutiérrez-Puebla, and A. Monge, *J. Chem. Soc., Dalton. Trans.*, 1069 (1992)
- ³⁰ L. E. Levchuk, J. R. Sams, and F. Aubke, *Inorg. Chem.*, **11**, 43 (1972)
- ³¹ A. P. Minoja and R. K. Harris, personal communication
- ³² L. A. Crowe, personal communication

7 Structural and Electronic Information of Iminophosphoranes

In the preceding chapters I have reported the use of solid-state NMR to find bond lengths and structures. Here such work is extended to provide information about the electronic structure in iminophosphorane systems and the nature of the P-N bond.

Iminophosphoranes have the general formula $R_3P=NH$ and are isoelectronic with ylides ($R_3P=CH_2$). Phosphorus ylides have been extensively studied and have earned Wittig a Nobel Prize for the reaction that bears his name.¹ Ylides have recently been shown to be powerful ligands to s-block metals.² Iminophosphoranes are expected to have similar properties, with predictions that they will be even stronger ligands than ylides. The compounds studied include the parent iminophosphorane, its hydrobromide salt, some complexes and N-metallated derivatives. The compounds are novel and have only recently been characterised by X-ray diffraction. The electronic structure and bonding in these compounds can be elucidated by ^{13}C , $^{14,15}N$ and ^{31}P NMR spectroscopy. The compounds are generally air and moisture sensitive. For solid-state NMR measurements, the samples can be completely sealed in a glass insert. In addition, the lineshapes, that would be lost in solution, give information about the sizes and orientations of the shielding anisotropy, dipolar and quadrupolar tensors. The hydrobromide salt is air stable and has been extensively studied as a model compound.

Previous solid-state ^{31}P NMR studies have looked at N-phenyl(triphenyl) iminophosphorane³ and the isoelectronic series $R_3P=X$ ($X = BH_3, CH_2, NH, O$).⁴ These concentrated on the properties at the ^{31}P nucleus, whereas information from ^{13}C , and indirectly ^{14}N , NMR gives further insight into the electronic structure of these molecules. For the compounds discussed here, the X-ray diffraction data allow the dipolar information to be calculated. The crystal structures have also been used for ab initio calculations of the shielding and quadrupolar tensors using the Gaussian 94 molecular modelling package.

7.1 Samples

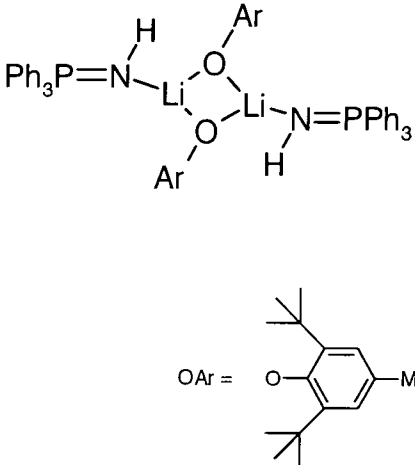
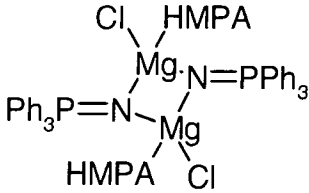
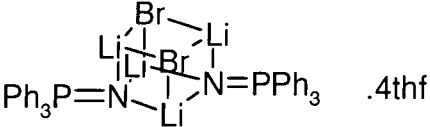
The samples were synthesised in Durham by Price and Davidson. They are shown schematically in Table 22, along with their chemical names. They all have a common triphenylphosphonium group bonded to nitrogen. The nitrogen environment varies through the compounds from the hydrobromide salt, through the imino to the N-lithio complex and is most clearly seen with the trend in the P-N bond lengths determined by X-ray diffraction. The changes at nitrogen are also reflected through the molecule in the NMR spectra of the phosphorus and adjacent carbon atoms.

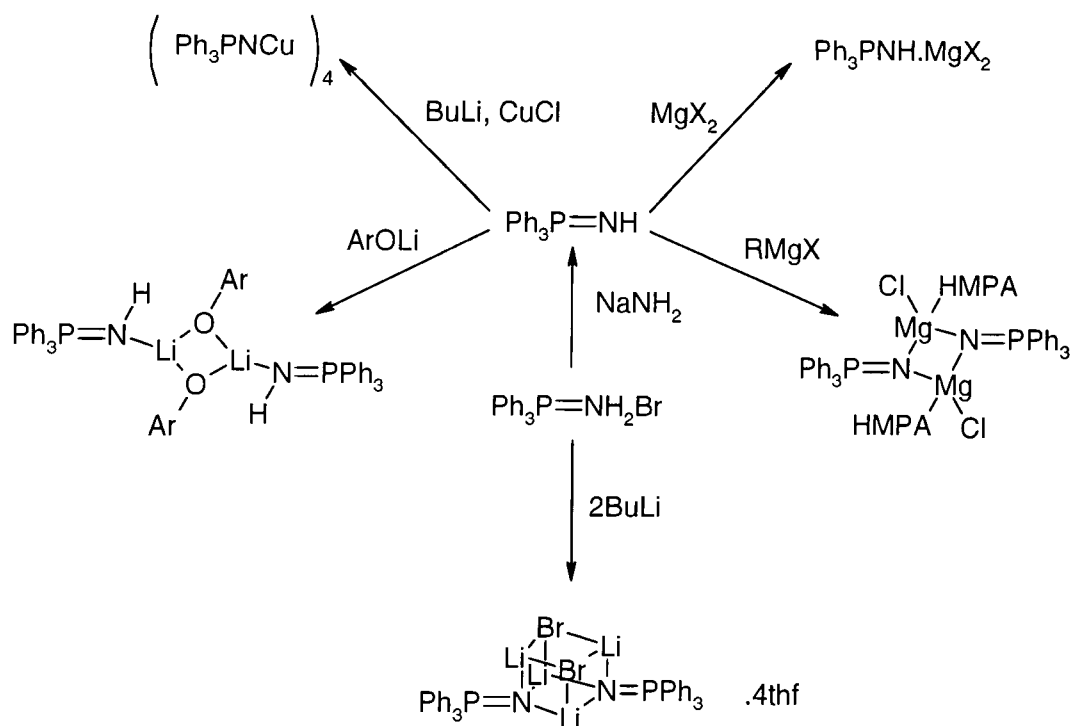
All compounds were assumed to be air sensitive and have been prepared in an inert atmosphere using either a glove box or Schlenk techniques. A broad reaction scheme for these compounds is shown in Scheme 3. More detailed descriptions of the syntheses for compounds **IV** and **V** can be found in references 5 and 6 respectively. The top two complexes in Scheme 3 have also been synthesised with dimethylamido instead of phenyl groups. The extra nitrogen atoms in these two complexes would complicate the residual dipolar coupling lineshape in the ^{31}P NMR spectra, so these compounds have not been studied here.

As most of the samples are air sensitive, for solid-state NMR measurements they were packed in a glove box and sealed in glass ampoules as described in Chapter 2. The exception to this was compound **I** which was air stable. It is possible that some of the compounds, particularly **III** and **V**, are air stable on a short timescale so they have been used with plastic inserts on occasions. Using the glass inserts has restricted the NMR measurements to the HX probe and slow spinning speeds. However, the plastic inserts can also be used in the HXY probe. In either case, the smaller sample volumes have reduced the available NMR signal. This then requires longer experimental times and has precluded the measurement of ^{15}N NMR.

As compound **I** is air stable, it has been studied extensively by NMR. With no requirement to pack the sample into inserts, more of the sample can be packed in the rotor, giving better signal-to-noise ratios and the flexibility to study this compound in a variety of probes.

Table 22: The iminophosphorane compounds and complexes studied

I	Amino(triphenyl)phosphonium bromide	$\text{Ph}_3\text{P}=\text{NH}_2\text{Br}$
II	Lithium-2,6-di-tert-butyl-4- methylphenoxide· imino(triphenyl)phosphorane	
III	Imino(triphenyl)phosphorane	$\text{Ph}_3\text{P}=\text{NH}$
IV	N-(chloro)magnesio imino(triphenyl)phosphorane· hexamethylphosphoramide	
V	N-lithioimino(triphenyl) phosphorane·lithium bromide· tetrakis tetrahydrofuran	



Scheme 3: Reaction scheme for the iminophosphorane derivatives and their complexes.

7.1.1 Crystallographic data

Diffraction crystallography has been one of the primary methods used to characterise these compounds. Bond lengths and angles in the solid-state structure can give information about the nature of the P-N bond. The X-ray diffraction (XRD) patterns have been measured and solved in Durham at 153 K. For compound **III**, neutron diffraction measurements have also been made at 20 K⁷ and the results give more accurate positions for the protons. Thus for this compound, the neutron data have been used to give the base structure for calculations.

Table 23 summarises the P-N and P-C bond lengths as found from the XRD data. For **III**, the P-N and P-C bond lengths are given from the XRD structure, rather than the neutron data, for consistency. The neutron P-N bond length is 1.582 (2) Å and was measured at a lower temperature. For the P-C bond lengths, the neutron data give 1.822 (2), 1.810 (2) and 1.796 (2) Å. Compound **I** is air stable and has been

characterised by XRD before.⁸ The structure for this compound was retrieved from the Cambridge Structural Database (CSD). The data for all the other structures have been used as supplied, directly from Davidson. Literature references and CSD refcodes are given in the table where they have been assigned.

Table 23: Summary of crystallographic data measured at 298 K

Compound	P-N / Å	P-C / Å			Refcodes
I	1.615 (3)	1.797 (3)	1.791 (3)	1.791 (3)	LALJAJ (8)
II	1.578 (2)	1.821 (2)	1.813 (2)	1.805 (2)	
III	1.562 (3)	1.818 (3)	1.817 (3)	1.810 (3)	7
IV	1.555 (1)	1.845 (2)	1.833 (2)	1.830 (2)	5
V(a)	1.541 (3)	1.854 (3)	1.835 (3)	1.834 (3)	6
V(b)	1.541 (3)	1.844 (3)	1.841 (3)	1.840 (3)	

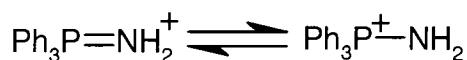
7.1.2 Electronic structure and bonding

The electronic structure and bonding of the iminophosphoranes has previously been discussed based on the crystallographic data. These arguments are presented here so that the information from NMR studies of these compounds can be evaluated.

The iminophosphoranes are isoelectronic to phosphorus ylides and phosphane oxides. For this series of compounds, the P-X bond length is observed to decrease from P-C (1.66 Å), P-N (1.58 Å) to P-O (1.49 Å). This trend can be attributed to a combination of factors: decrease in covalent radius of X, increase in electronegativity of X and an increase in the bond order. From the XRD data in Table 23, it can be seen that the P-N bond gets shorter on going down the series of compounds, i.e. from **I** to **V**. For the complexes **IV** and **V**, the P-N bond length is shorter than in the parent iminophosphorane, **III**. In these complexes there is effectively an iminophosphorane anion. The short bond lengths suggest that the double-bond character is retained as the iminophosphorane is deprotonated to form the anion. It also suggests that the

interaction between the anion and the metal cation is essentially electrostatic. With this electrostatic interaction, the P-N bond is polarised, giving $P^{\delta+}$ and $N^{\delta-}$. The induced charges increase the electrostatic attraction between phosphorus and nitrogen and give shorter bond lengths relative to the neutral iminophosphorane.

The iminophosphorane **III** has only one proton attached, leaving a lone pair of electrons. This lone pair bonds datively to a lithium group in **II** whilst in **I** an additional hydrogen atom fills this space, leading to a net positive charge on the imino group (counterbalanced by the bromide ion). Thus, the electron density at the nitrogen atom diminishes running from **III** to **I**. This weakens the electrostatic interaction and hence the P-N bond, which can be seen as an increasing bond length. A resonance structure can be drawn for **I**, Scheme 4, in which the positive charge is centred on the more electropositive phosphorus atom.



Scheme 4

The strength of the P-N bond can be observed indirectly via the average length of the P-C_{ipso} bond. It can be seen that, as the P-N bond gets shorter on going down the series, the P-C bond lengthens. In addition, the Ph₃P group can be distorted from C_{3v} symmetry to C_s such that there is a unique ipso carbon. For compound **I**, the P-C_{ipso} bond vector lies perpendicular to the plane defined by the three atoms of the NH₂⁺ group. For **IV**, the phenyl group lies perpendicular to the plane defined by the Mg₂N₂ ring. The phenyl group can alternatively be considered to lie in the local mirror plane of the molecule. For both cases, the P-C bond length is longer for this unique group compared to the other two P-C bond lengths. For compounds **II**, **III** and **V**, the effect is still present, though it is not always possible to define a unique plane. The longer bond lies in the mirror plane of the molecule, whilst the shorter of the two other bonds (where present) lies approximately trans to the iminic proton. A possible explanation for this effect is (N)π-(P)σ* bonding (negative hyperconjugation), which weakens the unique P-C bond.

For compound **IV**, the Mg_2N_2 ring is planar. The chloride ions are trans to this ring with HMPA, making the magnesium atoms four-coordinate. This ring is tilted relative to the P-N bond (the angle P-N-X, where X is the centroid of the ring, is 166°). This effect is also observed in ylides, though there is no steric reason for the tilt. Instead, the cause is believed to be that the remaining pair of electrons on nitrogen are available for π -bonding. The other two electron lone-pairs are involved with interactions with the Mg atoms. The unique phenyl group is found to be tilted towards the nitrogen atom.

For compound **V**, the P-N bond is shorter than that in any other known compound. In this compound, lithium bromide is solvated to form a pseudo-cubane $\text{Li}_4\text{N}_2\text{Br}_2$ rather than forming an infinite lattice. This shows the powerful Lewis-base donor properties of the iminophosphorane anion.

7.2 Phosphorus-31 NMR

Phosphorus-31 spectra have been recorded in solution and in the solid state. They are a good point to start from for NMR studies, as ^{31}P is 100% naturally abundant and a spin- $1/2$ nucleus. For the solid-state measurements, cross polarisation (CP) was always used, and both static and MAS spectra have been recorded.

Solution-state NMR spectra have been measured with the compounds dissolved in deuterated benzene. The shifts in the solid state, whilst close to those for solution state, are dependent on the solid-state structure, crystal packing and interactions rather than solvation effects. For compound **I** there is one peak at $\delta = 36.2$ ppm, which is close to the solid-state NMR shift of $\delta = 34.8$ ppm. For compound **V** the solution-state spectrum is complicated as four distinct peaks are observed in the ^{31}P spectrum and three peaks are observed in the ^7Li spectrum. These peaks can be assigned to various monomers and oligomers of LiNPPPh_3 , LiBr and $\text{LiBr}\cdot\text{LiNPPPh}_3$ with coordinated thf. When the spectrum is run in deuterated toluene, LiBr precipitates out of solution and fewer peaks are observed, although a little LiBr remains solvated by the ligand. The relative intensities of the peaks have been shown to be dependent on concentration. These observations indicate that the nature of the reactive species present in solution varies with concentration, which will in turn have an effect upon the reactivity and selectivity of these reagents.

In the solid state, the ^{31}P CPMAS NMR spectra of these compounds have good signal-to-noise ratios and narrow lines for short experimental measuring times. A typical ^{31}P spectrum, that of compound **I**, is shown in Figure 37. At spinning speeds above 1 kHz, the ^{31}P - ^{14}N heteronuclear dipolar coupling would be expected to be removed, but a residual dipolar coupling (RDC) is observed that splits all the peaks in the ssb manifold. The cause of this splitting is explained in the next section. Spinning speeds were low (< 3 kHz) as glass inserts were used in the HX probe. The ssb peak intensities were measured by integration in order to account for the second-order splitting. A spectrum was run at a different spinning speed to confirm the position of the centreband.

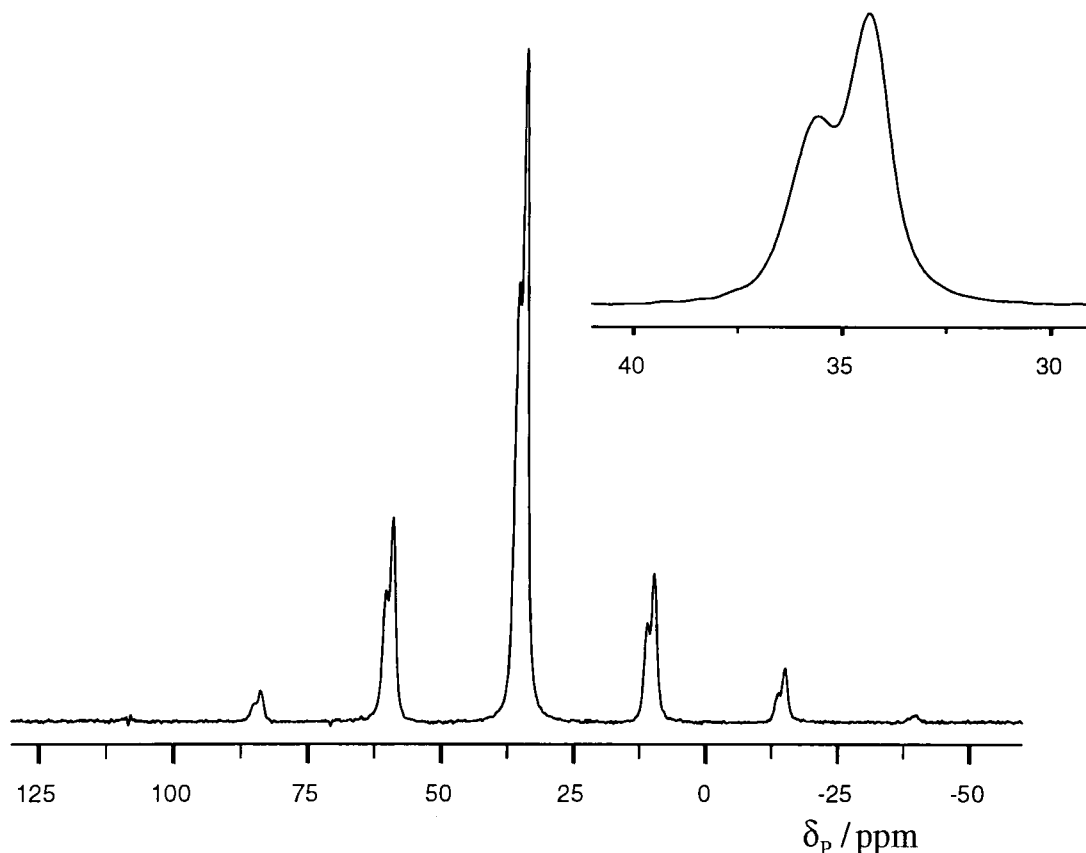


Figure 37: ^{31}P CPMAS NMR spectrum of compound **I** measured with the sample spinning at 2 kHz and proton decoupling. The inset shows the splitting due to residual dipolar coupling and is the sum of all the spinning sideband peaks. Acquisition parameters were: pulse duration 4.5 μs , contact time 1 ms, recycle delay 30 s, and number of acquisitions 32.

Simulation of the spinning-sideband manifold, using the *ssb97.o* program, gave the isotropic and shielding tensor data shown in Table 24. The values in brackets are the estimated fitting errors. Those in italics are from Gaussian 94 GIAO calculations at the *hf/6-31g** level. The isotropic shielding is given in absolute terms, i.e. relative to the bare nucleus. To relate this to the chemical shift scale, the absolute shielding of a known reference compound is used. Here we have used $\text{H}_3\text{PO}_4 = 328.35 \text{ ppm}$,⁹ which is defined as 0 ppm on the chemical shift scale. The accuracy of the *ab initio* calculations for the isotropic shift and shielding in these compounds is discussed in detail later. The agreement between experimental and calculated values for the anisotropy is remarkably good.

For compound **IV**, there is an extra peak at $\delta = 22.9$ ppm (not tabulated) which arises from the phosphorus atom of HMPA. For compound **V**, two isotropic peaks are observed. This would be expected as there are two slightly different molecules in the asymmetric unit. However, the values for the anisotropy and splitting are not noticeably different between the two molecules.

Table 24: Data from ^{31}P CPMAS NMR spectra. The calculated values given in italics are from Gaussian 94 calculations at hf/6-31g* level on the structures derived from XRD and neutron diffraction.

Compound	$\delta_{\text{iso}} / \text{ppm}$	$\sigma_{\text{iso}} / \text{ppm}$	ζ / ppm	η
I	34.8	<i>392.9</i>	42 (0.5) <i>32</i>	0.52 (0.01) <i>0.56</i>
II	30.4	<i>396.3</i>	95 (0.7) <i>91</i>	0.23 (0.03) <i>0.26</i>
III	21.8	<i>402.5</i>	107 (1.3) <i>98</i>	0.19 (0.03) <i>0.24</i>
IV	4.0	<i>419.0</i>	154 (1.1) <i>135</i>	0.13 (0.04) <i>0.02</i>
V	-2.1	<i>430.8</i>	181 (1.8) <i>167</i>	0.00 (0.09) <i>0.05</i>
	-5.7	<i>429.8</i>	<i>161</i>	<i>0.06</i>

From Table 24 it can be seen that δ_{iso} becomes more shielded going from compound **I** to **V**. Although there is a trend observed with δ_{iso} , it is minor when compared to those found for the individual tensor components. These components allow the three-dimensional nature of the electronic structure to be discussed. The orientation of the shielding tensor relative to the molecule is measured and discussed later.

Figure 38 shows the tensor components plotted against the P-N bond length. It can be seen that the δ_{33} component, lying approximately along the bond, is more shielded in compound **V** than the other compounds. This corresponds to a shorter bond length and more electron density on the phosphorus atom. The asymmetry arises from the varying twist angles of the phenyl groups. For compound **V** there is local C_3 symmetry at the phosphorus atom, which also explains the approximately axial symmetry of the tensor. The extra electron density reduces the asymmetry, indicating that δ_{11} and δ_{22} , lying perpendicular to the bond, are more evenly shielded

than in the other compounds. It can be conjectured that the $p\pi-d\pi$ back bonding is largest in this case.

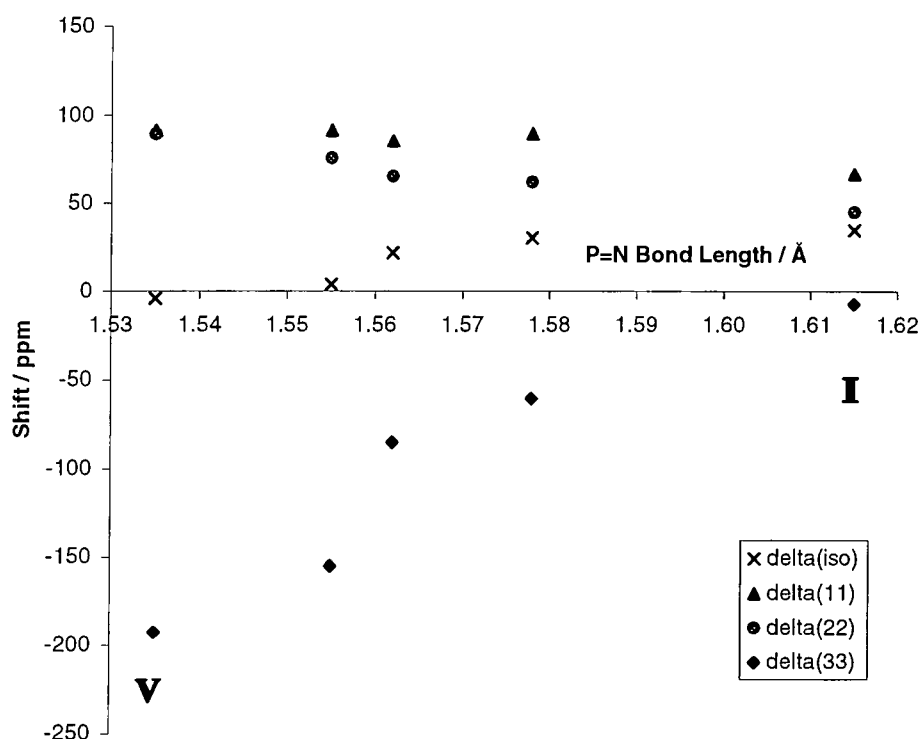


Figure 38: Plot of the shielding tensor components against the P-N bond length. Note that this is given on a chemical shift scale.

For the static ^{31}P NMR spectrum, the powder lineshape is determined predominantly by the shielding and dipolar tensor interactions and their relative orientations. The dipolar coupling is modulated by the spin of ^{14}N so that there are three powder lineshapes for $m_N = 1, 0, -1$. The equations for these lineshapes have been described in the literature and have been implemented in the computer program JCSim, as described in Chapter 3. Reported solution-state NMR values for $^1J(\text{PN})$ are 32.9 Hz for N-phenyl(triphenyl)iminophosphorane¹⁰ and 36.6 Hz for N-phenyl(diphenylmethyl)iminophosphorane,¹¹ which reduces to 26.8 Hz on α -lithiation. Thus $^1J(\text{PN})$ is small and the powder lineshapes are very nearly superimposed. Homonuclear ^{31}P dipolar coupling would be expected to mask this and other fine structure in the lineshape. The application of homonuclear dipolar

decoupling was considered, but was found unnecessary for **I** as the turning points in the ^{31}P NMR spectrum could be discerned with the use of only proton decoupling.

The ^{31}P static NMR spectrum of **I** is shown in Figure 39. It can be seen that the asymmetry is non-zero and the powder pattern is still broadened by homonuclear ^{31}P dipolar broadening, making some of the turning points indistinct. As the crystal structure is known, the P-N dipolar coupling constant can be calculated to be $D = 835$ Hz. The scalar coupling is small and assumed to be negligible; hence $D' \sim D$. Spinning-sideband analysis, discussed below, gives the size of the anisotropy and asymmetry. The shielding tensor has also been calculated from the experimental structure using Gaussian94 with the Hartree-Fock approximation and a 6-31g* basis set. The resulting shielding tensor, fully described in Appendix A, gives a non-axial tensor that is aligned with the angles $\beta = 49^\circ$ and $\alpha = 2^\circ$ from the dipolar tensor.

The simulated spectra of **I** are shown Figure 39 below the experimental spectrum. These spectra were simulated using an iterative method to find the best fit. The anisotropy, asymmetry, angles α and β , and linewidth were varied in the fit using the information given above as a starting point. This gives $\zeta = 45$ ppm and $\eta = 0.78$, which are in good agreement with the experimental spinning-sideband spectrum results. The shielding and dipolar tensors are orientated with angles of $\beta = 30^\circ$ and $\alpha = 70^\circ$. Changing these angles by more than 10° makes a noticeable difference to the fit, though the angle α is less sensitive to changes than β . From the fitted values for the angles and the ab initio calculated orientation, it is clear that the largest component of the shielding tensor lies in the plane of the P-N-C (unique) atoms. The value of D' is confirmed from the stepped shoulders to low frequency. The sub-spectra are included so that the turning points can be related to the features in the experimental spectrum. It can be seen that the agreement is still poor for certain turning points. The middle sub-spectrum, for which $m_N = 0$, can be seen as a faint shoulder in the simulation and is unclear in the experimental data.

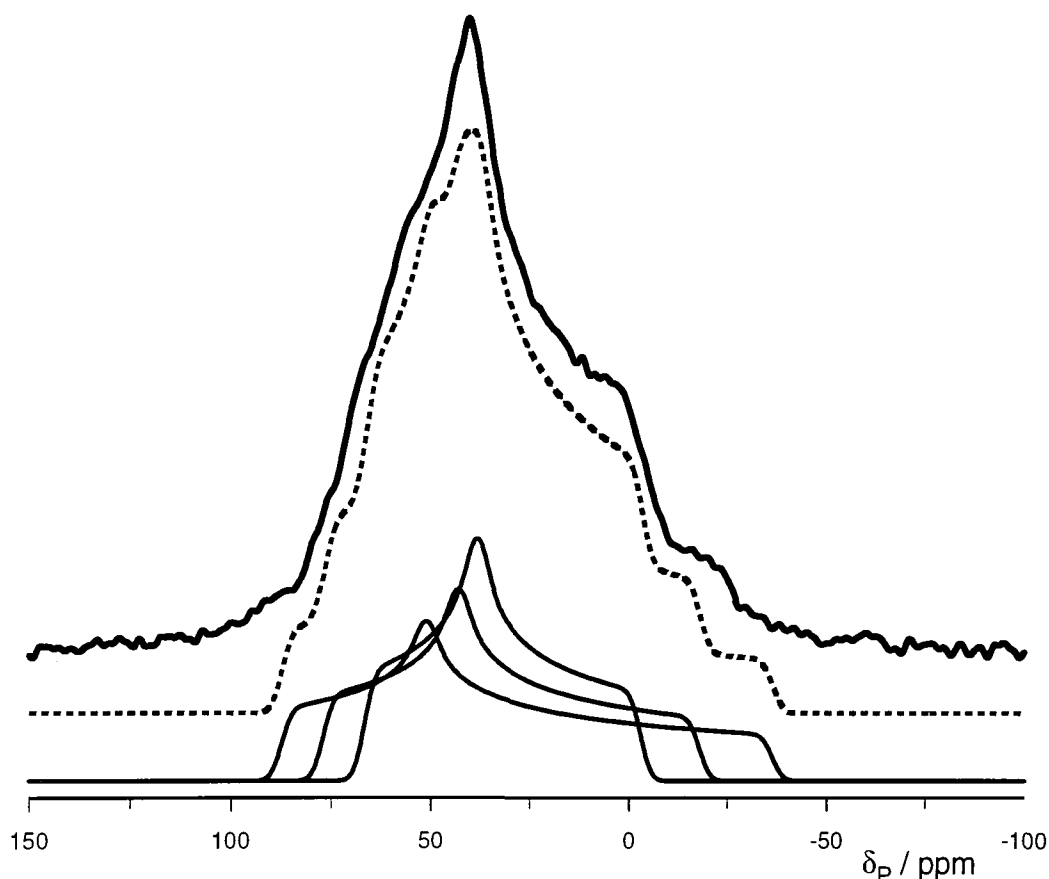


Figure 39: Experimental static ^{31}P NMR spectrum of compound **I** with the simulated total spectrum and individual sub-spectra below. The experimental spectrum was acquired with CP, a Hahn echo and proton decoupling during acquisition. Acquisition parameters were: pulse duration $4.5\ \mu\text{s}$, contact time $1\ \text{ms}$, echo time $40\ \mu\text{s}$, recycle delay $10\ \text{s}$, and number of acquisitions 1024. Simulation parameters are listed in the text.

For comparison, in *N*-phenyl(triphenyl)iminophosphorane the shielding tensor is axial, with a larger anisotropy, so the turning points in the powder pattern are more distinct.³ Values for the shielding and dipolar tensors can then be calculated by simulation. In this case the data are sufficient to determine the relative orientation of the two tensors by simulation of the static spectrum. The shielding tensor is found to be nearly axial, with the most shielded component lying along the P-N bond, whereas in **I** the most shielded component lies at 30° to the P-N bond. The errors in α and β are estimated to be less than 10° . These results are in agreement with other P-X systems⁴ and ab initio calculations. The dipolar coupling, assuming that ΔJ is negligible, gives a bond length of $1.60 \pm 0.02\ \text{\AA}$.

The theoretical basis of ab initio calculations for NMR has been described earlier. In the calculations reported here, the atomic positions used have been obtained from the measured X-ray and neutron diffraction crystal structures as starting geometries. For the NMR and EFG calculations these geometries were used without further energy minimisation. Energy minimisation gave similar overall geometries though longer bond lengths compared to the experimental data. Subtle low-energy distortions such as the twist in the phenyl rings are thought to arise from crystal-packing considerations, so they would not be expected to be found in the energy-minimised structure. Additionally, some of the molecules form oligomers in the solid state, which makes for a larger molecule and more basis functions. Initial computing restrictions only allowed us to use the smaller 3-21g* basis set and make approximations with the molecule, e.g. removing distant thf ligands and converting phenyl groups to methyl. Whilst this gives reasonable results for the relative NMR shifts of the compounds, the absolute shift is in error by 170 ppm.

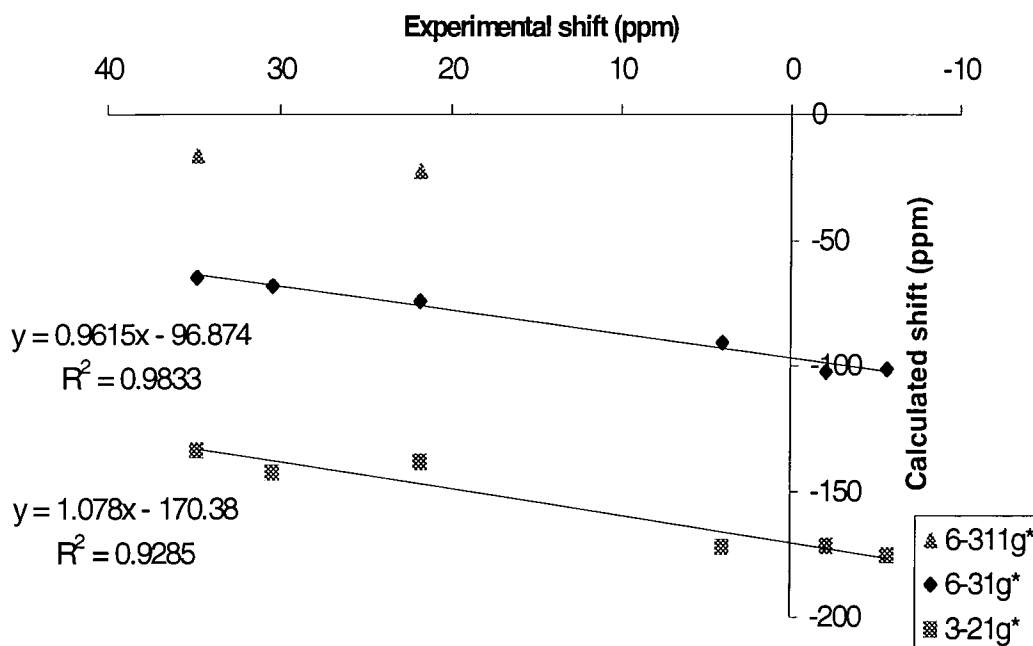


Figure 40: Trends in the calculated isotropic shifts with basis set size, compared to the experimental values for iminophosphanes.

Subsequent calculations were run with the larger 6-31g* basis set. As shown in Figure 40, these calculated values are closer to the measured values, but still nearly 100 ppm from the measured value. For the smaller compounds **I** and **III**, larger basis sets were also used. The basis set limit may have been reached with the 6-311g(2d,p) basis. This basis set adds extra polarised d functions to the heavy atoms, i.e. phosphorus, and p functions to the protons. This gave the isotropic shift as -1 and -9 ppm for compounds **I** and **III** respectively. By using the B3LYP hybrid density functional, values for the isotropic shift were in better agreement still, giving 61 and 47 ppm respectively. This latter method allows for electron correlation, but has overcorrected the shift in this case.

As the anisotropy uses an internal difference, some errors will cancel out. A clear trend can be seen in the anisotropy and asymmetry, mirroring the experimental data. The calculation also gives the orientation of the tensor relative to the molecule, which has been used in the static simulation above. The anisotropy and, to a lesser extent, the asymmetry are in very good agreement with the experimentally measured values. The orientation is in reasonable agreement with the experimental data, considering the level of theory used and the accuracy of the experimental data. These findings give us confidence in using this theory to predict general trends from ab initio calculations in the more complex molecules.

Power⁴ has recently studied solid-state ³¹P NMR spectra of the isoelectronic series R₃P-X where X = BH₃, CH₂, NH and O. The experimental results were measured with R = phenyl. However, the ab initio calculations have replaced these phenyl groups by methyl groups to reduce the size and time of the calculation. In the study, the trend in the isotropic component of the shielding is unclear whereas the three components are seen to diverge for shorter bond lengths, in common with our study. By using ab initio calculations and the LORG formalism,¹² the shielding tensor may be broken into component parts: phosphorus inner core orbitals (1s and 2s), phosphorus outer core (valence) orbitals, methyl group orbitals, P-X and X group orbitals. From this it can be seen that the main component of the shielding comes from the inner core orbitals and is isotropic. The δ_{33} component comes mainly from the ligand X, whilst the δ_{11} and δ_{22} components come from a combination of

the deshielding influence of the inner core and methyl electrons, and the shielding influence of the ligand. The balance of these contributions gives an increase in the anisotropy (from δ_{33}) and an uncertain variation in the isotropic shift from a combination of factors.

In carbon and nitrogen NMR, an increase in bond order is accompanied by a deshielding in one or two tensor components of the chemical shift. However, in both the isoelectronic series and our compounds, the shielding nature of the δ_{33} component balances the shielding nature of the other two components to give little change in the isotropic shift. This difference has been suggested to arise from the charge-transfer, or dative nature, of the P-X interaction. Power also calculated the shielding tensors for the X nuclei and found small anisotropies. These give no support for a multiple-bonding model, where larger anisotropies would be expected.

7.2.1 Residual dipolar coupling

So far in this thesis the high-field approximation, where the Zeeman interaction is dominant, has been assumed. Typically this has a value of many MHz, and the approximation is increasingly valid as magnet field strengths increase. Shielding anisotropies and dipolar couplings are less than 100 kHz, but quadrupolar interactions can be many MHz. The shielding interaction has a $(3\cos^2\theta-1)$ angular term, which is averaged to zero by MAS.

When observing a spin- $1/2$ nucleus, the MAS NMR spectrum will have spinning-sideband peaks that arise from the shielding interaction. When this nucleus is directly bonded to a quadrupolar nucleus, with a large quadrupole coupling constant (χ), these ssb peaks will have a superimposed powder pattern caused by the second-order quadrupolar interaction. This powder pattern gives a characteristic splitting, and the phenomenon is often referred to as residual dipolar coupling. The theory is well understood and has been explained both by first-order perturbation methods (generally applicable, for instance to the ^{13}C - ^{14}N case) and full diagonalisation of the Hamiltonian matrix.^{13,14} For the sizes of quadrupole couplings

and fields used here, perturbation theory is valid. Full matrix diagonalisation is not required whilst $\chi / 4S(2S-1)\nu_S < 1$, where ν_S is the Larmor frequency and S is the spin of the quadrupolar nucleus. For ^{14}N , on the Chemagnetics system, the Larmor frequency is 14.46 MHz. Thus perturbation theory is valid for $\chi < 58$ MHz. As the ratio of χ / ν_S is low, the static dipolar spectrum calculated earlier will not be noticeably affected by the perturbation, so it is valid to ignore it.

A brief summary of the perturbation theory is given here for a spin-1 nucleus and the characteristic splitting, s , is given in Equation 6 at the end. The eigenstates of the quadrupolar nucleus are given by the Hamiltonian

$$H|\psi_m\rangle = (H_z + H_Q)|\psi_m\rangle = E_m|\psi_m\rangle$$

When H_Q is considered to be negligible $|\psi_m\rangle = |n\rangle$. However, for small perturbations,

$$|\psi_m\rangle = \sum_{n=-1}^1 a_{mn}|n\rangle, \text{ and } a_{mn} = {}^0a_{mn} + {}^1a_{mn} + \dots$$

$${}^0a_{mn} = \delta_{mn}, {}^1a_{mm} = 0 \text{ and } {}^1a_{mn} = -\frac{\langle n|H_Q|m\rangle}{E_n^0 - E_m^0}$$

In this way the first-order perturbations to the Zeeman states of the quadrupolar nucleus are calculated. It has been shown that only those coefficients with $n = m \pm 1$ are required.¹³ Taking the dipolar interaction between the spin-1/2 and quadrupolar nuclei gives a shift, $\Delta\nu_m$, which transfers the quadrupole eigenstate information to the spin-1/2 nucleus. The anisotropy in J can be introduced, as previously described, by assuming that the \mathbf{J} and \mathbf{D} tensors are colinear with an effective dipolar coupling constant $D' = D - \Delta J/3$. For the present cases it may be assumed that J is sufficiently small for its anisotropy to be ignored. The first-order shift is

$${}^1\Delta v_m = -mJ - mD(1 - 3\cos^2 \Omega)$$

which is the usual scalar and dipolar-coupling interaction. The angular part, where Ω is the angle between B_0 and the r_{IS} , will be averaged by MAS to zero. Note that a first-order perturbation gives up to second-order effects on the spin- $1/2$ nucleus. The second-order effect adds a detailed powder pattern to each peak in the spinning-sideband manifold. In practise, this pattern is frequently obscured by line broadening. The powder lineshape equation has been implemented in a computer program, based on an example from Olivieri,¹⁵ for simulations and fitting of data. The second-order effect is described by averaging over all possible crystallite orientations to give the centre of mass of each peak as given below:

$${}^2\Delta v_m = \left(\frac{3D\chi}{20v_s} \right) \left[\frac{S(S+1) - 3m^2}{S(2S-1)} \right] (3\cos^2 \beta^D - 1 + \eta_q \sin^2 \beta^D \cos 2\alpha^D)$$

β^D and α^D describe the relative orientation of the quadrupolar and dipolar tensors. It can be seen from this equation that the splittings are dependent on the magnitude of m . For ${}^{31}\text{P}$ - ${}^{14}\text{N}$ systems, two peaks would be expected in a 2:1 (or 1:2) ratio with a splitting, s , given by Equation 6. The sign of s can be either positive or negative.

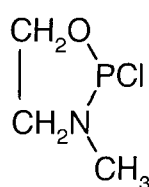
$$s = \left(\frac{9D\chi}{20v_s} \right) (3\cos^2 \beta^D - 1 + \eta_q \sin^2 \beta^D \cos 2\alpha^D)$$

Equation 6

There are many parameters in the splitting equation for RDC, which tell us about the quadrupolar and dipolar tensors and their relative orientations. The RDC can be removed from the lineshapes by isotopic substitution or by going to higher magnetic fields (since the splitting is proportional to the inverse of v_s). In solution and when the quadrupolar nucleus relaxes rapidly, self decoupling occurs, removing the effects of RDC. With rising magnetic fields and triple-channel probes, it is hoped in future to decouple ${}^{14}\text{N}$ from ${}^{31}\text{P}$ and thus remove RDC effects.

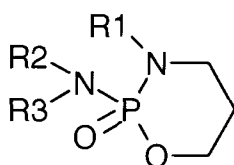
From the crystallographic results we can calculate D . The measured values of s , from the ^{31}P CPMAS NMR spectra, are given in Table 25. The natural linewidths of the ^{31}P peaks are ca. 60 Hz, which leads to errors in measuring s of ± 20 Hz. For the spectrum of compound **III**, where the splitting is comparable to the linewidth, the relative intensity of the peaks is uncertain, which would be reflected in an uncertain sign of the splitting. The splitting value is presumed to be positive by comparison with the value for **II** and the ab initio calculated value. The splittings for the two sites in compound **V** were confirmed by re-running the spectrum at 300 MHz, which reduced their magnitude. The spectra of compound **V** are shown in Figure 41 with expansions in Figure 42.

We might be able to predict the orientation of the quadrupolar tensor from symmetry arguments,¹⁶ but not its size. Few experimental results exist for the size of χ in ^{31}P - ^{14}N systems. Two results from NQR data are given below, though neither of these are very representative of our systems.

Phosphorus(III) Acid Chloride¹⁷

$$\chi = 4.28 \text{ MHz}$$

$$\eta = 0.24$$

Phosphamide¹⁸

$$\chi = 4 - 5 \text{ MHz}$$

$$\eta = 0.2 - 0.4$$

The lack of results is due to the low frequency of ^{14}N , which lies outside the observable range of most NMR and NQR spectrometers. More data exist for ^{13}C - ^{14}N systems, where there is interest in the relationship of pharmaceutical properties to the electron charge densities that can be obtained from these measurements. Gaussian 94 has been used to calculate the quadrupolar tensor and its orientation. These calculations will be discussed in detail in section 7.2.2. For the moment the results presented are as calculated using the crystal structure and Hartree-Fock 6-31g* level of theory. The magnitude of $\chi(^{14}\text{N})$ is expected to be less than 5 MHz based on

previous measurements. The orientation of the quadrupolar tensor orientation will depend mainly on the presence or absence of electron lone pairs.

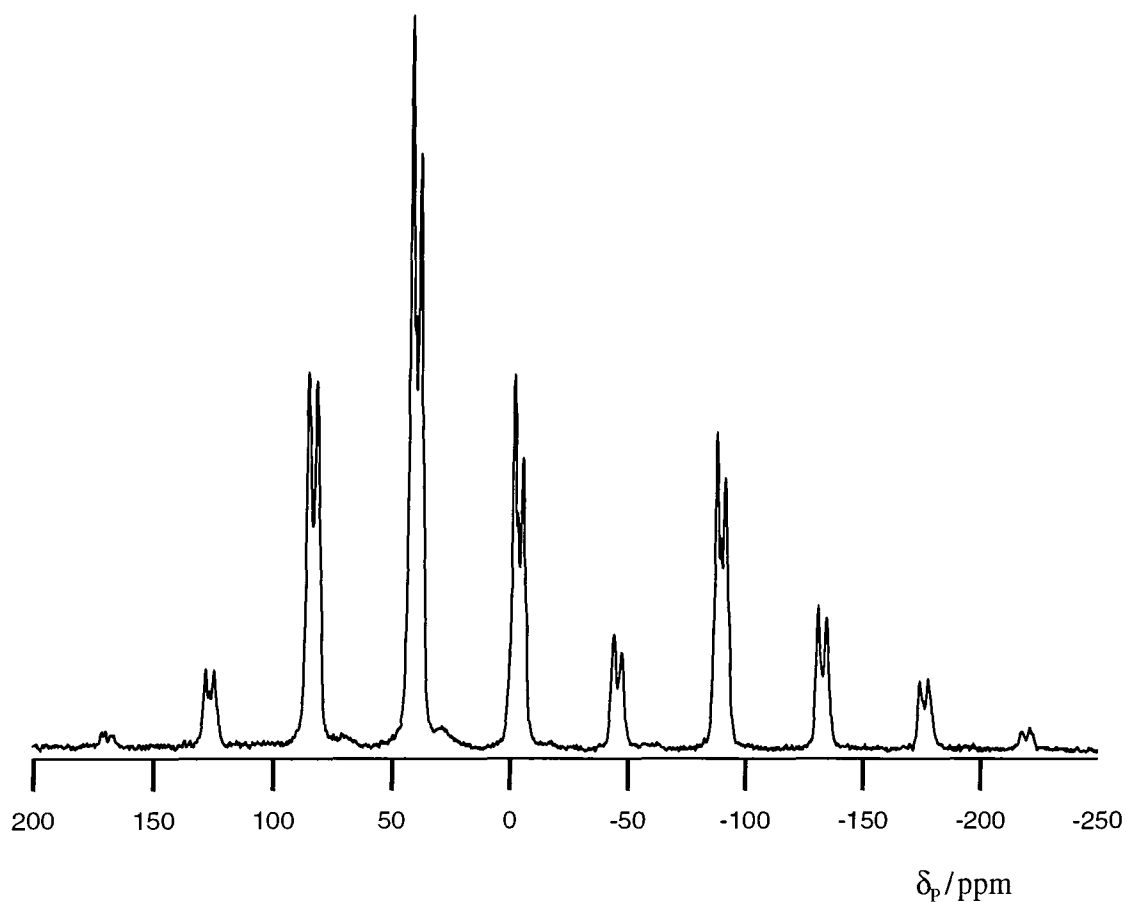


Figure 41: ^{31}P CPMAS NMR spectrum of V, spinning at 3.5 kHz with proton decoupling during acquisition. Acquisition parameters were: pulse duration 4.5 μs , contact time 2 ms, recycle delay 5 s, and number of acquisitions 600.

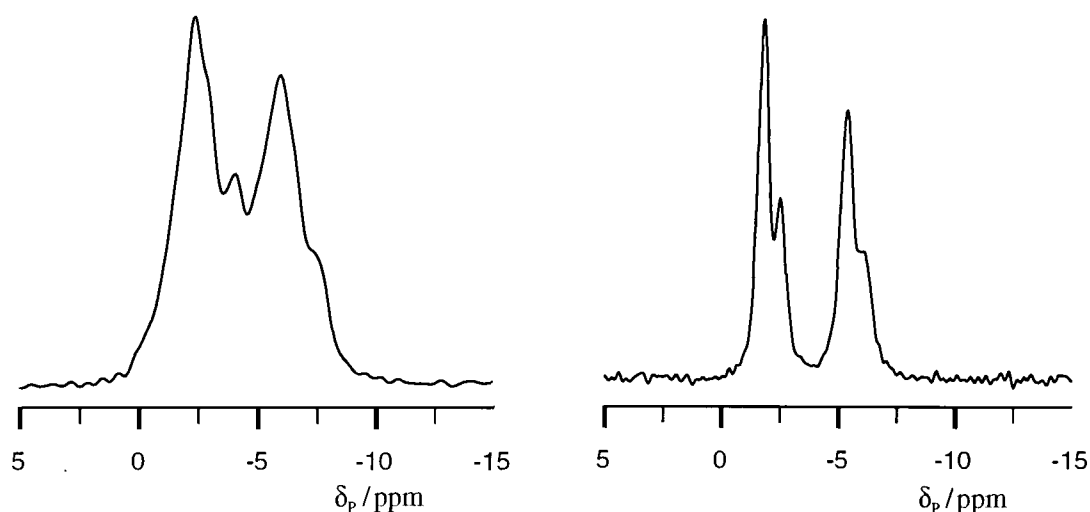


Figure 42: The left hand figure shows an expansion of the isotropic peak in Figure 41 with all the spinning-sideband peaks rolled back as if at infinite spinning speed. The right hand figure is only the centreband peak from a spectrum measured at 121.42 MHz. Other acquisition parameters were: pulse duration 4 μ s, contact time 10 ms, recycle delay 3 s, and number of acquisitions 500.

Table 25: RDC splittings from experiment and calculation.

Compound	D / Hz	χ / MHz	η_q	α^D	β^D	s (calc.) / Hz	s (exp.) / Hz
I	835	-3.53	0.25	0	95	66	101
II	895	2.38	0.66	-21	21	109	72
III	923	2.71	0.67	-27	27	114	75
IV	936	1.67	0.11	-	0	96	100
V	961	1.44	0.06	-	0	85	-128

The splitting can be calculated from the ab initio value for the quadrupolar tensor, its orientation and the value of D. It can be seen in Table 25 that the calculated splittings are in reasonable agreement with the experimental data, considering the errors in both values. With the number of variables involved in the equation for s, the experimental splitting values have not been used to estimate χ .

In compound I χ is negative, indicating that it arises mainly from a lone pair of electrons; the orientation of $\beta^D = 95^\circ$ is in the direction where a lone pair would be expected. In this case χ has been underestimated, indicating that the lone-pair

contribution may be larger than the calculations suggest. The effect of isotropic scalar coupling on the position of the lines has been ignored, which could change the observed splitting. Simulation of the total lineshape would resolve this question.

In compound **III** the iminophosphorane has a lone pair of electrons equivalent to those that are directed towards the lithium atom in compound **II**. This will reduce the proximity of the lone pair to the nitrogen atom (there is ca. 10% covalent bonding) and hence reduce the electric field gradient at the nitrogen atom, as observed from size of χ . The principal component of χ is not aligned parallel to the P-N bond in these two compounds, but at an angle of 20 to 30°. This angle is approximately where the lone pair of electrons might be expected. It is quite sensitive to the accuracy of the calculation. By varying this angle, the size of s is reduced. It is not possible to comment on the relative differences in the size of s between these two compounds as the experimental data are not clear and both values are the same within experimental error.

Compound **IV** has a similar geometry to **I**, but with two magnesium atoms attached to the nitrogen rather than hydrogen atoms. The calculation shows the quadrupolar tensor lying parallel to the P-N bond and gives a positive splitting. For $\beta = 0$, the angle α is undefined. It is possible that the lineshape of compound **IV** is further complicated by possible RDC to ^{25}Mg and / or $^{35,37}\text{Cl}$ where these atoms lie close in space to the phosphorus and have large quadrupolar coupling constants. However, calculations show that these splittings would be less than 5 Hz even though the values of χ are large, as the orientations are not favourable. The measurement of the splitting is complicated by the shapes of the individual spinning sidebands.

Compound **V** shows local C_3 symmetry at the nitrogen centre. It is also expected to have the greatest overall electron density at the nitrogen for this series of compounds. For these two reasons, it might be expected that this compound would have a smaller χ compared to the other compounds, aligned parallel with the P-N bond and near zero quadrupolar asymmetry. If the experimentally determined splitting is taken and it is assumed that $\beta^D = 0$ and $\eta_q = 0$, it is found that $\chi = -2.2$ MHz. This experimental value for χ is similar to, though smaller than, those

for cyanides ($\chi = -3.87$ MHz), where there is a lone pair directed away from the C-N bond. The splitting has been confirmed by re-running the spectrum at a higher field, so there is no uncertainty over the sign of the splitting. However, the experimental value of χ is larger than the magnitude of the ab initio calculated value and opposite in sign. This suggests that the ab initio calculation is a poor approximation in this case.

It is clear that the simple Hartree-Fock approximations, used in the ab initio calculations, give a reasonable description for most of these compounds. However, there is scope for further high-level calculations that include electron correlation and larger basis sets in order to improve the calculated data. This is particularly true for **V**, where the ab initio calculation gives a reasonable magnitude for χ , but the wrong sign.

7.2.1.1 Off magic-angle spinning

In principle, each residual dipolar-coupled spinning-sideband peak is a powder pattern. To this point, it has been assumed that all measurements have been made with the sample spinning at the magic angle. When this is not the case, a scaled powder pattern is observed. The appearance of each spinning sideband depends on the ratio of the shielding anisotropy to the spin rate. With RDC, in the limit of slow off-angle sample spinning compared to the size of the shielding anisotropy, the observed splitting of the centreband is 25% larger than that observed with fast spinning.¹⁹ This arises due to the angular dependence of the centreband intensity with crystallite, and hence tensor, orientation. The signal from crystallites with tensor components perpendicular to the spinning axis are less affected by the spinning speed than those which are orientated near the magic angle with respect to the spinning axis. For slow spinning speeds, the observed intensity of the perpendicular crystallites is greater and dominates the observed splitting. This theory has been recently extended by Olivieri²⁰ to allow for non-colinear tensors and has been implemented, by Olivieri, in a simulation program.

As both the RDC splitting and the shielding anisotropy in these compounds are large, the effects of measuring spectra spinning off-angle are noticeable. The full ^{31}P NMR spectrum of compound **IV**, recorded with the sample spinning off the magic angle is shown in Figure 43, and the expansion of the centreband peak is shown in Figure 44. The spinning angle β can be estimated by $\frac{1}{2}(3\cos^2\beta-1)$, which is equal to the ratio of the linewidths of the off-angle spinning spectrum to the static spectrum. In this case the ratio is ca. 10 / 225 (ppm), which gives the spinning angle as 53.0° , a difference of 1.8° from the magic angle. For the expansion, the top and middle spectra were recorded with the sample spinning off-angle. Individual spinning sidebands emphasise different crystallite orientations. The scaled powder pattern is only visible when all the spinning sidebands are summed together (top spectrum).

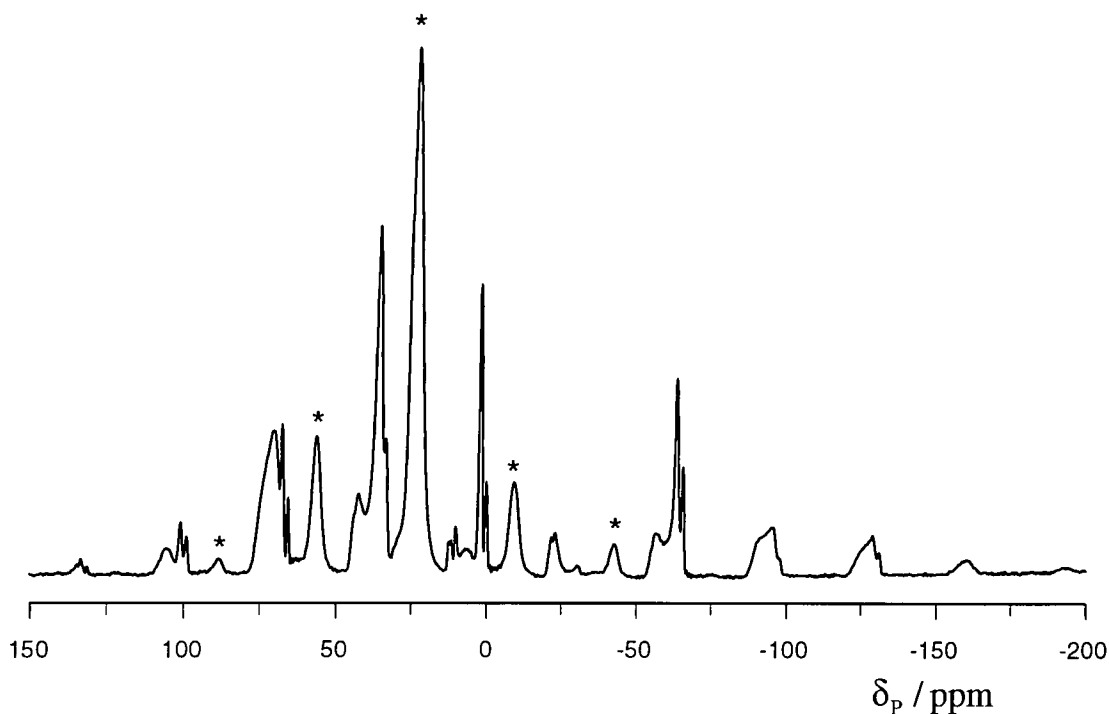


Figure 43: ^{31}P CPMAS spectra of compound **IV**, recorded with spinning at 2.6 kHz off the magic angle and proton decoupling. The asterisks mark the signal from HMPA. Acquisition parameters were: pulse duration 4 μs , contact time 0.5 ms, recycle delay 10 s, and number of acquisitions 360.

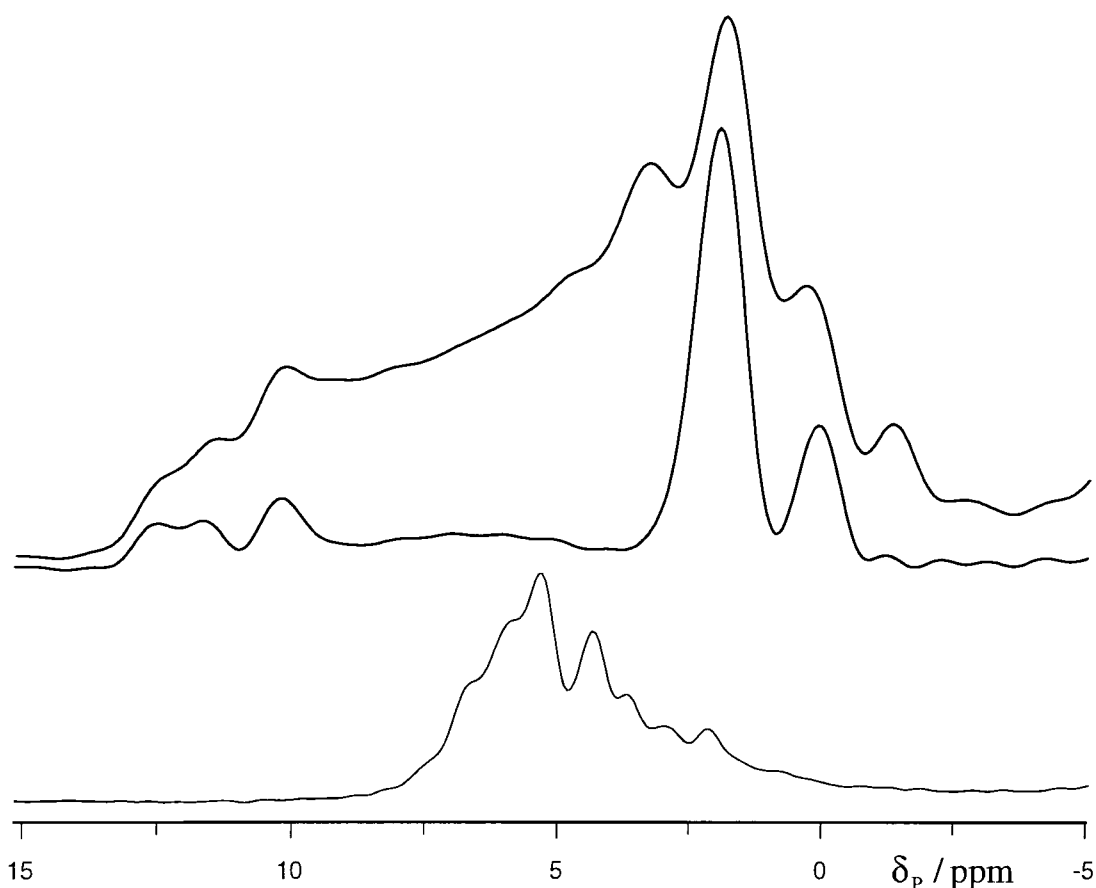


Figure 44: ^{31}P CPMAS spectra of compound **IV**, recorded with spinning at 2.6 kHz and proton decoupling. The bottom spectrum is the sum of all the spinning-sideband peaks for the spectrum recorded after setting the magic angle. The middle spectrum is an expansion of the centreband for the spectrum shown in Figure 43, recorded off angle. The top spectrum is the sum of all the spinning-sideband peaks for this same spectrum. Acquisition parameters were: pulse duration 4 μs , contact time 0.5 ms, recycle delay 10 s, and number of acquisitions 360.

The bottom spectrum, shown for comparison, was measured directly after setting the magic angle using KBr. It can be seen, from the presence of a scaled static powder pattern, that in this spectrum the sample was also spinning off the magic angle by about 0.9° . The spectrum shown here is the sum of all the spinning-sideband peaks. The RDC splitting observed in the centreband peak without summation, has the same magnitude though opposite sign when compared to the splitting observed in the centreband peak with summation. Thus, care must be taken when measuring the splitting in RDC spectra to allow for the setting of the magic angle and the spinning speed.

From ^{31}P spectra recorded of compound **III**, recorded both near to (53.8°) and off (53.0°) the magic angle, the splitting was measured as 75 and 106 Hz respectively. The size of the latter splitting is over 25% larger than when measured on angle. This difference is attributable mainly to the effects mentioned above, but also to the errors involved in measuring splittings that are similar in size to the linewidth.

7.2.2 Ab initio calculations of ^{14}N quadrupolar coupling constants

The quadrupolar tensor, χ , is directly related to the electric field gradient tensor, \mathbf{q} , through the equation $\chi = (eQ/h) \cdot \mathbf{q}$. Here Q is the quadrupole moment, which can be derived experimentally. In the ab initio calculations, \mathbf{q} is given in atomic units. Using $e/h = 2.3495 \times 10^{36} \text{ C J}^{-1} \text{ s}^{-1}$ gives χ in Hz. The EFG tensor can be further broken down into two components with contributions from the surrounding nuclei, \mathbf{q}_N , and electrons, \mathbf{q}_E . Here, \mathbf{q} is calculated at nucleus K , with contributions from the other nuclei A and electrons I described by the wavefunction Φ .

$$q_\text{N} = -\sum_A \left\{ \frac{3r_{\text{AK}}r_{\text{AK}} - r_{\text{AK}}^2}{r_{\text{AK}}^5} \right\} Z_A$$

$$q_\text{E} = \left\langle \Phi \left| \sum_I \left\{ \frac{3r_{\text{IK}}r_{\text{AK}} - r_{\text{IK}}^2}{r_{\text{IK}}^5} \right\} \right| \Phi \right\rangle$$

The value of \mathbf{q}_N is dependent only on the crystal geometry, which in the present case is known accurately from XRD data. The equation assumes a point charge model. The value of \mathbf{q}_E requires the wavefunction for the molecule to be calculated. This is possible through ab initio calculations with packages such as Gaussian 94. Brown et al.²¹ have investigated the effects of the size of basis set, and elimination of

systematic errors. The size of basis set is important as large molecules are under consideration and the calculation time is significant, whilst systematic errors are harder to quantify as no similar compounds have been studied for comparison of experimental and calculated values.

For small basis sets, ignoring electron correlation with the Hartree-Fock approximation will give a small error compared to that from basis set truncation. The best results were found to come from using a triple-zeta basis set such as [5s3p/3s] from Dunning, with 4-31g (double-zeta) giving a reasonable result and STO-4G giving a noticeably worse result.²¹ Zeta refers to the number of atomic orbitals used, with single-zeta being the norm and multiple-zeta basis sets adding extra orbitals. It is also possible to add extra polarised functions, which may be important for second-row atoms. For molecules with first-row atoms only,²¹ the results were only slightly better with polarisation, which was therefore not worth the extra computational expense. This can be understood, as polarisation functions are quite diffuse and the equations for the EFG have an r^{-3} dependence. For the same reason, improving the calculation locally for large molecules will give better results. For a test calculation with HCN, a mixed basis set was used with a 4-31g basis for the ^{14}N centre and the less demanding STO-4G basis on other atoms. The value of the EFG tensor was within 10% of that found for the larger basis set.

From Table 26 it can be seen that the value predicted for the EFG has converged using the 6-31g* basis set. Larger sets give only marginally improved results for a much larger computational effort. The extra-polarised forms of the basis sets have been used, as NMR and EFG results were calculated simultaneously. The extra-polarised functions in the basis sets would not be expected to give a much better result than the normal basis set as the EFG is dependent on r^{-3} , as mentioned above. It has been shown here that errors due to the truncation of the basis set are small when using the 6-31g* basis set and the Hartree-Fock limit has been reached. Thus, differences between the calculated and real values for the EFG are likely to be due to the approximations in the method used for the calculation. Calculations using three-parameter hybrid DFT methods are currently being investigated. The

Configuration Interaction (CI) method is too demanding on resources to be usable for this size of molecule.

Table 26: Values for the largest component of the EFG in atomic units (a. u.) calculated with Gaussian 94 using the Hartree-Fock approximation and the basis sets shown.

Compound	STO-3G	3-21g*	6-31g*	6-311g*
I	1.92	0.88	0.92	0.93
II	1.65	-0.59	-0.63	-
III	-1.65	-0.70	-0.71	-0.77
IV	-1.58	-0.41	-0.44	-
V	-1.12	-0.36	-0.38	-

Systematic errors can be eliminated by regression analysis between calculated and known experimental values. The correction factor is usually incorporated into a scaled value for Q . High level ab initio calculations and experiments on small molecules, e.g. ammonia, have been used to calculate $Q(^{14}\text{N})$. The IUPAC²² recommended experimental value for $Q(^{14}\text{N})$ is $2.01 \times 10^{-30} \text{ m}^2$. However, the recommended value has doubled in the last 15 years as more accurate results and calculations have become possible.

For the scaled value of Q , two factors should be used, one for each of q_{N} and q_{E} . In theory, the factor for q_{N} does not need scaling when the geometry is accurately known, as it is not dependent on the wavefunction. The errors are largely contained in the value for q_{E} . However, Brown et al.²¹ found that the variance when scaling q_{total} compared to q_{E} was similar and in fact smaller for q_{total} with 28 different compounds. This was presumed to be caused by non-systematic basis set truncation effects. They suggest using the value of $Q(^{14}\text{N}) = 1.61 \times 10^{-30} \text{ m}^2$.

Power,³ in the absence of any ^{14}N -P(V) data, used the experimental data from $\text{HN}=\text{SOF}_2$ ²³ with ab initio calculations using the 6-31g basis set to scale the values of Q and hence derive a value for $\text{HN}-\text{PH}_3$. They found that the calculated value for the EFG was overestimated by 40% for $\text{HN}=\text{SOF}_2$, in common with the results above.

This gave a value of $\chi = 3.17$ MHz and $\eta = 0.92$ for HN-PH₃. No value was given in the paper for Q and there was insufficient information to enable its calculation.

For the values of χ given in Table 25, we have used the value of $Q(^{14}\text{N}) = 1.61 \times 10^{-26} \text{ cm}^2$. We believe this is more consistent than basing the scaling on only one compound. The EFG tensor values have been calculated using the Hartree-Fock approximation and 6-31g* basis set with the crystallographic structures. The orientation of the EFG tensor relative to the P-N bond can be found from the calculation and gives the values of α^{D} and β^{D} listed.

The EFG tensor was also calculated using an optimised geometry and found to give similar results. To simplify the calculations further, the phenyl groups were changed for either methyl groups or protons. There was little difference in the results when substituting methyl groups into the calculation, though using only protons did give a noticeably different result. The time for calculations scales as the fourth power of the number of basis functions, so reducing the basis set size or changing phenyl groups for methyl groups can reduce the calculation time from days to hours.

7.3 Carbon-13

All of the compounds studied had phenyl rings directly bonded to the phosphorus. Using a non-quaternary suppression sequence (NQS) with a dephasing time of 50 μ s removed carbon peaks directly bonded to protons and left just the quaternary carbons. These include the carbon atoms that are directly bonded to the phosphorus atom. An expansion of the phenyl region of the ^{13}C NMR spectrum for compound **I** recorded with CPMAS and proton decoupling is shown in Figure 45(a). The other two spectra are recorded with NQS and isolate the quaternary carbons.

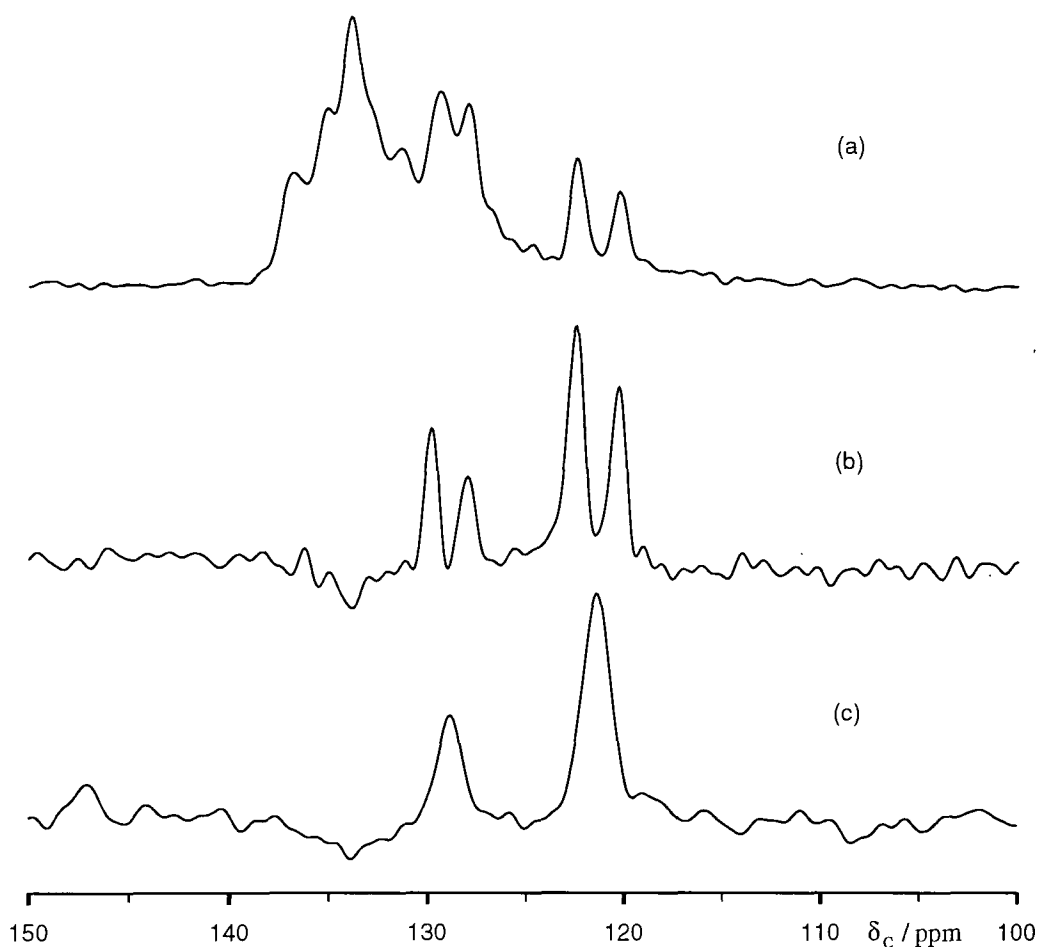


Figure 45: ^{13}C $\{^1\text{H}\}$ NMR spectra of compound **I** with the sample spinning at 4 kHz. (a) CPMAS, (b) NQS, and (c) NQS with additional ^{31}P decoupling. Acquisition parameters used for all spectra were: pulse duration 5 μ s, contact time 1 ms, dephasing time 50 μ s, recycle delay 5 s, and number of acquisitions (a, b) 1500 and (c) 1328.

The peaks in Figure 45(b) appear as doublets due to $^1J(\text{PC})$ coupling. The dip around $\delta = 134$ ppm is due to incomplete suppression of the other phenyl ^{13}C peaks. The ^{31}P decoupled spectrum can be seen in Figure 45(c). Integration yields a ratio of 0.8 : 2 for the peaks at $\delta = 128.7$ and 121.4 ppm in Figure 45(c), respectively. Theoretically, a ratio of 1:2 would be expected, corresponding to the single phenyl group lying along the mirror plane and the other two phenyl groups. In practice, as cross polarisation and an echo have been used, the integrals are only approximate.

The ^{13}C NMR spectra of compound **II** are further complicated by the substituted aromatic rings bonded to the oxygen. These give extra quaternary peaks at $\delta = 118$, 137 and 165 ppm for the para, ortho and directly-bonded carbons respectively, and non-quaternary peaks at $\delta = 22.2$, 32.3 and 35.7 ppm from the methyl and t butyl carbons. The proton-decoupled NQS spectrum shows five peaks in the range 129 to 135 ppm. The peaks are at $\delta = 129.5$, 131.1, 133.0, 133.6 and 134.8 ppm, with that at 131.1 ppm having approximately twice the intensity of the other peaks. Phosphorus decoupling would further simplify the spectrum but was not undertaken as the sample is air sensitive. Thus, the quaternary carbon shifts are tentatively assigned as $\delta = 130.3$, 132.1 and 134.2 ppm. The size of the coupling constants follow the same trend as for compound **I**, though the coupling for the carbon atom at $\delta = 132.1$ ppm is greater than that for the low-frequency carbon atom.

For compound **III**, the ^{13}C NMR spectra have very poor signal-to-noise ratios owing to the long recycle delay that is required. The double-decoupled NQS spectrum shows three sharp peaks at $\delta = 128.3$, 130.6 and 135.6 ppm. It was not possible to estimate the values for the scalar coupling constants from the proton-decoupled spectra.

Most of the phenyl carbon shifts lie in the range 130 to 140 ppm. For compound **IV**, the signal-to-noise ratio is again poor, and the quaternary carbon peaks are believed to lie under the peaks that arise from the other carbon atoms. The proton-decoupled NQS spectrum shows three sharp peaks at $\delta = 137.8$, 139.7 and 145.9 ppm, but there are also three smaller peaks at $\delta = 136.8$, 138.7, and 144.7 ppm. It is not known which of these peaks form the doublets arising from the quaternary carbon atoms.

As the signals from the quaternary carbon atoms are shifted to high-frequency, they can be clearly seen in the normal ^{13}C CPMAS NMR spectrum. From the two doublets, $\delta = 140.9$ and 143.4 ppm and $^1\text{J}(\text{PC}) = 34$ and 70 Hz respectively. The extra peaks for compound **V** at $\delta = 25.2$ and 68.1 ppm arise from the carbon atoms in the co-crystallised thf.

Table 27: Quaternary ^{13}C chemical shifts and coupling constants.
The assignments are uncertain for compounds **III** and **IV**.

Compound	$\delta_{\text{iso}} / \text{ppm}$	$^1\text{J}(\text{PC}) / \text{Hz}$	$\delta_{\text{iso}} / \text{ppm}$	$^1\text{J}(\text{PC}) / \text{Hz}$	$\delta_{\text{iso}} / \text{ppm}$	$^1\text{J}(\text{PC}) / \text{Hz}$
I	121.4	108	121.4	108	128.7	72
II	130.3	80	132.1	95	134.2	60
III	(128.3)	-	(130.6)	-	(135.6)	-
IV	(137.8)	-	(139.7)	-	(145.9)	-
V	140.9	34	143.4	70	143.4	70

The ^{13}C NMR data for all the compounds are summarised in Table 27. Literature values²⁴ for $^1\text{J}(\text{PC})$ range from -40 to 500 Hz, whilst those for $^2\text{J}(\text{PC})$ lie between -20 and 90 Hz, which confirms that the couplings are only across one bond. The ^{13}C NMR shifts are plotted in Figure 46 against the P-N bond lengths and in Figure 47 against the P-C bond lengths as given in Table 23.

From these data, it can be seen that there is a clear trend between average quaternary carbon shift and both the P-N and P-C bond lengths. It has already been noted that the P-C bond length increases as the P-N bond length shortens. As the P-N bond length shortens, due to greater electrostatic interaction between the phosphorus and nitrogen atoms, the carbon atoms become more deshielded. There is expected to be no influence of one phenyl ring on another due to ring currents as they are far apart in space and twisted, like a propeller, relative to each other.

In addition, the shift data for compound **I** show that the unique quaternary carbon atom is deshielded and has a weaker coupling to the ^{31}P compared to the two other carbon atoms. This shows that the nature of the P-N bond is reflected in the

P-C bonds. This agrees with the theory of the electronic structure and the XRD results discussed before, where one longer P-C bond length is seen compared to the other two. The reverse situation is observed for compound **V**, which could not be explained by the same arguments. The differences in the ^{31}P NMR shifts of this compound were not obviously reflected in two sets of ^{13}C NMR peaks. The data for compounds **III** and **IV** need to be remeasured before any comments are possible for these compounds.

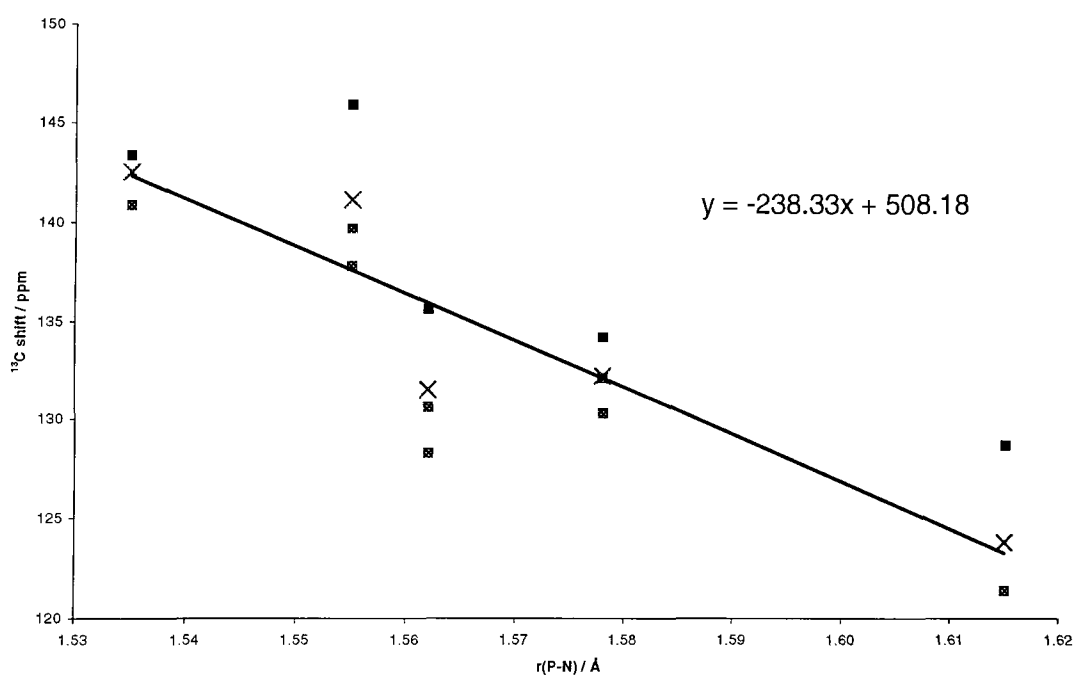


Figure 46: Plot of the ^{13}C shift against P-N bond length. The trendline is for the crosses that are the average ^{13}C shift over the three quaternary carbons. The square symbols show the individual values of the ^{13}C shifts.

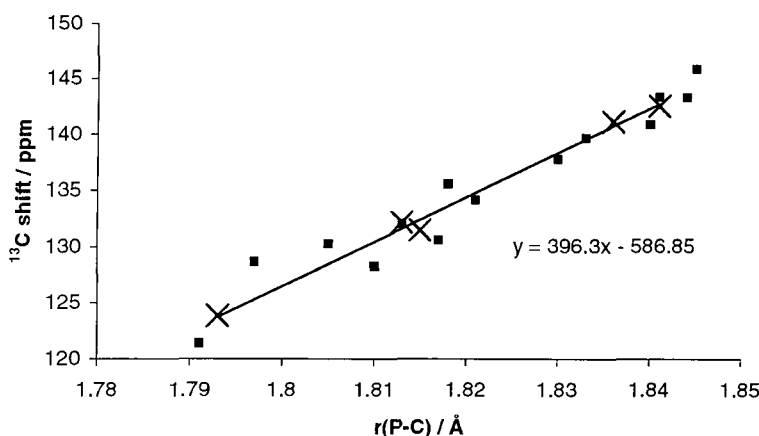


Figure 47: Plot of the ^{13}C shift against P-C bond length. The trendline is for the crosses that are the average ^{13}C shift and bond length over the three quaternary carbons for each compound. The square symbols show the individual values of the ^{13}C shifts and are plotted against the individual bond lengths. The assignment of shifts to bond lengths is based on the general trend observed here, i.e. increasing shift with bond length.

7.4 Other NMR results

The solid-state ^{15}N CPMAS NMR spectrum of compound **I** has been measured on the 300 MHz spectrometer. With the NMR spectrum measured for one day, the signal was barely sufficient to measure the isotropic shift ($\delta = -340$ ppm) and too weak to measure the shielding anisotropy. This is as might be expected for natural abundance ^{15}N NMR measurements. From the ab initio calculations, given in Table 28, it can be seen that the calculated values of the isotropic shift cover a reasonable range and the anisotropy is small. The errors in calculating the isotropic shift, discussed in chapter 3, are large (approaching 50 ppm), but the relative errors are smaller than this. Thus, differences would be expected in the ^{15}N NMR spectra of these compounds, if they could be measured for the other air-sensitive compounds.

Table 28: Ab initio calculated values for ^{15}N based on the crystal structures and using the hf/6-31g* level of theory. The shift values are based on the shielding value for NH_3 of 264.5 ppm being -380.2 ppm on the shift scale (CH_3NO_2 is set to zero ppm on the shift scale).

Compound	σ_{iso} / ppm	δ_{iso} / ppm	ζ / ppm	η
I	283.1	-398.8	26	0.35
II	280.2	-395.9	17	0.70
III	246.5	-362.2	57	0.30
IV	240.2	-355.9	60	0.38
V	235.3	-351.0	76	0.26

As compounds **II** and **V** also contain lithium, the $^{6,7}\text{Li}$ NMR spectra have been recorded. The ^7Li NMR spectra of these compounds are shown in the next chapter along with those of some other lithium containing compounds. The values of χ have been estimated to be 280 and 225 kHz for **II** and **V** respectively, in good agreement with the ab initio data.

7.5 Conclusions from the NMR data

The electronic structures for these compounds have been described at the start of this chapter. Now, with the benefit of NMR data, they are revisited. The NMR spectra have been measured for the carbon, phosphorus and (indirectly) nitrogen atoms. In addition, these spectra can provide information about the strength of bonds between these atoms. The discussion here refers to compound **I** as it has been extensively studied. The tensor information for compound **I** is shown in Figure 48, superimposed on its XRD structure.

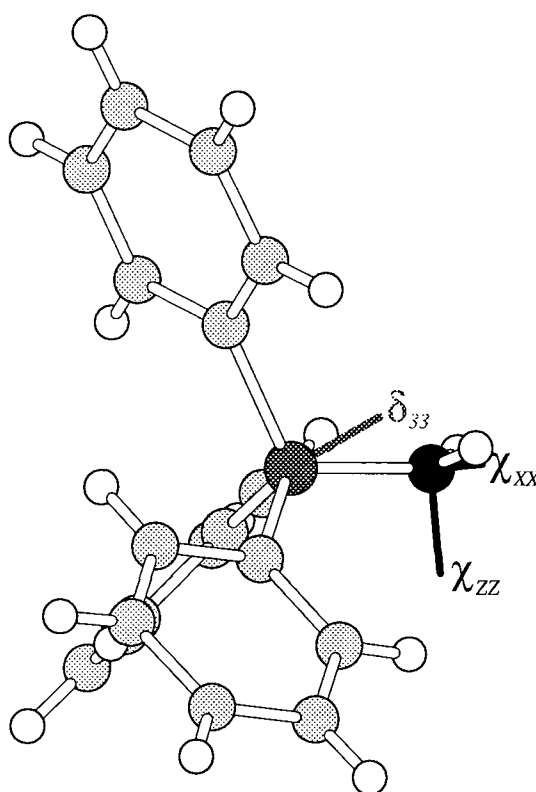


Figure 48: Structure of **I** from the XRD data, with the directions of the shielding and quadrupolar tensors superimposed. The black atom is nitrogen, grey atom is phosphorus, light grey atoms are carbon and white atoms are hydrogens.

From the different quaternary ^{13}C NMR isotropic shifts it can be seen that there is reduced symmetry about the phosphorus atom. Two peaks are visible, with a 1:2 intensity ratio. From consideration of the $^1\text{J}(\text{PC})$ coupling constants, the higher intensity peak has shorter bonds than the lower intensity peak. There is also a good

correlation between the NMR shifts and the experimental XRD P-C and P-N bond lengths across all the compounds. This correlation and the carbon shifts could be used to predict bond lengths and the local symmetry about the phosphorus atom from the NMR data.

The ^{31}P NMR spectra yield the most information. Analysis of either the spinning or static spectra gives the shielding anisotropy and asymmetry. This gives more information about the electronic structure around the phosphorus atom than just the isotropic shift. The anisotropy increases as the bond order increases and the bond length becomes shorter. It has been suggested that these shorter bond lengths could be due to either greater electrostatic interactions between the phosphorus and nitrogen atoms, or by π back-bonding from the nitrogen atom to phosphorus. In either case, with shorter bond lengths, the phosphorus atom is observed by NMR to be more shielded. Further analysis of the static spectrum also yielded the orientation of the shielding tensor relative to the dipolar tensor. The largest component of the shielding tensor is found to lie along the P-N bond vector. The P-N bond length can be found from the P-N dipolar coupling constant. The error in calculating the bond length is large compared to that from XRD data and is estimated as ± 0.02 Å.

From the ^{31}P MAS spectrum, residual dipolar coupling gives indirect information about the ^{14}N atom. The splitting observed in the ^{31}P MAS spectrum is dependent on the size and orientation of the quadrupolar tensor relative to the dipolar tensor. This gives many parameters to fit to only one measured parameter. In practice, assumptions must be made about the system in order to estimate some parameters. Here we have used the XRD-derived structure to calculate the dipolar coupling constant, and ab initio calculations for the quadrupolar tensor and its orientation. Using these data gives a value for the splitting that can be compared to the experimental value. For compound **I**, the tensor is predicted to lie at 95° to the P-N bond vector, shown as χ_{zz} in Figure 48, which is roughly aligned with the direction expected for the nitrogen lone pair. In this case, the experimental and calculated splittings are in broad agreement, considering the errors involved in both the experimental and ab initio calculated values.

-
- ¹ For a review: E. Vedejs, *Science*, **207**, 42 (1980)
- ² D. R. Armstrong, M. G. Davidson, and D. Moncrieff, *Angew. Chem., Int. Ed. Engl.*, **34**, 478 (1995)
- ³ W. P. Power, R. E. Wasylishen, and R. D. Curtis, *Can. J. Chem.*, **67**, 454 (1989)
- ⁴ W. P. Power, *J. Am. Chem. Soc.*, **117**, 1800 (1995)
- ⁵ A. S. Batsanov, P. D. Bolton, R. C. B. Copley, M. G. Davidson, J. A. K. Howard, C. Lustig, and R. D. Price, *J. Organomet. Chem.*, **550**, 445 (1998)
- ⁶ A. S. Batsanov, M. G. Davidson, J. A. K. Howard, S. Lamb, C. Lustig, and R. D. Price, *J. Chem. Soc., Chem. Commun.*, 1211 (1997)
- ⁷ M. G. Davidson, A. E. Goeta, J. A. K. Howard, C. W. Lehmann, G. M. McIntyre, and R. D. Price, *J. Organomet. Chem.*, **550**, 449 (1998)
- ⁸ E. Pohl, H. J. Gosink, R. Herbst-Irmer, M. Noltemeyer, H. W. Roesky, and G. M. Sheldrick, *Acta Crystallogr., Sect. C (Cr. Str. Comm.)*, **49**, 1280 (1993)
- ⁹ C. J. Jameson, A. De Dios, and A. K. Jameson, *Chem. Phys. Lett.*, **167**, 575 (1990)
- ¹⁰ M. Pomerantz, B. T. Ziemnicka, Z. M. Merchant, W. Chou, W. B. Perkins, and S. Bittner, *J. Org. Chem.*, **50**, 1757 (1985)
- ¹¹ F. López-Ortiz, E. Peláez-Arango, B. Tejerina, E. Pérez-Carreño, and S. García-Granda, *J. Am. Chem. Soc.*, **117**, 9972 (1995)
- ¹² A. E. Hansen and T. D. Bouman, *J. Chem. Phys.*, **82**, 5035 (1985)
- ¹³ A. C. Olivieri, L. Frydman, and L. E. Diaz, *J. Magn. Reson.*, **75**, 50 (1987)
- ¹⁴ R. K. Harris and A. C. Olivieri, *Prog. NMR Spect.*, **24**, 435 (1992)
- ¹⁵ A. C. Olivieri, *Concepts in Magn. Reson.*, **8**, 279 (1996)
- ¹⁶ S. Vega, *J. Chem. Phys.*, **60**, 3884 (1974); R. K. Harris, P. Jonsen, and K. J. Packer, *Magn. Reson. Chem.*, **23**, 565 (1985)
- ¹⁷ I. A. Nuretdinov, O. N. Nuretdinova, I. A. Safin, and D. Ya. Osokin, *Russian J. Phys. Chem.*, **53**, 66 (1979)
- ¹⁸ S. G. Greenbaum and P. J. Bray, *Phys. Lett. A*, **75**, 438 (1980)
- ¹⁹ N. A. Davies, R. K. Harris, and A. C. Olivieri, *Mol. Phys.*, **87**, 669 (1996)
- ²⁰ A. C. Olivieri, *Solid State NMR*, **10**, 19 (1997)
- ²¹ R. D. Brown and M. P. Head-Gordon, *Mol. Phys.*, **61**, 1183 (1987)
- ²² I. Mills, T. Cvitas, K. Homann, N. Kally, and K. Kuchitsu, "Quantities, Units and Symbols in Physical Chemistry," Blackwell (for IUPAC), Oxford, pp. 98-104 (1993)
- ²³ P. Cassoux, A. Serafini, G. Fong, and R. L. Kuczkowski, *Inorg. Chem.*, **17**, 1204 (1978)
- ²⁴ K. Karaghiosoff, Phosphorus-31 NMR in "Encyclopaedia of NMR" (D. M. Grant and R. K. Harris, Eds.), 2612, Wiley, Chichester (1997)

8 Lithium NMR

Lithium is a widely used element in inorganic and organic chemistry. It has two NMR active nuclei, of which ${}^7\text{Li}$ is present in much higher natural abundance than ${}^6\text{Li}$. The chemical shift range for ${}^{6,7}\text{Li}$ is small, but the quadrupole moment, though small compared to other nuclei, is measurable and different for each isotope in the approximate ratio 50 (${}^7\text{Li}$) to 1 (${}^6\text{Li}$). These differences between the isotopes allow both interactions to be measured: ${}^6\text{Li}$ has a greater relative influence from shielding anisotropy than ${}^7\text{Li}$ because quadrupolar interactions dominate for the latter.

Measuring the NMR spectra for lithium is complicated by the quadrupolar coupling, which can spread the signal out over hundreds of kHz. With such wide spectral widths, the crucial first few points of the free-induction decay (FID) for static samples will be lost due to the probe ring-down time. The Q factor of the probe, effects of improper excitation and off-resonance terms must also be considered. Cross polarisation from ${}^1\text{H}$ to ${}^6\text{Li}$ has been used throughout the work described in this chapter. This technique was initially demonstrated using lithium diborate ($\text{Li}_2\text{B}_4\text{O}_7 \cdot 5\text{H}_2\text{O}$).¹ The ${}^6\text{Li}$ static NMR spectra are heavily broadened compared to the size of the quadrupole coupling constant (χ), which hampers accurate simulations and fitting of the lineshape. Dipolar coupling to ${}^7\text{Li}$ was thought to cause some of this broadening, so decoupling ${}^7\text{Li}$ was investigated.

Recent reviews concentrate on solution-state NMR measurements.² The isotropic shift has been extensively measured in solution-state studies and linked to different types of structure. However, the purpose of the work described here was to measure χ and the shielding anisotropy, and to relate these parameters to structure. By using static and magic-angle spinning (MAS) NMR observations of both isotopes, in a similar method to the triple-fit experiments described earlier for the organotin compounds, it should be possible to measure the relative orientation of the tensors. Using a combined fit of the data for both nuclei has the potential to give results that are more accurate than individual fits. In practice, it has only proved

possible to use the static and MAS spectra to measure χ and η_q , except for certain special cases. The simulated MAS spectra differ slightly from the experimental spectra, and the effects of changing the shielding anisotropy are too subtle to be fitted. It is possible that there may be a distribution of χ perhaps from crystal imperfections, internal motion, or flawed assumptions made in the simulations.

8.1 NMR properties

The two isotopes of lithium were mentioned briefly in the experimental chapter. Lithium-7 has a higher natural abundance than lithium-6 (92.58 cf. 7.42%), and the larger quadrupole moment. The product of the electric field gradient and the quadrupole moment gives the quadrupole coupling constant. The ratio of the quadrupole moments is ca. 50: 1 for ${}^7\text{Li}$: ${}^6\text{Li}$, though the error in reported values for the quadrupole moment can be as high as 30%. The receptivity of both isotopes is better than that for ${}^{13}\text{C}$, with the receptivity of ${}^7\text{Li}$ being similar to that for protons. It is possible, in some cases, to measure a ${}^7\text{Li}$ MAS NMR spectrum with good signal-to-noise with just one transient.

As an indication for the following discussion, typical quadrupole coupling constant values for ${}^7\text{Li}$ are up to 330 kHz. Those for ${}^6\text{Li}$ are a fraction of this i.e. up to 6.6 kHz. For this reason, ${}^6\text{Li}$ is often treated as an “honorary spin- $1/2$ ” nucleus. With the Chemagnetics 200 MHz system, the resonant frequency for ${}^6\text{Li}$ is 29.451 MHz. The chemical shift range is measured with respect to an aqueous 1 M solution of LiCl at 0 ppm. Most common compounds have shifts in the range 5 to -10 ppm, though it is known that ring current effects can induce low-frequency shifts of up to 5 ppm.³ This corresponds to a total shift range of 500 Hz at this field. For ${}^6\text{Li}$, the shielding anisotropy is comparable to the size of χ so both interactions need to be considered. However, for ${}^7\text{Li}$, the anisotropy is dwarfed by the much larger quadrupolar interaction.

The sensitivity of ${}^7\text{Li}$ is higher than that for ${}^6\text{Li}$, though the linewidths in ${}^7\text{Li}$ NMR spectra are generally greater than those for ${}^6\text{Li}$. This makes ${}^6\text{Li}$ the nucleus of

choice for NMR studies of the shielding tensor. However, for the quadrupolar tensor, studying ^7Li NMR is preferable as the ratio of χ to linewidth is generally higher for this nucleus than for ^6Li .

For the static spectra, the turning points can be used to estimate the size of χ . Previously recorded ^7Li static NMR spectra have been complicated by extra unexplained features.⁴ For the static NMR spectra of ^7Li all three transitions should, in principle, be visible. The sharp centreband peak gives the isotropic chemical shift and is unaffected by the quadrupolar interaction. Second-order quadrupolar effects are generally too small to affect spectra significantly. For ^6Li , there is no sharp centreband peak and the static NMR spectrum can appear similar to the Pake doublet from the dipolar interaction. Often the line broadening factor (arising from dipolar interactions, for example) is similar in size to the quadrupolar interaction and only a broad peak is observed.

8.2 Experimental techniques

8.2.1 Broad lines

With the large spectral width that is necessary when recording the NMR spectra of quadrupolar nuclei, the loss of data points during the probe ring-down time is noticeable. This ring-down time varies between probes and is between 8 and 15 μs . For a spectral width of 500 kHz, the dwell time is 2 μs and so between 4 and 7 points of the FID are lost. Various methods are available to correct for this lost signal. Though many of the methods rely on the value of the transverse relaxation time, T_2 , being long relative to the delays in acquiring the FID.

Using an echo will refocus the magnetisation and allow the FID to be acquired after the probe ring-down time. The position of the top of the echo is hard to predict, as it is dependent on the offset of the signal from the transmitter. With spinning samples, the echo time must be a multiple of the rotor cycle. This echo time is much longer than the probe ring-down time and the delay in acquisition will

reduce the signal intensity. This delay can be a problem for weak signals. The echo techniques assume that the pulse is 'hard' and excite all frequencies evenly. This assumption may not be valid and is discussed later.

Other methods work by correcting for the lost points in the FID after it has been acquired. For a spinning sample, rotor echoes appear in the FID at multiples of the spinning speed. From the position of these rotor echoes, the lost time at the start of the FID can be found. By shifting the point where $t = 0$ to the top of the next rotor echo, the problems with dead-time is alleviated. This is only possible if there is only one signal in the spectrum, or if the signals are related by multiples of the spinning speed, e.g. spinning-sideband peaks.

First-order phase correction effectively shifts the position of the FID relative to the acquisition time. It can be used to correct the phasing across a spectrum but often introduces a baseline roll at the same time. Applying a polynomial baseline correction will remove this baseline roll, but then the spectrum has been extensively processed. These sinusoidal distortions were noted by Hoult,⁵ who discussed the elimination of baseline artefacts. A more recent article⁶ looks at the optimum setting of the timing delays between the final pulse and acquisition. It is often the case that the FID is $\frac{1}{2}$ point offset so that 180° of first-order phasing is also required to correct the phase of all the sidebands. This occurs as the start of the FID effectively starts at the centre of the final pulse.

Another method reinserts the lost points into the FID and calculates their intensities by back linear prediction. This method has been used out of choice as the signal-to-noise ratio is often insufficient to use echo techniques. For the few points that are lost at the start of the FID, the intensity is predicted from the following 400 points with 40 poles used in the prediction. This is the 'best' processing panel option available in Spinsight. The 'good' option uses 200 points and 28 poles. In general, using about 25% of the acquisition time as valid points will give the best results without introducing too much noise. Care is needed as any broad components in the spectrum might disappear if you back predict too many points.

8.2.2 Probe tuning and excitation profile

When a spectrum is measured, the signal intensity that is observed depends on the probe tuning and excitation profile. For signals that span a small spectral width, corrections for these effects are not required. However, for large spectral widths this is not the case, and some form of correction is necessary. This effect has already been noted for the ^{119}Sn NMR spectra of the organotin compounds, which have signals spreading over a wide frequency range. From the observations on ^{119}Sn , the HX probe-tuning range has been found to be 100 kHz. The excitation profile for the HX probe is shown in Figure 49. It was measured by observing the central peak signal intensity of ^7Li MAS NMR spectra in lithium diborate, $\text{Li}_2\text{B}_4\text{O}_7 \cdot 5\text{H}_2\text{O}$, whilst changing the transmitter offset. For each measurement, the transmitter was offset by a range of values and the probe was retuned before measuring each point. This removes any effects of the probe-tuning profile. Fewer points have been measured to low frequency as the end of the probe-tuning range with this set of capacitors was reached. The curve shown in Figure 49 is a sinc function that is calculated based on the pulse duration being 5 μs . It can be seen that this is a good fit to the data. A similar experiment with the pulse duration equal to 1 μs was also measured and shows a flatter profile with no null points. The phasing of the peaks varied with the offset.

The excitation profile has been considered for quadrupolar nuclei in MAS NMR spectra.⁷ For short pulses relative to the rotor period, the MAS time dependence can be ignored. In fact, with short pulses (1 μs) the whole MAS spectrum can be phased to absorption by using first-order phasing of $-360^\circ \cdot \text{dwell} \cdot (\tau_p/2)$. This is equivalent to setting the start of the FID at the centre of the pulse. By comparing the simulated spectra, shown in ref. 7, measured with either an ideal pulse or real pulses and first-order phase correction, it can be seen that some intensity has still been lost with increasing offset. This shows that the excitation efficiency of the pulse is not perfect, though some of this intensity loss is due to the probe-tuning profile.

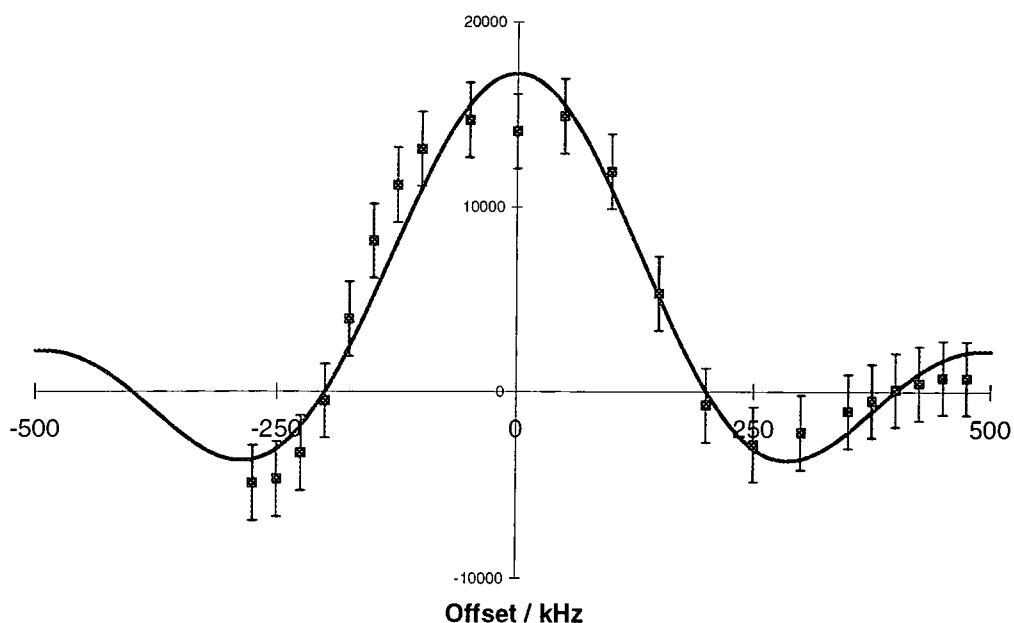


Figure 49: HX probe-tuning profile for ${}^7\text{Li}$ measured as described in the text. The line is a sinc function with only the amplitude adjusted to achieve the best fit to the data.

8.2.3 Cross polarisation

Cross polarisation has been widely used to measure the ${}^{119}\text{Sn}$ and ${}^{31}\text{P}$ NMR spectra. With quadrupolar nuclei, the theory of CP is more complicated. Fortunately, for ${}^6\text{Li}$, the quadrupole moment is small and it can be treated as a spin- $1/2$ nucleus. It has been shown for lithium diborate that the ${}^6\text{Li}$ NMR signals can be enhanced by CP from protons.¹ This compound has most of the properties required for a CP matching standard, namely its ready commercial availability and good air stability.

The CP profile has been measured with the optimum contact time found to be 2 ms. The longitudinal relaxation time for ${}^6\text{Li}$ is often long as there are few mechanisms for the relaxation, since both the shielding anisotropy and quadrupolar tensors are small. For this compound $T_1({}^1\text{H}) = 2$ s whilst $T_1({}^6\text{Li}) = 600$ s. From these relaxation times, the advantage of using CP can be easily seen. Few spinning sidebands are observed in the ${}^6\text{Li}$ spectrum, even with slow spinning speeds of 1.5 kHz.

The bound water molecules are used as a source of proton spins, but at moderate spinning speeds (above 3 kHz), the Hartmann-Hahn match profile breaks up into sidebands. This profile can be seen in Figure 50 for which the sample is spinning at 5 kHz and the intensity of the signal is measured as the ${}^6\text{Li}$ CP power is varied. The maxima can be seen above and below the match point. In theory, they should appear at multiples of the spinning speed. This is believed to be the case and shows that the calculated powers, calibrated by measuring 90° pulse durations for ${}^6\text{Li}$, are inaccurate (perhaps due to offset effects).

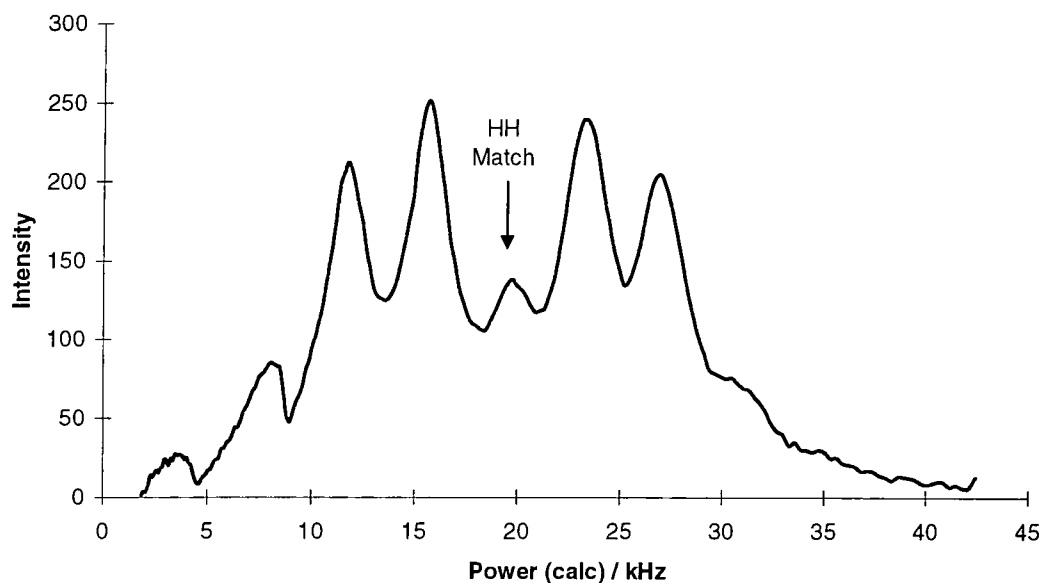


Figure 50: Hartmann-Hahn match profile for CP from protons to lithium-6 in lithium diborate. The powers are matched at 20 kHz as shown by the arrow.

Penner⁸ has suggested the use of lithium acetate dihydrate ($\text{CH}_3\text{COOLi}\cdot 2\text{H}_2\text{O}$) as a CP standard. This compound is commercially available and air stable. It gives a narrower linewidth than lithium diborate, which in turn gives a better signal-to-noise ratio. The optimised conditions, as given in the paper, are contact time = 10 ms and recycle delay = 90 s. Additional data from a variable contact time experiment were $T_{\text{HLi}} = 3.4$ ms and $T_{1\rho}({}^1\text{H}) = 89.5$ ms. Measurements in Durham confirmed these values and found the proton longitudinal relaxation time to be $T_1({}^1\text{H}) = 80$ s. The proton recycle delay is much longer than that found for lithium

diborate, but is compensated for by the better signal-to-noise ratio. No change in the ${}^6\text{Li}$ NMR signal was observed for recovery times up to 600 s, indicating that $T_1({}^6\text{Li})$ is long. The spectra of both compounds are discussed and analysed in detail in later sections.

8.2.4 Decoupling ${}^7\text{Li}$ whilst observing ${}^6\text{Li}$

In some of the compounds, there is the possibility of two lithium atoms being closely spaced. As ${}^7\text{Li}$ has a much higher natural abundance than ${}^6\text{Li}$, dipolar effects from ${}^7\text{Li}$ could be significant. For the ${}^7\text{Li}$ NMR spectra, this could result in extensive homonuclear dipolar broadening, whereas for ${}^6\text{Li}$ NMR spectra, the linewidth could be broadened by heteronuclear dipolar coupling. Dipolar ${}^6\text{Li}$ - ${}^6\text{Li}$ coupling would be relatively insignificant due to the low magnetic moment and natural abundance. For lithium acetate, this was suggested as one of the main line-broadening mechanisms.⁸ The crystal structure for this compound has not been published, so the distance between the lithium atoms is unknown. For the compound $[\text{LiBH}_4\cdot\text{TMEDA}]_2$, the crystal structure shows that the lithium atoms are 3.09 Å apart,⁹ which gives a ${}^6\text{Li}$ - ${}^7\text{Li}$ dipolar coupling constant of 233 Hz.

The HXY probe is capable of observing ${}^6\text{Li}$ with double decoupling of ${}^1\text{H}$ and ${}^7\text{Li}$. To isolate the channels high-power filters are required. These already existed for the ${}^1\text{H}$ and ${}^7\text{Li}$ channels at 200.13 and 77.78 MHz respectively. However, making a high-power narrow-pass filter for ${}^6\text{Li}$ is hindered by its low frequency. Instead, a low-pass filter was chosen with a cut-off point at 42 MHz. This combination of filters with the HXY probe allowed the use of 6 μs pulses on all channels, with continuous double decoupling for up to 50 ms.

The doubly-decoupled ${}^6\text{Li}$ static and MAS NMR spectra of lithium acetate and lithium diborate were recorded. For comparison, the proton-decoupled spectra were also recorded. Figure 51 shows the ${}^6\text{Li}$ static NMR spectrum of lithium acetate recorded with both proton and double (proton and lithium-7) decoupling. The doubly-decoupled spectrum may be slightly narrowed compared to the singly-

decoupled spectrum, but it has extra intensity around the transmitter (placed at 0 kHz), which obscured the Pake-like static powder lineshape. Table 29 gives the linewidth at half-height with different decoupling schemes and spinning speeds. From this, it can be seen that using ^7Li decoupling had little effect on the overall linewidth for these compounds. This finding is in agreement with recent results observed for lithium-intercalated SnS_2 .¹⁰ The best linewidths achieved by using fast MAS, double decoupling and no line broadening were 12 Hz for lithium acetate and 20 Hz for lithium diborate. Spinning the sample faster than 4 kHz gave no further improvement in linewidth.

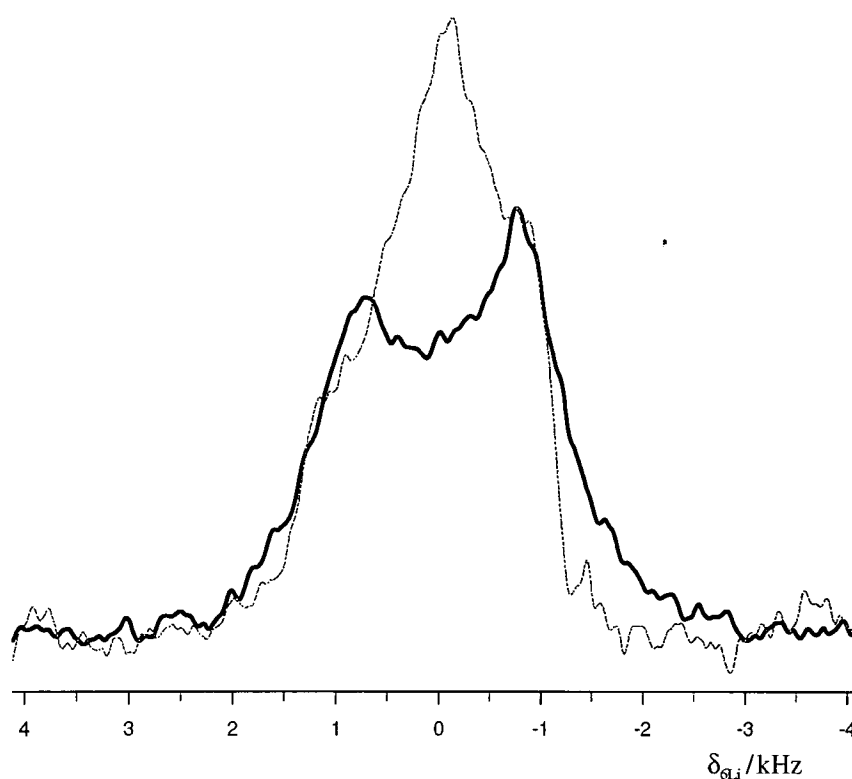


Figure 51: Static ^6Li NMR spectrum of lithium acetate recorded with a quad echo and either proton (bold line) or double (proton and lithium-7, narrow line) decoupling. Acquisition parameters were: pulse duration 6 μs , contact time 10 ms, echo time τ 60 μs , recycle delay 90 s, number of acquisitions 864. For the doubly-decoupled spectrum, acquisition parameters were: pulse duration 6 μs , contact time 10 ms, echo time τ 50 μs , recycle delay 30 s, number of acquisitions 1696.

Table 29: Summary of the ${}^6\text{Li}$ NMR linewidth for lithium diborate and lithium acetate at different spinning speeds. Note that 20 Hz of exponential line broadening was added, in each case, during processing.

Speed / kHz	Lithium diborate					Lithium acetate	
	Static	1.5	2	4	6	2	4
${}^6\text{Li}$	-	370	300	99	63	-	-
${}^6\text{Li} \{ {}^1\text{H} \}$	2340	50	49	44	47	32	29
${}^6\text{Li} \{ {}^1\text{H}, {}^7\text{Li} \}$	1970	43	42	37	35	27	25

8.3 Second-order quadrupolar effects

With large quadrupole coupling constants, first-order approximations are no longer valid and second-order effects are visible in the NMR spectra. This has already been indirectly observed for the residual dipolar coupling of ${}^{31}\text{P}$ to ${}^{14}\text{N}$ discussed in the previous chapter. For ${}^{6,7}\text{Li}$ these effects are small, but are mentioned in passing. For them to be observable χ must be sufficiently large, usually when compared to the Zeeman frequency. During a pulse, that is on resonance, χ must be large when compared to the B_1 rf field strength.

The isotropic shift is commonly the first parameter that is measured in an NMR experiment. However, with quadrupolar nuclei, the experimentally observed isotropic shift is affected by the second-order quadrupolar shift. To correct for this, χ and η must be measured. The real isotropic shift is then given by Equation 7.¹¹

$$\delta_{\text{iso}} = \delta_{\text{exp}} + \frac{1}{30} \left(1 + \frac{1}{3} \eta^2 \right) \cdot \left[I(I+1) - \frac{3}{4} \right] \cdot \left[\frac{3 \cdot \chi}{2I(2I-1)\omega_0} \right]^2$$

Equation 7

For ${}^7\text{Li}$, this effect is small; for example with $\chi = 100$ kHz, $\eta = 0$ and $\omega_0 = 77.78$ MHz, the correction is vanishingly small (0.04 ppm). In solution, rapid tumbling of the molecule averages out this effect.

For solid-state samples, this shift is also orientation dependent. The lineshape from the central transition can be simulated to extract δ_{iso} , χ and η_{q} . However, for small quadrupolar interactions, the second-order central transition cannot be resolved as it is more extensively broadened by other interactions. This is the case when $\chi / [4I(2I - 1)] > 50$ kHz. For ${}^7\text{Li}$ with $I = 3/2$, χ must be larger than 600 kHz. No ${}^7\text{Li}$ containing compounds have values for χ near to this value, the largest value reported herein being 330 kHz. On a positive note, this does mean that simulations of the ssb manifold do not need to include second-order effects for the ssb peak lineshapes. For comparisons between simulated and experimental ${}^{6,7}\text{Li}$ MAS NMR spectra, the peak intensities or integrals can be used to describe the spinning-sideband peaks.

In complex systems with multiple environments, these centreband lineshapes may overlap. A recent multiple-quantum MAS (MQMAS) experiment¹² has been used to separate out the isotropic centreband peaks from the second-order lineshape. There have been many subsequent variations of this experiment, e.g. to add a zero coherence filter,¹³ or to correlate the quadrupolar nucleus to a spin-1/2 nucleus.¹⁴ These pulse sequences have been implemented in Durham by Hanaya. The original technique has been used here to in an attempt to measure the ${}^7\text{Li}$ MQMAS NMR spectrum of lithium diborate, though unsurprisingly no second-order lineshapes or separate sites could be observed in the heavily broadened spectrum. The pulses used were strong and non-selective so that they would not have created the required triple-quantum coherence. For the small shift range and χ in ${}^7\text{Li}$, this experiment is unlikely to be able to separate out different sites.

Normally during a pulse, the magnetisation will nutate (precess) with frequency $\omega_{\text{rf}} = \nu_{\text{rf}} / 2\pi$. However, when χ is similar in size to ν_{rf} , the assumption that the pulse is infinitely short is no longer valid. In the limit when $\chi > \nu_{\text{rf}}$, the magnetisation will nutate with a frequency $(I + 1/2)\omega_{\text{rf}}$. A two-dimensional nutation experiment¹⁵ separates out the nutation and normal spectra. From this the ratio of χ / ν_{rf} may be calculated.

Figure 52 shows the nutation frequency for three compounds when the rf field strength is equivalent to 10 kHz. For these spectra the FID in the direct dimension was processed, then the intensity of the central transition was extracted. This lineshape, containing only real data points, was then Fourier transformed to give the spectra shown. The mirror image of the spectra is visible for negative frequencies (not shown). As there were only 40 data points in the indirect dimension, which was then zero filled to 1024 points, truncation artefacts (sinc peaks) are also visible.

Lithium chloride solution is stored in a sealed glass ampoule. From the mobility of the solution, the EFG tensor is averaged on the NMR timescale and the nutation frequency of 10 kHz is observed, i.e. the same as the rf field strength. For lithium diborate, with $\chi = 125$ kHz, using an rf field strength equivalent to 50 kHz gave hard, non-selective pulses (not shown). Only once the rf field strength had been reduced to 10 kHz, was a nutation frequency of 16 kHz observed. For $[\text{H}_2\text{C}(\text{CH}_2)_5\text{NLi}]_6$, where $\chi = 330$ kHz, the nutation frequency was measured to be 20 kHz. With these low powers, the nutation peaks for different samples and crystalline environments are too broad to separate out different possible values for χ . Any calculated values of χ will have large errors. This experiment also shows that for ^7Li , the pulses are non-selective except at very low rf powers. Only one ^7Li NMR nutation spectrum has been published that shows the resolution of three different ^7Li NMR signals in an amidinolithiate.¹⁶ For this compound, $\chi = 300$ kHz and $\nu_{\text{rf}} = 35$ kHz.

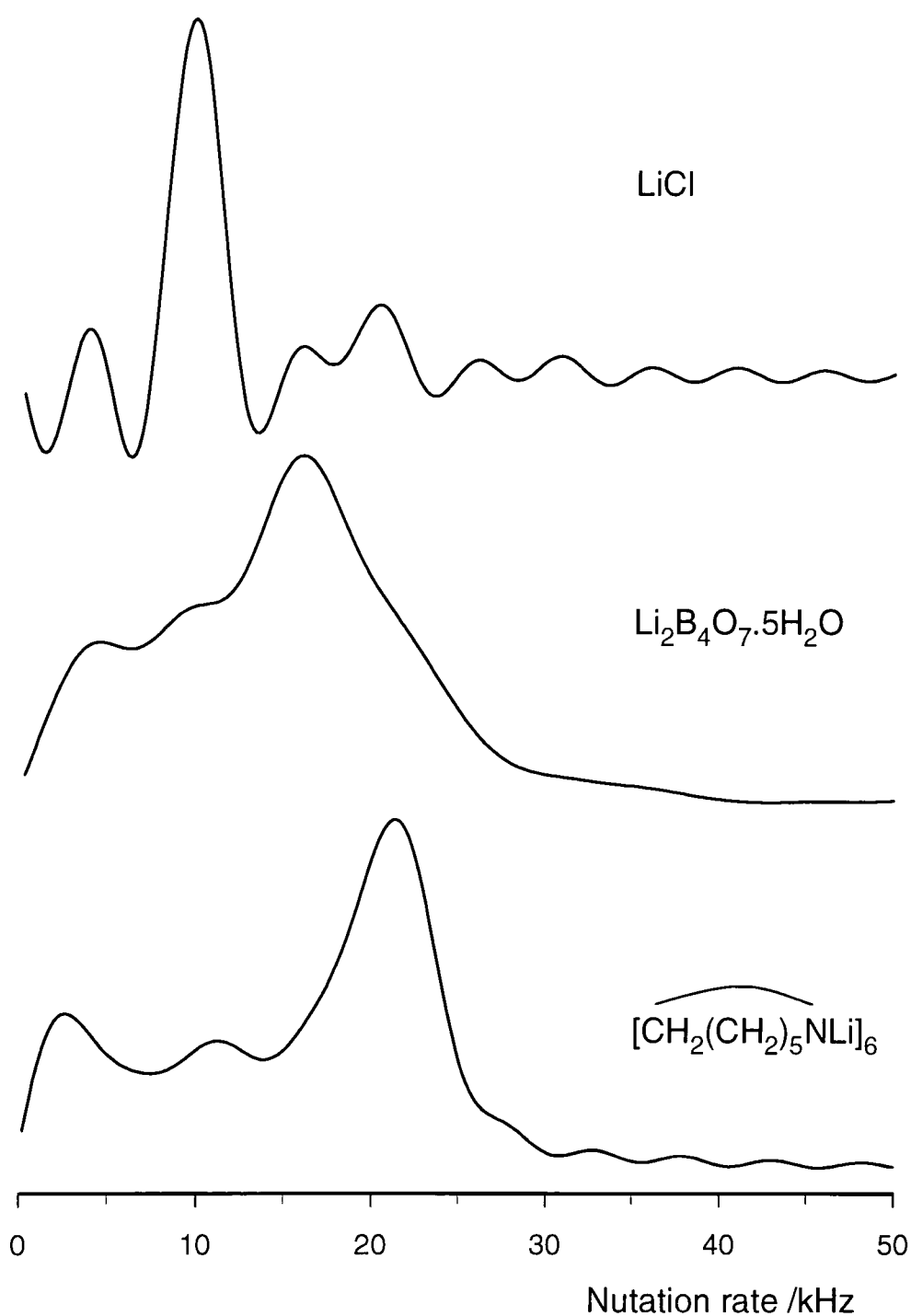


Figure 52: ^7Li nutation NMR spectra of the compounds shown. The rf field strength is equivalent to 10 kHz. Acquisition parameters were: (Common) pulse duration arrayed from 0 μs in 40 steps of 5 μs to 195 μs , number of acquisitions per step 16; (LiCl) recycle delay 2 s, static; (lithium diborate) recycle delay 30 s, spinning speed 4 kHz; (Hexamethyleneimidolithium) recycle delay 2 s, spinning speed 5 kHz.

8.4 Simulations and experimental results

Much of the work for this chapter was involved with writing the simulation program, JCSim. Although there are already programs that are capable of simulating shielding and quadrupolar interactions, none were available that could simulate a combination of the two tensors. At present, the program does not allow the tensors to be non-colinear. However, the experimental NMR spectra were found to be too heavily broadened to allow the relative orientations of tensors to be fitted. The program has purposely been written in a modular style so that this could be added later if required.

8.4.1 Use of both ^7Li and ^6Li measurements

As mentioned earlier, the quadrupole moments of ^6Li and ^7Li are in a fixed ratio and the chemical shift range for $^{6,7}\text{Li}$ is small. This means that, on the Chemagnetics 200 MHz system, for ^7Li the quadrupolar interaction will dominate and the shielding anisotropy can be neglected as a first approximation. For ^6Li , the shielding anisotropy is similar in size to the quadrupolar interaction so both must be considered. This combination of interactions reduces the symmetry that is usually observed in the spectra of quadrupolar nuclei. By increasing the external field strength, the shielding interaction becomes more dominant when compared to the quadrupolar interaction. If the NMR spectra of both nuclei are measured, the quadrupolar tensor can be estimated from the ^7Li spectrum and then used in the simulation of the ^6Li spectrum to find the shielding tensor.

The dipolar interactions have been ignored in the simulations. For moderate spinning speeds they will be effectively averaged by MAS, whilst in the static case, they contribute to the overall linewidth to give broad featureless lineshapes. For the ^6Li NMR spectrum of lithium diborate, there is so much line broadening that no turning points in the lineshape are observed.

8.4.2 Combinations of shielding anisotropy and χ

8.4.2.1 Static

The static ${}^6\text{Li}$ NMR spectrum of lithium acetate measured at 29.45 MHz is shown in Figure 53. A simulation of the lineshape is shown above the experimental spectrum, the simulation parameters being given in the figure caption and derived from the spectrum described below without further fitting. The experimental spectrum shows the classic Pake doublet that arises from the orientational dependence of the two transitions. The linewidth is sufficiently narrow to observe the two broadened turning points. On increasing the external magnetic field by a factor of 2.5, the difference in the intensities of the two peaks increases, which confirms that the shielding anisotropy is the main cause of this intensity difference. However, another possibility for the difference in peak intensities could be uneven CP to the different transitions. This cause has not been checked though is unlikely to be significant for the small spectral width observed here.

The spectrum measured at 73.63 MHz, shown as Figure 4 in reference 8, shows a greater difference in the intensity of the two peaks than the spectrum shown in Figure 53. For this reason, the spectrum measured at the higher external magnetic field has been simulated by us and found by eye to give a good fit when $\chi = 2.5$ kHz and the SA = 6.8 ppm. The quadrupolar asymmetry parameter is small, but could not be accurately fitted. It is assumed to be zero hereafter. Changing the shielding asymmetry parameter has a negligible effect on the simulated spectrum. Thus it was also assumed to be zero. Varying the relative orientation of the two tensors changes the intensity distribution of the two peaks. From this there are two possible parameter sets that give the same simulated spectrum: (a) with the tensors colinear, (b) with the tensors perpendicular ($\beta = 90^\circ$) and the sign of the shielding tensor reversed.

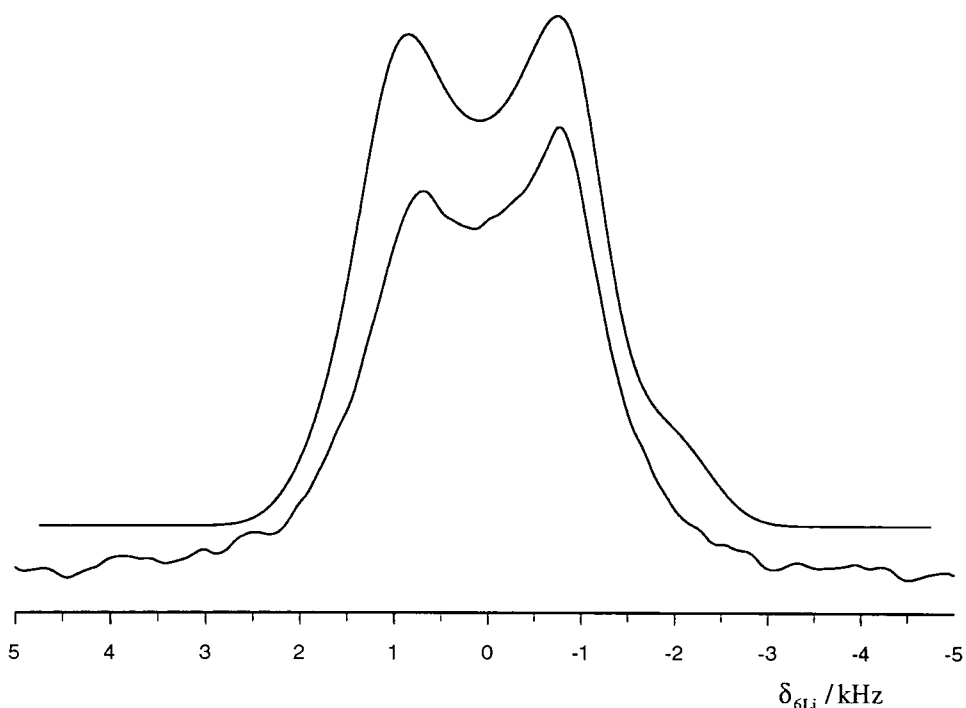


Figure 53: Static ${}^6\text{Li}$ NMR spectrum of lithium acetate recorded with proton decoupling and a quad echo. A simulation is shown above. Acquisition parameters were: pulse duration $6\ \mu\text{s}$, contact time $10\ \text{ms}$, echo time $\tau\ 60\ \mu\text{s}$, recycle delay $90\ \text{s}$, number of acquisitions 864, exponential line broadening $250\ \text{Hz}$. Simulation parameters were: $\chi = 2.5\ \text{kHz}$, $\eta_q = 0.0$, SA $\zeta\ 6.8\ \text{ppm}$, $\eta = 0.0$ and line broadening $800\ \text{Hz}$.

The best fit for the ${}^6\text{Li}$ NMR spectrum measured at $73.63\ \text{MHz}$ also found that the lineshape was broadened by $250\ \text{Hz}$ of exponential line broadening. As the line is so broad, the lineshape contains little detail, which prohibits accurate fitting for parameters apart from χ and shielding anisotropy. Until the resolution is better, finding the relative orientations of tensors will not be possible. The paper⁸ noted that a previous single-crystal ${}^7\text{Li}$ NMR study found $\chi = 155\ \text{kHz}$ and $\eta_q = 0.9$.¹⁷ These results were discounted in the paper and here by comparing simulations using these parameters and the experimental ${}^6\text{Li}$ static NMR spectra. No explanation can be given as to why the reported asymmetry is so different from that found here.

8.4.2.2 Spinning

When the sample is spun at the magic angle, the spectrum breaks into spinning sidebands. The simulations in Figure 54 show the different effects of the tensor interactions on the ${}^6\text{Li}$ (or any spin-1 nucleus) NMR spectra. The simulation parameters have been chosen to be the same as those found from the static spectra above. With the resonant frequency of ${}^6\text{Li}$ at 73.63 MHz (as on a spectrometer with a 11.7 T magnet), the shielding anisotropy of 0.5 kHz for lithium acetate is 6.8 ppm. It can be seen that the spectrum from just the shielding tensor shows few spinning sidebands and is not symmetric. By contrast, the spectrum from just the quadrupolar tensor is symmetric and has many more ssb's at this spinning speed. When both tensors are considered, the intensity of the centreband is increased relative to the ± 1 spinning sidebands, and the overall symmetry found in χ spectrum is lost. It can also be seen that this asymmetry of the spectrum extends out to all the ssb's and not just the central ones. As the external magnetic field strength is reduced, the differences between χ and combined spectrum will decrease. For fitting the shielding tensor, there will be very little variation in the spectrum, and any fitted values will have large, almost infinite, errors. For nuclei where the shielding interaction is more significant, e.g. vanadium-51, the effect of the shielding tensor is much more noticeable and the relative orientation of the two tensors can also be extracted from MAS spectra.¹⁸

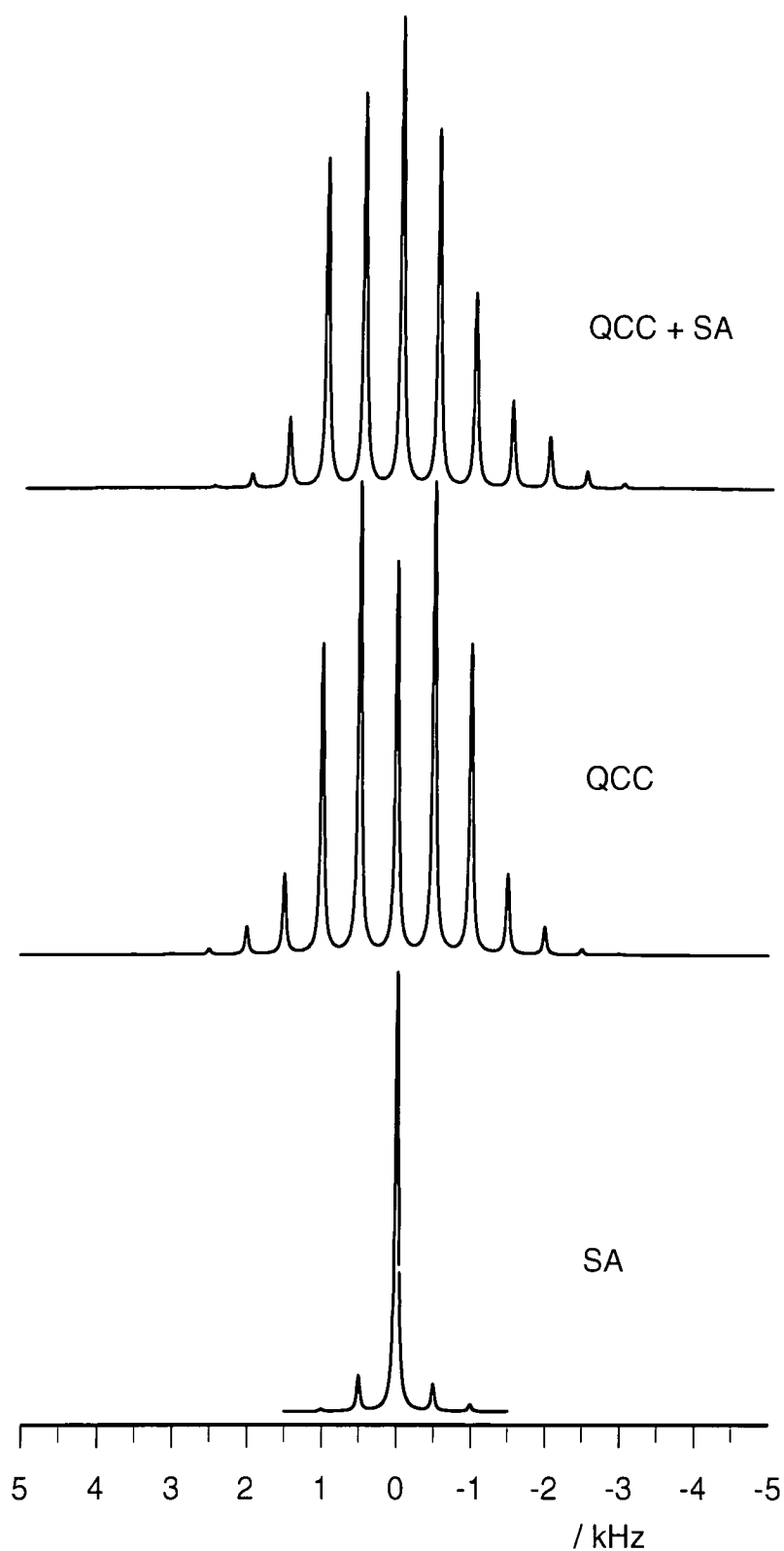


Figure 54: Simulation of quadrupolar and shielding interactions for ${}^6\text{Li}$. The parameters used (relevant to lithium acetate) are: $\chi = 2.5$ kHz, $\eta_q = 0.0$, SA $\zeta = 0.5$ kHz, $\eta = 0.0$ with a sample spinning speed of 0.5 kHz and line broadening 50 Hz.

8.5 Summary of results and ab initio calculations

Several NMR results have been reported for compounds containing lithium. The values for χ are summarised in Table 30 (at end), the asymmetry parameters are omitted as they are hard to measure accurately for ^7Li and are not always quoted. Ab initio calculations for lithium would be expected to be accurate even with small basis sets. These calculations can be used to predict the shielding tensor and the electric field gradient tensor. This latter tensor in turn can be used to calculate the quadrupolar tensor.

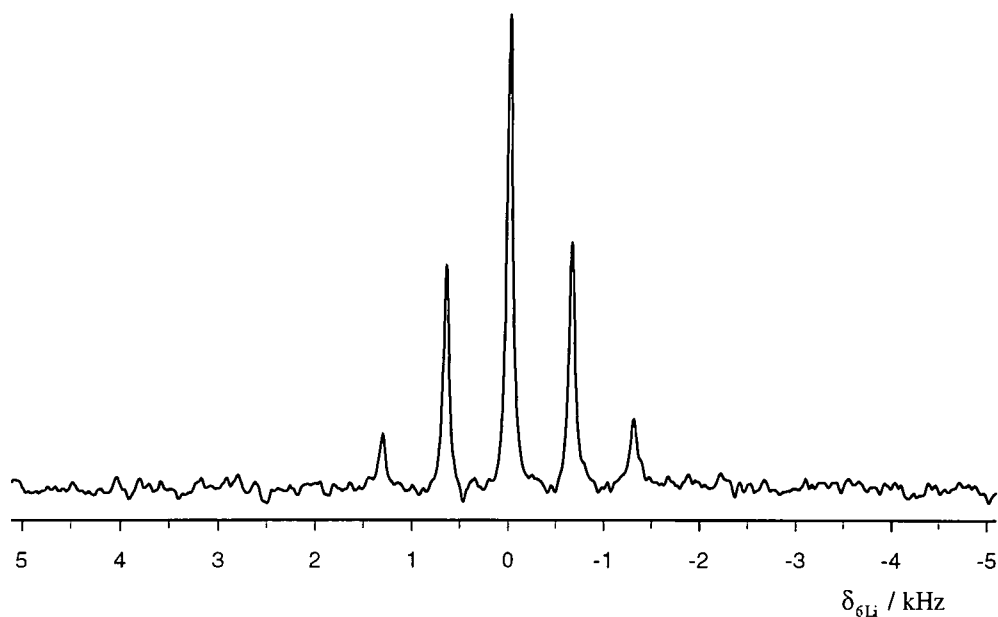


Figure 55: ^6Li CPMAS NMR spectrum of lithium acetate recorded with proton decoupling and the sample spinning at 650 Hz. Acquisition parameters were: pulse duration 6 μs , contact time 10 ms, recycle delay 90 s, number of acquisitions 8.

At low spinning speeds the ^6Li CPMAS NMR spectrum of lithium acetate breaks into spinning sidebands. For speeds above 3 kHz, the interactions are fully averaged and only the centreband peak is visible. The experimental ^6Li CPMAS NMR spectrum is shown in Figure 55 with the sample spinning at 650 Hz. This is shown for comparison to the simulated spectra shown in Figure 54, above, in which the sample spinning was 500 Hz. The spinning sidebands, in the experimental spectrum, are found to be non-symmetrical about the centreband as might be

expected from the discussion above. Fitting this spectrum gives the best-fit value for $\chi = 2.1$ kHz. This is smaller than that measured in the static ${}^6\text{Li}$ NMR spectra. No attempt has been made to fit this spectrum in order to find the shielding tensor as the differences in the ssb peaks are only small.

The ${}^7\text{Li}$ static NMR spectrum of lithium acetate, in Figure 56, shows signals, presumably from the outer transitions, at ± 26 kHz. There are also other peaks visible in the static lineshape, possibly from ${}^7\text{Li}$ nuclei at sites with crystal imperfections and thus other smaller values for χ . From the turning points, $\chi = 104$ kHz, which is not substantially different to that found from the static ${}^6\text{Li}$ spectrum (this estimates that $\chi({}^7\text{Li}) = 125$ kHz). The MAS NMR spectra show a tail off in the intensity of the spinning sidebands with increasing offset. Both of these spectra were recorded with cross polarisation, which explains the rapid tail-off in intensity for signals offset by more than 40 kHz from the transmitter (centred at 0 kHz). A simulation of the experimental NMR spectrum measured with the sample spinning at 4 kHz, using $\chi = 125$ kHz is in broad agreement after the intensity losses have been considered. As expected, the simulated spectra were indistinguishable whether the shielding interaction was included or not.

Although lithium diborate hydrate has been used to find the CP match, no values for χ have been reported. These have been measured here from the ${}^6\text{Li}$ CPMAS NMR spectra. Fitting the spectrum, measured with the sample spinning at 500 Hz, gives $\chi = 2.5$ kHz and $\eta_q = 0.64$. This is the same size of χ as measured for lithium acetate. The crystal structure of the anhydrous compound, determined by single-crystal XRD, is found to form an infinite three-dimensional network.¹⁹ A single-crystal ${}^7\text{Li}$ NMR study found $\chi = 104$ kHz and $\eta_q = 0.65$,²⁰ in good agreement with the ${}^6\text{Li}$ NMR results. The orientation of the tensor had been measured, but was not given in the poster abstract.

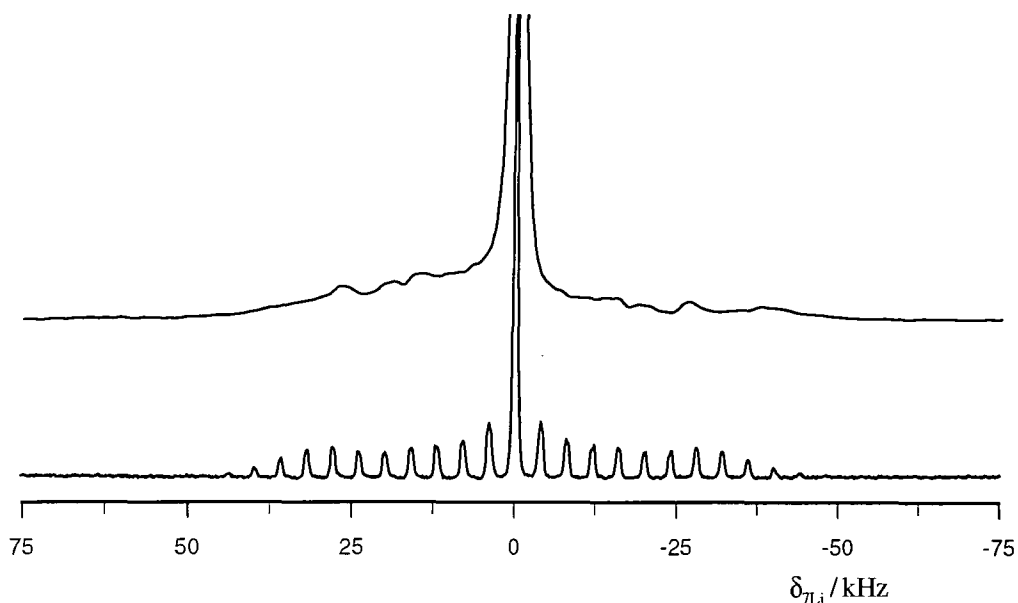


Figure 56: ${}^7\text{Li}$ CP NMR spectra of lithium acetate, with the top spectrum static and the bottom spectrum measured with spinning at 4 kHz. Acquisition parameters were: (top) pulse duration 4 μs , contact time 2 ms, quad-echo τ 20 μs , recycle delay 120 s, and number of acquisitions 2000; (bottom) pulse duration 4 μs , contact time 2 ms, recycle delay 15 s, and number of acquisitions 64.

An ab initio calculation for $(\text{LiBH}_4\cdot\text{TMEDA})_2$ using the XRD structure as shown in Figure 57,⁹ was found to converge to consistent results when using the Hartree-Fock approximation and the 6-31g* basis set. This gave the $\chi({}^7\text{Li}) = 104$ kHz, $\eta_q = 0.3$ and SA of $\zeta = 7$ ppm, $\eta_{\text{SA}} = 0.45$. The equivalent χ for ${}^6\text{Li}$ would be 2.08 kHz. These values are similar to those used for the simulation shown in Figure 54. The orientation of the tensors is included in the calculation, which shows that the main component of the shielding tensor lies in the plane of the paper along the line joining both lithium atoms. The quadrupolar tensor also lies in the plane of the paper and parallel to the line between the two boron atoms. Thus, the two tensors are calculated to be perpendicular to each other. These relative orientations could, in theory, be found from simulations of the experimental NMR spectra. However this is not possible in practice, and there may be ambiguities in the relative orientation and sign of the tensors.

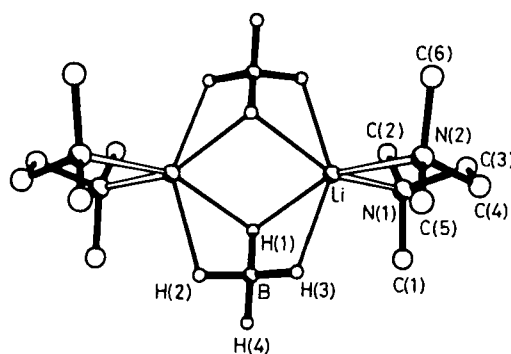


Figure 57: XRD structure of $(\text{LiBH}_4.\text{TMEDA})_2$ (from ref. 9)

This compound has been previously studied by solid-state ^7Li NMR.⁴ In the ^7Li MAS NMR spectra, the intensity of the spinning sidebands tails off more rapidly than expected. The static ^7Li NMR spectrum shows a doublet for the centreband, with a splitting of 1.58 kHz, and multiple peaks that could be the turning points of the outer transitions. This splitting of the centreband peak could not be explained by consideration of dipolar coupling to other nuclei. The multiple outer turning points could be attributed to there being a distribution of χ caused by motion or crystal imperfections. The ^6Li MAS NMR spectrum has spinning-sideband peaks over a range of ca. ± 1 kHz, but no fine structure. The value of χ is concluded, from the ^7Li static NMR measurements, to lie in the range 90 – 140 kHz. This is in agreement with the calculated value found above (104 kHz). The other lithium tetrahydroborate compounds studied in the same paper do not have readily available XRD structures, so no further calculations have been made.

Hexamethyleneimidolithium, $[\text{H}_2\text{C}(\text{CH}_2)_5\text{NLi}]_6$, contains three coordinate lithium atoms arranged as a cyclised lithium amide ladder. This compound is air sensitive so it has been sealed in a glass insert. The ^7Li MAS NMR of this compound has been previously measured in Durham.²² Difficulties were experienced with measuring the spectrum as the ssb peaks extend over 300 kHz. A spinning-sideband analysis of the spectrum, after baseline correction, gave $\chi = 330$ kHz and $\eta_q = 1.0$. In the present work the ^6Li MAS NMR spectrum of this compound has been measured. In this case, loss of signal intensity is not a problem as the signal is spread over a much smaller range. Fitting the spectrum measured with spinning at 2 kHz, gives

$\chi = 7 \pm 0.2$ kHz. This corresponds to $\chi(^7\text{Li}) = 350 \pm 10$ kHz and is in agreement with the previous results. In this case, ab initio results predict a larger value of $\chi = 500$ kHz, in poor agreement with the experimental results. A recent study of lithium amides has given a correlation between χ and the N-Li-N bond angle.²¹

$$\chi / \text{kHz} = 4.1 \times \text{angle (N-Li-N) in degrees} - 111$$

For a nearly linear compound, $\chi = 610$ kHz. As the bond angle decreases, so does χ . However, this equation is not applicable to the above compound as the lithium is coordinated to three nitrogen atoms. The above compound was examined during the study and found to give $\chi = 310$ kHz and $\eta_q = 0.7$, in agreement with the experimental NMR results above.

Two of the iminophosphorane compounds studied in the previous chapter also contain lithium. For $(\text{Ph}_3\text{PNLi}\cdot\text{LiBr})_2$, the ^6Li MAS NMR spectrum (not shown), recorded with spinning at 1.5 kHz, gives $\chi = 4.5$ kHz. This equates to $\chi(^7\text{Li}) = 225$ kHz. The signal-to-noise ratio was poor because the sample, being air sensitive, was stored in a sealed glass insert. The ^7Li CPMAS spectrum has ssb peaks near to the centreband with large intensities, which indicates that the asymmetry in this compound is large. The ^7Li static NMR spectrum in Figure 58 shows weak peaks at ca. ± 40 kHz and a splitting of the central transition peak. The splitting of the central transition peak was about 3.6 kHz when measured at 77.78 MHz, this is similar to the splitting observed in the spectrum of $(\text{LiBH}_4\cdot\text{TMEDA})_2$. As in that case, no explanation can be given for the cause of the splitting. The splitting is larger than any of the dipolar couplings to other nuclei and outside the chemical shift range. However, the centre of gravity for the sum of the peaks lies at -2.6 ppm.

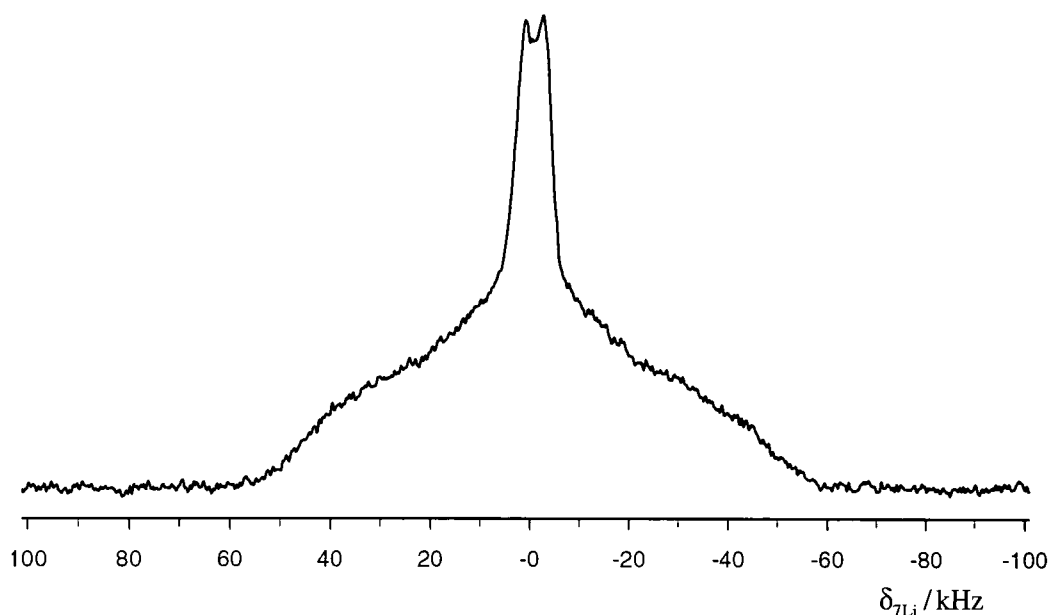


Figure 58: Static ${}^7\text{Li}$ NMR spectrum of $(\text{Ph}_3\text{PNLi.LiBr})_2$ recorded with CP, proton decoupling and a quad-echo. Acquisition parameters were: pulse duration $5\ \mu\text{s}$, contact time $5\ \text{ms}$, quad-echo $\tau\ 50\ \mu\text{s}$, recycle delay $5\ \text{s}$, and number of acquisitions 10000.

Only the ${}^7\text{Li}$ CPMAS NMR spectra of $(\text{Ph}_3\text{PNH.LiOAr})_2$ have been recorded. These suffer from loss of signal intensity towards the edge of the spectrum, prohibiting an accurate measurement of χ . From a visual comparison with the ${}^7\text{Li}$ CPMAS NMR spectra of $(\text{Ph}_3\text{PNLi.LiBr})_2$, it would be expected to be larger than χ for this compound, perhaps 280 kHz. Considering the loss of intensity in the spectrum, it may be larger than this, approaching the ab initio value of 350 kHz. The asymmetry, estimated from the experimental NMR spectrum, is moderate, $\eta_q = 0.2$.

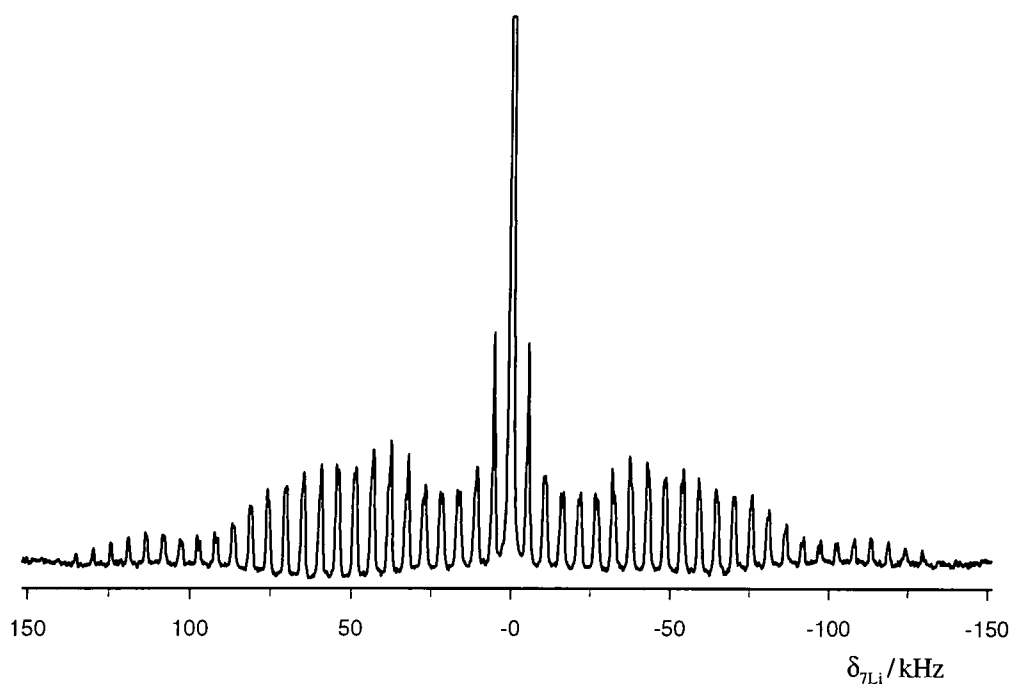


Figure 59: ^7Li CPMAS NMR spectrum of $(\text{Ph}_3\text{PNLi.LiBr})_2$ recorded with CP and proton decoupling with the sample spinning at 5.4 kHz. Acquisition parameters were: pulse duration 5 μs , contact time 5 ms, recycle delay 5 s, and number of acquisitions 1000.

Table 30: Summary $\chi(^7\text{Li})$

Compound	χ / kHz	χ / kHz	Reference
	Experimental	Ab initio (rhf/6-31g*)	
Lithium diborate	125	-	This work
Lithium acetate	125	-	This work
$(\text{LiBH}_4.\text{TMEDA})_2$	90 – 140	104	4
$\text{LiBH}_4.\text{PMDETA}$	125	-	4
$\text{LiBH}_4.\text{Pyr}_4$	34	-	4
$\text{LiBH}_4.\text{HMPA}_4$	11	-	4
$[\text{H}_2\text{C}(\text{CH}_2)_5\text{NLi}]_6$	330	500	9, 22
$(\text{Ph}_3\text{PNLi.LiBr})_2$	225	210 – 250	This work
$(\text{Ph}_3\text{PNH.LiOAr})_2$	280	350	This work

In summary, further experimental work needs to be carried out in order to obtain consistent $^{6,7}\text{Li}$ NMR results for these compounds. The experimental techniques have been investigated here, which should allow better measurements to be made in the future. At present, the ^7Li static NMR spectra have been used to estimate the value of χ , given in Table 30. The ^6Li static NMR spectra are heavily line-broadened compared to the size of the quadrupole coupling constant, so that estimates of NMR parameters will have large errors. The $^{6,7}\text{Li}$ MAS NMR spectra give similar values for χ to those found from the ^7Li static NMR spectra. With the small amount of new data given here, it is not possible to discuss correlations between the NMR parameters and structure. However, ab initio calculations appear to agree well with the currently measured NMR data.

-
- ¹ R. K. Harris and A. P. Minoja, *Magn. Reson. Chem.*, **33**, 152 (1995)
- ² H. Günther, Lithium NMR, in "Encyclopaedia of NMR" (D. M. Grant and R. K. Harris, Eds.), 2807, Wiley, Chichester (1997); H. Günther, High-resolution ⁷Li NMR of Organolithium Compounds, in "Advanced Applications of NMR to Organometallic Chemistry" (M. Gielen, R. Willem, and B. Wrackmeyer, Eds.), Wiley, Chichester (1996)
- ³ D. Johnels, A. Andersson, A. Bouman, and U. Edlund, *Magn. Reson. Chem.*, **34**, 908 (1996)
- ⁴ J. E. Espidel, R. K. Harris, and K. Wade, *Magn. Reson. Chem.*, **31**, 166 (1994)
- ⁵ D. I. Hoult, C. N. Chen, H. Eden, and M. Eden, *J. Magn. Reson.*, **51**, 110 (1983)
- ⁶ R. Kyburz, 'Varian NMR Basics' in *Magnetic Moments*, **7**, p.33
- ⁷ J. Skibsted, N. C. Nielsen, H. Bildsøe, and H. J. Jakobsen, *J. Magn. Reson.*, **95**, 88 (1991)
- ⁸ G. H. Penner and J. Hutzal, *Magn. Reson. Chem.*, **35**, 222 (1997)
- ⁹ D. R. Armstrong, W. Clegg, H. M. Colquhoun, J. A. Daniels, R. E. Mulvey, I. R. Stephenson, and K. Wade, *J. Chem. Soc., Chem. Commun.*, 630 (1987)
- ¹⁰ T. Pietrass, F. Taulelle, P. Lavela, J. Olivier-Fourcade, J. Jumas, and S. Steuernagel, *J. Phys. Chem. B*, **101**, 6715 (1997)
- ¹¹ see for example: P. P. Man, Quadrupolar Interactions in "Encyclopaedia of NMR" (D. M. Grant and R. K. Harris, Eds.), 3838, Wiley, Chichester (1997)
- ¹² L. Frydman and J. S. Harwood, *J. Am. Chem. Soc.*, **117**, 5367 (1995)
- ¹³ J.-P. Amoureux, C. Fernandez, and S. Steuernagel, *J. Magn. Reson. A*, **123**, 116 (1996)
- ¹⁴ S. H. Wang, S. M. De Paul, and L. M. Bull, *J. Magn. Reson.*, **125**, 364 (1997)
- ¹⁵ A. Samoson and E. Lippmaa, *J. Magn. Reson.*, **79**, 255 (1988)
- ¹⁶ F. Pauer, J. Rocha, and D. Stalke, *J. Chem. Soc., Chem. Commun.*, 1477 (1991)
- ¹⁷ V. S. Bhat, A. C. Padmanabhan, and S. Srinivasan, *Acta Cryst. B*, **30**, 846 (1975)
- ¹⁸ J. Skibsted, N. C. Nielsen, H. Bildsøe, and H. J. Jakobsen, *Chem. Phys. Lett.*, **188**, 405 (1992)
- ¹⁹ J. Krogh-Moe, *Acta Cryst.*, **15**, 190 (1962)
- ²⁰ I. G. Kim, N. K. Sung, S. H. Choh, and J. N. Kim, 37th Experimental NMR Conference, Asilomar (1996)
- ²¹ M. Hartung, H. Günther, J. Amoureux, and C. Fernández, *Magn. Reson. Chem.*, **36**, S61 (1998)
- ²² A. P. Minoja, unpublished results

9 Suggestions for Future Work

The uses and limitations of the spectrometer including its probes have been explored during this work. Air sensitive samples can be readily measured by sealing them in glass or plastic inserts. Multinuclear NMR experiments have enabled us to manipulate the spectra in order to measure the separate interactions. Double decoupling with the ^1H and ^{19}F decoupler powers at the Hartmann-Hahn match appears to be efficient for Me_3SnF . However, this effect should be verified for a range of compounds, and a theoretical description to explain this effect is still lacking.

The loss of signal intensity away from the transmitter due to cross polarisation, and the probe tuning and excitation profile has been observed in both ^{119}Sn and ^7Li NMR spectra. The simulation programs have been developed to fit NMR spectra measured in ideal conditions. This has not always been the case for the spectra measured herein, and these programs could be extended to allow for the observed losses in signal intensity. In particular, by modelling for the different losses when using cross polarisation in static and spinning samples, the arguments given in Chapter 6 could be confirmed.

The organotin compounds have been extensively studied. With the better understanding of the ^{19}F NMR shifts, we have been able to suggest that neO_3SnF is four-coordinate. This coordination needs to be confirmed by the ^{119}Sn NMR shift and the size of the shielding anisotropy. From the $^1\text{J}(\text{SnF})$ coupling constants measured in the ^{19}F NMR spectra we have observed, for the first time, the effects of uneven Sn-F bridging. This effect can now be checked in the ^{19}F NMR spectra of the other compounds. As yet, we have been unable to measure the angular nature of the Sn-F-Sn bonds by NMR techniques.

Ideally, the ^{119}Sn NMR spectra of Me_2SnF_2 and $^n\text{Bu}_2\text{SnF}_2$ should be re-measured with the transmitter in different positions in order to confirm the turning points. The assignment of the ^{19}F NMR shifts, as opposed to the impurity signals, could be confirmed by a $^{19}\text{F} \rightarrow ^{119}\text{Sn}$ HETCOR experiment, though the measurement

could take many days to achieve a good signal-to-noise ratio. It is hoped that the structure suggested here for ${}^n\text{Bu}_2\text{SnF}_2$ will be confirmed by other techniques.

Our understanding of ΔJ is still limited by the lack of results. It is hoped that this will improve with more NMR measurements of D' and with new determinations of the structures for these compounds by single crystal and powder X-ray diffraction and other techniques. The semi-empirical calculations are, at present, only qualitative. With the new data given herein and ever increasing computing power, it is hoped that these calculations can develop into a technique with predictive quality.

The NMR data have proved useful in determining the electronic structure and nature of bonding in the iminophosphorane compounds. The results from ab initio calculations also agree remarkably well with the NMR data. In this work, most of the time and effort was spent measuring the NMR spectra for the air-stable salt. Given sufficient time, the static ${}^{31}\text{P}$ and other NMR spectra could be measured for the other compounds. From these spectra, it should be possible to measure the P-N bond length and the relative orientations of the shielding and dipolar tensors. The simulation programs for compounds with residual dipolar coupling measured spinning off the magic angle, were not used here, though they would be expected to give yet more information about the internal electronic structure of the compounds.

For the lithium containing compounds, it has been observed that using CP when observing ${}^6\text{Li}$ can give a spectrum with a good signal-to-noise ratio, in a shorter time than when using direct polarisation. This is also partly true for ${}^7\text{Li}$, however the loss of signal intensity due to CP is significant, which makes it impractical. For ${}^7\text{Li}$, using short high-power pulses will give a spectrum with the least loss of signal. With better measurements, on high-field spectrometers, it would be hoped to measure relative orientational information for the shielding and quadrupolar tensors. From this point, it may then be possible to discuss the correlations between the NMR parameters and structure.

This appendix describes the rotation of the shielding tensor into the Principal Axis System (PAS). The example is taken from the Gaussian 94 calculation results for $\text{Ph}_3\text{NH}_2\text{Br}$ using the Hartree-Fock approximation and the 6-31g* basis set.

Shielding Tensor in Standard Orientation
 (Note that the shielding is given relative to the bare nucleus.)

$$A = \begin{bmatrix} 367.7779 & 8.5051 & 1.0643 \\ -8.1319 & 403.6719 & 26.5552 \\ -1.5608 & 12.6549 & 407.2967 \end{bmatrix}$$

The standard orientation is used by Gaussian to optimise the efficiency of the calculation. This tensor can be decomposed into Isotropic, Symmetric tensor and Antisymmetric tensor components. The isotropic component can be related to the chemical shift scale by using the absolute shielding of a known reference compound, for example $\text{H}_3\text{PO}_4 = 328.35$ ppm.

$$\text{Isotropic}(\text{shielding}) = \frac{\text{trace}(A)}{3} = 392.916 \text{ ppm}$$

$$\text{Isotropic}(\text{shift}) = 328.35 - 392.916 = -64.565 \text{ ppm}$$

$$\text{Symmetric} = \frac{A + A^T}{2} - \text{Isotropic} \cdot \text{Identity} = \begin{bmatrix} -25.138 & 0.187 & -0.248 \\ 0.187 & 10.756 & 19.605 \\ -0.248 & 19.605 & 14.381 \end{bmatrix}$$

$$\text{Antisymmetric} = \frac{A - A^T}{2} = \begin{bmatrix} 0 & 8.319 & 1.313 \\ -8.319 & 0 & 6.95 \\ -1.313 & -6.95 & 0 \end{bmatrix}$$

The eigenvalues and eigenvectors of the symmetric part of A may be calculated. The eigenvalues correspond to the tensor in the principal axis system. The eigenvectors (given in columns) relate the PAS to the internal (standard) coordination system. They give the direction in space of the principal tensor components.

$$\text{Eigenvalues} = [-25.142 \quad -7.115 \quad 32.258]$$

$$\text{Eigenvectors} = \begin{bmatrix} 1 & 0.017 & -0.001 \\ -0.012 & 0.739 & 0.674 \\ 0.012 & -0.674 & 0.739 \end{bmatrix}$$

The similarity transform $U^T A U = \Lambda$ can be checked as shown below. U is the matrix containing the eigenvectors and Λ (Lambda) is a diagonal matrix with the principal components of the tensor (eigenvalues) along the diagonal

$$\text{Eigenvectors}^T \cdot \text{Symmetric} \cdot \text{Eigenvectors} = \begin{bmatrix} -25.143 & 0 & 0 \\ 0 & -7.115 & 0 \\ 0 & 0 & 32.258 \end{bmatrix}$$

The Molecular Geometry (in the standard coordinate system) gives the atom positions. From this, the P-N bond vector can be calculated and hence the orientation of the dipolar tensor. The modulus of PN gives the bond length = 1.615 Å

$$P = \begin{bmatrix} 0.0306 \\ -0.0171 \\ 0.8355 \end{bmatrix} \quad N = \begin{bmatrix} 0.0638 \\ -0.2063 \\ 2.4389 \end{bmatrix} \quad PN = N - P = \begin{bmatrix} 0.033 \\ -0.189 \\ 1.603 \end{bmatrix}$$

To find the orientation of the shielding tensor relative to the dipolar tensor, we can use vector algebra. The angle β is given by the arccosine of the dot product of the PN vector and the eigenvector corresponding to the largest component of the shielding tensor (σ_{33}). If we define a vector $\{B\}$ perpendicular to the plane containing PN and the eigenvector corresponding to largest component of the shielding tensor (σ_{33}), which is the cross product of these vectors. Then the angle α can be found finding the arcsine of the dot product between the vector $\{B\}$ and the eigenvector corresponding to the largest component of the shielding tensor (σ_{22}). All vectors must be normalised.

$$\beta = \arccos(\text{PN} \cdot \text{Eigenvector}_{33}) = 49.101^\circ$$

$$\alpha = \arcsin(\text{Eigenvector}_{22} \cdot \{\text{PN} \wedge \text{Eigenvector}_{33}\}) = -1.949^\circ$$

Publications

“New Multinuclear Experiments on Solid Organotin Fluorides”

J. C. Cherryman and R. K. Harris, *J. Magn. Reson.*, **128**, 21 (1997)

“2,2′/6′,4″-Terpyridine - A Cyclometallating Analog of 2,2′/6′,2″-Terpyridine for Metallo-supramolecular Chemistry”

E. C. Constable, A. M. W. Thompson, J. Cherryman, and T. Liddiment, *Inorg. Chim. Acta*, **235**, 165 (1995)

Research Conferences Attended

Inorganic and Organometallic NMR, Turin, 26th March – 1st April 1995

NMR of Solids and Solid-Like Materials, NMR discussion group meeting, University College, London, 19th December 1995.

EPS-2 The Second Electronic NMR Conference, on the World Wide Web (www), 17-21st June 1996.

Summer School on NMR of Solids, University of Durham, 16-20th September 1996.

Royal Society of Chemistry 13th International meeting on NMR Spectroscopy, University of Exeter, 6-11th July 1997.

New Dimensions in Solid State NMR of Quadrupolar Nuclei, BRSG Autumn Meeting, London, 19th November 1997.

39th Experimental NMR Conference, Asilomar, California, 22-27th March 1998.

Royal Society of Chemistry Annual Congress and Young Researchers Meeting, University of Durham, 6-9th April 1998.

Main Group Symposium, University of Durham, 29th June 1998

Oral Presentations

New Multinuclear Experiments on Solid Organotin Fluorides
Royal Society of Chemistry 13th International meeting on NMR Spectroscopy, University of Exeter, 6-11th July 1997.

New Multinuclear Experiments on Solid Organotin Fluorides
Final year Graduate symposium, University of Durham, 1st June 1998

Poster Presentations

New Multinuclear Experiments on Solid Organotin Fluorides
EPS-2 The Second Electronic NMR Conference, on the World Wide Web (www), 17-21st June 1996.

New Multinuclear Experiments on Solid Organotin Fluorides
I.C.I. Poster Competition, University of Durham, 22nd December 1997

Structural and Electronic Information from a Combined Multinuclear Solid-State Magnetic Resonance and Ab Initio Study of Iminophosphoranes
39th Experimental NMR Conference, Asilomar, California, 22-27th March 1998.

Structural and Electronic Information from a Combined Multinuclear Solid-State Magnetic Resonance and Ab Initio Study of Iminophosphoranes
R. S. C. Young Researchers Meeting, University of Durham, 6th April 1998.

Research colloquia, seminars and lectures given by
invited speakers

(‡ denotes lectures attended)

1995

- October 11 Prof. P. Lugar, Frei University of Berlin, FRG
Low Temperature Crystallography ‡
- October 13 Prof. R. Schmutzler, University of Braunschweig, FRG
Calixarene-Phosphorus Chemistry: A New Dimension in Phosphorus
Chemistry
- October 18 Prof. A. Alexakis, Universit e de Pierre et Marie Curie, Paris
Synthetic and Analytical Uses of Chiral Diamines
- October 25 Dr. D. Martin Davies, University of Northumbria
Chemical reactions in organised systems ‡
- November 1 Prof. W. Motherwell, UCL London
New Reactions for Organic Synthesis
- November 3 Dr B. Langlois, University Claude Bernard-Lyon
Radical Anionic and Pseudo Cationic Trifluoromethylation
- November 8 Dr. D. Craig, Imperial College, London
New Strategies for the Assembly of Heterocyclic Systems
- November 15 Dr Andrea Sella, UCL, London
Chemistry of Lanthanides with Polypyrazoylborate Ligands
- November 17 Prof. David Bergbreiter, Texas A&M, USA
Design of Smart Catalysts, Substrates and Surfaces from Simple
Polymers
- November 22 Prof. I Soutar, Lancaster University
A Water of Glass? Luminescence Studies of Water-Soluble
Polymers ‡
- November 29 Prof. Dennis Tuck, University of Windsor, Ontario, Canada
New Indium Coordination Chemistry
- December 8 Professor M. T. Reetz, Max Planck Institut, Mulheim
Perkin Regional Meeting, Untitled

1996

- January 10 Dr Bill Henderson, Waikato University, NZ
Electrospray Mass Spectrometry - a new sporting technique ‡
- January 17 Prof. J. W. Emsley, Southampton University
Liquid Crystals: More than Meets the Eye ‡
- January 24 Dr Alan Armstrong, Nottingham University
Alkene Oxidation and Natural Product Synthesis
- January 31 Dr J. Penfold, Rutherford Appleton Laboratory,
Soft Soap and Surfaces
- February 7 Dr R. B. Moody, Exeter University
Nitrosations, Nitrations and Oxidations with Nitrous Acid
- February 12 Dr Paul Pringle, University of Bristol
Catalytic Self-Replication of Phosphines on Platinum(O)
- February 14 Dr J. Rohr, University of Gottingen, FRG
Goals and Aspects of Biosynthetic Studies on Low Molecular
Weight Natural Products
- February 21 Dr C. R. Pulham, University of Edinburgh
Heavy Metal Hydrides - an exploration of the chemistry of stannanes
and plumbanes ‡
- February 28 Prof. E. W. Randall, Queen Mary & Westfield College
New Perspectives in NMR Imaging ‡
- March 6 Dr Richard Whitby, University of Southampton
New approaches to chiral catalysts: Induction of planar and metal
centred asymmetry
- March 7 Dr D. S. Wright, University of Cambridge
Synthetic Applications of Me₂N-p-Block Metal Reagents
- March 12 RSC Endowed Lecture - Prof. V. Balzani, University of Bologna
Supramolecular Photochemistry ‡
- March 13 Prof. Dave Garner, Manchester University
Mushrooming in Chemistry
- April 30 Dr L. D. Pettit, Chairman, IUPAC Commission of Equilibrium Data
pH-metric studies using very small quantities of uncertain purity

- October 9 Professor G. Bowmaker, University of Auckland, NZ
Coordination and Materials Chemistry of the Group 11 and Group 12
Metals: Some Recent Vibrational and Solid-State NMR Studies ‡
- October 14 Professor A. R. Katritzky, University of Gainesville, University of
Florida, USA
Recent Advances in Benzotriazole Mediated Synthetic
Methodology
- October 16 Professor Ojima, Guggenheim Fellow, State University of New York
at Stony Brook
Silylformylation and Silylcarbocyclisations in Organic Synthesis
- October 22 Professor Lutz Gade, University of Wuerzburg, Germany
Organic transformations with Early-Late Heterobimetallics:
Synergism and Selectivity
- October 22 Professor B. J. Tighe, Department of Molecular Sciences and
Chemistry, University of Aston
Making Polymers for Biomedical Application - Can we meet
Nature's Challenge? (Joint lecture with the Institute of
Materials)
- October 23 Professor H. Ringsdorf (Perkin Centenary Lecture), Johannes
Gutenberg-Universitat, Mainz, Germany
Function Based on Organisation
- October 29 Professor D. M. Knight, Department of Philosophy, University of
Durham.
The Purpose of Experiment - A Look at Davy and Faraday ‡
- October 30 Dr Phillip Mountford, Nottingham University
Recent Developments in Group IV Imido Chemistry ‡
- November 6 Dr Melinda Duer, Chemistry Department, University of
Cambridge
Solid-state NMR Studies of Organic Solid to Liquid-crystalline
Phase Transitions ‡
- November 12 Professor R. J. Young, Manchester Materials Centre, UMIST
New Materials - Fact or Fantasy? (Joint Lecture with Zeneca &
RSC) ‡
- November 13 Dr G. Resnati, University of Milan
Perfluorinated Oxaziridines: Mild Yet Powerful Oxidising Agents

- November 18 Professor G. A. Olah, University of Southern California, USA
Crossing Conventional Lines in my Chemistry of the Elements ‡
- November 19 Professor R. E. Grigg, University of Leeds
Assembly of Complex Molecules by Palladium-Catalysed
Queueing Processes
- November 20 Professor J. Earnshaw, Department of Physics, Belfast University
Surface Light Scattering: Ripples and Relaxation ‡
- November 27 Dr Richard Templer, Imperial College, London
Molecular Tubes and Sponges
- December 3 Professor D. Phillips, Imperial College, London
"A Little Light Relief" ‡
- December 4 Professor K. Muller-Dethlefs, York University
Chemical Applications of Very High Resolution ZEKE Photoelectron
Spectroscopy ‡
- December 11 Dr Chris Richards, Cardiff University
Stereochemical Games with Metallocenes
- 1997
- January 15 Dr V. K. Aggarwal, University of Sheffield
Sulfur Mediated Asymmetric Synthesis
- January 16 Dr Sally Brooker, University of Otago, NZ
Macrocycles: Exciting yet Controlled Thiolate Coordination
Chemistry
- January 21 Mr D. Rudge, Zeneca Pharmaceuticals
High Speed Automation of Chemical Reactions ‡
- January 22 Dr Neil Cooley, BP Chemicals, Sunbury
Synthesis and Properties of Alternating Polyketones ‡
- January 29 Dr Julian Clarke, UMIST
What can we learn about polymers and biopolymers from computer-
generated nanosecond movie-clips? ‡
- February 4 Dr A. J. Banister, University of Durham
From Runways to Non-metallic Metals - A New Chemistry Based
on Sulfur

- February 5 Dr A. Haynes, University of Sheffield
Mechanism in Homogeneous Catalytic Carbonylation
- February 12 Dr Geert-Jan Boons, University of Birmingham
New Developments in Carbohydrate Chemistry
- February 18 Professor Sir James Black, Foundation/King's College London
My Dialogues with Medicinal Chemists ‡
- February 19 Professor Brian Hayden, University of Southampton
The Dynamics of Dissociation of Molecules at Surfaces ‡
- February 25 Professor A. G. Sykes, University of Newcastle
The Synthesis, Structures and Properties of Blue Copper Proteins
- February 26 Dr. Tony Ryan, UMIST
Making Hairpins from Rings and Chains
- March 4 Professor C. W. Rees, Imperial College
Some Very Heterocyclic Chemistry
- March 5 Dr. J. Staunton FRS, Cambridge University
Tinkering with biosynthesis: towards a new generation of antibiotics
- March 11 Dr A. D. Taylor, ISIS Facility, Rutherford Appleton Laboratory
Expanding the Frontiers of Neutron Scattering
- March 19 Dr Katharine Reid, University of Nottingham
Probing Dynamical Processes with Photoelectrons ‡
- October 8 Prof. E. Atkins, Department of Physics, University of Bristol
Advances in the control of architecture for polyamides: from nylons to genetically engineered silks to monodisperse oligoamides
- October 15 Dr. R. Mark Ormerod, Department of Chemistry, Keele University
Studying catalysts in action ‡
- October 21 Prof. A. F. Johnson, IRC, Leeds
Reactive processing of polymers: science and technology
- October 22 Prof. R.J. Puddephatt (RSC Endowed Lecture), University of Western Ontario
Organoplatinum chemistry and catalysis ‡

- October 23 Prof. M.R. Bryce, University of Durham, Inaugural Lecture
New Tetrathiafulvalene Derivatives in Molecular, Supramolecular
and Macromolecular Chemistry: controlling the electronic properties
of organic solids
- October 29 Prof. Bob Peacock, University of Glasgow
Probing chirality with circular dichroism
- October 28 Prof. A P de Silva, The Queen's University, Belfast
Luminescent signalling systems
- November 5 Dr Mimi Hii, Oxford University
Studies of the Heck reaction
- November 11 Prof. V. Gibson, Imperial College, London
Metallocene polymerisation ‡
- November 12 Dr. Jeremy Frey, Department of Chemistry, Southampton
University
Spectroscopy of liquid interfaces: from bio-organic chemistry to
atmospheric chemistry ‡
- November 19 Dr. Gareth Morris, Department of Chemistry, Manchester
University
Pulsed field gradient NMR techniques: Good news for the Lazy
and DOSY
- November 20 Dr. Leone Spiccia, Monash University, Melbourne, Australia
Polynuclear metal complexes
- November 25 Dr. R. Withnall, University of Greenwich
Illuminated molecules and manuscripts
- November 26 Prof. R.W. Richards, University of Durham, Inaugural Lecture
A random walk in polymer science ‡
- December 2 Dr. C. J. Ludman, University of Durham
Explosions
- December 3 Prof. A. P. Davis, Department of Chemistry, Trinity College
Dublin.
Steroid-based frameworks for supramolecular chemistry
- December 10 Sir Gordon Higginson, former Professor of Engineering in Durham
and retired Vice-Chancellor of Southampton University.
1981 and all that ‡

December 10 Prof. Mike Page, Department of Chemistry, University of Huddersfield
The mechanism and inhibition of beta-lactamases

1998

- January 14 Prof. David Andrews, University of East Anglia
Energy transfer and optical harmonics in molecular systems
- January 20 Prof. J. Brooke, University of Lancaster
What's in a formula? Some chemical controversies of the 19th century ‡
- January 21 Prof. David Cardin, University of Reading
Untitled
- January 27 Prof. Richard Jordan, Dept. of Chemistry, University of Iowa, USA
Cationic transition metal and main group metal alkyl complexes in olefin polymerisation
- January 28 Dr Steve Rannard, Courtaulds Coatings (Coventry)
The synthesis of dendrimers using highly selective chemical reactions
- February 3 Dr J. Beacham, ICI Technology
The chemical industry in the 21st century ‡
- February 4 Prof. P. Fowler, Department of Chemistry, Exeter University
Classical and non-classical fullerenes ‡
- February 11 Prof. J. Murphy, Dept of Chemistry, Strathclyde University
Untitled
- February 17 Dr. S. Topham, ICI Chemicals and Polymers
Perception of environmental risk: The River Tees, two different rivers
- February 18 Prof. Gus Hancock, Oxford University
Surprises in the photochemistry of tropospheric ozone ‡
- February 24 Prof. R. Ramage, University of Edinburgh
The synthesis and folding of proteins ‡

- February 25 Dr. C. Jones, Swansea University
Low coordination arsenic and antimony chemistry
- March 4 Prof. T. C. B. McLeish, IRC of Polymer Science Technology, Leeds University
The polymer physics of pyjama bottoms (or the novel rheological characterisation of long branching in entangled macromolecules)
- March 11 Prof. M. J. Cook, Dept of Chemistry, UEA
How to make phthalocyanine films and what to do with them
- March 17 Prof. V. Rotello, University of Massachusetts, Amherst
The interplay of recognition & redox processes - from flavoenzymes to devices
- March 18 Dr John Evans, Oxford University
Materials which contract on heating (from shrinking ceramics to bulletproof vests)

